KU-18-3

Dynamic Performance of Cantilevered Sign Trusses for Fatigue

By

Hunter Senior, M.S.

Caroline Bennett, Ph.D., P.E.

William Collins, Ph.D., P.E.

Jian Li, Ph.D., P.E.

Mark Ewing, Ph.D.

Matt Fadden, Ph.D., P.E.

A Report on Research Sponsored by
The Kansas Department of Transportation

Structural Engineering and Engineering Materials
SM Report No. 133
July 2019

THE UNIVERSITY OF KANSAS CENTER FOR RESEARCH, INC.

2385 Irving Hill Road – Campus West, Lawrence, Kansas 66045

Executive Summary

Cantilevered overhead sign structures (COSS) experience cyclic loading due to stochastic loads such as natural wind gusts (NWG). Wind loading can produce large deflections in the cantilever and large-magnitude stresses can develop at the box-type connection between the cantilevered arm and mast where fatigue performance is a concern. Modifications to the sign structures pose further concerns as changes to the aerodynamic properties could have unintended consequences. A design consideration of COSS is serviceability of the sign through use of a steel grate walkway that workers can use for maintenance on the sign. The steel grate walkways on COSS are rarely used for maintenance anymore, hence are being removed by multiple state DOTs to prevent vandalism. However, the impact on COSS with the removal of the walkways is unknown.

This report describes an investigation in which the dynamic and aerodynamic properties of COSS was studied, and the effect of the walkway presence on structural response was explored. Computer simulations of 32 different COSS configurations were carried out to see the effect of the grate removal on the natural frequency and the mass of the overall structural system. Aerodynamic performance was considered through the use of computational fluid dynamics (CFD) and experimental testing, where wind pressure on the sign in both axial directions and effects of vortex shedding were examined. Findings include: 1) the walkway had a minimal effect on the system's mass and natural frequencies, 2) the walkway had a minimal influence on the wind-induced force on the sign, 3) vortex shedding was not exacerbated with removal of a walkway attachment, and 4) walkway removal did not significantly change stress magnitudes at the connection between the cantilever and mast. Based on these findings, the removal of walkways from KDOT's COSS was not found to problematic.

Acknowledgements

The authors of this report would like to gratefully acknowledge the Kansas DOT for their support of the work performed under this project. Additionally, Mr. Wes Anderson's (KU Aerospace Engineering) generous help and support during wind tunnel testing was greatly appreciated.

Table of Contents

List of Figures

List of Tables

Introduction and Background

1.1 Background

Cantilevered overhead sign structures (COSS) are ubiquitous in highway infrastructure across the United States. COSS are used to convey information to traveling motorists in an efficient and effective manner. However, fatigue cracks have been discovered in COSS connections over the past few decades, limiting the service lives of these structures, and sometimes even resulting in complete failures. Because of such incidences, highway sign structures have received increasing attention surrounding fatigue performance and design, with fatigue design provisions first being included in the American Association of State Highway Transportation Officials (AASHTO) Standard Specifications for Structural Supports for Highway Signs, Luminaires, and Traffic Signals (SLTS) in 2001.

There are four popular construction types for COSS: 1) monotube, 2) two-chord truss, 3) three-chord truss, and 4) four-chord truss, all of which are shown in Figure 1. These have the same function and general shape, but different assemblies. The construction type is generally uniform within a State, but varies across the United States.

COSS only require one support which reduces materials, earthwork, labor costs, and road closures; thus, COSS can be a more attractive option to state DOTs when compared to a full-span overhead sign structure. Additionally, using a single support reduces the number of hazards a motorist can face in the event of an accident (Dexter and Ricker 2002).

(a)

(b)

(c) (d)

Figure 1 Popular COSS Construction Types: (a) monotube, (b) two-chord truss; (c) three-chord truss; and (d) four-chord truss

COSS can experience high wind fluctuations from natural wind gusts. Natural wind produces a significant load on COSS because the aluminum signs have a large surface area that catches the wind. This wind loading can displace the COSS both vertically and horizontally, and deflections can be quite substantial at the end of the cantilever. COSS undergo significant cyclical loading in their lifetime due to wind loads, and experience substantial deflections in the mast truss. Because of this, COSS are now designed with fatigue as a consideration.

Over the past three decades, a number of fatigue related failures have been observed in COSS (Dexter and Ricker 2002). Specifically, two-chord COSS experienced the highest number of fatigue failures due to the dynamic response of natural wind gusts and susceptibility to vortex shedding (Gallow et al. 2015). Additionally, defective welds have been observed in two-chord COSS. Such fabrication-related issues have resulted in the prevalence of crack development and crack propagation in the connection between the mast truss and pole, called the "box connection". Figure 2 shows where state DOTs have been monitoring crack growth in a box connection through discrete visual inspections. (Although the cracks are not visible in the figure, marks indicating their growth are shown.)

Figure 2 Typical crack monitoring at the box connection of a two-chord COSS

To accommodate maintenance of the signage and structure, COSS often include a steel grate walkway in front of the sign, as shown in Figure 3 and Figure 4. The walkway usually spans the whole length of the sign and is typically made of steel grating supported on L-shaped hanger supports suspended from the bottom chord of the truss. On occasion, the walkway attachment is removed to reduce incidences of vandalism. The influence of walkway removal on the dynamic properties of the structures and the aerodynamic shape of the sign is unknown. It is possible that removal of the walkway could result in worsened fatigue performance of COSS, if it serves to substantially disrupt air flow around the structure.

Figure 3 Steel grate walkway on a two-chord COSS

Figure 4 Steel grate walkway on a two-chord COSS

1.2 Problem Statement

While intended to be a component for serviceability, the steel grate walkway can be a liability for overhead sign structures (OSS). Vandals have been able to use walkways to deface signs. To combat this, multiple state DOTs have removed walkways from OSS. Additionally, state DOTs tend to now use bucket trucks for most maintenance on OSS, rendering the walkway attachment somewhat unnecessary.

It is not evident what impact walkway removal has on the structural performance of COSS. Two important structural characteristics are changed when the attachment is removed: 1) dynamic properties of the COSS and 2) aerodynamic shape of the COSS. It is conceivable that such changes may have significant effects on the fatigue performance of COSS. It is unclear how removing the walkway attachment may affect the fatigue performance of two-chord COSS.

At first consideration, it may seem that removing mass at the end of a cantilever would help improve fatigue performance of the structure by reducing natural frequencies, but it is possible that other effects may have negative influence on fatigue performance. The removal of mass could cause two-chord COSS to experience more fatigue cycles (Craig and Kurdila 2006). The walkway attachment could deflect wind gusts away from the sign, resulting in larger stress demands when removed. The walkway could act as a diffuser to disrupt eddy interaction which leads to vortex shedding. In other words, the steel grate walkway may be an unintended but important piece for satisfactory fatigue performance.

1.3 Research Objectives

The aim of the research presented in this report is to characterize how the removal of walkway attachments affects the dynamic properties and aerodynamic shape of two-chord COSS used in the Kansas Department of Transportation highway inventory. This was achieved by using both analytical and experimental techniques, specifically:

- ***Dimensional analysis of two-chord COSS*** – to capture a range of realistic design characteristics and to produce a diverse group of two-chord COSS for subsequent analytical modeling.

- ***Modal response definition*** – to characterize how two-chord COSS react under natural wind gusts and certain aeroelastic phenomena, such as vortex shedding.
- ***Fundamental frequency calculation*** – to calculate changes in the dynamic response for COSS with and without the walkway attachment.
- ***Computation fluid dynamic (CFD) modeling*** – to characterize how the aerodynamic influence of the sign varies depending on the presence of the walkway, considered by computing pressures on the sign, observing how wind flows around the sign, and observing how eddies and vortices form and interact in the wake of the sign.
- ***Experimental verification*** – to validate results obtained from the CFD modeling through use of a wind tunnel at the University of Kansas.
- ***Dynamic loading*** – to characterize how COSS respond to natural wind using loading data obtained from the CFD modeling.

By using this approach, conclusions have been drawn regarding the influence of the walkway attachment on the fatigue performance of two-chord COSS.

It is important to note that truck-induced wind gusts (TIWG) were not investigated in this research. TIWG result in considerably smaller-magnitude wind gusts when compared to natural wind gusts (Creamer et al. 1979). Also, the walkway attachment is the most influential area affected by TIWG. Without the attachment, TIWG would have negligible area to project onto resulting in negligible force.

1.4 Report Organization

Section 1.5 presents a literature review of pertinent studies and findings on current problems affecting COSS. The literature review also provides background information on the basis of the methodology used in this research. Chapter 2 describes how the research was conducted. Both analytical modeling techniques and experimental methods are described. Chapter 3 outlines the results of both the analytical modeling and experimental testing. Chapter 4 summarizes the results and formulates conclusions. Chapter 4 also includes recommendations for future work around fatigue performance of COSS. The Appendix provides construction documentation and additional results from the analytical modeling.

1.5 Literature Review

This section serves as background and context regarding performance problems encountered with COSS, and outlines topics used as baseline assumptions in modeling techniques summarized in Chapter 2.

1.5.1 – Damage Reporting:

Section 11 of the AASHTO LRFD SLTS Specification (AASHTO 2015a) outlines the requirements and recommendations provided in NCHRP Reports 412 (Kaczinski et al. 1998) and 494 (Fouad et al. 2003) for adequate fatigue design. Section 11 of this specification includes updated loads for application on horizontal areas and also recommends the design of infinite service life connections for both connections identified in NCHRP Report 412 (Kaczinski et al. 1998).

Specification commentary provides additional information about galloping. The commentary specifies that galloping produces the worst effects on nonsymmetrical cross sections when including the shape of the sign in the cross section. Four-chord COSS have a more symmetrical cross section than do two-chord COSS, when considering the sign in the cross section. For that reason, the commentary specifies that galloping can be ignored for four-chord COSS, which is one reason why more state DOTs are opting for the four-chord COSS construction type over the two-chord design. Additionally, four-chord COSS do not utilize a box-connection, instead using a collared plate connection.

1.5.1.1 NCHRP Report 412 (Kaczinski et al. 1998):

The National Cooperative Highway Research Program (NCHRP) Report 412 (Kaczinski et al. 1998) describes the first phase of NCHRP Project 10-38, which aimed to improve the performance of COSS by mitigating fatigue, improving established design criteria, and investigating the root causes of why COSS are failing across the United States. Four wind loading categories were identified as likely sources for large-amplitude vibrations, which when paired with natural frequencies of COSS, could lead to fatigue failures. The four categories were: 1) natural wind gusts, 2) truck-induced wind gusts, 3) galloping, and 4) vortex shedding. Revisions to the AASHTO Specifications for Structural Supports for Highway Signs, Luminaires, and Traffic Signals were recommended.

NCHRP Report 412 included descriptions of the characteristics of natural wind gusts and how they affect COSS. Natural wind gusts have a variability in velocity and direction of air flow, and are characterized by a spectrum of fluctuating velocity components over a given plane projected onto a structure. The fluctuating pressure inherent to natural wind gusts induces vibrations onto a structure. Kaczinski et al. (1998) claimed that variations in velocity fluctuations associated with natural wind gusts typically increase between 5 percent and 25 percent with intense gusts. The subsequent AASHTO SLTS (AASHTO 2001) compensates for this by applying a gust factor of at least 1.14 to the design load, increasing for structures that require it. A case is made that this factor is adequate for ultimate strength design of COSS, because state DOTs have "no reported failures directly attributed to the exceedance of the ultimate strength of cantilevered support structures due to extreme gust loading conditions" (Kaczinski et al. 1998). The authors showed that natural wind gusts are purely aerodynamic and not aeroelastic like galloping and vortex shedding. Therefore, "stiffening the structure or adding mass does not reduce the loading effect as it does for aeroelastic phenomena" (Kaczinski et al. 1998). The authors also claimed that "changing the natural frequency through changes of mass and/or stiffness does not reduce the load effect significantly…" (Kaczinski et al. 1998). This suggests that the variances in shape and mass across structures have little effect on natural wind gusts.

A goal of NCHRP 10-38 was to categorize fatigue-critical connections in sign structures to provide an ability to better estimate remaining service life. Connections considered were: 1) the base of the supporting pole to the anchor bolts and 2) the connections between the supporting pole and the mast truss, which vary by construction style. The connections were categorized with respect to the AASHTO fatigue design curves shown in Figure 5 (AASHTO 2015b). The majority of connections between the supporting pole and the mast truss were classified as E or E' connections, indicating very poor fatigue performance.

Evidence was presented that all COSS designed using the 1994 AASHTO Standard Specifications for Structural Supports for Highway Signs, Luminaries, and Traffic Signals needed to be reevaluated. In fact, 36 DOTs reported that they experienced fatigue problems with wind-induced vibration of COSS. Generally, the reported vibrations were observed to occur in the plane of the structure, activated by aeroelastic phenomena. The subsequent AASHTO SLTS (AASHTO 2001) compensates for this by applying a vertical 21 psf (1005 Pa) pressure to all horizontal areas of the sign structures for sufficient strength for galloping.

1.5.1.2 NCHRP Report 494 (Fouad, et al. 2003):

Work described in NCHRP Report 494 (NCHRP Project 17-10(2), Fouad, et al. 2003) was a continuation of the work begun under NCHRP Project 10-38, extending the research to non-cantilevered signs structures, which have also exhibited fatigue problems. Eight state DOTs reported problems with OSS. Fouad, et al. (2003) made the case that COSS and OSS fatigue problems stemmed from the same wind induced vibration. This resulted in the creation of new fatigue criteria that would change the existing loading recommendation. As in the work done under NCHRP 10-38, the four categories responsible for wind induced vibration were 1) natural wind gusts, 2) TIWG, 3) galloping, and 4) vortex shedding. The loading recommendations are as follows, where the values are applied to all horizontal areas of all OSS:

- Natural wind gusts – 5.2 psf (250 Pa).
- TIWG – 10.2 psf (490 Pa), recommendation also provides a 7.5 psf (360 Pa) horizontal load to vertical faces, but this is dramatically less than natural wind gusts.
- Galloping – 21 psf (1000 Pa), can be ignored for non-cantilevered structures.
- Vortex Shedding – may be disregarded as long as "…sign blanks are used during the construction…" (Fouad et al. 2003). This is to prevent exposed shapes that are susceptible to eddy interaction at critical points in the span of the sign structures.

These loading recommendations were adapted in the successive AASHTO Specifications (AASHTO 2009). Despite the research conducted in the report, it is still unclear whether or not fatigue failures in COSS and OSS are primarily induced by large-magnitude loads produced by galloping and vortex shedding, or if the problems primarily stemmed from fabrication errors. The authors concluded that additional testing, inspections, and data collection is required before definitive conclusions can be drawn.

The authors recommended using additional gusset plates or thicker steel plates in the connections between the supporting pole and the mast truss (typical connection shown in Figure 2), to increase the stiffness of the structure and provide additional moment capacity at the connection.

1.5.2 – Fatigue:

1.5.2.1 Mechanical Behavior of Materials (Dowling 1999):

A structure's service life is a function of how adequately it can mitigate fatigue, where fatigue is the progressive deterioration of a material over time. Fatigue is caused by crack development at stress concentrations produced under cyclical loading. Cyclical stress range and the anticipated number of loading cycles are used in engineering designs of structures subjected to repeated loading. Fabrication of metal connections involves welding together steel plates and drilling or punching holes for bolts. Both processes develop microscopic cracks in the connections. This is due to residual stresses caused by rapid heating and cooling, and material yielding exacerbating slip planes.

Fatigue cracks can develop in connections due to stress concentrations and the prevalence of connection features, such as welds or holes. Knowing the nominal cyclical stress and anticipated number of loading cycles, the fatigue life of a connection can be estimated. This is done using S-N (stress range-number of cycles) curves, which are based on categories of connections, by estimating the number of cycles until failure occurs under a certain stress range. Figure 5 shows AASHTO S-N curves for all detail categories (AASHTO 2015b). The fatigue performance of a connection is categorized as showing decreasing fatigue performance as reference lines move from A to E'. The horizontal lines represent a constant amplitude fatigue limit, such that a detail will not experience failure under that stress range.

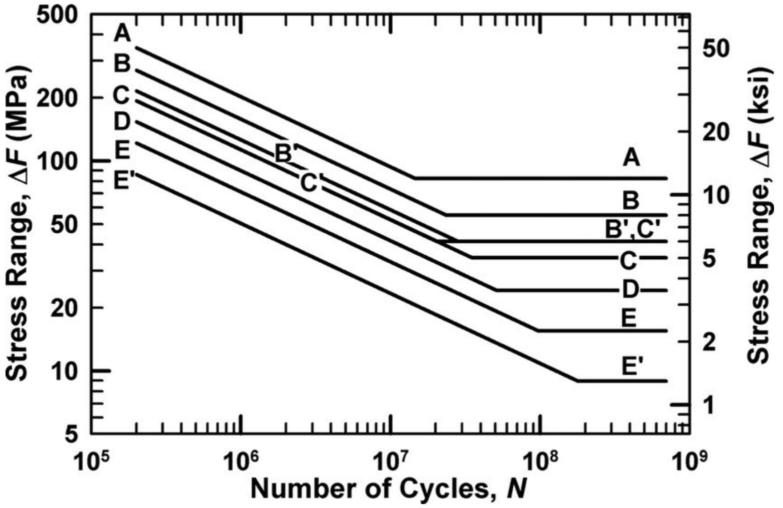

Figure 5 AASHTO S-N curves for all detail categories (AASHTO 2015b)

1.5.3 – Dynamic Properties:

1.5.3.1 Fundamentals of Structural Dynamics (Craig and Kurdila 2006):

Resonance is an important consideration in the design of structures with large spans and/or cantilevers, and is a phenomenon that occurs when the frequency of an oscillating load applied to a structure matches the structure's natural frequency. Even with seemingly insignificant loads, resonance can result in harmonic, large-amplitude motion with catastrophic consequences. A structure's natural frequency is a dynamic property derived from two characteristics: mass (m) and stiffness (k). Equation 1 defines a structure's natural frequency (f_n):

$$f_n = \frac{1}{2\pi}\sqrt{\frac{stiffness}{mass}} = \frac{1}{2\pi}\sqrt{\frac{k}{m}}$$ **Equation 1**

Damping (ζ) is not present in the relationship because damping reduces the amplitude of the response over time and does not affect natural frequency. Damping characterizes energy loss in a system, and cannot be derived from structural properties, unlike mass and stiffness. In most cases, a damping magnitude is assumed in analyses based on engineering judgment; otherwise, damping may be experimentally measured.

Most practical structures have multiple ways of deflecting due to varying directionally of loading. These structures are multiple-degree-of-freedom (MDOF) systems, meaning that they have more than one mode shape. A mode shape describes how a structure will deform under certain loading patterns, and each mode shape has an associated natural frequency. Mode shapes are activated under different loading conditions and result in different deflections and system behavior. Stiffness and mass are not isotropic; thus, the dynamic properties of a system change depending on the system's orientation. Structures with long spans and/or cantilevers have multiple ways of deflecting; thus, making them MDOF structures. Two-chord COSS are MDOF structures with two characteristic mode shapes defined in Section 2.2.

1.5.4 – Vortex Shedding:

Vortex shedding is an aeroelastic phenomena that can produce vibrations in structures to the point of extreme deflections and even failure. Vortex shedding occurs from the interaction of eddies and vortices that curl behind an object in a constant stream of fluid. The formation of eddies is caused by "a laminar boundary layer on the [edge of a surface that] often separates and forms a separated shear layer" (Yarusevych et al. 2009). This separation and creation of two different layers of flow are shown in Figure 6 and Figure 7.

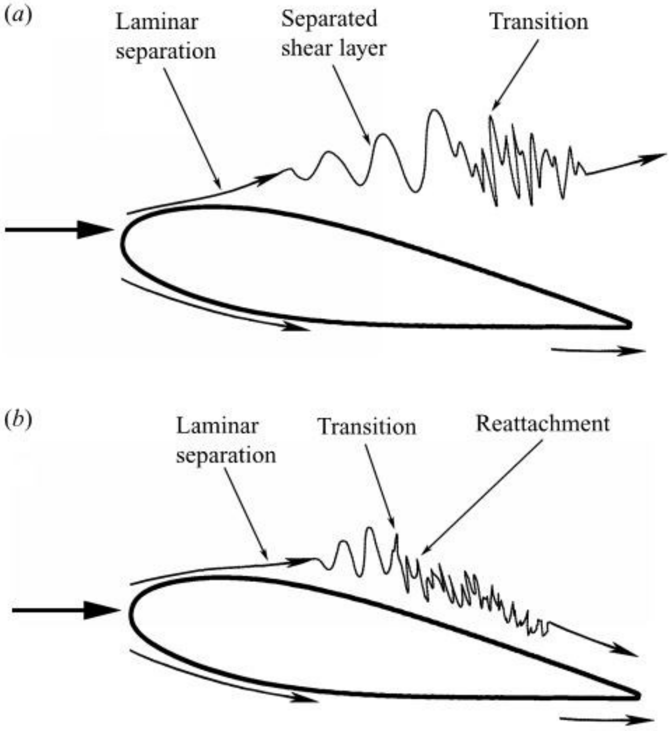

Figure 6 Flow layer development on an airfoil with a) separation and b) reattachment to the

cross section (Yarusevych et al. 2009)

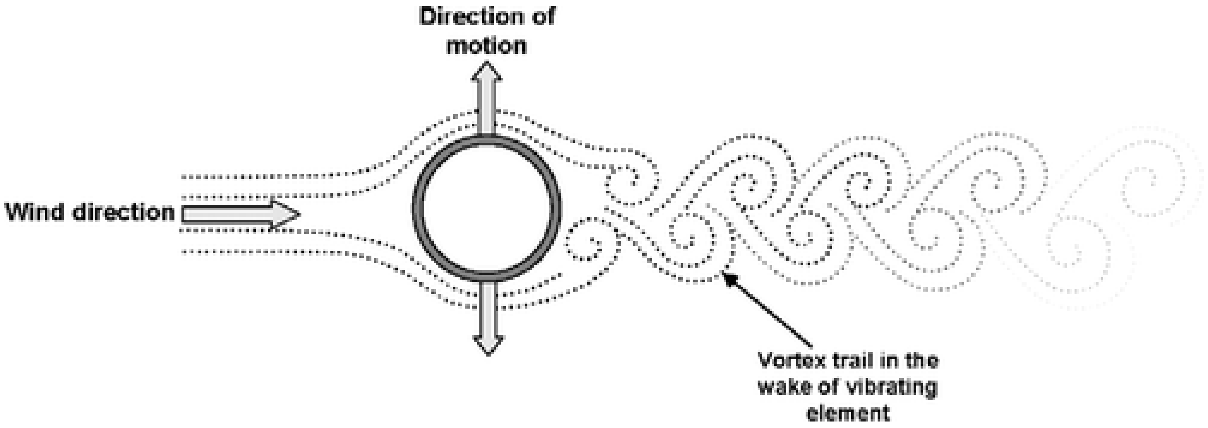

Figure 7 Vortex shedding on a cylinder (Rice et al. 2008)

Figure 6 shows the effect of the air stream reattachment to the structure, which causes curls in the wake of the shape (Figure 7). These curls represent shear, and if the developing shear begins to alternate symmetrically about a structure, movement will be induced (Holmes 2007). The eddies that form in the shear layer push on the edges of a structure incrementally, and if the oscillation of the eddy formation matches the structure's natural frequency, resonance can occur - especially in structures with long spans and cantilevers, such as cable-stayed bridges and sign structures. Infamously, the Tacoma Narrows Bridge collapsed in 1940 due to vortex shedding interacting with the long span of the bridge shown in Figure 8.

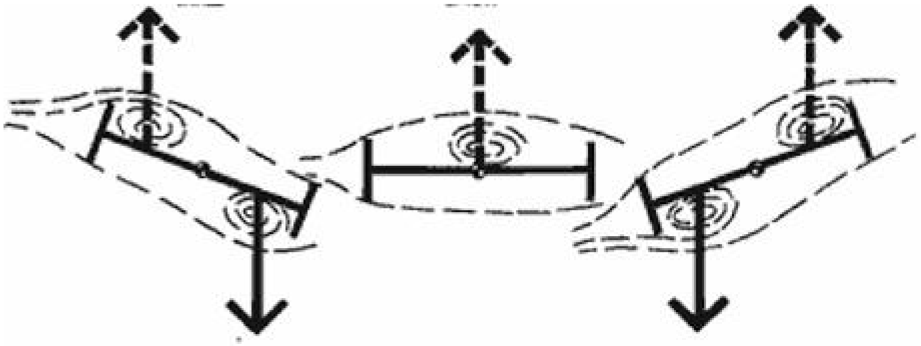

Figure 8 Vortices interacting with the Tacoma Narrows Bridge cross section (Voss 2016)

Vortex shedding typically develops at constant wind speeds of 45 mph (20.1 m/s) or lower (AASHTO 2001) and vibrates a structure in a direction perpendicular to the flow. Vortex shedding typically affects shapes with large and smooth cross sections, such as large-diameter cylinders, but "can occur in other bluff bodies such as triangles, rectangles, or H and L shapes" (Kacin 2009). Monotube-style COSS and OSS have been especially susceptible to vortex shedding. Figure 9 and Figure 10 show the large deflections that can occur under vortex shedding, with the long, exposed cylindrical tube creating the conditions for this phenomenon.

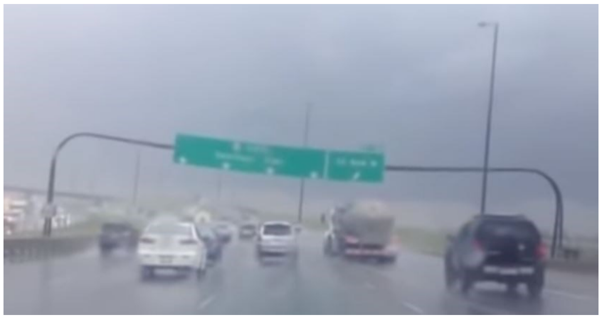

Figure 9 Monotube OSS experiencing galloping effects of vortex shedding (downward) (Mangat 2016)

Figure 10 Monotube OSS experiencing galloping effects of vortex shedding (upward) (Mangat 2016)

AASHTO SLTS (AASHTO 2001) provides commentary describing when natural wind gusts can affect sign structures to the point of producing vortex shedding. If wind speeds are between 10 mph (4.47 m/s) and 45 mph (20.1 m/s) then vortex shedding has a higher probability of occurring (AASHTO 2001). Conditions tend to be too turbulent at wind speeds higher than 45 mph (20.1 m/s) to produce vortex shedding, and not significant enough to produce vortex shedding at wind speeds under 10 mph (4.47 m/s) (AASHTO 2001).

Although vortex shedding is not a common phenomenon, its effects can be catastrophic, so it is important to mitigate eddy interaction to combat this aeroelastic phenomena.

Methods

This chapter describes the research methodology used in this investigation. Both analytical modeling techniques and experimental methods are detailed in this chapter.

2.1 Design Envelope and Model Selection

The Kansas Department of Transportation (KDOT) provided this project with construction specifications for two-chord COSS used in the KDOT highway inventory. The specifications include six “Dimension Design” groups, which define member sizes, dimensions, and spacing. A Dimension Design group is usually dependent on the size of the sign the two-chord COSS is supporting. Characteristics such as pole height, mast truss length, and sign size are site dependent, for which KDOT provided 110 examples of constructed COSS. From the specifications and constructed examples, three variable design characteristics were identified as shown in Figure 11: 1) sign size (x_1), 2) mast truss length (x_2), and 3) pole height (x_3). It is important to note that the sign’s aspect ratio (x_1/y_1) is generally dependent on the size of the sign. Large signs generally have lower aspect ratios where $x_1 \approx y_1$, while smaller signs generally have higher aspect ratios where $x_1 > y_1$.

The constructed examples display a wide range of variable design characteristics. Figure 12 shows a labeled photograph of a KDOT COSS, indicating common terminology for the various elements of the structure. Figure 13 shows a dimensional envelope derived from the 110 constructed examples provided by KDOT. Since the size of the sign usually determines the Dimension Design group for a given two-chord COSS, member section, dimensions, and spacing are all a function of the sign size. Because of this, changes in sign size are strongly correlated with structural mass and stiffness. The walkway has little effect on structural stiffness due to its connection to butterfly supports which are not critical to the structure from a strength perspective.

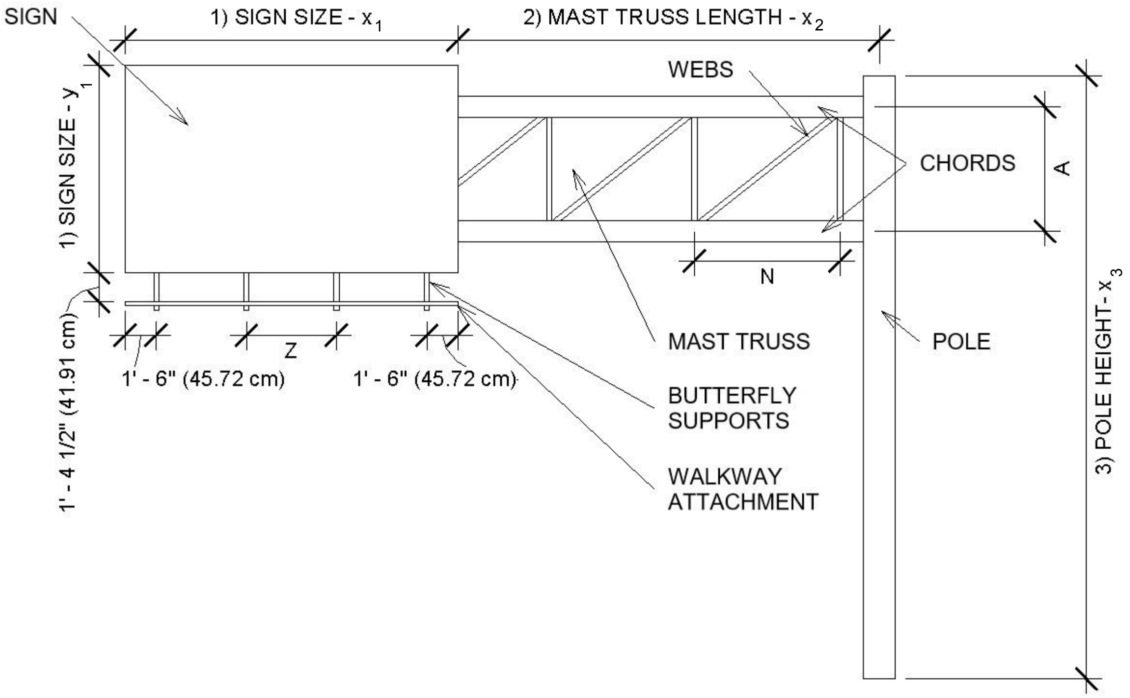

Figure 11 COSS variable design dimensions

Figure 12 Constructed KDOT COSS

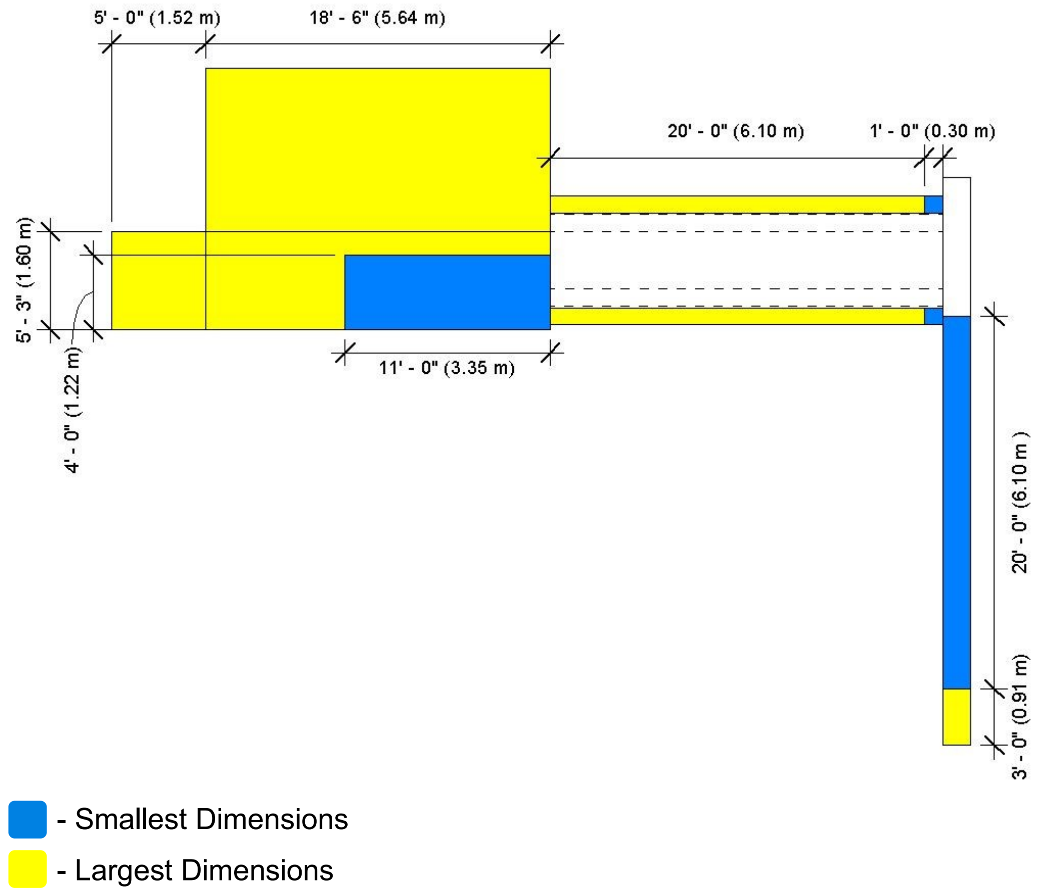

Figure 13 COSS dimensional envelope (based on 110 examples provided by KDOT)

Twenty-seven base models were created, to capture combinations of three sizes for the three variable design dimensions (sign size, x_1 & y_1; mast truss length, x_2; and pole height, x_3). The sizes chosen were intended to capture a range of small/short, medium, and large/long dimensions, based on the example set provided by KDOT. Medium values were chosen by calculating the rounded average of the constructed examples. Small (short) and large (long) values were chosen by the rounded-up standard deviation of the constructed examples in each direction. Table 1 shows the calculated values for each design parameter.

In addition to the 27 base models an additional five models representing extreme cases were added, which represented the smallest and largest bounds of the constructed examples provided by KDOT (one of the constructed examples had both the shortest pole and shortest mast truss length which is why the addition is five and not six).

Because sign size is closely correlated with the dimensions of two-chord COSS, Table 2 outlines each of the member sections and number of butterfly supports based on sign size, while Table 3 outlines the member spacing as a function of sign size. This dimensional analysis yielded 32 sign structures that encompass the diverse dimensional parameters for KDOT two-chord COSS.

Table 1 Design Parameter Values

Characteristic	**Small (Short)**	**Medium**	**Large (Long)**
	ft-in. (m)	**ft-in. (m)**	**ft-in. (m)**
Sign Length	12’-0” (3.658)	16’-0” (4.877)	20’-0” (6.096)
Sign Height	6’-0” (1.829)	9’-0” (2.743)	12’-0” (3.658)
Aspect Ratio, (x_1/y_1)	2.0	1.8	1.7
Mast Truss Length	12’-0” (3.658)	16’-0” (4.877)	20’-0” (6.096)
Pole Height	25’-0” (7.620)	27’-0” (8.230)	29’-0” (8.839)

Table 2 Member Sections Based on Sign Size

Section	**Small Sign**	**Medium Sign**	**Large Sign**
Chord	HSS8.625x0.5 (HSS21.91x1.27)	HSS10.75x0.307 (HSS27.31x0.78)	HSS12.75x0.375 (HSS32.39x0.95)
Web	HSS3x0.375 (HSS7.62x0.95)	HSS3x0.375 (HSS7.62x0.95)	HSS3x0.375 (HSS7.62x0.95)
Pole	HSS16x0.375 (HSS40.64x0.95)	HSS18x0.375 (HSS45.72x0.95)	HSS18x0.375 (HSS45.72x0.95)
Butterfly Supports*	Z4x8.2 (Z10.16x20.83)	Z4x8.2 (Z10.16x20.83)	Z4x8.2 (Z10.16x20.83)

*Z-Shapes are similar to small wide flange beams, and not Z-Channels.

Table 3 Member Spacing Based on Sign Size

Section	**Small Sign**	**Medium Sign**	**Large Sign**
	ft-in. (m)	**ft-in. (m)**	**ft-in. (m)**
Vertical spacing between chords, *A*	4’-0” (1.219)	6’-0” (1.829)	6’-0” (1.829)
Truss panel length, *N*	7’-0” (2.134)	7’-0” (2.134)	7’-0” (2.134)
Spacing between butterfly supports, *Z*	4’-6” (1.372)	4’-4” (1.321)	5’-8” (1.727)
No. of Butterfly Supports	*3*	*4*	*4*

Model nomenclature represents the three variable design dimensions: x_1 & y_1, x_2, and x_3. The arrangement of the model nomenclature is shown below with x and y representing dimensions in feet:

$$\mathbf{S}x_1 \text{ x } y_1 - \mathbf{L}x_2 - \mathbf{P}x_3 \quad \textbf{Equation 2}$$

The first two values following S define the sign size, where x_1 defines the sign length, y_1 defines the sign height, and the “x” separates the two dimensions. x_2 defines the mast truss length from the pole. Finally, x_3 defines the pole height. Figure 11 displays where the dimensions correspond on a two-chord COSS.

2.2 Characteristic Mode Shapes

Two-chord COSS have two characteristic modes. These modes are characterized by different deflections and are activated under different loading scenarios. The two modes are dramatically different and produce peak stresses in different locations in COSS members and connections. These critical loads come from wind, which is random in nature (stochastic) and can cause harmonic responses under certain aeroelastic phenomena.

The first characteristic mode has a torsional mode shape and is produced at the lowest natural frequency of all two-chord COSS systems. In this torsional mode, the sign and mast truss rotate about the fixed pole. This mode is activated by natural wind gusts, and can cause large, out-of-plane stress concentrations in the connection between the pole and mast arms. Figure 14 and Figure 15 display the torsional mode shape.

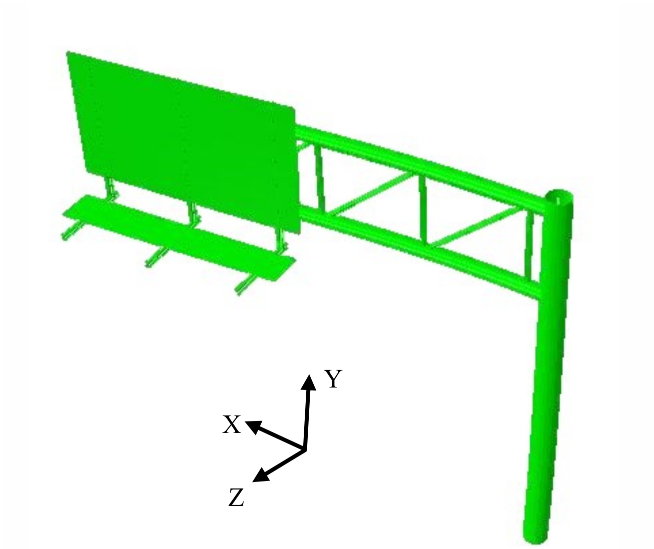

Figure 14 Torsional mode shape (3D perspective view)

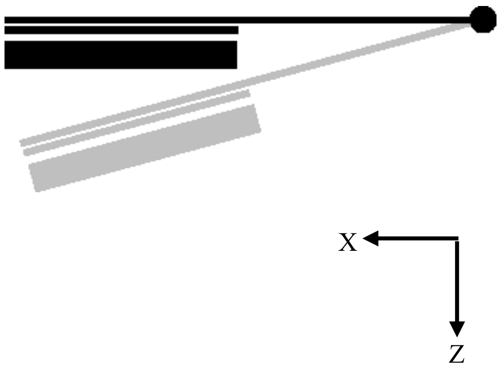

Figure 15 Torsional mode shape (top-down view)

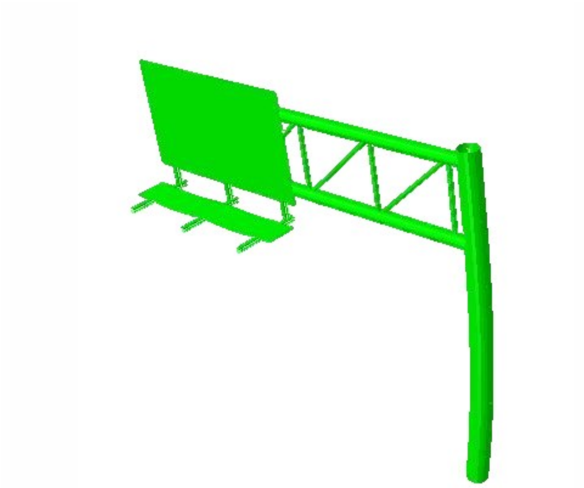

Figure 16 Chopping mode shape (3D perspective view)

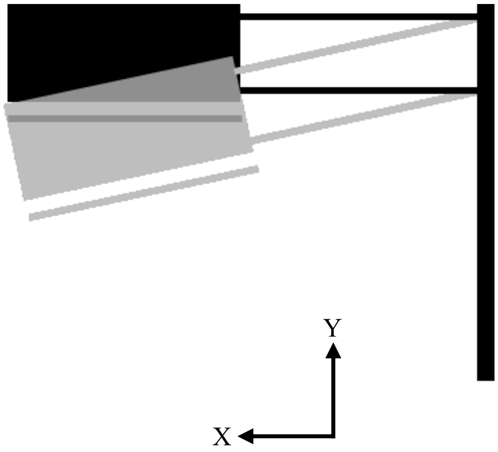

Figure 17 Chopping mode shape (front-on view)

The second characteristic mode has a distinct "chopping" mode shape and occurs at the second lowest natural frequency of all two-chord COSS systems. In the chopping mode, the sign and mast truss displace vertically in-plane with the pole. This mode is activated by truck-induced wind gusts and global and local vortex shedding. Global vortex shedding can occur in the wake of the sign, while local vortex shedding can occur in the wake of both chords. The chopping mode can produce large, in-plane stress concentrations in the connection between the pole and mast arms. Figure 16 and Figure 17 display the chopping mode shape.

Both of these characteristic modes are investigated as removal of the walkway results in a significant mass loss on the end of the cantilever. The end of a cantilever is the most influential part when investigating the effect mass has on a systems response frequency. The removal of the walkway has little effect on the stiffness of the system, since it is not directly connected to any critical members.

2.3 Finite Element Modeling – Fundamental Frequencies

The commercially-available finite element software package, Abaqus/CAE 2016 (DSS 2014) was used to create 3D, linear-elastic, finite element models of the thirty-two COSS described in Section 2.1.

2.3.1 – Part and Assembly Creation and Meshing:

Five parts were created for each COSS model. The butterfly supports, mast truss, and pole were modeled using wire elements with sections defined from the construction specifications provided by KDOT. The mast truss, which includes the two tube chords and pipe diagonals, was created as one part, as opposed to separate parts and brought into the assembly for later connectivity. The sign was modeled with infinitely stiff, 3D shell elements with a thickness of 1/16" (0.159 cm). In practice, large, overhead signs are created with aluminum channels where the flanges are bolted together to achieve the desired height and thus are quite rigid. In addition, the signs are laterally supported along the bottom chord, which provides additional stiffness. The walkway was also modeled with infinitely stiff, 3D shell elements, here with a thickness of 1 1/2" (3.81 cm). The sign and walkway were modeled as having infinite stiffness to help mediate local vibrations contributing to global response frequencies. To consider the validity of these simplifications, the dynamic properties of the COSS were also computed using the specified material stiffness, and the global dynamic properties were negligibly affected as compared to the models with infinite stiffness parameters defined for the sign and walkway. All five parts were initialized into the assembly and placed according to the specifications.

After the parts were created and sections and orientations were assigned, the parts were assigned a mesh. Meshing is generally not critical for frequency steps and should be assigned based on the complexity of a member (DSS 2015). Linear-beam meshing techniques were applied to the butterfly supports, mast truss, and pole due to the parts being wire elements. Quad-dominated meshing techniques were applied to the sign and walkway. The typical mesh density used for each part (nodes are highlighted) is shown in Figure 18. All five parts' mesh were sized controlled, and Table 4 outlines the seed size of each part.

Table 4 Part Meshing Seed Size

Part	**Seed Size**
	in. (cm)
Sign	10.0 (25.4)
Butterfly Support	4.00 (10.2)
Mast Truss	4.00 (10.2)
Pole	12.0 (30.5)
Walkway	10.0 (25.4)

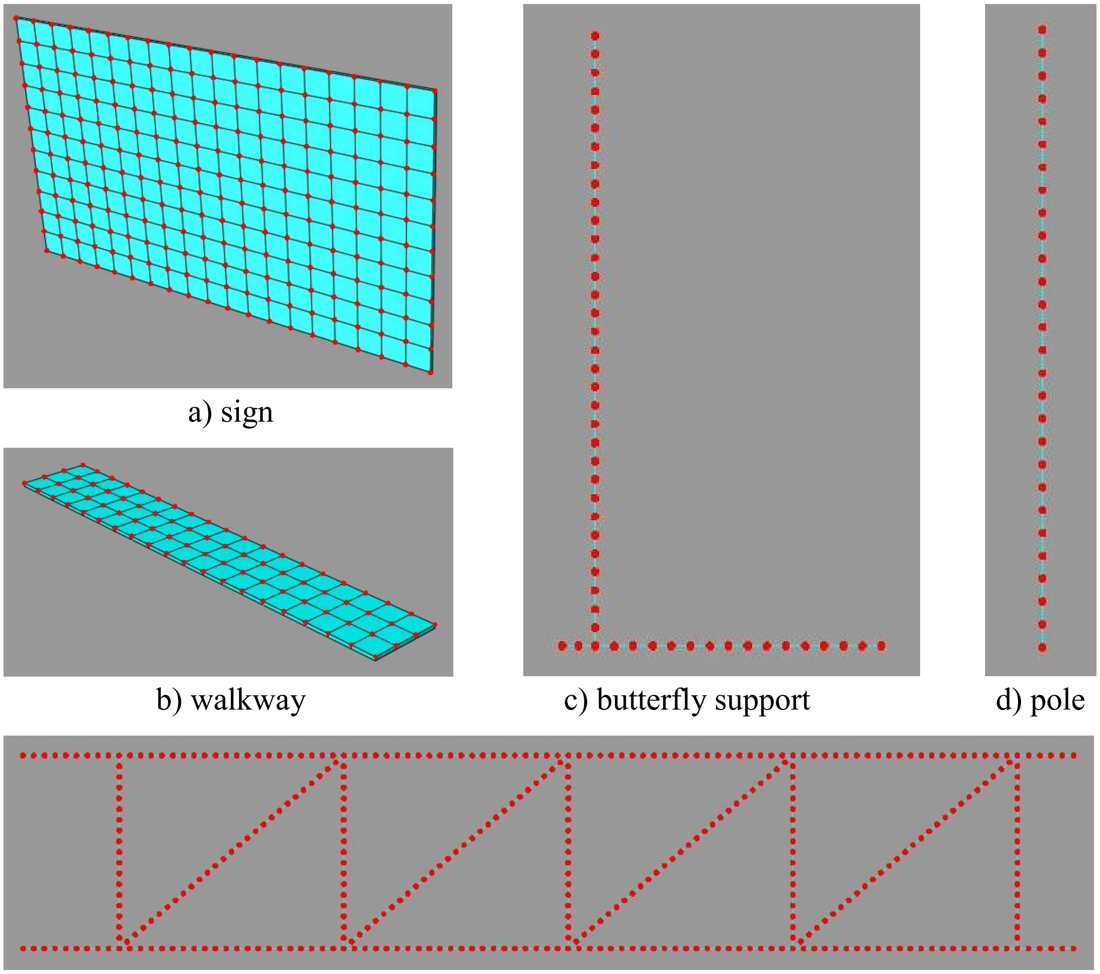

a) sign

b) walkway

c) butterfly support

d) pole

e) mast truss

Figure 18 Typical mesh used for each part in the COSS dynamic models: a) sign, b) walkway, c) butterfly support, d) pole, and e) mast truss

2.3.2 – Material Definition:

Two materials were used for the modeling of the COSS in accordance with the construction specifications. The pole, mast truss, butterfly supports, and walkway were modeled with nominal linear-elastic properties for steel, while the sign was modeled with nominal linear-elastic properties for aluminum. Table 5 outlines the materials and their pertinent properties (ASTM A709/A709M-18 2018) (ASM International 1990). It is important to note that the construction specifications allow for either a steel or aluminum walkway, but steel was chosen due to its higher density, resulting in a greater effect on the reduction of mass when removed.

Table 5 Dynamic Modeling Material Properties

Material	Description	ρ	E	ν
		lb/ft^3 (kg/m^3)	ksi (GPa)	-
Steel	A709 Gr. 36	490.0 (7849)	29000 (200)	0.29
Aluminum	6061-T6	168.5 (2699)	10150 (70)	0.33

2.3.3 – Connections and Boundary Conditions:

All connections between parts were modeled using tied constraints, which is reasonable referencing the construction specifications. Below is a list of all the connections and how they were modeled:

- Connections between pipe diagonals and tube chords (mast truss) – wire part tied constraint – the end nodes in the pipe webs were connected to corresponding nodes in the tube chords to create a single, rigid part.
- Connections between the walkway and butterfly supports – surface to node region tied constraint – the wire elements in the butterfly supports' horizontal members contacting the walkway were master node regions, and the bottom of the walkway was taken to be the slave surface.
- Connections between the sign and the butterfly supports – surface to node region tied constraint – the wire elements in the butterfly supports' vertical members contacting the sign were made master node regions, and the surface facing the butterfly supports was the slave surface.
- Connections between the butterfly supports and mast truss – node region to node region tied constraint – the wire elements in the chords of the mast truss contacting the butterfly supports were assigned as master node regions, and the wire elements in the butterfly supports' vertical members contacting with the chords of the mast truss were slave node regions.
- Connections between the mast truss and pole – node region to node region tied constraint – the wire elements in the pole contacting the chords of the mast truss

were master node regions, and the two end nodes in the mast truss contacting the pole were slave node regions.

- The base of the pole was modeled as a fully-fixed support.

2.3.4 – Step Creation:

Natural frequencies were computed using a frequency step with computations performed using linear perturbation. After the natural frequencies were computed, the walkway was removed from the assembly along with Constraint 1 from Section 2.3.3 and the model execution was repeated. Therefore, natural frequencies were determined for each model geometry twice – once with the walkway in place, and once with the walkway removed. The mass percentage of the walkway when compared to the whole system was recorded as well.

2.4 Loading Methodology

To analyze how the walkway attachment affected the aerodynamic shape of the sign, a two-step approach was taken, utilizing computational fluid dynamics models and dynamic structural models. The computational fluid dynamics models were created to determine the forces acting on the sign under different wind velocities, and to examine interactions between the sign (with and without the walkway) and wind. This done by modeling the influential part of the sign structure as a void space in a fluid domain. However, it is extremely difficult to also capture structural interactions within a computational fluid dynamics model (i.e., true fluid-structure interaction). Therefore, dynamic structural models were also utilized to examine structural responses (such as in plane vibrations and associated stresses stimulated by aeroelastic phenomena) of the overall COSS under time history loadings extracted from the computational fluid dynamics models. Therefore, the first step was to create computational fluid dynamics (CFD) models of the COSS and extract member forces induced by wind across a time history. The second step was to apply those extracted forces from the CFD models and apply them as time-dependent loads within the dynamic structural models. Figure 19 outlines the methodology framework.

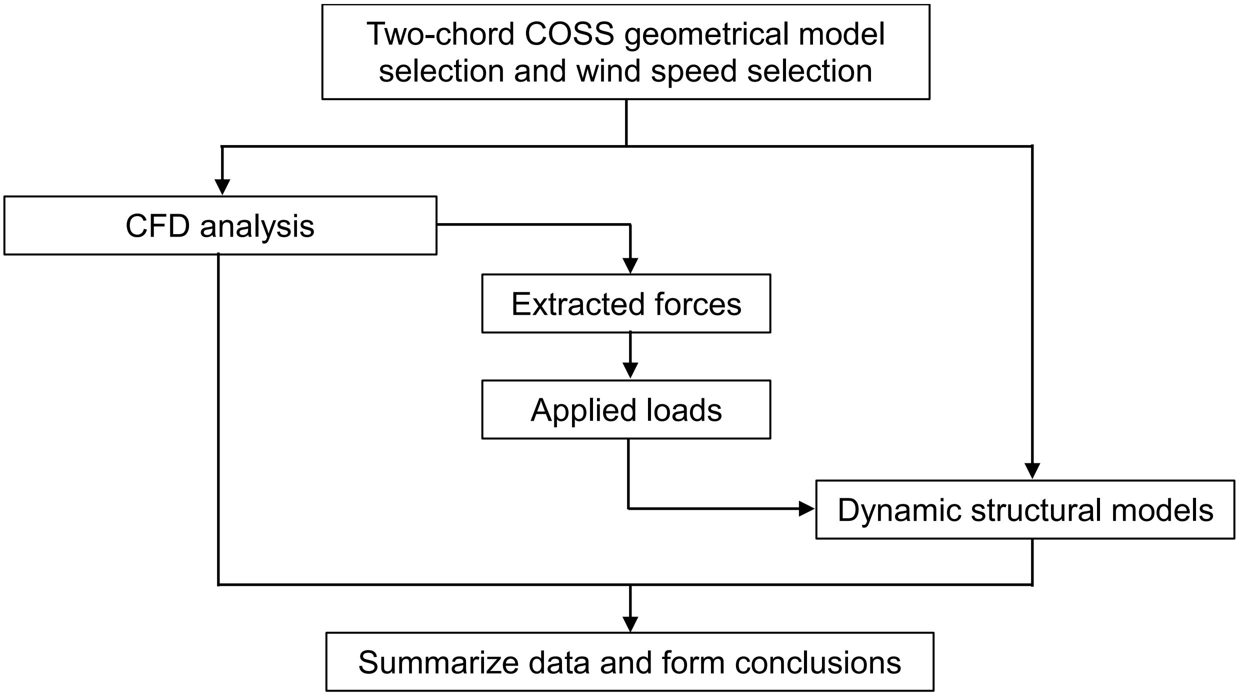

Figure 19 Methodology framework

This process can be described as quasi-fluid-structure-interaction, since the whole sign structure was not modeled in the fluid domain in the CFD analysis. Figure 20 highlights the influential surfaces investigated between the two models. Detailed descriptions of the modeling techniques are described in the subsequent section.

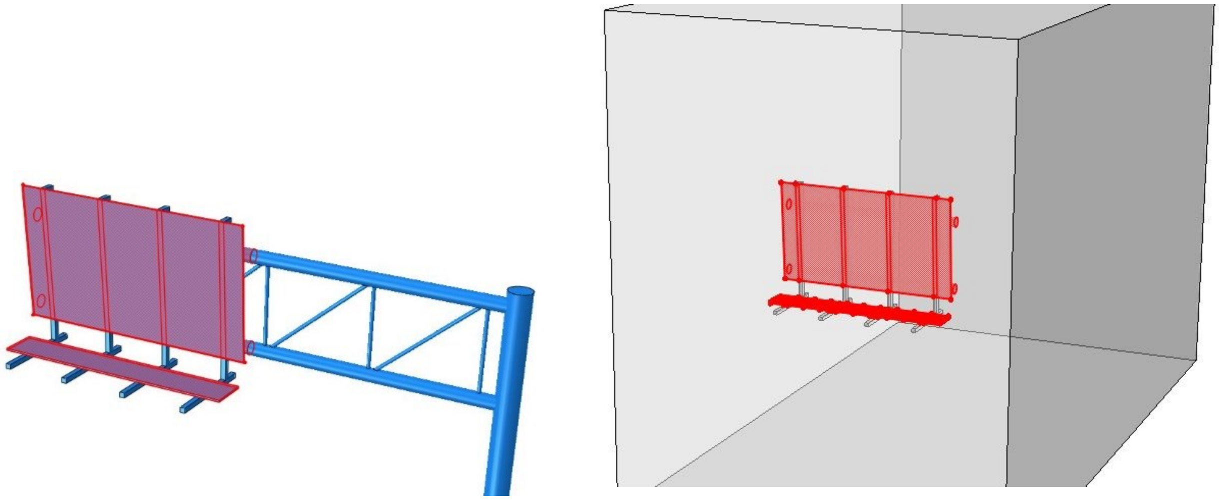

Figure 20 Investigated surfaces between the dynamic loading model (left) and the CFD model (right)

2.4.1 – Design Loads and Wind Speed Selection:

AASHTO LRFD Specifications for Structural Supports for Highway Signs, Luminaires, and Traffic Signals, 2015 First Edition (AASHTO 2015a) in conjunction with American Society of Civil Engineers (ASCE) 7-10: Minimum Design Loads for Buildings and other Structures (ASCE 2010) define the wind loads that COSS must be designed to resist.

Equation 3 defines the design wind pressure and is derived using standard air (defined in Section 2.5.1) and the theoretical pressure equation for a fluid contacting a surface. The resulting Pressure (P) is a function of the fluid's density (ρ) and the speed at which the fluid is moving (V).

$$\boldsymbol{P = \frac{1}{2}\rho V^2} \qquad \textbf{Equation 3}$$

Equation 4 is defined in ASCE 7-10 and calculates the design wind pressure for a structure. This equation takes into account the structure's location, height, surrounding features, and dynamic response, giving it more factors than the previous equation. The first factor in Equation 4 (0.00256) is equal to half of the density of air multiplied by the squared conversion of mph to ft/s (this factor changes to 0.613 for SI units). The design wind pressure (P_z) is calculated in psf using the basic wind speed (V) in mph. K_z, K_d, G, and C_d are all unitless factors and coefficients and are defined in Table 6.

$$\boldsymbol{P_z = 0.00256K_zK_dGV^2C_d} \qquad \textbf{Equation 4}$$

Table 6 Wind Pressure Equation Calculated Factors and Coefficients

Factor/Coefficient	Variable	Value
Height and Exposure Factor	K_z	0.94
Directionality Factor	K_d	0.85
Gust Effect Factor	G	1.14
Drag Coefficient	C_d	1.18

Kansas DOT's COSS are designed to resist a 105 mph (46.9 m/s) wind speed for natural wind loading, which corresponds to a wind load of 30.4 psf (1460 Pa). Changing the wind speed in Equation 4 results in a second order change in the design wind pressure.

The Gust Effect Factor which combines the dynamics of a structure with its design wind load (more rigid structures have lower Gust Effect Factors), was calculated using Section 26.9 in ASCE 7-10. It is typically used if a structure has a natural frequency lower than 1 Hz, which is characteristic for some two-chord COSS. The Gust Effect Factor is a function of the natural frequency of a structure and the height of the influential area. The Gust Effect Factor was calculated to be less than the minimum of 1.14, so 1.14 was used. The mean hourly wind speed ($\bar{V}_{\bar{z}}$) was calculated in the process and was determined to be 61.2 mph (27.4 m/s). The mean hourly wind speed is an important value because it defines the average wind speed a structure is likely to see at the structure's height during severe weather events. The average sign height defined in Section 2.1 was used to compute the mean hourly wind speed.

Three wind speeds were ultimately chosen for investigation: 1) 105 mph (46.9 m/s), 2) 61.2 mph (27.4 m/s), and 3) 30 mph (13.4 m/s) representing: 1) the basic design wind speed, 2) the mean hourly wind speed, and 3) a relatively equidistant lower wind speed, respectively.

2.5 Computational Fluid Dynamics (CFD) Modeling

The commercially-available Abaqus/CFD 2016 finite element analysis software (DSS 2014) was used to create computational fluid dynamics models to quantify the forces that developed in the COSS from natural wind gusts. The CFD models were also used to examine changes in the aerodynamic behavior of the sign structures with removal of the walkway. *It is important to note that the CFD models are time-dependent.*

The CFD models included the sign, chords directly behind the sign, butterfly supports, and walkway attachment, which together are referred to as the "CFD Structure" herein. The pole, webbing in the mast truss, and chords connecting the sign and pole were excluded from the CFD model for simplicity and convergence. This portion of the COSS is at the end of the cantilever and experiences the most significant loading when compared to the rest of the structure, making it the most influential part for stress development in the connections. Additionally, the walkway only spans in the CFD Structure's domain, and has no effect on the aerodynamic behavior of the pole or mast truss connecting the sign and the pole.

Since the mast truss and pole were omitted from the CFD models, the sign size and presence of a walkway attachment were the influential design characteristics captured in the fluid domain. The three sign sizes from the construction specifications, two attachment conditions, and three wind speeds defined in Section 2.4.1 accounted for the 18 CFD models that were constructed. The model creation process was similar across the different sign sizes and attachment conditions. The fluid domains were the same for each wind speed. Different wind speeds only changed the velocity and the time period.

2.5.1 – Defining CFD Interaction Surfaces and Material Definition:

Important characteristics of the CFD models were defined before modeling commenced. Air is a compressible fluid, and its material properties change with atmospheric temperature and pressure. Atmospheric pressure and temperature can vary throughout the year, resulting in a change of density of ±10%. (Hall 2015). Because of this, standard air was modeled. Standard air has a pressure of 14.7 psi (1 atm) and a temperature of 59° F (15° C). The properties used for air in the CFD are detailed in Table 7 (Hall 2015) (Kadoya et al. 1985).

Table 7 CFD Material Properties

Material	Description	ρ	μ
		lb/ft^3 (kg/m^3)	lb·s/ft^2 (Pa·s)
Air	Standard Air	$2.37 \cdot 10^{-3}$ ($3.80 \cdot 10^{-2}$)	$3.785 \cdot 10^{-7}$ ($1.789 \cdot 10^{-5}$)

The various surfaces in the CFD model were examined to determine how forces changed on the sign over time. These surfaces were: a) sign face, b) back of sign, c) top of sign, d) bottom of sign, e) top chord, f) bottom chord, g) top of grate, and h) bottom of grate, and are shown in Figure 21. Surfaces g) and h) did not exist in the CFD models without the walkway attachment. The vertical sides on the sign, walkway attachment, and chords were ignored for data extraction due to the symmetry of the fluid domain, and pressure applied to the vertical edges of the dynamic loading models would have a negligible effect on the torsional and chopping modes. The butterfly supports were ignored for data extraction, since the sections are very small resulting in negligible forces.

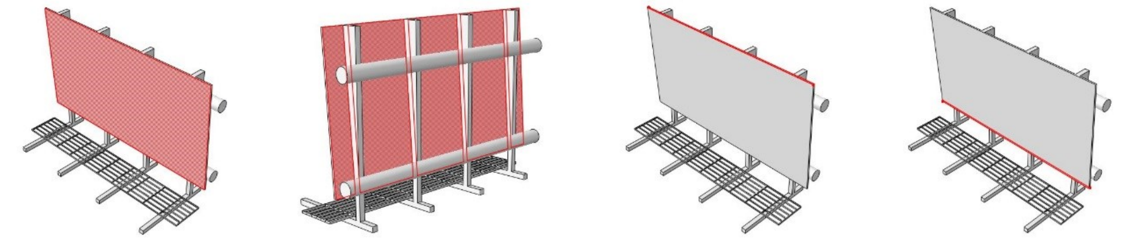

a) sign face
b) back of sign
c) top of sign
d) bottom of sign

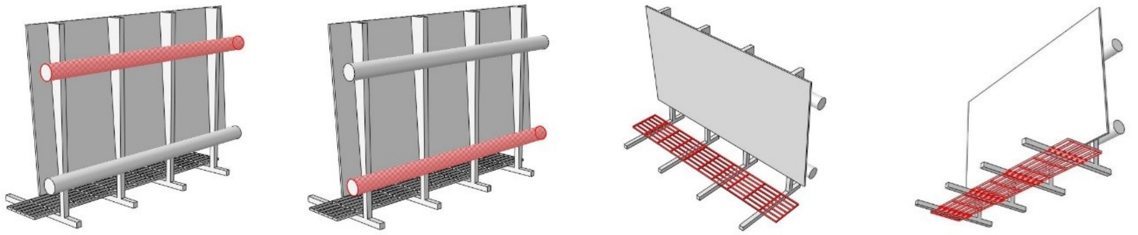

e) top chord
f) bottom chord
g) top of grate
h) bottom of grate

Figure 21 Influential surface locations used for force extraction from the CFD models: a) sign face, b) back of sign, c) top of sign, d) bottom of sign, e) top chord, f) bottom chord, g) top of grate, and h) bottom of grate

2.5.2 – Part and Assembly Creation, and Boundary Condition Selection:

The fluid domain for a CFD model can be very sophisticated, especially if the domain is fluid moving around an object and not fluid moving through a space. Researched performed by Chao et al. (2016) aimed to accurately describe the force applied by wind loading on large signs. They achieved this by creating a CFD model of a very simple sign shape. The CFD modeling was done using CFX by Ansys and the fluid domain is shown if Figure 22. Chao et al. (2016) described the steps to produce a typical fluid domain around a large sign shape. There are two important steps for correct fluid domain creation: 1) void space modeling and 2) boundary condition selection. In particular:

- The CFD Structure being investigated should be modeled and cut from a larger domain, leaving behind walls or void spaces that match the actual structure.

- Boundary conditions are the exterior faces of the larger domain. The faces should be far enough away so that boundary effects do not interfere with the aerodynamic effects being investigated.

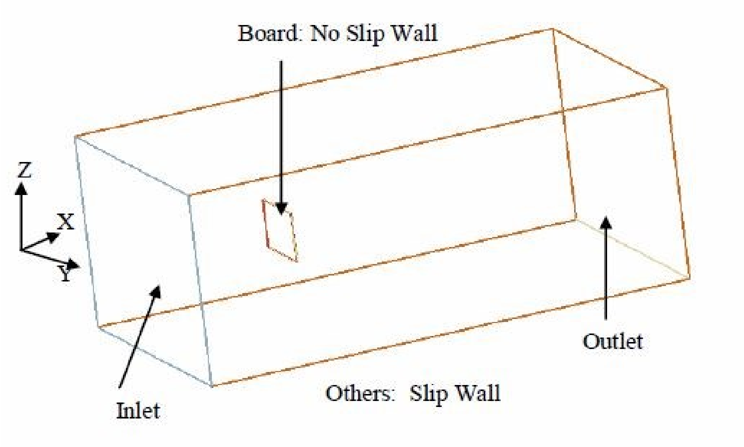

Figure 22 CTX fluid domain (Chao et al. 2016)

If the CFD Structure is too near a boundary condition, wakes and eddies will contact the boundary faces and produce boundary effects. The effects will likely result in model divergence as the low pressure turbulence contacting an inlet/outlet condition will cause cavitations. Model divergence results in invalid data or model instability. This is most important for the fluid outlet boundary condition due to the significant turbulence in the wake of a flat plate. The outlet boundary condition should be placed approximately eight times further away from the CFD Structure than the fluid inlet.

The type of boundary condition is important, as well. If surrounding boundary conditions (other than the inlet and outlet) are modeled as no-slip walls, turbulence from the walls will act in conjunction with turbulence from the CFD Structure, creating a faux-bottleneck condition which increases the fluid's speed around the CFD Structure. Therefore, boundary conditions other than the inlet and outlet should be modeled as slip walls, or as having pressurized inlet/outlet conditions.

A study performed by Gemba (2007) described the boundary layer created by flow over a flat plate, and investigating functions to describe its shape in both laminar and turbulent flow. A boundary layer inherently grows as it moves past its influential shape. It shifts from laminar to turbulent flow, as shown in Figure 23. The boundary layer thickness is important to estimate to mitigate boundary effects for both CFD modeling and wind tunnel testing.

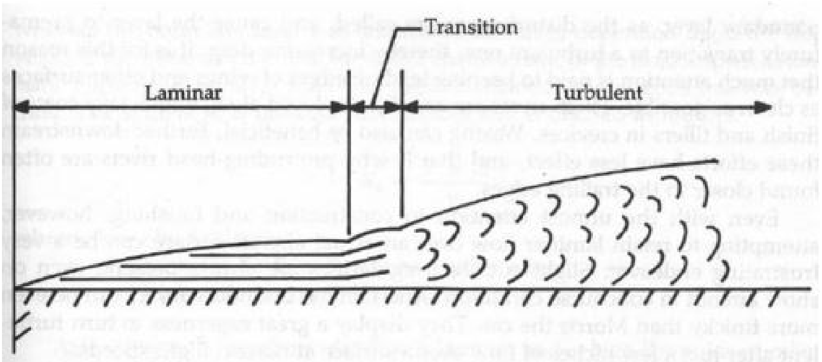

Figure 23 Profile of flow over a flat plate (Gemba 2007)

Equations 5 and 6 can be used to estimate the boundary layer thickness (δ) as a function of distance away (L) from the influential area for laminar and turbulent flow, respectively.

$$\boldsymbol{\delta_L = {}^{5L}/_{\sqrt{Re}}}$$ **Equation 5**

$$\boldsymbol{\delta_T = {}^{0.382L}/_{\sqrt[5]{Re}}}$$ **Equation 6**

The Reynolds number (R_e) is an important constant in these equations as it characterizes the flow as laminar or turbulent. The Reynolds number of a fluid is defined by Equation 7, and its variables are defined in Table 8 for standard air.

$$\boldsymbol{Re = \frac{\rho V L}{\mu}}$$ **Equation 7**

Table 8 Reynolds Number for Standard Air (CFD Modeling)

Variable	Notation	Value	Units (S.I.)
Density	ρ	$2.37 \cdot 10^{-3}$ ($3.79 \cdot 10^{-2}$)	lb/ft^3 (kg/m^3)
Velocity*	V	44 (13.4)	ft/s (m/s)
Characteristic Length**	L	0.125 ($3.81 \cdot 10^{-2}$)	ft (m)
Dynamic Viscosity	μ	$3.785 \cdot 10^{-7}$ ($1.789 \cdot 10^{-5}$)	lb·s/ft^2 (Pa·s)
Reynolds Number	Re	34400	-

---

*30 mph = 44 ft/s (13.4 m/s)

**1.5 in. = 0.125 ft (3.81 cm)

The lower the fluid's velocity, the larger the boundary layer thickness, and because of this the lowest wind speed was chosen for this calculation. In this application, the characteristic length is the thickness of the sign. Using the Reynolds number for a wind speed of 30 mph (13.4 m/s) and a characteristic length of 1.5 in. (38.1 mm), a turbulent boundary layer thickness (δ_T) was computed as a function of distance away from the CFD Structure (L). This is shown in Equation 8:

$$\boldsymbol{\delta_T = 0.0473L} \qquad \textbf{Equation 8}$$

The turbulent boundary layer is critical for CFD modeling because turbulence can cause cavitation conditions which results in model instability (Chao et al. 2016). Although this expression estimates the size of the turbulent boundary layer, it is suggested that a larger distance be used.

In the CFD models created as part of this investigation, one part was created which was used as the fluid domain for the assembly, the process for which is shown in Figure 24. The domain was created by: (1) modeling a large, rectangular fluid domain, (2) cutting out the filled CFD Structure, (3) resulting in a fluid domain around the CFD Structure. The fluid domain was modeled as a solid object encompassing the air around the CFD Structure.

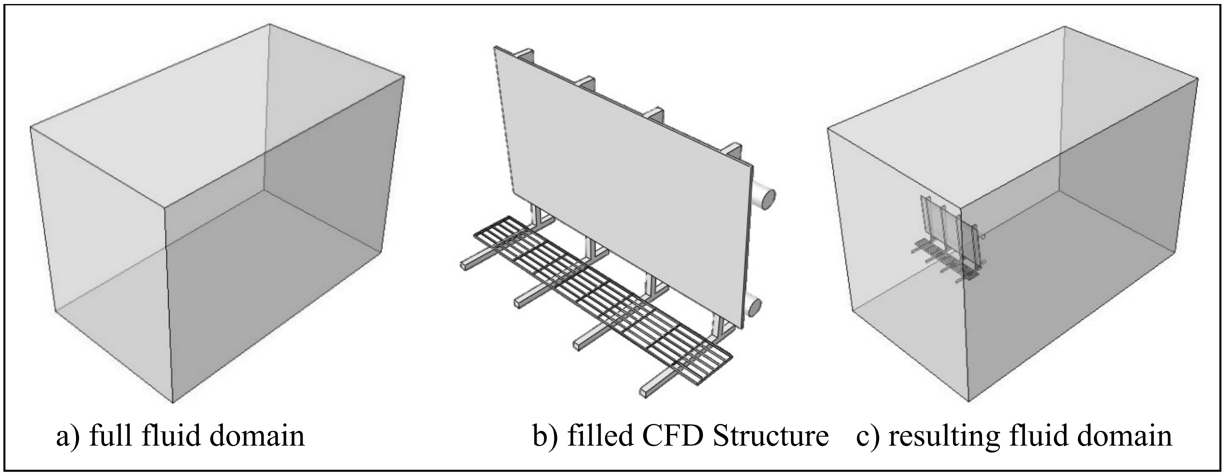

a) full fluid domain b) filled CFD Structure c) resulting fluid domain

Figure 24 Fluid domain creation: a) full fluid domain, b) filled CFD Structure, and c) resulting fluid domain

Below is a list of the boundary conditions that were assigned to the resulting fluid domain, and their distance to the CFD Structure denoted by δ_n:

- Walls and ceiling – fluid inlet/outlet condition – specified pressure of 14.7 psi (1 atm), δ_{walls} = 0.6·(Sign Length), $\delta_{ceiling}$ = 1.5·(Sign Height).
- Ground – no slip fluid wall condition – δ_{ground} = 17' - 4" (5.28 m). δ_{ground} is defined in the construction specifications.
- Inlet – fluid inlet/outlet condition – specified velocity (see Section 2.4.1), δ_{inlet} = Sign Height.
- Outlet – fluid inlet/outlet condition – specified pressure of 14.7 psi (1 atm), $\delta_{outlet} = 8 \cdot \delta_{inlet}$ (DSS 2015).
- Sign Interface – no-slip fluid wall condition – these boundaries are walls in the fluid domain.

Dimensions of the boundary conditions were initially selected using Equation 8 with an additional 2 ft (0.61 m) added to the calculation. Even with the extra distance, some models still experienced boundary interactions at 30 mph (13.4 m/s). To resolve this, additional space was formulated to create the rules defined in boundary condition distances (1) and (3).

2.5.3 – Fluid Domain Meshing:

All of the CFD models utilized large, sophisticated domains, which required careful meshing techniques. In Abaqus/CFD 2016, data can only be extracted at nodes (not elements), so faces cannot be defined for data extraction. To determine the forces resulting on the CFD Structure from natural wind gusts in the CFD simulations, nodes were carefully spaced such that forces at nodes could be easily multiplied by the element's area to obtain pressures. Additionally, Abaqus/CFD 2016 produced the best results with a hex-mesh. (DSS 2015) Because of this, a hex-mesh technique was assigned. This could only be done after systematic partitioning of the fluid domain. Every face created by the cut-out region of the CFD Structure in the fluid domain was extended to create a partition in the fluid domain. A typical, final extension-partitioned fluid domain is shown in Figure 25. This step creates geometrically-sound baselines for seed propagation, and is the only way a hex-meshing technique was able to be applied to this type of domain. The mesh size was size controlled using 3” (7.62 cm) seed size. Nodes on the CFD Structure’s surfaces were grouped by elemental area before the model was executed.

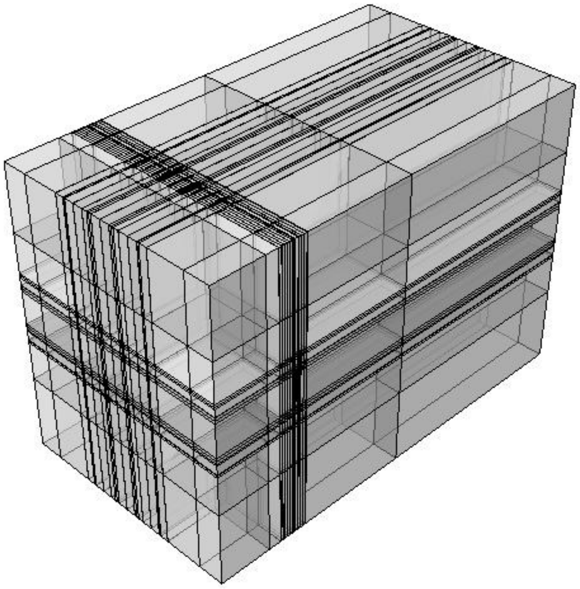

Figure 25 Typical partitioned fluid domain

Regions directly surrounding the CFD Structure were the most important to monitor. Regions nearer to the boundaries were of less interest, other than checking for convergence and mitigating boundary interactions. Because of this, the mesh was assigned an increased size around the perimeter of the fluid domain to improve efficiency of the model executions. The mesh size was increased to a 9 in. (23 cm) seed size in these areas. Figure 26 shows the mesh for a typical CFD model with a walkway attachment, and Figure 27 shows the mesh for a typical CFD model without an attachment. Note, both figures are zoomed in, and do not show the full domain for the sake of clarity.

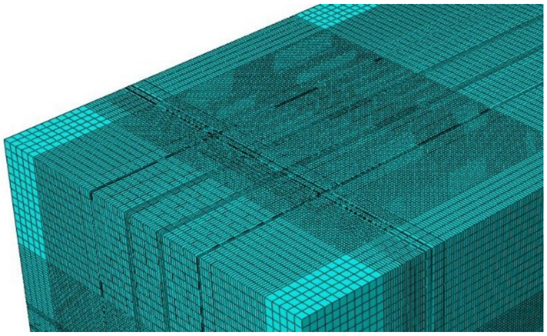

Figure 26 Typical fluid domain mesh, with walkway attachment

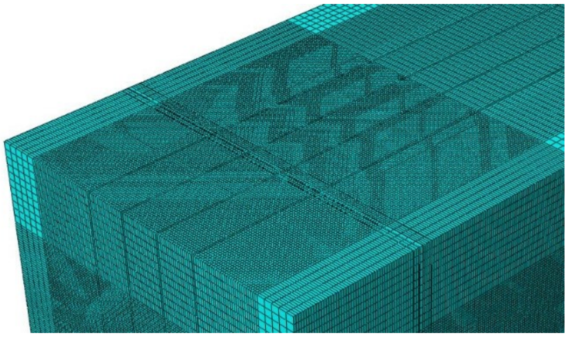

Figure 27 Typical fluid domain mesh, without walkway attachment

2.5.4 – Step Creation and Turbulence Modeling Parameters:

Each CFD model underwent a time history flow step with a fixed time increment size of 0.01 seconds. The models' time period was selected based on how long it took the model to produce a constant laminar flow in the wake of the sign, rounded up to the nearest half second. Table 9 presents the time period modeled at the desired wind speeds in the CFD analysis.

Table 9 CFD Model Time Period Definition

Wind Speed	CFD Time Period
mph (m/s)	s
105 (46.9)	2.5
61.2 (27.4)	3
30 (13.4)	5

Turbulence modeling is an important and complex feature of CFD programs and is a function of the fluid being modeling, the fluid speed, the fluid domain, and expected turbulence. Most turbulence modeling modules in CFD programs require constants to be defined before the model is processed. These constants stem from fluid properties to eddy propagation. Generally, the more complex a model, the more calibration is required for valid results.

Although the CFD models being created in this research project are unusual in nature, the CFD Structure in the domain was relatively simple and large, which produce simple vortices in its wake. Additionally, the fluid was modeled as a homogenous material, wind speeds were kept constant in individual model runs, and boundary effects were mitigated. Ultimately, the turbulence was experienced to be simple. For this reason, default turbulence modeling parameters were selected. The default is Spalart-Allmaras turbulence modeling, and the constants prescribed with this technique have been defined in Table 10.

Table 10 Spalart-Allmaras Turbulence Modeling Constants (DSS 2015)

Constants	Value
C_{b1}	0.1355
C_{b2}	0.622
C_{v1}	7.1
C_{v2}	5
C_{w1}	3.2391
C_{w2}	0.3
C_{w3}	2
σ	0.6667
K	0.41

Because turbulence was being modeled, all inlet/outlet boundary conditions needed to be defined with kinematic eddy viscosities. This defines how turbulent the flow is as it enters the domain. The CFD models in this research utilized constant, laminar wind speeds; therefore, all kinematic eddy viscosities needed to be a small, non-zero value: 0.01 in.^{2}/s ($6.45\cdot10^{-6}$ m^2/s) was selected.

Three variables were defined in the field output request: pressure, velocity, and vorticity. Variables for the solver equations for the field output request were defined through an iterative process that produced model convergence. Table 11 defines these variables for the time history flow step. These variables were maintained the same for each CFD model and for each wind speed.

Table 11 CFD Model Solvers' Variables Definition

Solver	Momentum Equation	Pressure Equation	Transport Equation
Iteration Limit	600	1200	600

Convergence Checking Frequency	1	10	1
Linear Convergence Limit	$1\cdot10^{-12}$	$1\cdot10^{-14}$	$1\cdot10^{-12}$

With converged output files from the CFD models, time history forces were extracted from the influential surfaces defined in Section 2.5.1. Additional data, both qualitative and quantitative, could also be extracted and observed anywhere in the fluid domain across the time history. This included (but was not limited to) pressure heat-maps of the influential surfaces, velocity profiles around the sign, velocity vector outputs, eddy location and propagation, critical eddy interaction, porosity of the grate, and vorticity. See Appendix A1 and A2 for eddy interaction and velocity profile data.

2.6 Finite Element Modeling – Dynamic Loading

Using the same Abaqus/CAE 2016 models used to determine the fundamental frequencies (described in Section 2.3), in conjunction with the time-dependent forces extracted from the Abaqus/CFD 2016 models described Section 2.5, dynamically-loaded models were constructed.

Only the 27 base models described in Section 2.1 were modeled dynamically, and not the five extreme case models. This is because the CFD models only captured the small, medium, and large sign sizes, and not the additional five unique sizes considered in the extreme case models. The 27 base models, two grate conditions (with grate vs. without grate), and loading at the three specified wind speeds accounted for 162 dynamically-loaded structural models. The only changes to the Abaqus/CAE 2016 models from Section 2.3 and the dynamic loading models in this section were the step creation and time-dependent load application.

2.6.1 – Step Creation and Load Application:

The step was changed from the frequency step used in prior models to a dynamic, implicit loading step. The time period used for the dynamic loading step matched the output from the CFD models for the respective wind speed outlined in Table 9, as well as the fixed time increment size of 0.01 seconds. Stresses, strains, displacements, forces, and reactions were the variables defined in the field output request.

Loads were modeled as a uniform unit load (with a value of 1) on the respective part in the structural model. The unit loads would be later multiplied by the imported time-dependent amplitudes from the CFD data. The top and bottom chord loads were modeled as being loaded by uniform line loads. The sign face, back of sign, top of grate, and bottom grate loads were loaded with uniform pressures. The top of sign and bottom of sign loads were modeled as uniform shell edge loads. The loads from the CFD data were imported as smooth step amplitudes. The amplitudes were then multiplied to each unit load from the influential surface for the given wind speed on the respective part.

Displacements in the Y and Z direction at the top chord in the mast truss at the end of the cantilever were extracted. Stresses in both box-connections and at the base of the pole were also extracted. After the results were computed for the COSS with the walkway, the walkway was removed from the assembly along with Constraint 1 from Section 2.3.3, and the model was executed in the new geometric configuration. The updated displacements and stresses were recorded, producing two data sets for every sign geometry considered.

2.7 Experimental Methods

Experimental testing was conducted to validate and contextualize the CFD modeling results. The experimental testing consisted of wind tunnel tests with the goal of determining forces acting on the sign at various wind speeds. A scale model sign was constructed, supported in a wind tunnel, and subjected to multiple wind speeds. Both qualitative and quantitative data were collected from the wind tunnel testing, but due to physical limitations, some of the data observed in the CFD modeling was unable to be observed in the experimental testing (such as pressure heat-maps or velocity profiles). The quantitative data collected from wind tunnel testing consisted of force data collected at different wind speeds. The qualitative data consisted of turbulence prevalence, which revealed eddies and vortices.

2.7.1 – Scale Model Construction:

Similar to the CFD Structure modeled in the CFD analyses, the scaled physical model did not include the pole, webbing in the mast truss, or chords connecting the sign to the pole. The scaled model included the sign, three butterfly supports, and walkway attachment (grate). The chords were excluded to simplify the contact connection from the scaled model to the load cells. (It is important to note that the chords were found to not have experienced significant forces in the CFD analysis.)

The wind tunnel used for the experimental testing had a closed, 4 ft. (1.22 m) x 3 ft. (0.91 m) cross sectional testing area. Although the scaled model was significantly smaller than its constructed counterpart, significant forces can still develop, especially at higher speeds (Barlow 1999). For this reason, similar materials from the construction specifications were selected for the scaled model, and for the sake of structural integrity. The sign was made out of aluminum, and the butterfly supports and walkway components were steel.

The large sign size was selected (from Section 2.1) to be investigated in the wind tunnel testing. This was partially to accommodate potential future testing of smaller sign sizes, which could be accommodated in the wind tunnel at the same scale of the large sign size. Using the same process in Section 2.5.2, the boundary layer thickness for wind tunnel testing was estimated. Unlike the CFD modeling, the laminar boundary layer was critical due to its stronger boundary interaction. Boundary interactions from turbulent boundary layers are relatively small, and do not affect experimental models (Barlow 1999).

Table 12 Reynolds Number for Standard Air (Wind Tunnel Testing)

Variable	Notation	Value	Units (S.I.)
Density	ρ	$2.37 \cdot 10^{-3}$ ($3.79 \cdot 10^{-2}$)	lb/ft^3 (kg/m^3)
Velocity*	V	7.333 (2.235)	ft/s (m/s)
Characteristic Length**	L	0.0417 (0.0127)	ft (m)
Dynamic Viscosity	μ	$3.785 \cdot 10^{-7}$ ($1.789 \cdot 10^{-5}$)	lb·s/ft^2 (Pa·s)
Reynolds Number	R_e	1910	-

*5 mph = 7.333 ft/s (2.24 m/s)

**0.5 in. = 0.0416 ft (12.7 mm)

Using the Reynolds number for a wind speed of 5 mph (2.24 m/s) (5 mph was the lowest wind speed for wind tunnel testing) and a characteristic length of 0.5 in. (12.7 mm) (0.5 in. was the thickness of the scale model sign), a laminar boundary layer thickness (δ_L) was derived as a function of distance away from the model sign (L). This is shown in Equation 9:

$$\boldsymbol{\delta_L = 0.114L} \qquad \textbf{Equation 9}$$

The laminar boundary layer thickness was calculated to be 4.3 in. (109 mm) on each side of the sign to mitigate boundary effects up to 3 ft (0.91 m) downwind of the test set up. The thickness was rounded up to 6 in. (152 mm). The sign's length controlled the scale, which was selected at a 20:3 size reduction. Drawings of the scaled sign are provided in the Appendix.

The scaled model aluminum sign imitated the shape of the construction specifications, and not the CFD model. The aluminum sign piece, even at a 20:3 scale, would be too heavy to hang if it was a solid piece. The construction specifications called for extruded aluminum channels to compose the sign. The channels are connected to each other with bolts through their flanges, as shown in Figure 28. The aluminum sign piece imitated this by attaching aluminum bars to the back of the aluminum sheet shown in Figure 29. The ribbing was attached to the aluminum sheet using a two-part adhesive epoxy. The scaled aluminum sign piece was bolted to the butterfly supports with angled wooden blocks between the two pieces. The wooden blocks gave the sign its necessary 4% tilt.

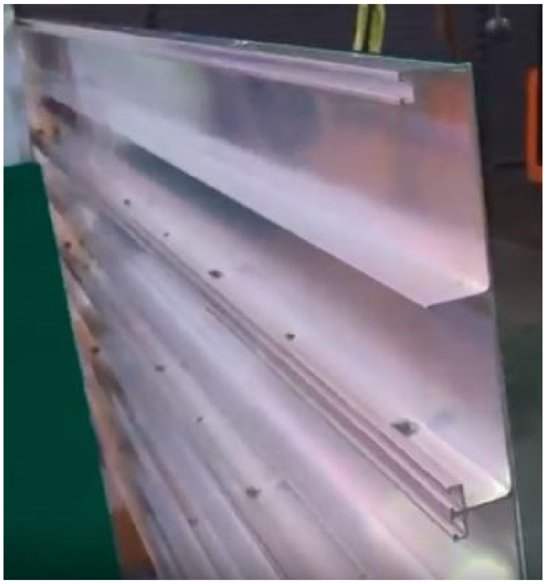

Figure 28 Constructed extruded aluminum sign (LA DOT)

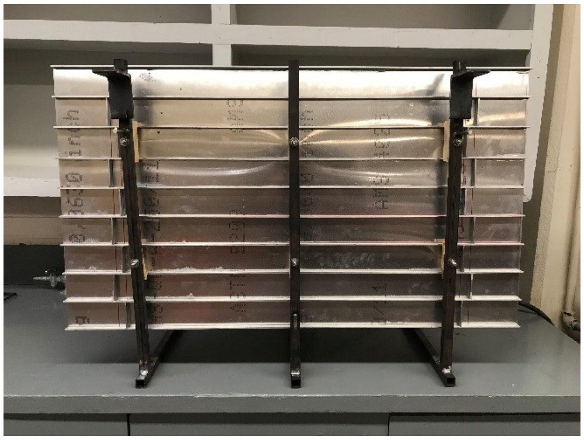

Figure 29 Physical scaled sign model

Although the construction specifications call for Z-Shapes (similar to small wide flange beams, and not Z-channels) for the butterfly supports, it is commonplace to use similarly-sized square HSS in the field. The scale model used scaled square HSS sections for the butterfly supports. The connection between the vertical and horizontal square HSS were welded together. Only three butterfly supports were constructed instead of four to allow for easier walkway attachment connectivity.

The scaled model walkway was constructed to have a similar porosity as walkways used in the field. The walkway was constructed out of small steel bars. The bars were notched and then welded together at each intersection. The walkway was attached to the butterfly supports with zip ties for easy removal and reattachment. The heads of the zip ties were tucked into the voids of the scaled walkway.

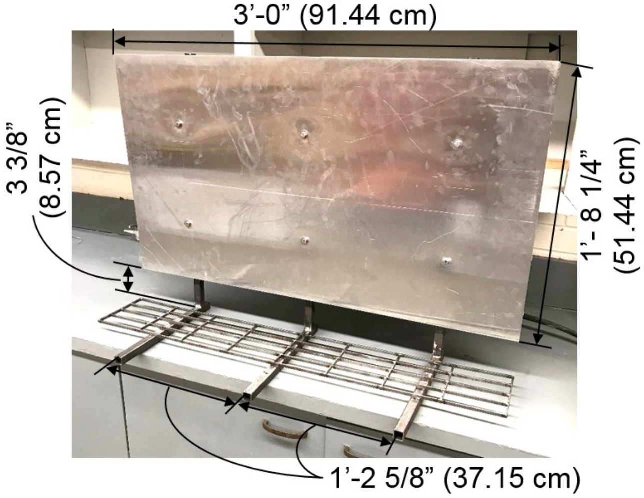

Figure 30 Scaled model used for experimental testing in the wind tunnel

2.7.2 – Experimental Setup:

Two series of experimental tests were conducted in the wind tunnel. The first series of tests was aimed at collecting forces acting on the sign, produced by different wind speeds. These forces were measured through use of load cells. Forces were recorded at wind speed increments of 5 mph (2.24 m/s), starting at 10 mph (4.47 m/s) and capping at 40 mph (17.88 m/s). Each wind speed increment was repeated three times. The test series was limited to a maximum wind velocity of 40 mph due to the turbulence caused by the large shape in the wind tunnel. The second series of tests involved observing this turbulence through use of fog and lasers. Videos were recorded during this test, and qualitative data was collected. Due to sensitive instrumentation in the wind tunnel, this test was only conducted at a wind speed of 5 mph (2.24 m/s). Both test series were conducted both with and without the walkway attachment to observe its influence on the results.

The scaled model was hung in the wind tunnel using a system of rollers. Figure 31 shows a schematic of the restraints used in the wind tunnel, and Figure 33 shows the actual test setup. The rollers only supported the sign in the y-direction and were greased to mitigate friction forces in the x-direction. Three load cells were placed behind the scaled model facing the x-direction; their contact locations shown in Figure 32. The three load cells behind the sign captured the forces that developed under the action of the experimental wind gusts. A fourth load cell was placed underneath the sign in the y-direction. This load cell never came into contact with the sign assembly during the tests and served as a vestigial instrument to record data if the scale model dislodged from the test set-up.

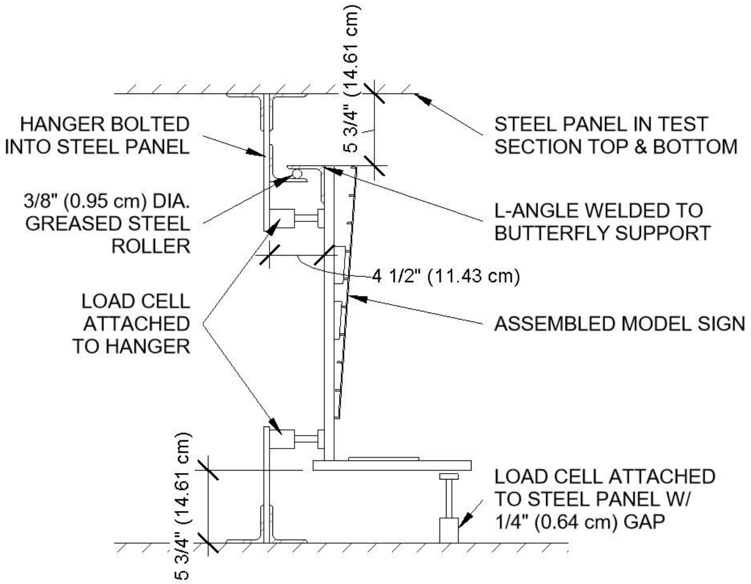

Figure 31 Wind tunnel test setup connectivity

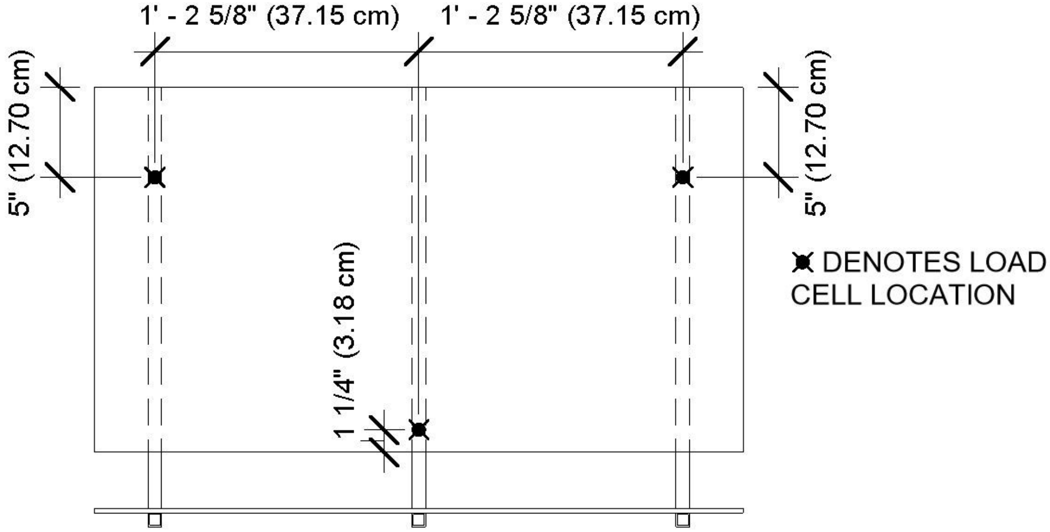

Figure 32 Load cell locations, behind the sign face

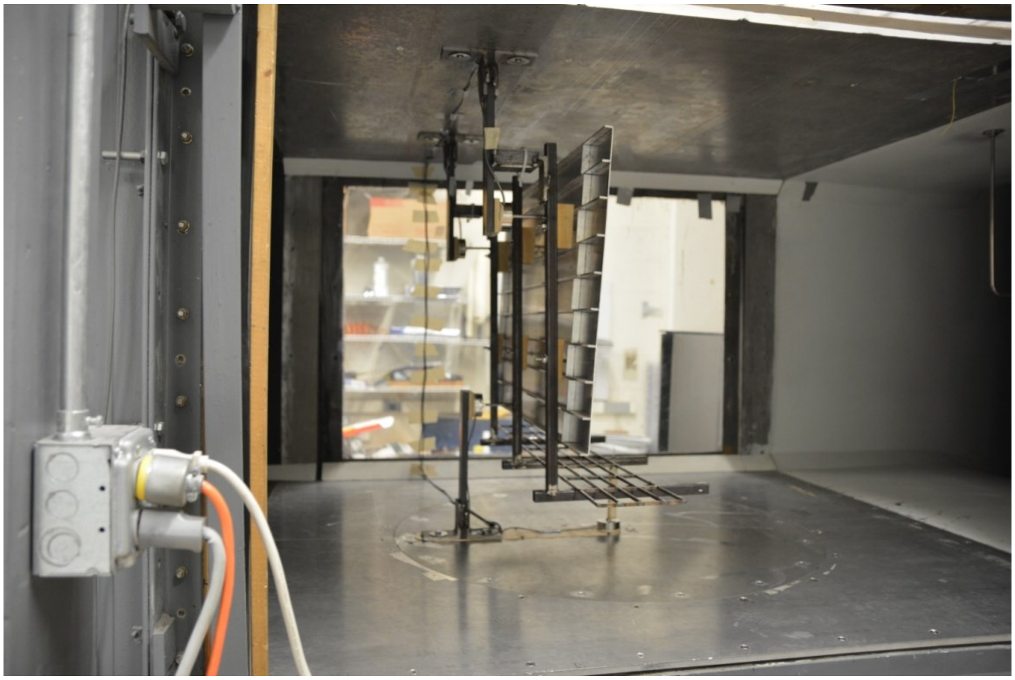
Figure 33 Experimental test setup

A fog machine was placed upstream of the scale model in the wind tunnel. The wind tunnel used recycles the circulating air, yielding a uniformly translucent gas. A laser was placed outside of the wind tunnel pointing into the testing area. The laser illuminated a plane where incongruities in the fog could be easily seen. The incongruities in the fog displayed eddies and vortices created by the presence of the scaled model. The laser plane was placed in front of the model, at the sign face, and behind the model. Figure 34 displays the laser plane used in this portion of the experimental testing.

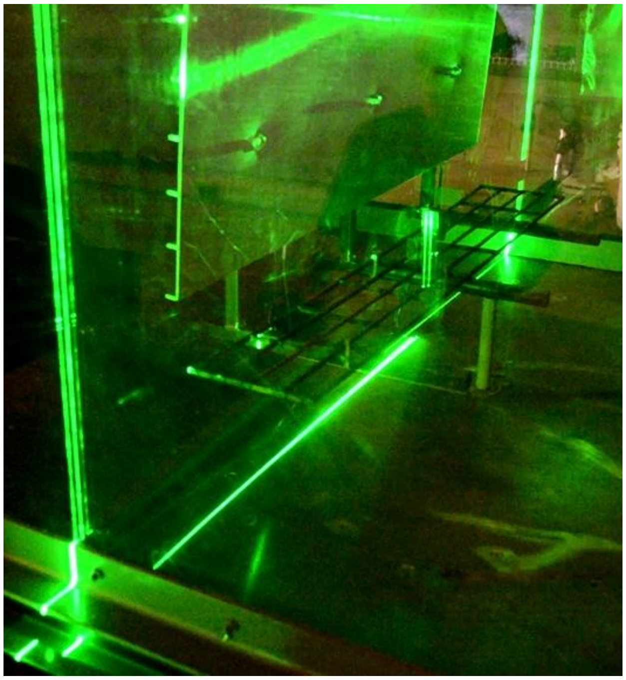

Figure 34 Typical laser plane (placed at the model sign face)

Results

In this chapter, the data produced from the finite element models and the experimental wind tunnel testing is summarized. In each section, trends are identified in the data. Due to the number of models produced from the dimensional analysis, most of the comparison data is graphed with respect to the walkway attachment's mass in terms of a percentage of the system mass. Trends are better observable with this variable chosen as the control.

3.1 Finite Element Modeling – Fundamental Frequencies of the COSS

All 32 models' modal response frequencies were computed, both with and without a walkway, as shown in Table 13. Changes in mass resulted in changes in the modal frequency, as defined in Equation 1. Mass and stiffness changed with each model, but only the mass significantly changed upon removal of the walkway.

Table 13 COSS Modeled Natural Frequencies

Model	**walkway mass %**	**with walkway**	**without walkway**	**Δ**	**with walkway**	**without walkway**	**Δ**
	%	**Hz.**	**Hz.**	**%**	**Hz.**	**Hz.**	**%**
S20x12-L20-P25	4.63%	0.87	0.91	4.31%	1.25	1.30	4.35%
S20x12-L20-P27	4.52%	0.84	0.88	4.26%	1.17	1.21	3.79%
S20x12-L20-P29	4.45%	0.81	0.85	4.21%	1.10	1.14	3.68%
S20x12-L16-P25	4.81%	1.02	1.08	5.67%	1.39	1.44	3.70%
S20x12-L16-P27	4.70%	0.98	1.04	5.59%	1.30	1.35	3.57%
S20x12-L16-P29	4.63%	0.94	1.00	5.50%	1.22	1.26	3.46%
S20x12-L12-P25	5.14%	1.20	1.25	3.84%	1.61	1.67	3.71%
S20x12-L12-P27	5.02%	1.15	1.20	3.87%	1.49	1.55	3.57%
S20x12-L12-P29	4.93%	1.10	1.15	3.86%	1.39	1.44	3.44%
S16x9-L20-P25	4.14%	0.97	1.02	4.87%	1.46	1.52	3.91%
S16x9-L20-P27	4.04%	0.94	1.00	5.31%	1.37	1.42	3.76%
S16x9-L20-P29	3.94%	0.92	0.97	5.55%	1.28	1.33	3.62%
S16x9-L16-P25	4.44%	1.25	1.35	7.17%	1.70	1.77	3.85%
S16x9-L16-P27	4.33%	1.21	1.30	6.58%	1.58	1.64	3.68%
S16x9-L16-P29	4.24%	1.18	1.25	5.79%	1.47	1.53	3.52%

S16x9-L12-P25	4.80%	1.55	1.68	7.80%	1.99	2.07	3.96%
S16x9-L12-P27	4.70%	1.48	1.60	7.24%	1.84	1.91	3.74%
S16x9-L12-P29	4.57%	1.41	1.52	7.22%	1.70	1.77	3.56%
S12x6-L20-P25	3.34%	0.97	1.01	3.86%	1.33	1.37	3.20%
S12x6-L20-P27	3.25%	0.94	0.97	3.79%	1.24	1.28	3.09%
S12x6-L20-P29	3.19%	0.90	0.93	3.71%	1.16	1.20	2.98%
S12x6-L16-P25	3.63%	1.19	1.24	4.01%	1.55	1.60	3.25%
S12x6-L16-P27	3.55%	1.14	1.19	3.91%	1.44	1.48	3.12%
S12x6-L16-P29	3.45%	1.09	1.13	3.81%	1.34	1.38	2.99%
S12x6-L12-P25	3.88%	1.44	1.49	3.81%	1.78	1.83	3.05%
S12x6-L12-P27	3.79%	1.36	1.41	3.70%	1.64	1.69	2.91%
S12x6-L12-P29	3.68%	1.28	1.33	3.60%	1.51	1.55	2.80%
S23.5x11.5-L5.25-P29	5.83%	1.28	1.33	3.61%	1.55	1.60	3.38%
S11x6-L19-P25	3.16%	0.95	0.99	3.57%	1.16	1.20	3.59%
S16x11-L21-P27	3.94%	0.89	0.93	3.71%	1.31	1.36	3.66%
S18x8.5-L1-P23	6.11%	2.03	2.10	3.18%	2.34	2.41	2.94%
S18.5x11.5-L12.75-P30	4.59%	1.12	1.17	3.85%	1.39	1.44	3.29%

To determine the effect of the walkway on the modal response, the differential percentage of the modal frequency was graphed over the walkway mass percentage of the system in Figure 35 for the torsional mode shape and in Figure 37 for the chopping mode shape. This data seems marginally uncorrelated but clear groupings of data points are shown. Figure 36 (torsional mode shape) and Figure 38 (chopping mode shape) display the same data in accordance to the models' sign size. Here, groupings of data are easily seen as all similar sign sizes resulted in grouped data points. Each sign size group, except the extreme models, show three sets of three points that make three straight lines. Each line resembles a mast truss length and each dot on the line accounts for one of the three pole heights.

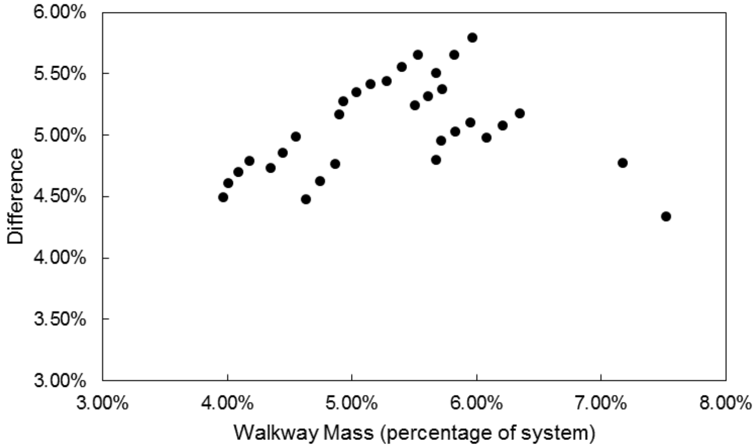

Figure 35 Torsional Mode Natural Frequency Change by Walkway Mass Percentage

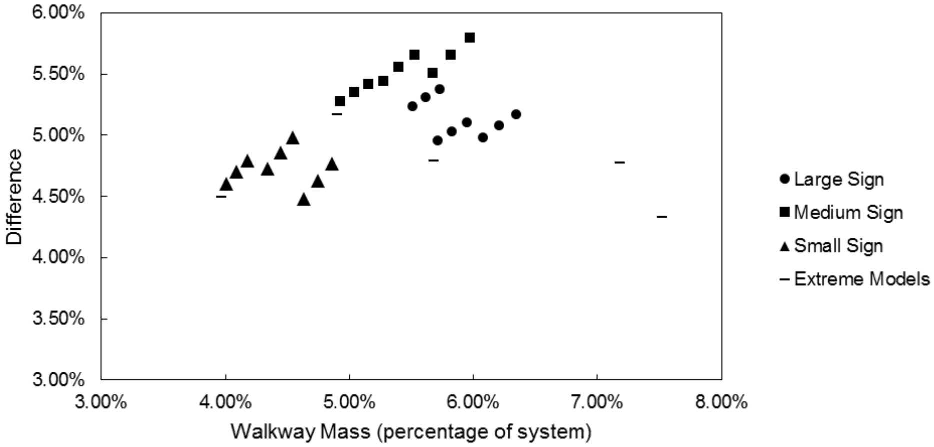

Figure 36 Torsional Mode Natural Frequency Change Grouped by Sign Size

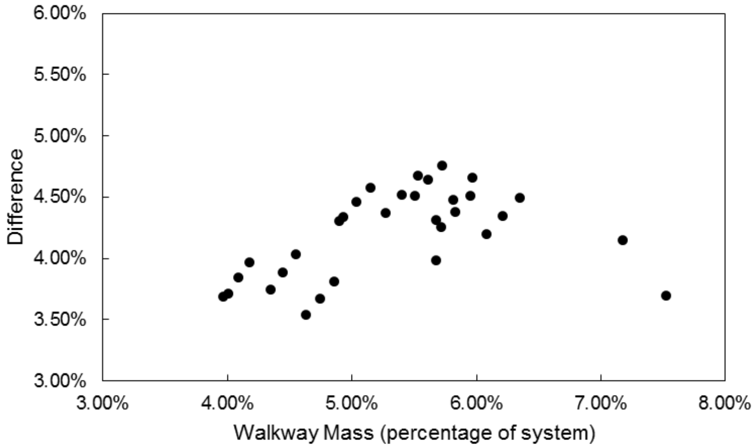

Figure 37 – Chopping Mode Natural Frequency Change by Walkway Mass Percentage

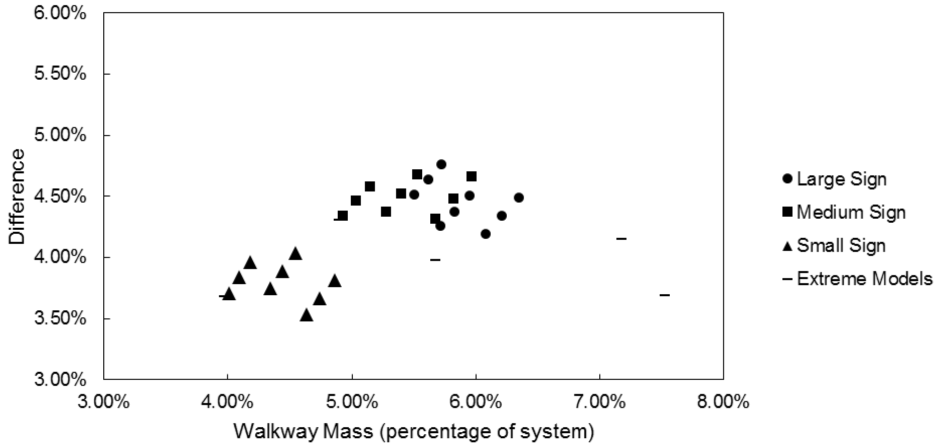

Figure 38 Chopping Mode Natural Frequency Change Grouped by Sign Size

The following trends were identified using the data shown in Figure 36 and Figure 38, in conjunction with the data in Table 13:

- A larger sign size, and subsequent structure, generally corresponded with a higher natural frequency.
- The medium sign size COSS exhibited the largest average change in natural frequency with removal of the walkway, followed by large sign size, then by the extreme models, then by small sign size.
- Larger mast truss lengths corresponded with lower natural frequencies when compared to shorter mast truss lengths; thus, a larger difference of natural frequency with the walkway removed.
- Larger pole height corresponded with lower natural frequencies when compared to smaller pole heights; thus, a larger difference of natural frequency with the walkway removed.
- Removal of the walkway always resulted in a higher natural frequency when compared to the case where the walkway was attached.

These trends were the same for both characteristic modes. Each of these trends was consistent with typical cantilever dynamic behavior. The average percent change observed after walkway removal was 5.06% for the torsional mode and 3.47% for the chopping mode.

3.2 Computation Fluid Dynamic Modeling Results

Pressures were extracted from the influential surfaces from the 18 CFD models and were then multiplied by respective areas to produce a time history of the applied force. The pressure output was given in absolute pressure, so a correction of 14.7 psi or 1 atm (101.4 kPa) was subtracted from each pressure value. The force applied to the CFD Structure in the direction of flow is denoted here as the "X-Force", and the force applied to the CFD Structure normal to the direction of flow is denoted here as the "Y-Force". The X-Force is the difference between the pressure at the sign face and the pressure behind the sign, shown as surfaces a) (sign face) and b) (back of sign), respectively in Figure 2.5.1.1. The resulting pressure behind the sign was negligible in every test. The Y-Force was taken as the sum of the pressures sustained on surfaces 'c' through 'h' in Figure 2.5.1.1 (surfaces 'g' and 'h' were ignored if the model did not have a walkway attachment). Each force has been plotted against time, showing a comparison between the grate/no-grate conditions. The X-Force is denoted in the figures ending in "a", and the Y-Force is denoted in the figures ending in "b". The results for the force time-histories are presented in Figure 39 - Figure 56.

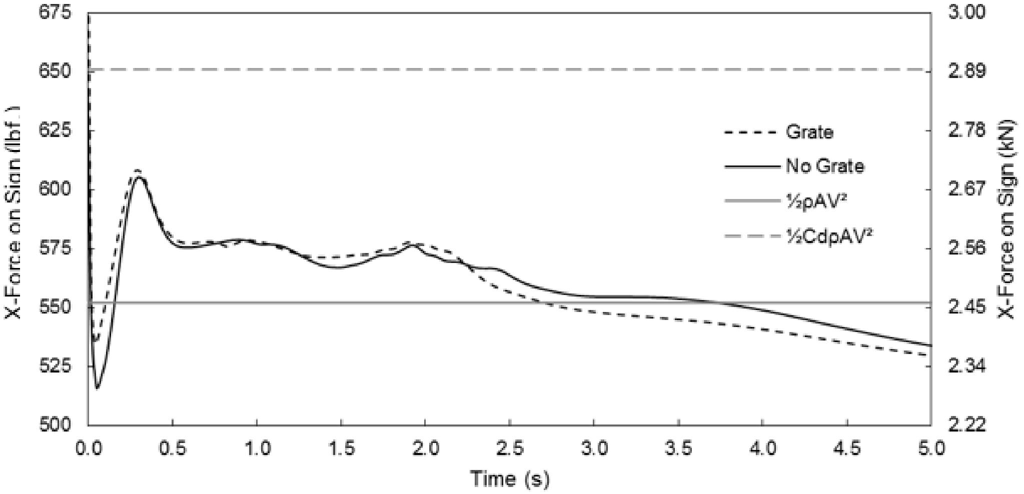

Figure 39 X-Force on Large Sign at V=30 mph (13.4 m/s)

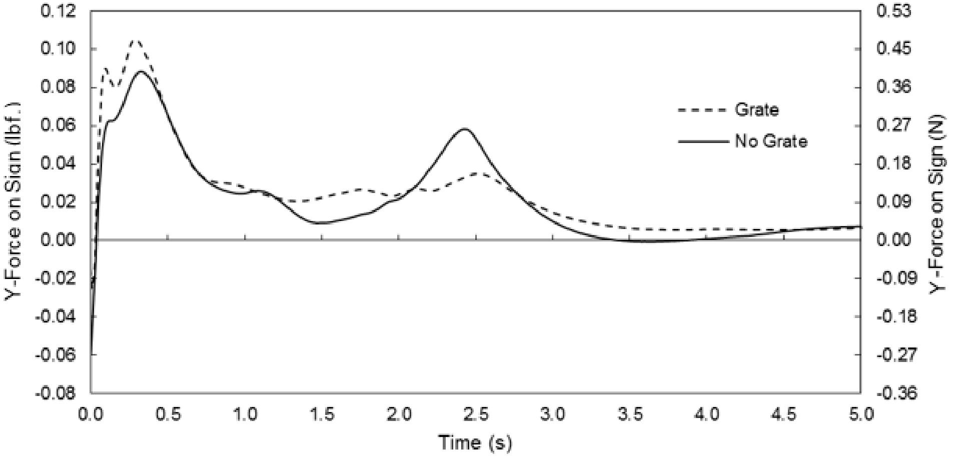

Figure 40 Y-Force on Large Sign at V=30 mph (13.4 m/s)

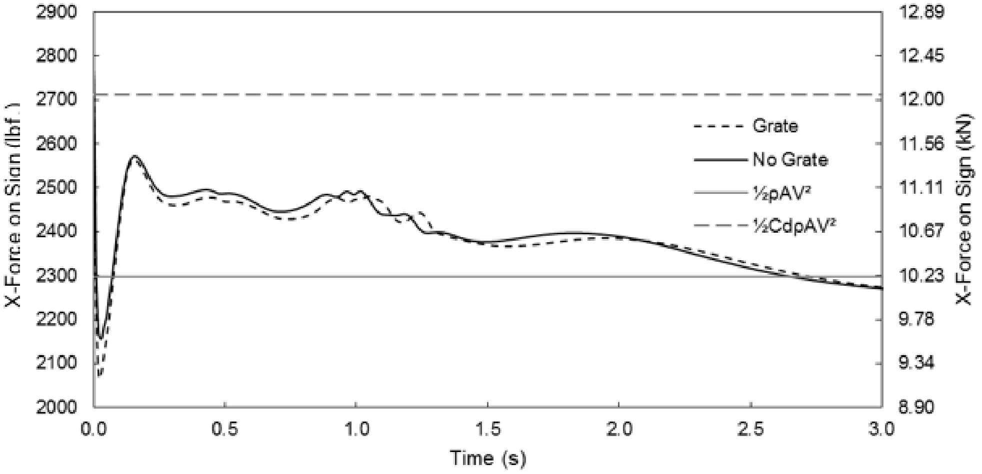

Figure 41 X-Force on Large Sign at V=61.2 mph (27.4 m/s)

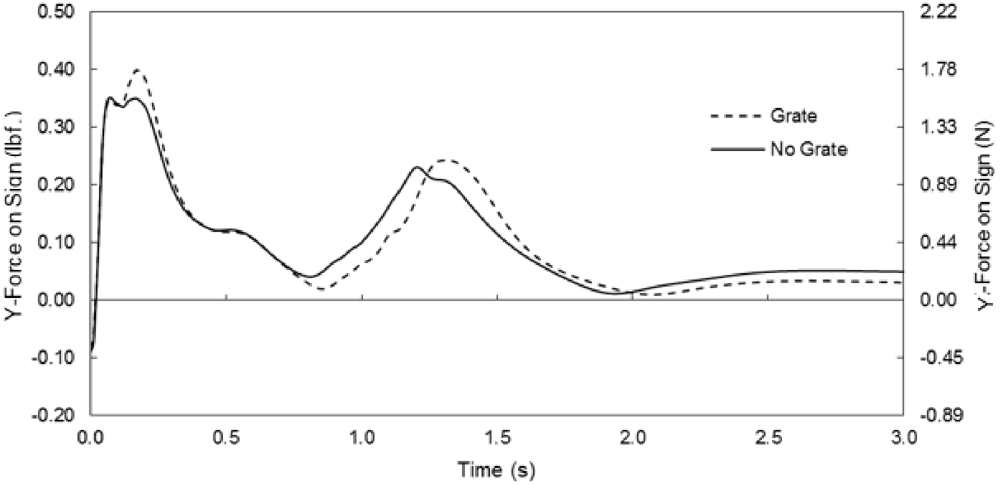

Figure 42 Y-Force on Large Sign at V=61.2 mph (27.4 m/s)

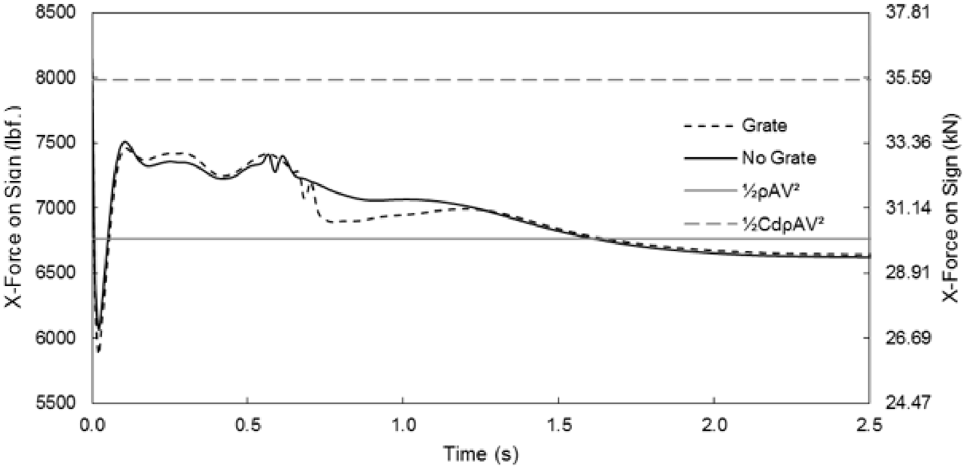

Figure 43 X-Force on Large Sign at V=105mph (46.9 m/s)

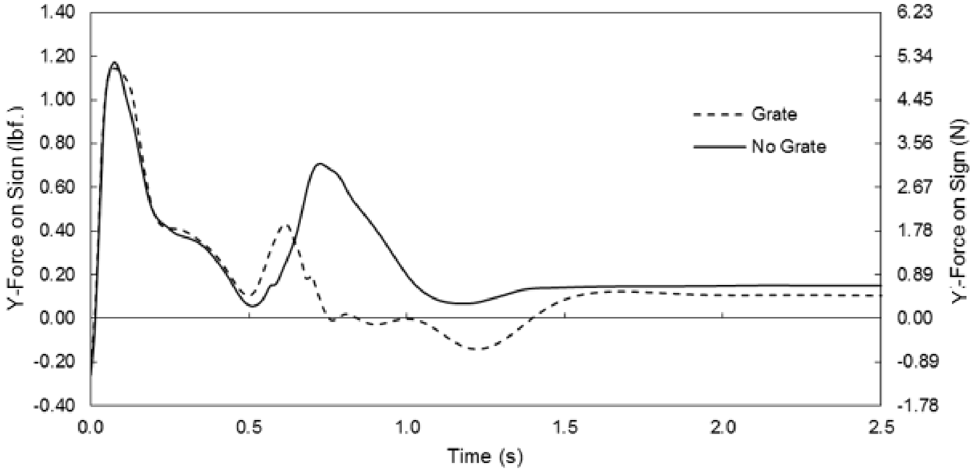

Figure 44 Y-Force on Large Sign at V=105mph (46.9 m/s)

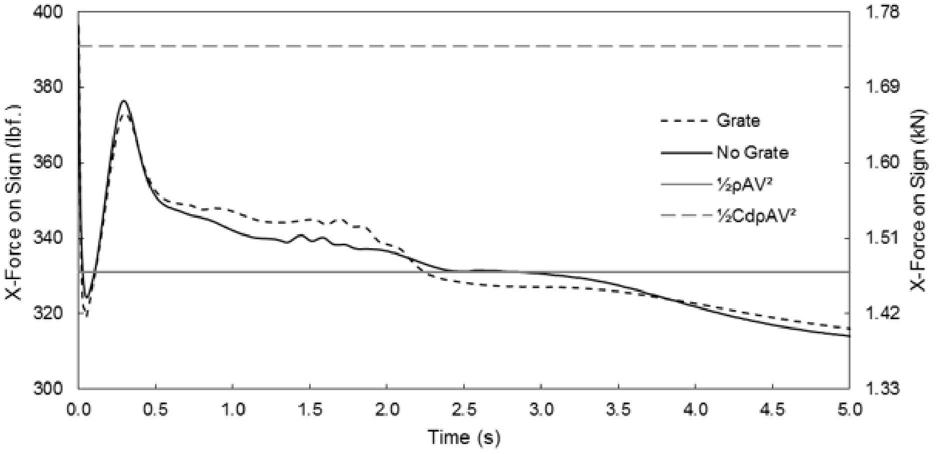

Figure 45 X-Force on Medium Sign at V=30 mph (13.4 m/s)

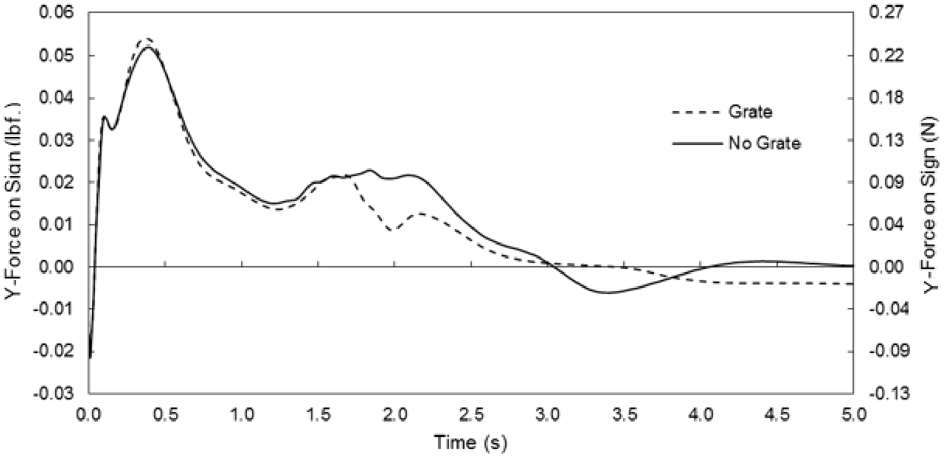

Figure 46 Y-Force on Medium Sign at V=30 mph (13.4 m/s)

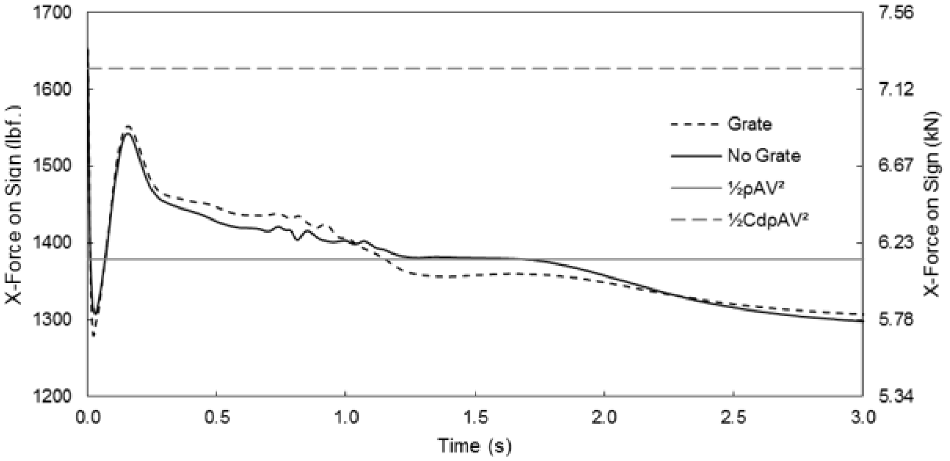

Figure 47 X-Force on Medium Sign at V=61.2 mph (27.4 m/s)

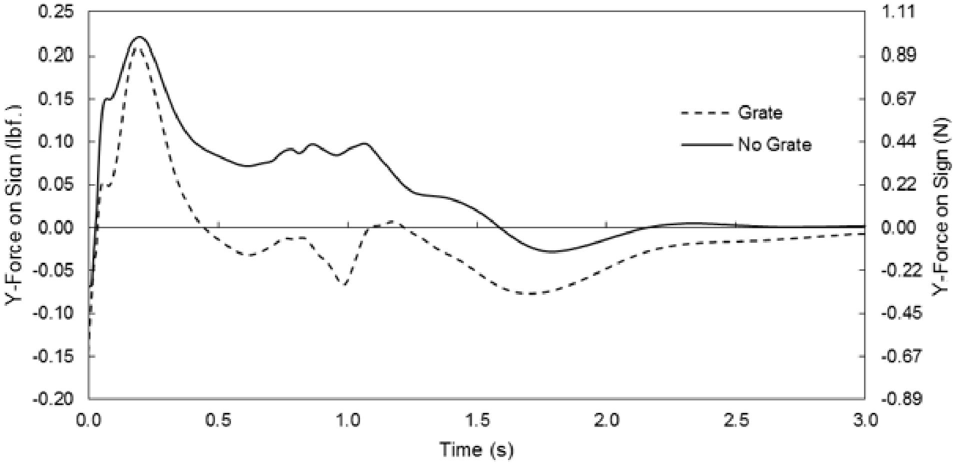

Figure 48 – Y-Force on Medium Sign at V=61.2 mph (27.4 m/s)

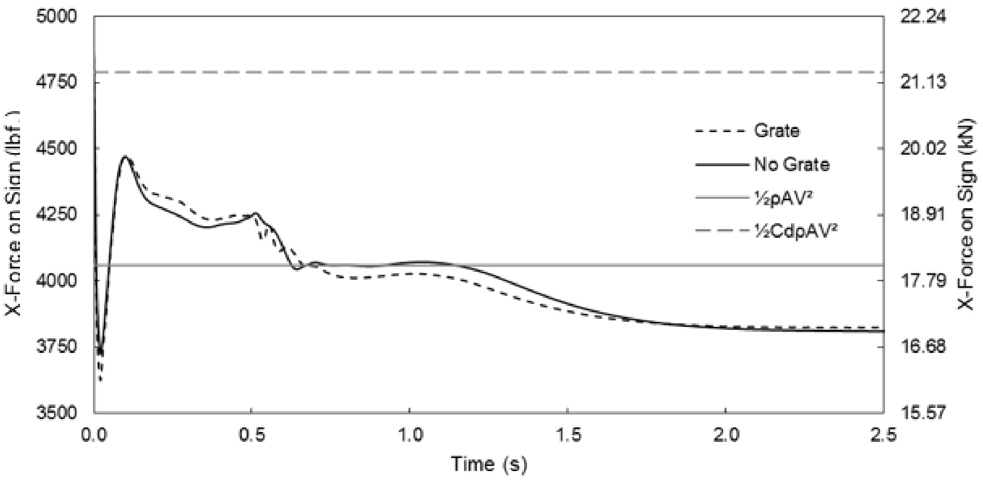

Figure 49 X-Force on Medium Sign at V=105mph (46.9 m/s)

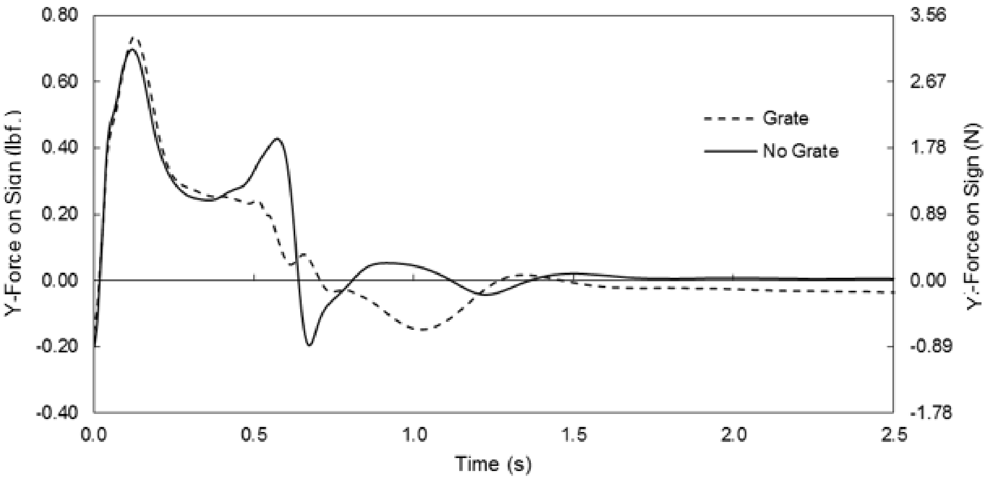

Figure 50 Y-Force on Medium Sign at V=105mph (46.9 m/s)

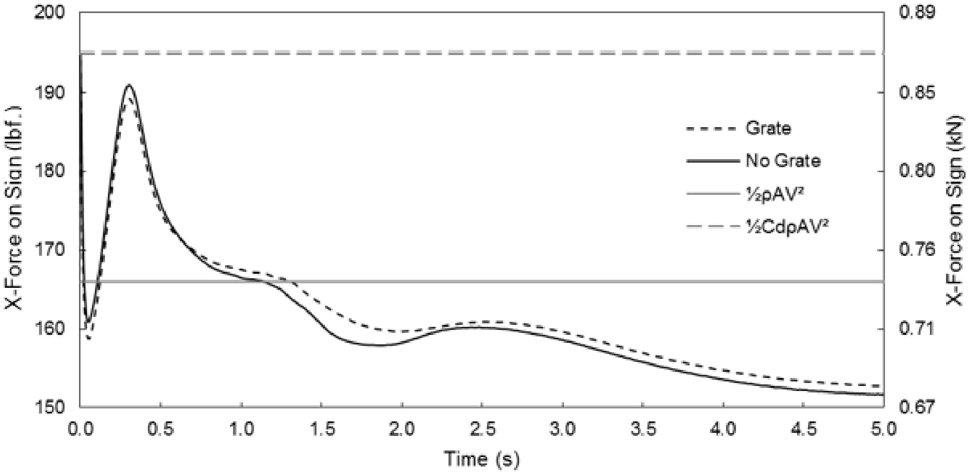

Figure 51 X-Force on Small Sign at V=30 mph (13.4 m/s)

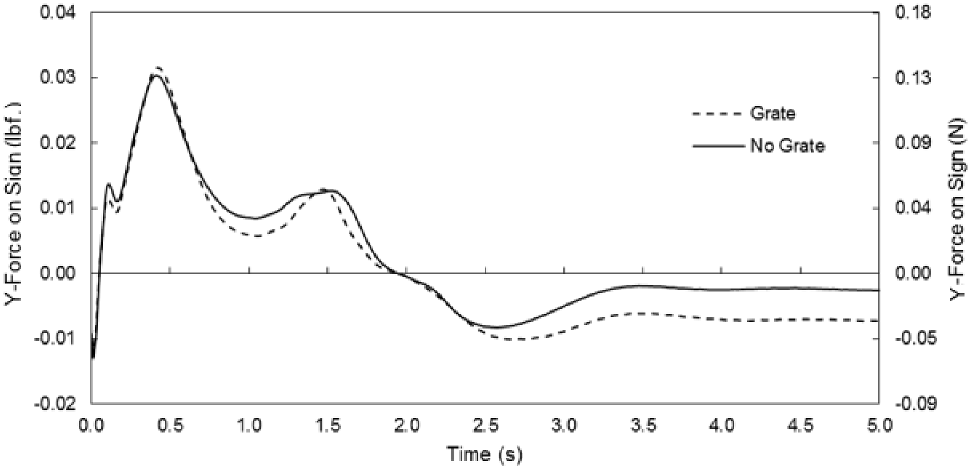

Figure 52 Y-Force on Small Sign at V=30 mph (13.4 m/s)

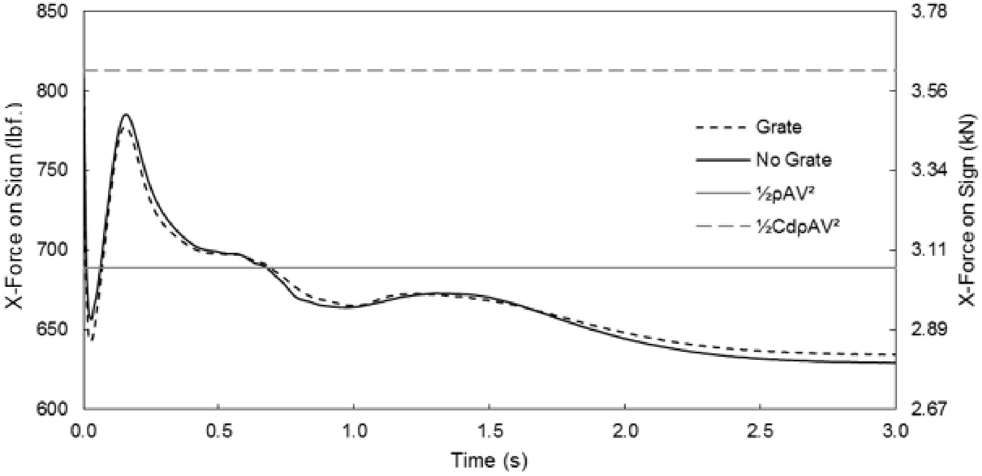

Figure 53 X-Force on Small Sign at V=61.2 mph (27.4 m/s)

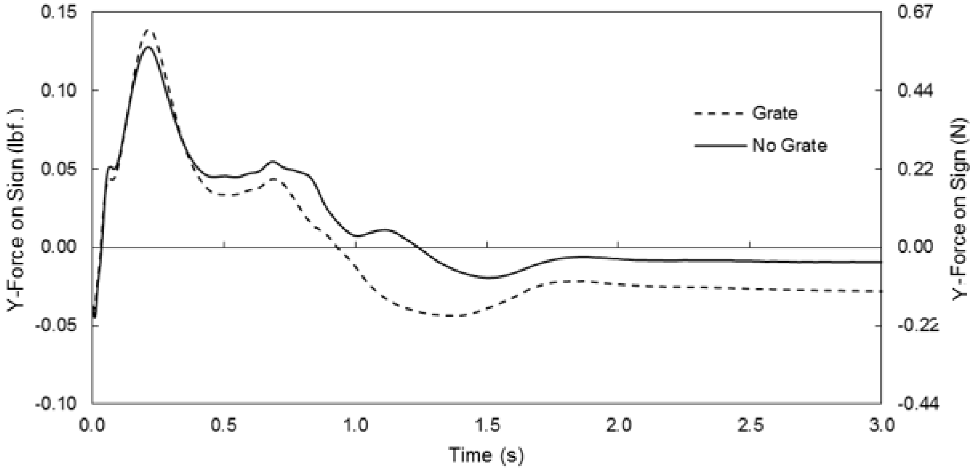

Figure 54 Y-Force on Small Sign at V=61.2 mph (27.4 m/s)

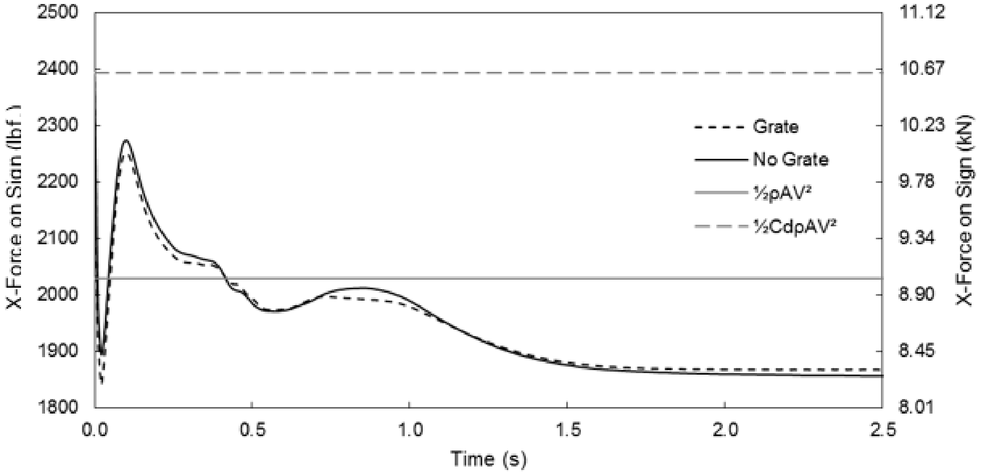

Figure 55 X-Force on Small Sign at V=105mph (46.9 m/s)

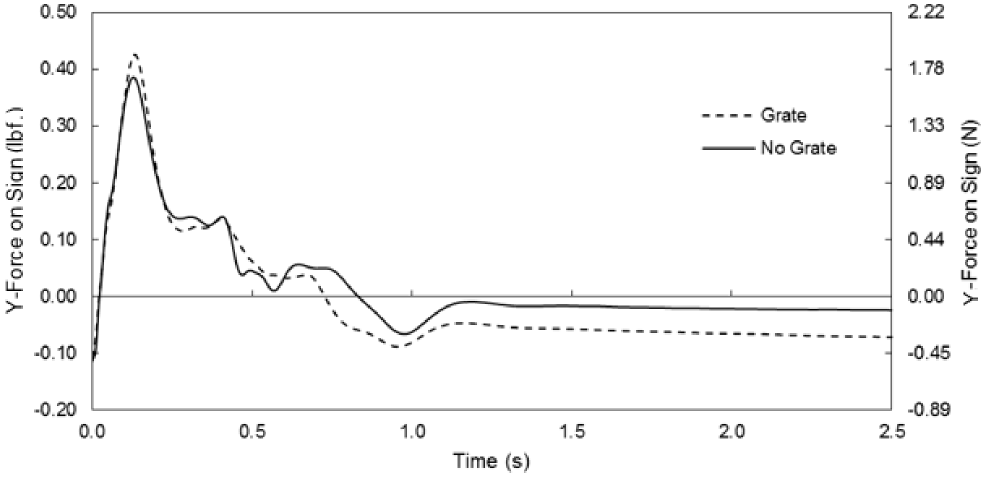

Figure 56   Y-Force on Small Sign at V=105mph (46.9 m/s)

All the time history data exhibited similar shapes across the suite of models, and were similar for both directions of loading. An initial spike in the load was recorded, where the peak corresponded with the time it took for the gust of wind to travel from the fluid domain inlet to the sign face. This spike was very pronounced in Figure 57 and Figure 58, which normalizes the force on the sign for both pressure and time. Figure 57 and Figure 58 also show the variance in eddies and vortices behind the sign that affected the wind loading on the sign over time. Some models experienced a second, less intense and smoother peak in the load, followed by another decline. This second peak was more prevalent and more pronounced in the Y-force data. The load continued to decrease at a decreasing rate until it eventually reached a constant value for most models. For the Y-force, this constant value was close to zero. The time history data followed typical behavior for a boundary layer forming on a bluff body subjected to a constant wind load, hence the gradual decrease in load over time.

Differences in the time history data between the grate and no-grate conditions were minor for almost all models, especially for the X-force data. There were greater differences between the two conditions for the Y-force, which contributes to wind induced vibration. The greatest observable differences were in the following three models: 1) Medium Sign at V=61.2 mph (27.4 m/s) model (Figure 48), 2) Medium Sign at V=105 mph (46.9 m/s) model (Figure 50), and 3) Large Sign at V=105 mph (46.9 m/s) model (Figure 56).

All of the figures showing the X-forces include the theoretical value of force (F) and the theoretical value of force with a shape factor (F_z), as obtained by Equation 10 and Equation 11, respectively. The values for force were derived from pressures applied to a surface multiplied by the surface's area (A). Equation 10 is expanded from Equation 3. Note, density is denoted by ρ, wind speed is denoted by V, and the shape factor is denoted by C_d.

$$\boldsymbol{F = ½\rho A V^2} \qquad \textbf{Equation 10}$$

$$\boldsymbol{F_z = ½C_d \rho A V^2} \qquad \textbf{Equation 11}$$

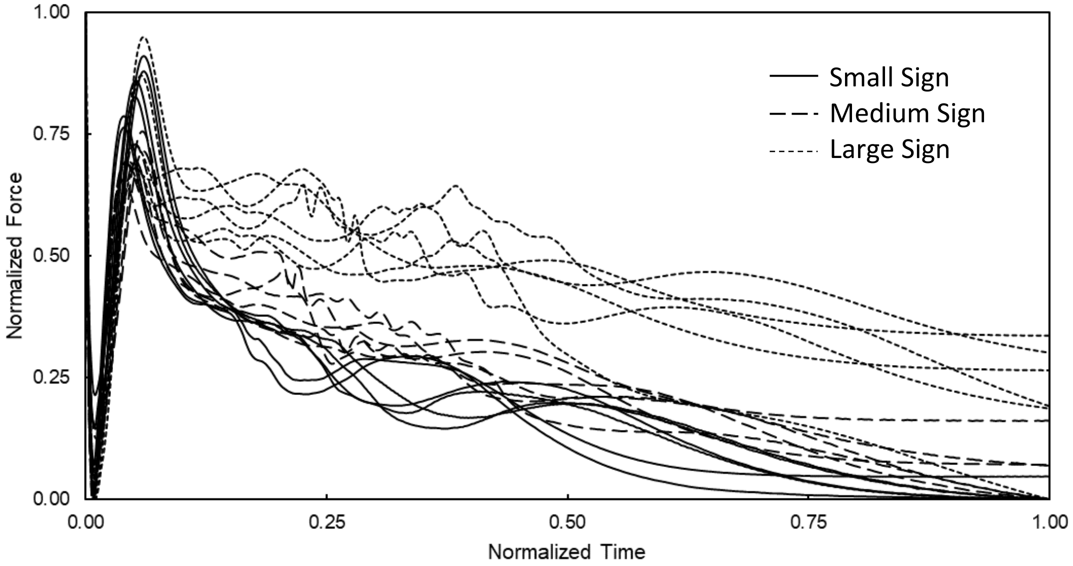

Figure 57 Normalized X-Force Time History Data

All the X-force data was bounded by *F* and F_z for the initial gust. The data trended to F before ultimately dropping under the theoretical value as the model established a laminar solution. The constant, final values were about 95% of the respective theoretical value.

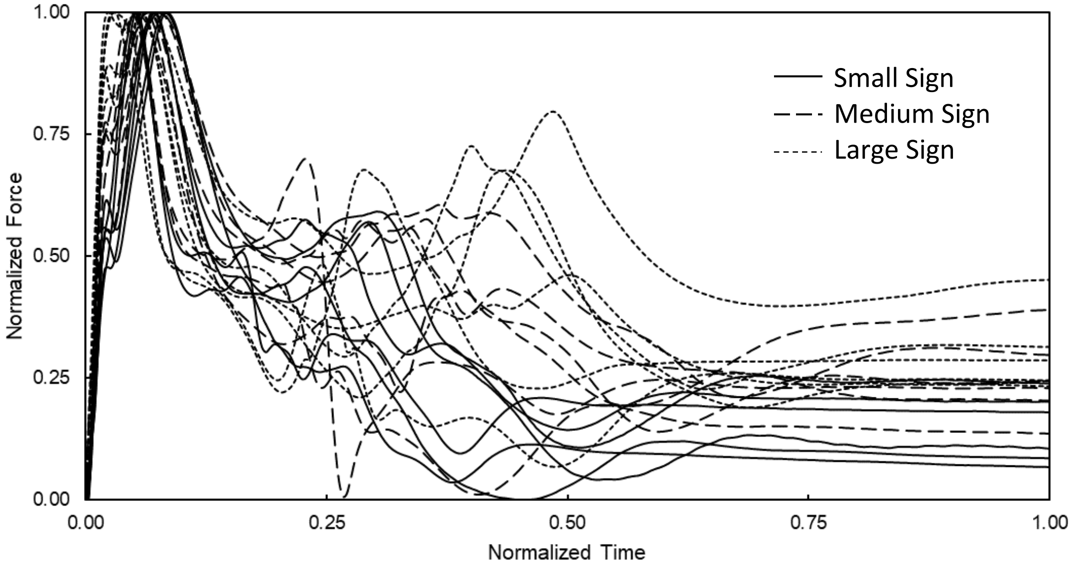

Figure 58 Normalized Y-Force Time History Data

Vortices and eddies were identified behind the sign shape. To study their interactions and how they might affect structural behavior, time histories of the Y-component of velocity were extracted at discrete points behind each CFD model. Where the Y-component of velocity consistently changed magnitude in a harmonic manner, it could be inferred that there is heavy eddy interaction which causes vortex shedding. The Y-component of velocity was extracted at the centerlines of the sign's height and length, behind the sign shape starting at a distance of 0.5·(Sign Height) and increasing in increments of 0.25·(Sign Height), up to a distance of 3.0·(Sign Height) for each CFD model. The time histories are shown in the Appendix, and all of the CFD models exhibited insignificant eddy interaction.

The velocity profile under the sign face, in the wake of the walkway, was extracted as well. The profile was extracted as wind velocity data points across a 6-ft line beneath the sign face. The profile was captured at increments of 0.10s up to 0.50s, then 0.75s and 1.00s, and then continued every 0.50s until the time history ended. The profile was also captured when the wind gust hit the sign face (this value changed for each wind speed), and these profiles have been presented in the Appendix. These profiles show an influence of the walkway attachment, which slows the air directly in its wake. The air moving around the walkway traveled slightly faster than the air traveled when no walkway was present, resulting in a similar amount of air flow moving beneath the sign.

3.3 Finite Element Modeling – Dynamic Loading

The loads discussed in Section 3.2 were applied to the influential surfaces of the finite element models. Time history data describing displacements and stresses were extracted from these models. The displacements were extracted from the top chord in the mast truss at the end of the cantilever, and stresses were extracted from both box-connections and at the pole base.

The displacements were recorded in two cardinal directions, Z and Y. Z-displacements, denoted as ΔU_Z, are the displacements associated with the torsional mode response, which was activated by the natural wind gusts. The mode shape is shown in Figure 14. Y-displacements, denoted as ΔU_Y, are displacements associated with the chopping mode response, which is activated by aeroelastic phenomena. The mode shape is shown in Figure 16. Z-displacements were found to be much larger than Y-displacements.

Stresses in the box connection between the pole and mast arm were extracted for bending about the Y-axis and about the Z-axis. Stresses caused by bending about the Y-axis, denoted as S33, were associated with the torsional mode response. Stresses caused by bending about the Z-axis, denoted as S11, were associated with the chopping mode response. The torsional stresses in the pole, denoted as S21, were also extracted. The stresses considered are shown in Figure 59.

All stress and displacement data were recorded as time histories. To simplify the data to a single value for each time history response, the range of displacements and the absolute maximum stress values were determined. These values were compared between the cases with and without the walkway attached, using a percent difference, with the case where the walkway was attached as the baseline. The percent change data for all critical loading demand cases are shown in Table 14, Table 15, and Table 16, organized by wind speed.

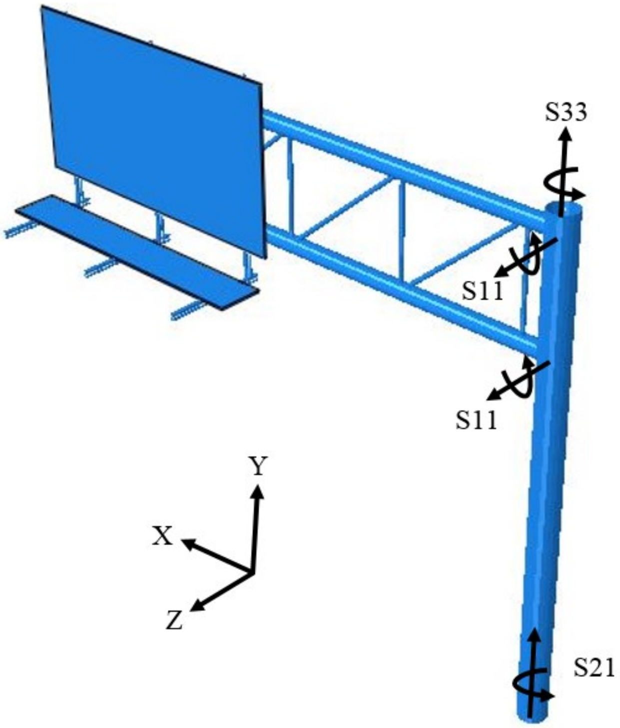

Figure 59 Pertinent locations where stresses were computed

Table 14 Percent Change in Loading Demands for V=30mph (13.4 m/s)

Model	Displacements		Top Chord		Bottom Chord		Pole
	ΔU_Z	ΔU_Y	S33	S11	S33	S11	S21
S20x12-L20-P25	-4%	-260%	-1%	-183%	-2%	-175%	-6%
S20x12-L20-P27	-4%	-278%	0%	-204%	-3%	-196%	-5%
S20x12-L20-P29	-4%	-253%	1%	-195%	-3%	-193%	-1%
S20x12-L16-P25	-3%	-223%	-2%	-210%	-3%	-209%	-4%
S20x12-L16-P27	-3%	-233%	-1%	-202%	-4%	-198%	-1%
S20x12-L16-P29	-3%	-239%	0%	-210%	-4%	-195%	-1%
S20x12-L12-P25	-6%	-237%	-2%	-174%	-5%	-192%	-7%
S20x12-L12-P27	-4%	-194%	-2%	-150%	-4%	-154%	-4%
S20x12-L12-P29	-5%	-191%	-1%	-145%	-4%	-171%	-6%
S16x9-L20-P25	3%	-12%	0%	-58%	0%	-58%	2%
S16x9-L20-P27	2%	-16%	0%	-55%	-1%	-56%	4%
S16x9-L20-P29	1%	-6%	1%	-31%	-1%	-33%	3%
S16x9-L16-P25	1%	-30%	0%	-62%	-1%	-64%	2%
S16x9-L16-P27	1%	-17%	0%	-43%	-1%	-49%	3%
S16x9-L16-P29	1%	-12%	-1%	-26%	-1%	-31%	2%
S16x9-L12-P25	0%	-27%	0%	-49%	-1%	-46%	1%
S16x9-L12-P27	0%	-24%	0%	-36%	0%	-38%	2%
S16x9-L12-P29	1%	-42%	-1%	-32%	0%	-46%	-1%
S12x6-L20-P25	2%	-37%	0%	-39%	1%	-43%	5%
S12x6-L20-P27	2%	-30%	0%	-24%	1%	-30%	4%
S12x6-L20-P29	2%	-36%	0%	-28%	1%	-36%	1%
S12x6-L16-P25	1%	-22%	1%	-27%	-1%	-31%	4%
S12x6-L16-P27	1%	-29%	1%	-23%	-1%	-25%	2%
S12x6-L16-P29	1%	-41%	1%	-19%	1%	-29%	1%

S12x6-L12-P25	1%	-37%	2%	-24%	-1%	-28%	0%
S12x6-L12-P27	2%	-26%	2%	-37%	-2%	-38%	2%
S12x6-L12-P29	0%	-27%	1%	-8%	1%	-15%	2%

Table 15 Percent Change in Loading Demands for V=61.2 mph (27.4 m/s)

Model	**Displacements**		**Top Chord**		**Bottom Chord**		**Pole**
	ΔU_Z	**ΔU_Y**	**S33**	**S11**	**S33**	**S11**	**S21**
S20x12-L20-P25	0%	-26%	2%	-38%	0%	-35%	-2%
S20x12-L20-P27	0%	-22%	2%	-35%	0%	-34%	0%
S20x12-L20-P29	0%	-23%	2%	-18%	-1%	-19%	2%
S20x12-L16-P25	1%	-27%	0%	-34%	0%	-29%	-3%
S20x12-L16-P27	3%	-31%	1%	-15%	-1%	-15%	3%
S20x12-L16-P29	0%	-28%	3%	-9%	-2%	-7%	2%
S20x12-L12-P25	-1%	-37%	0%	-21%	-1%	-29%	-4%
S20x12-L12-P27	0%	-29%	0%	-3%	-2%	-21%	1%
S20x12-L12-P29	-1%	-23%	0%	-6%	-1%	-17%	-2%
S16x9-L20-P25	2%	-39%	0%	-115%	-1%	-107%	2%
S16x9-L20-P27	0%	-45%	-1%	-122%	-1%	-123%	3%
S16x9-L20-P29	0%	-54%	-1%	-108%	-2%	-105%	2%
S16x9-L16-P25	0%	-56%	0%	-122%	-1%	-111%	3%
S16x9-L16-P27	0%	-35%	-1%	-115%	-1%	-108%	4%
S16x9-L16-P29	1%	-39%	-1%	-119%	-1%	-112%	1%
S16x9-L12-P25	-1%	-61%	0%	-129%	-3%	-118%	0%
S16x9-L12-P27	-2%	-72%	-1%	-115%	-1%	-118%	2%
S16x9-L12-P29	-1%	-62%	-1%	-104%	-1%	-104%	0%
S12x6-L20-P25	2%	-11%	1%	-32%	0%	-28%	5%
S12x6-L20-P27	2%	-9%	1%	-19%	1%	-37%	3%

S12x6-L20-P29	2%	-17%	0%	-14%	2%	-19%	5%
S12x6-L16-P25	2%	-23%	2%	-20%	0%	-31%	2%
S12x6-L16-P27	2%	-28%	2%	-22%	-1%	-39%	1%
S12x6-L16-P29	2%	-14%	2%	-27%	0%	-35%	-2%
S12x6-L12-P25	3%	-21%	3%	-23%	0%	-20%	1%
S12x6-L12-P27	3%	-28%	3%	-28%	-1%	-24%	1%
S12x6-L12-P29	2%	-25%	1%	-39%	-1%	-24%	2%

Table 16 Percent Change in Loading Demands for V=105mph (46.9 m/s)

Model	**Displacements**		**Top Chord**		**Bottom Chord**		**Pole**
	ΔU_Z	**ΔU_Y**	**S33**	**S11**	**S33**	**S11**	**S21**
S20x12-L20-P25	-3%	26%	0%	-27%	-1%	-22%	-4%
S20x12-L20-P27	-3%	18%	0%	-18%	-2%	-20%	-3%
S20x12-L20-P29	-3%	13%	1%	-15%	-2%	-15%	1%
S20x12-L16-P25	-3%	27%	-1%	2%	-1%	-1%	-3%
S20x12-L16-P27	-3%	28%	0%	9%	-2%	5%	2%
S20x12-L16-P29	-3%	21%	0%	7%	-2%	0%	0%
S20x12-L12-P25	-1%	25%	0%	14%	-2%	15%	-3%
S20x12-L12-P27	-1%	29%	-1%	20%	-2%	20%	2%
S20x12-L12-P29	-2%	31%	0%	22%	-2%	24%	-1%
S16x9-L20-P25	-1%	-12%	0%	-39%	-1%	-33%	2%
S16x9-L20-P27	-1%	-7%	-1%	-35%	-1%	-46%	-1%
S16x9-L20-P29	0%	-8%	-1%	-38%	-2%	-35%	2%
S16x9-L16-P25	-1%	-43%	0%	-51%	-1%	-47%	3%
S16x9-L16-P27	-1%	-44%	0%	-53%	0%	-54%	2%
S16x9-L16-P29	-2%	-25%	-1%	-48%	-1%	-32%	2%
S16x9-L12-P25	0%	15%	0%	-27%	-1%	-32%	0%

S16x9-L12-P27	-2%	-3%	0%	-31%	-1%	-36%	1%
S16x9-L12-P29	-2%	-24%	-1%	-40%	-1%	-48%	-1%
S12x6-L20-P25	2%	-1%	1%	-39%	0%	-28%	5%
S12x6-L20-P27	2%	-10%	1%	-33%	1%	-28%	3%
S12x6-L20-P29	1%	-12%	0%	-16%	2%	-23%	2%
S12x6-L16-P25	3%	7%	2%	-35%	0%	-38%	5%
S12x6-L16-P27	2%	-8%	2%	-37%	0%	-40%	6%
S12x6-L16-P29	3%	-11%	2%	-38%	-1%	-39%	-2%
S12x6-L12-P25	3%	-12%	3%	-76%	0%	-35%	3%
S12x6-L12-P27	4%	-10%	2%	-77%	1%	-30%	1%
S12x6-L12-P29	3%	-21%	2%	-62%	-1%	-32%	7%

Trends from both characteristic modes were identified from the values reported in Table 14, Table 15, and Table 16:

Removal of the walkway had a minimal effect on responses in the torsional mode, including displacements and stresses in both the box-connection and the pole. The maximum increase in ΔU_Z displacement was 4%. The maximum increase in bending stress in the box-connection under this mode (S33) was 3%. The maximum torsional stress increase (S21) was 7%.

Removal of the walkway decreased, and in some cases greatly decreased, displacements and stresses affected in the chopping mode in all sign structures at all wind speeds, except the large sign structures with an applied wind speed of 105 mph (46.9 m/s). This latter behavior was caused by a second distinct peak in the applied Y-Force shown in Figure 44 at approximately 0.75 seconds. This increased the ΔU_Y displacement by a maximum of 31%, and increased the bending stress in the box-connection (S11) by a maximum of 24%, both occurring in model S20x12-L12-P29.

Values extracted for stress and displacement can found in the Appendix.

3.4 Experimental Results

Force data was recorded for a scaled model sign shape subjected to experimental wind gusts in a wind tunnel using a series of load cells. Seven different wind speeds were used, with a maximum wind speed of 40 mph (17.9 m/s) and a minimum wind speed of 10 mph (4.5 m/s). The wind speed was changed in increments of 5 mph (2.2 m/s). Data was recorded three times for each wind speed, and the average response was calculated. Since the scaled model was a relatively large shape as compared to the cross-section of the wind tunnel, the force applied by the wind was artificially smaller due to the blockage effect (Sahini 2004). Corrected values were determined by multiplying the average force at each wind speed by the blockage correction factor (Ψ), defined by Equation 12:

$$\boldsymbol{\Psi = 1 + \phi C_d \frac{A_m}{A_w}} \qquad \textbf{Equation 12}$$

Variables for the blockage correction factor have been defined in Table 17. The blockage ratio (ϕ) is defined by Equation 13, where the height of the model is denoted by (h) and the height of the cross-sectional testing area is defined by (H).

$$\boldsymbol{\phi = h/H} \qquad \textbf{Equation 13}$$

Table 17 Blockage Correction Factor (Shaini 2004)

Variable	**Notation**	**Value**		**Units (S.I)**
		w/ Walkway	**w/o Walkway**	
Model Height	h	1.969 (0.600)	1.688 (0.515)	ft (m)
Wind Tunnel Height	H	3.00 (0.914)	3.00 (0.914)	ft (m)
Blockage Ratio	ϕ	0.6563	0.5625	-
Shape Factor	C_d	1.18	1.18	-
Model Area	A_m	5.063 (0.4703)	5.063 (0.4703)	ft^2 (m^2)
Wind Tunnel Area	A_w	12.00 (1.115)	12.00 (1.115)	ft^2 (m^2)
Blockage Correction Factor	Ψ	1.33	1.28	-

Figure 60 shows the measured forces behind the sign for the different wind speeds. Upper and lower theoretical bounds (Equation 10 and Equation 11) have also been included in the plot.

The measured forces corresponded well with the predicted range. Wind speeds between 20 mph (8.9 m/s) and 40 mph (17.9 m/s) produced forces that fell between the theoretical bounds, while the 10 mph (4.5 m/s) and 15 mph (6.7 m/s) produced measured forces that fell just under the lower theoretical bound, Equation 10. Overall, the walkway was found to have a minimal effect on the forces measured under wind loading, with removal of the walkway tending to result in slightly lower forces behind the sign.

To compare to the physical measurements against the CFD-dervied data, the peak force values from each CFD model at 30 mph (13.4 m/s) and the experimental results were normalized by area to yield the pressure applied to the sign conveyed in Table 18.

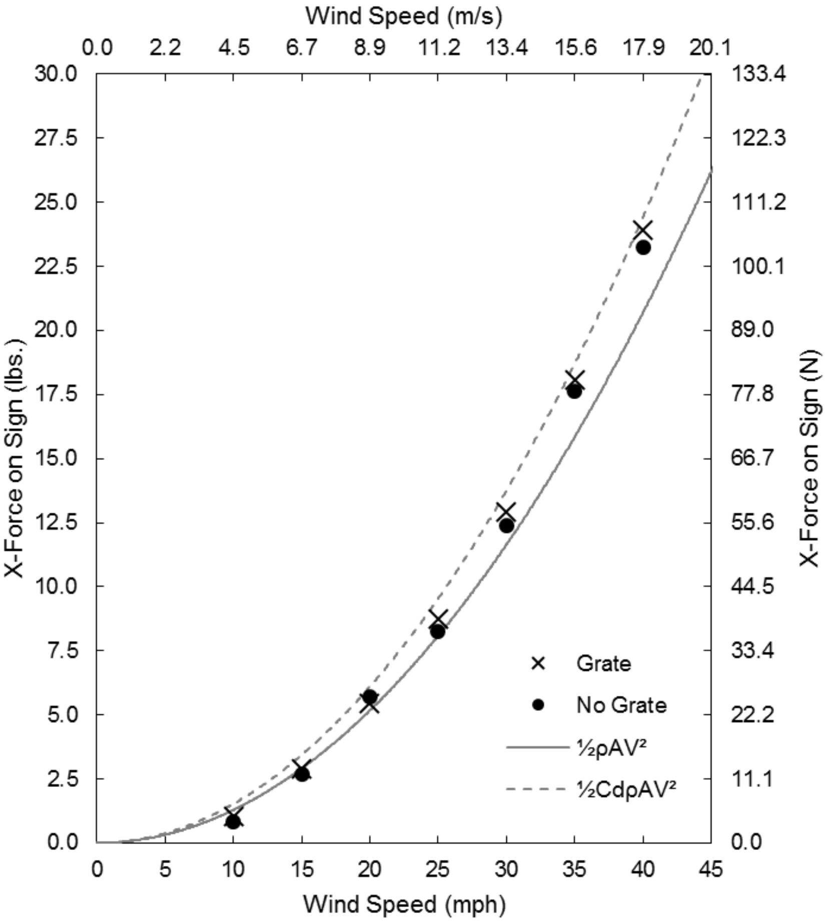

Figure 60 Experimental Loading Data

Table 18 Applied Pressure to CFD Models and Scale Model at V=30 mph (13.4 m/s)

Sign Size	w/ Walkway	w/o Walkway
	psf (Pa)	psf (Pa)
Small	2.66 (127.4)	2.63 (125.9)
Medium	2.66 (127.4)	2.70 (129.3)
Large	2.55 (122.1)	2.53 (121.1)
Experimental	2.56 (122.6)	2.45 (117.3)

Overall, the applied wind loading pressures from the CFD models and the experimental testing were similar, with the largest difference being 10%. The presence of a walkway attachment did not significant change the force response of the sign shape.

Turbulence created by wind loading on the sign shape and the walkway in the experimental testing was studied using a fog and laser technique. Laser planes at the sign face and behind the sign showed the largest change and the greatest turbulence when compared to the laser plane in front of the sign face. Figure 61 and Figure 62 show the turbulence with the walkway attachment in place, and Figure 63 and Figure 64 show the turbulence without the walkway attachment in place.

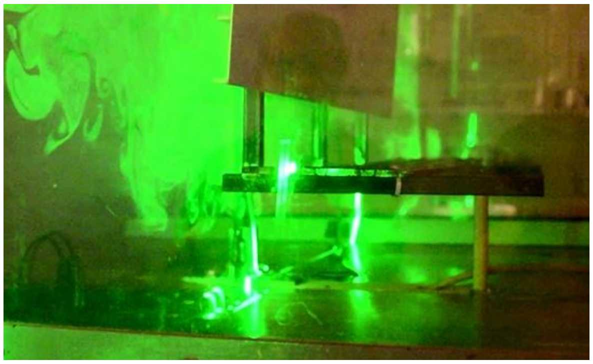

Figure 61 Laser plane behind scale model

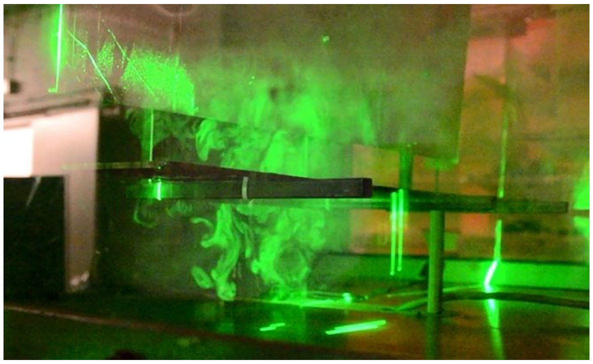

Figure 62 Laser plane at sign face

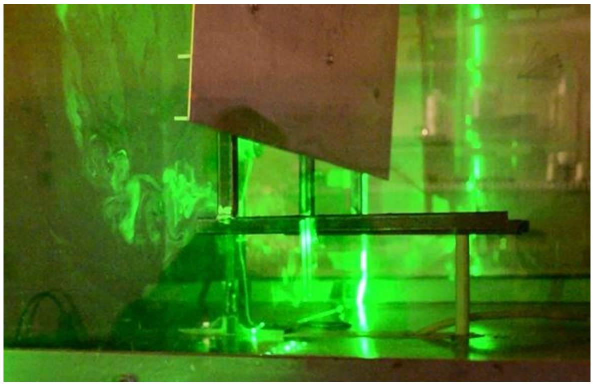

Figure 63 Laser plane behind scale model

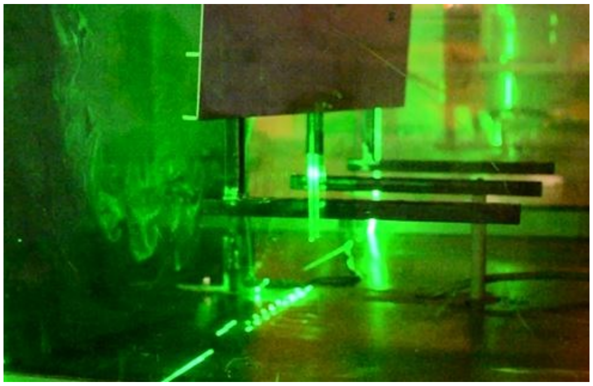

Figure 64 Laser plane at sign face

This technique indicated that the walkway itself produced turbulent flow, which can affect the downstream sign shape. The eddies and vortices in the wake of the sign developed over a greater distance below the sign shape when the walkway attachment was present.

Conclusions and Recommendations

In this chapter, conclusions are offered based on results presented in the previous chapter. These are organized by how the dynamic properties change (Section 4.1) and how the aerodynamic shape and subsequent forces on the sign shape changed (Section 4.2). Suggestions for future work are also offered in this chapter.

4.1 Conclusions Regarding Changes to Dynamic Properties with Walkway Removal

Analyzing the results of the fundamental frequencies for both characteristic mode shapes has led to multiple conclusions regarding two-chord COSS dynamic properties, and the effect that the presence of a walkway attachment has on them:

- Removal of the walkway always resulted in a higher natural frequency for COSS with an average of 5.1% increase in the torsional mode and 3.5% increase in the chopping mode.
- Variable design characteristics, such as: sign size, mast arm length, and pole height had a greater effect on both fundamental natural frequencies than did the presence of a walkway.

- The torsional mode shape always exhibited a lower natural frequency than the chopping mode shape.
- The torsional mode natural frequency exhibited more variability across models with the removal of the walkway, especially in medium sign sized COSS systems.
- The maximum differential percentage for the torsional mode natural frequency was 7.8%, for model S16x9-L12-P25, with the average resulting in 4.7% change.
- The maximum differential percentage for the chopping mode natural frequency was 5.1%, for model S20x12-L20-P25, with the average resulting in 3.5% change.
- The walkway had little to no effect on the damping ratio for the COSS studied.
- The walkway did not significantly change the dynamic properties of two-chord COSS systems.
- Comparing and contrasting the data in Table 3.1.1, sign size was found to have the greatest influence on the dynamic properties of two-chord COSS. This is because member sizes and spacing are dependent on the size of the sign the members are supporting. It is important to note that there are not three sign sizes on similar structures, but rather three sign sizes on *three different supporting structures*. After sign size, the mast truss length had the second greatest effect on the dynamic properties, followed by the pole length.

4.2 Conclusions Regarding Changes to Aerodynamic Shape and Loading Conditions

Examination of the results from the CFD and dynamically-loaded structural models has led to the following conclusions on how the walkway attachment changes the aerodynamic shape:

- The walkway did not deflect wind away from the sign, and wind loading on the sign shape was equivalent with or without the walkway attachment present.

- Wind loading in the experimental testing and CFD models produced similar pressures for a wind speed of 30 mph (13.4 m/s) (the common wind speed between the two modalities), with a 10% maximum difference.
- The Y-component of the velocity did not appear to change in a manner that would be consistent with vortex shedding and/or galloping based off the data in Appendix A1.
- Removal of the walkway did not significantly change or increase the stresses in the box-connection or the pole, with an average change of -0.3% in S33 stresses, -55% in S11 stresses, and 0.8% in S21 stresses.
- Removal of the walkway did not significantly change the aerodynamic shape.
- Expanding on these, it appears that the walkway does not significantly act as a diffuser to disrupt eddy interaction simply due to its placement on the sign structure. The walkway causes its own turbulence which can negatively affect the succeeding sign shape. Ultimately, the walkway attachment was found to have a very minimal effect on the load the sign structure experiences from natural wind gusts, the aeroelastic phenomena produced in the wake of the sign structure, and displacements and stresses developed by the natural wind gusts.

4.3 Future Work

The following suggestions are offered for future work, to improve the state-of-the-art around analyzing and designing COSS:

- Development of fluid-structure interaction models with deformable fluid domains for more accurate analytical models.
- Deployment of instruments such as accelerators and anemometers in the field on constructed COSS, to develop an improved understanding of how different wind loading scenarios affect sign structures.
- Additional wind tunnel testing with differently sized sign shapes to develop an improved understanding of how walkway removal affects sign shapes of all sizes and to further validate CFD modeling techniques.

- Extension of these methods to other COSS construction types.

References

American Association of State Highway and Transportation Officials (AASHTO) (2001). *Standard Specifications for Structural Supports for Highway Signs, Luminaires, and Traffic Signals*, 4th Edition. With Interims, Washington, D.C.

American Association of State Highway and Transportation Officials (AASHTO) (2004). *LRFD Bridge Design Specifications*, 3rd Edition. With Interims, Washington, D.C.

American Association of State Highway and Transportation Officials (AASHTO) (2015a). *LRFD Specifications for Structural Supports for Highway Signs, Luminaires, and Traffic Signals*, 1st Edition. With Interims, Washington, D.C.

American Association of State Highway and Transportation Officials (AASHTO) (2015b). *AASHTO LRFD Bridge Design Specifications*, 7th Edition. With Interims, Washington, D.C.

American Society for Metals (ASM) International Handbook Committee (1990). *Metals Handbook*: Vol. 2, Properties and Selection–Nonferrous Alloys and Pure Metals: ASM International Handbook. New York, NY.

American Society for Testing and Materials (ASTM) "ASTM Standard A709/A709M-18." (2018). *Standard Specification for Structural Steel for Bridge*: ASTM International. West Conshohocken, PA.

American Society of Civil Engineers (ASCE) (2010). *ASCE 7-10*: Minimum Design Loads for Buildings and Other Structures. With Interims, Washington, D.C.

Barlow, J. B., Rae Jr., W. H., and Pope, A. (1999). "Low-Speed Wind Tunnel Testing." John Wiley & Sons, Inc., New York, NY.

Beneberu, E., Goode, J., and Yazdani, N. (2014). "Computational Fluid Dynamics Application for Design of Highway Sign Support Structures." *International Journal of Civil and Structural Engineering*, 5(2), 101-111.

Chao, S., Jiao, C., and Liu, S. (2016). "Research on Feasibility of Computational Fluid Dynamics (CFD) Method for Traffic Signs Board Calculation." Paper presented at the IOP Conference Series: Earth and Environmental Science.

Cheung, J. O., and Liu, C.H. (2011). "CFD Simulations of Natural Ventilation Behaviour in High-Rise Buildings in Regular and Staggered Arrangements at Various Spacings." *Energy and Buildings*, 43(5), 1149-1158.

Constantinescu, G., Bhatti, A., and Tokyay, T. (2008). "A Numerical Study of Wind Loads on Large Highway Sign Structures." Paper presented at the 18th Structures Congress 2008: Analysis and Computation Specialty Conference.

Craig, R. R., and Kurdila, A. J. (2006). *Fundamentals of Structural Dynamics*: John Wiley & Sons. Hoboken, NJ.

Creamer, B.M., Frank, K.H. and Klinger, R.E. (1979). "Fatigue Loading of Cantilever Sign Structures from Truck Wind Gusts." Research Report 209-1F, Project 3-5-77-209, Center for Highway Research, The University of Texas, Austin, TX.

Dassault Systèmes Simulia (DSS) (2014). "Abaqus FEA Version 6.14." Dassault Systemes Simulia Corp.

DSS (2015). “Abaqus/CAE User's Guide.” Dassault Systemes Simulia Corp.

Dexter, R.J. and Johns, K.W. (2005). “The Development of Fatigue Design Load Ranges for Cantilevered Sign and Signal Support Structures.” *Journal of Wind Engineering*, 77, 315-325.

Dexter, R.J. and Ricker, M.J. (2002). “Fatigue Resistant Design of Cantilevered Signal, Sign and Light Supports.” NCHRP Report 469, Transportation Research Board, Washington, D.C.

Dowling, N. E. (1999). *Mechanical Behavior of Materials*: Engineering Methods for Deformation, Fracture, and Fatigue, 2nd Edition: Prentice-Hall, Inc., Upper Saddle River, NJ.

Fouad, F.H., Davidson, J.S., and Delatte, N. (2003). “Structural Supports for Highway Signs, Luminaires, and Traffic Signals.” NCHRP Report 494, Transportation Research Board, Washington, D.C.

Gallow, M. S. (2014). “Mitigating Fatigue of Cantilevered Overhead Sign Structures Due to Natural and Truck-Induced Wind Gusts.” MS thesis, The University of Alabama at Birmingham, Birmingham, AL.

Gallow, M. S., Fouad, F. H., and Hosch, I. E. (2015). “Mitigating Fatigue in Cantilevered Overhead Sign Structures.” *Transportation Research Record*: Journal of the Transportation Research Board, No. 2522, 18-26.

Gemba, K. (2007). “Measurement of Boundary Layer on a Flat Plate.” California State University, Long Beach, experimental report.

Gilani, A., and Whittaker, A. (2000). Fatigue-Life Evaluation of Steel Post Structures. II: Experimentation. *Journal of Structural Engineering*, 126(3), 331-340.

Ginal, S. (2003). “Fatigue Performance of Full-Span Sign Support Structures Considering Truck-Induced Gust and Natural Wind Pressures.” MSCE thesis, Marquette University, Milwaukee, WI.

Hall, N. (Ed.). (2015). “Air Properties Definitions.” Glenn Research Center, Nation Aeronautics and Space Administration (NASA). Cleveland, OH. Retrieved from: https://www.grc.nasa.gov/www/k-12/airplane/airprop.html.

Holmes, J. D. (2007). “Wind Loading of Structures.” Taylor & Francis, New York, NY.

Hong, H. P., Zu, G. G., and King, J. P. C. (2016). “Estimating Fatigue Design Load for Overhead Steel Sign Support Structures Under Truck-Induced Wind Pressure.” *Canadian Journal of Civil Engineering*, 43(3), 279-286.

Hosch, I. E. (2009). “Design of Highway Overhead Cantilever-Type Sign Support Structures for Fatigue Loads.” Ph.D Disertation, The University of Alabama at Birmingham, Birmingham, AL.

Johns, K. W., and Dexter, R. J. (1998a). “The Development of Fatigue Design Load Ranges for Cantilevered Sign and Signal Support Structures.” *Journal of Wind Engineering and Industrial Aerodynamics*, 77, 315-326.

Kacin, J. A. (2009). “Fatigue Life Estimation of a Highway Sign Structure.” MS thesis, University of Pittsburg, Pittsburgh, PA.

Kaczinski, M.R., Dexter, R.J. and Van Dien, J.P. (1998). “Fatigue Design of Cantilevered Signal, Sign, and Light Supports.” NCHRP Report 412, Transportation Research Board, Washington, D.C.

Kadoya, K., Matsunaga, N., and Nagashima, A. (1985). “Viscosity and Thermal Conductivity of Dry Air in the Gaseous Phase.” *Journal of Physical and Chemical Reference Data*, 14(4), 947-970.

Kuhl, E., Hulshoff, S., and De Borst, R. (2003). “An Arbitrary Lagrangian Eulerian Finite-Element Approach for Fluid–Structure Interaction Phenomena.” *International Journal for Numerical Methods in Engineering*, 57(1), 117-142.

Kwon, H.b., Park, Y.W., Lee, D.h., and Kim, M.S. (2001). “Wind tunnel experiments on Korean high-speed trains using various ground simulation techniques.” *Journal of Wind Engineering and Industrial Aerodynamics*, 89(13), 1179-1195.

Louisiana Department of Transportation and Development (La DOTD). (2016). The DOTD Sign Shop, YouTube. Retrieved from: https://www.youtube.com/watch?v=8i0qaekBs3Q.

Li, X., Whalen, T., and Bowman, M. (2006). “Fatigue Strength and Evaluation of Sign Structures.” West Lafayette, IN.

Li, X., Whalen, T., and Bowman, M. (2005). “Fatigue Strength and Evaluation of Double-Mast Arm Cantilevered Sign Structures.” *Transportation Research Record*: Journal of the Transportation Research Board, No. 1928, 64-72.

Mangat, J. (2012). Global News, YouTube. Retrieved from: https://www.youtube.com/watch?time_continue=3&v=rbtoeiP6Jwo.

McDonald, J. R., Mehta, K., and Oler, W. (1995). “Wind Load Effects on Signs, Luminaires, and Traffic Signal Structures.” Texas Department of Transportation. Austin, TX.

Montazeri, H., and Blocken, B. (2013). “CFD Simulation of Wind-Induced Pressure Coefficients on Buildings with and without Balconies: Validation and Sensitivity Analysis.” *Building and Environment*, 60, 137-149.

Puckett, J., Garlich, M., and Nowak, A. (2014). “Development and Calibration of AASHTO LRFD Specifications for Structural Supports for Highway Signs, Luminaires, and Traffic Signals.” NCHRP Report 796, Transportation Research Board, Washington, D.C.

Rice, J. A., LaFave, M. L., and Mehuys, C. H. (2008) “End Connection Effects on Vortex Shedding Susceptibility of Welded Aluminum Truss Tubular Web Members.” Journal of Performance of Constructed Facilities, 22(5).

Rizzo, P., and Zhu, X. (2010). “Sensing Technology for Damage Assessment of Sign Supports and Cantilever Poles.” Pennsylvania Department of Transportation. Pittsburgh, PA.

Sahini, D. (2004). “Wind Tunnel Blockage Corrections: A Computational Study.” MS thesis, Texas Tech University, Lubbock, TX.

Santiago, J. L., et al. (2007). “CFD Simulation of Airflow over a Regular Array of Cubes. Part I: Three-Dimensional Simulation of the Flow and Validation with Wind-Tunnel Measurements." *Boundary-Layer Meteorology*, 122(3), 609-634.

Sváček, P. (2017). “Numerical Simulation of Fluid-Structure Interactions with Stabilized Finite Element Method.” *Advances in Engineering Software*, 113, 96-107.

Tian, F. B., Dai, H., and Luo, H. (2014). "Fluid–Structure Interaction Involving Large Deformations: 3D Simulations and Applications to Biological Systems." *Journal of Computational Physics*, 258, 451-469.

Voss, D. (2016) "This Month in Physics History: November 7, 1940: Collapse of the Tacoma Narrows Bridge." American Physical Society, 25(10). Ridge, NY.

Yarusevych, S., Sullivan, P., and Kawall J. G. (2009). "On vortex shedding from airfoil in low-Reynolds-number flows." Journal of Fluid Mechanics, 632, 245-271.

Zuo, D. and Letchford, C. W. (2010). "Wind-Induced Vibration of a Traffic-Signal-Support Structure with Cantilevered Tapered Circular Mast Arm." *Engineering Structures*, 32(10), 3171-3179.

Zuo, D., Smith, D., and Mehta, K. (2012). "Benchmark Wind Tunnel Study of Wind Loading on Rectangular Sign Structures." Wind Science and Engineering Research Center, Texas Tech University. Lubbock, TX.

APPENDIX A1

A1.1 – Y-Component of Velocity Behind Large Sign at V=30 mph (13.4 m/s)

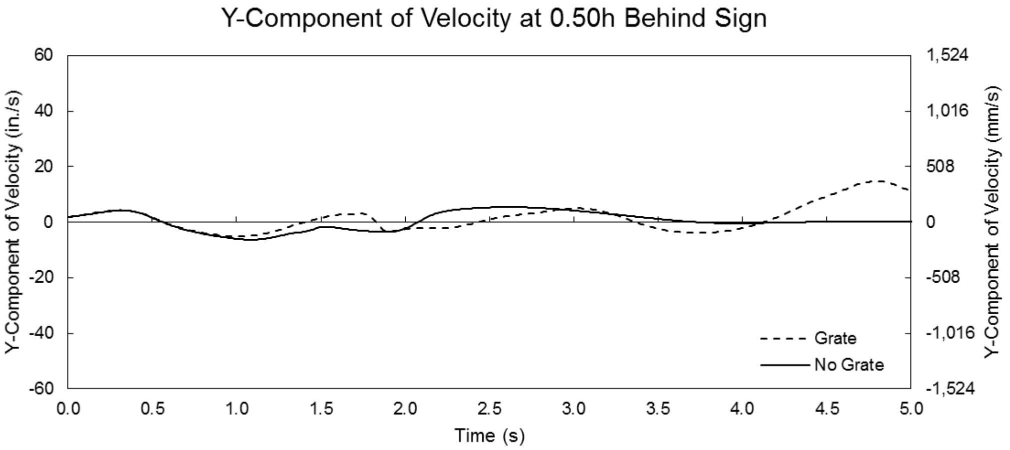

Figure 65 Y-component of velocity for the large sign at V=30 mph (13.4 m/s) at a distance = 0.5h behind the sign

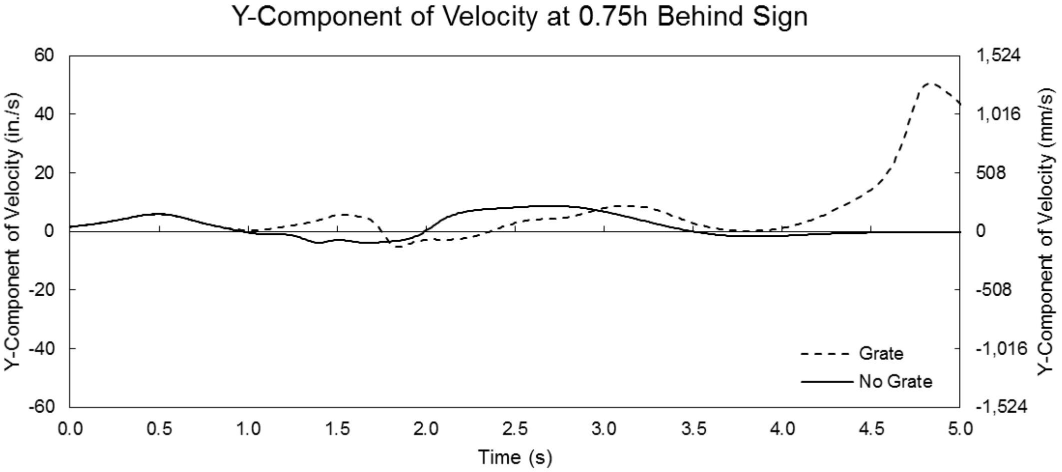

Figure 66 Y-component of velocity for the large sign at V=30 mph (13.4 m/s) at a distance = 0.75h behind the sign

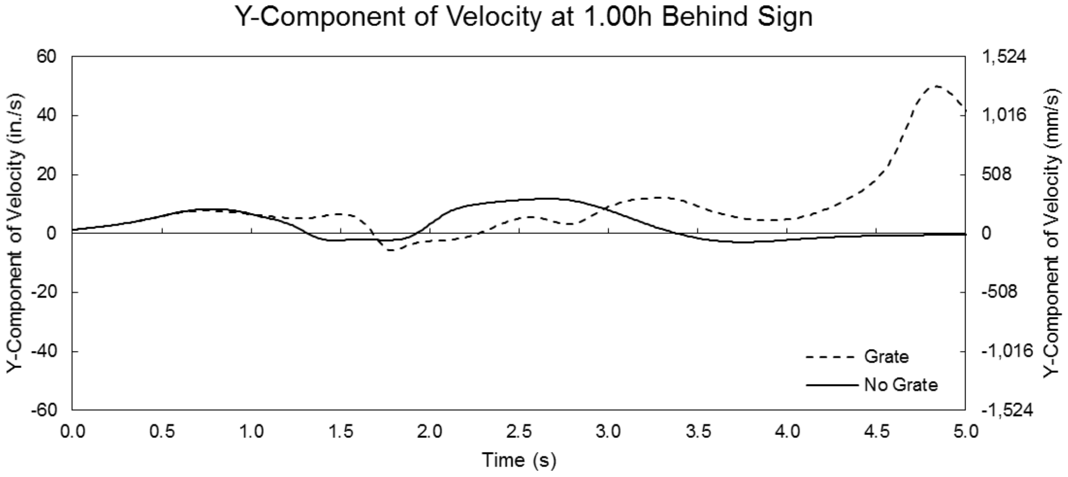

Figure 67 Y-component of velocity for the large sign at V=30 mph (13.4 m/s) at a distance = 1.0h behind the sign

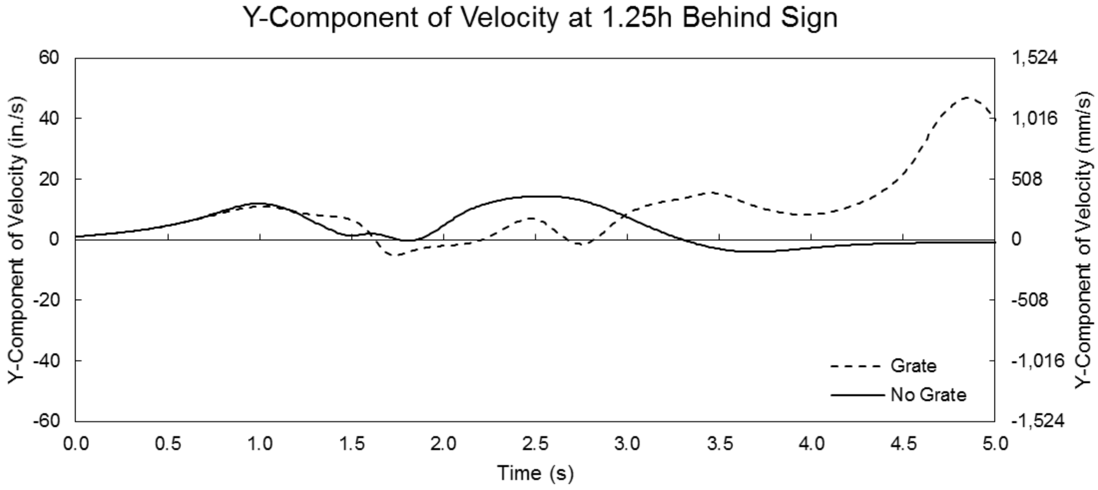

Figure 68 Y-component of velocity for the large sign at V=30 mph (13.4 m/s) at a distance = 1.25h behind the sign

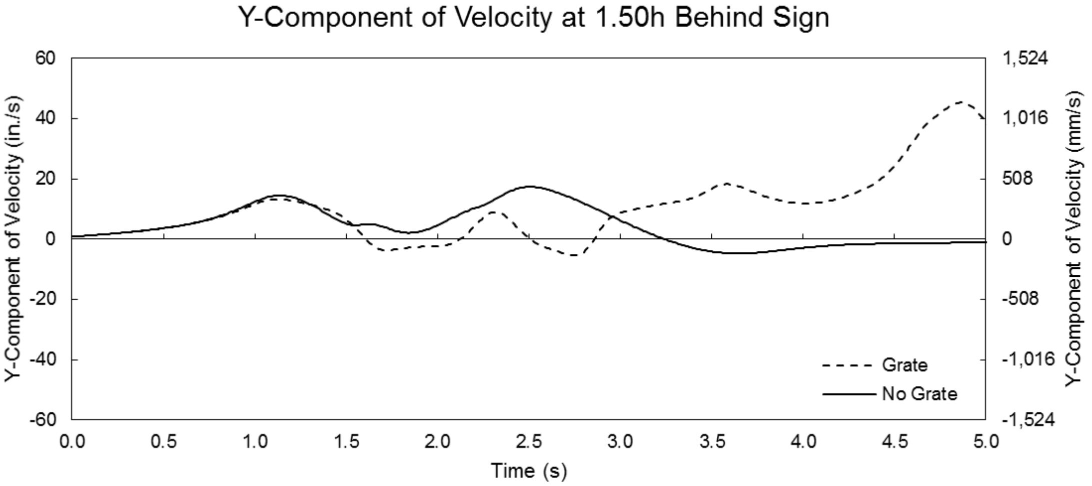

Figure 69 Y-component of velocity for the large sign at V=30 mph (13.4 m/s) at a distance = 1.5h behind the sign

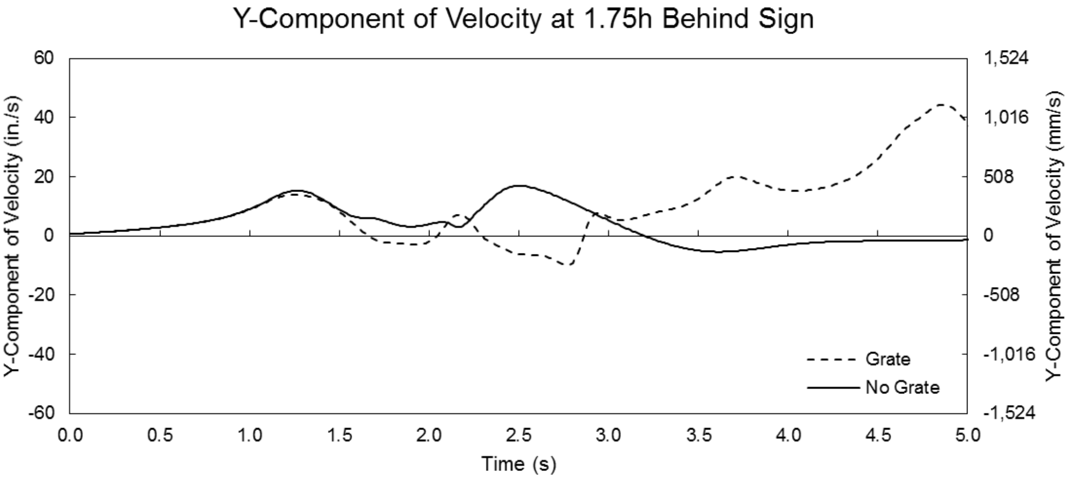

Figure 70 Y-component of velocity for the large sign at V=30 mph (13.4 m/s) at a distance = 1.75h behind the sign

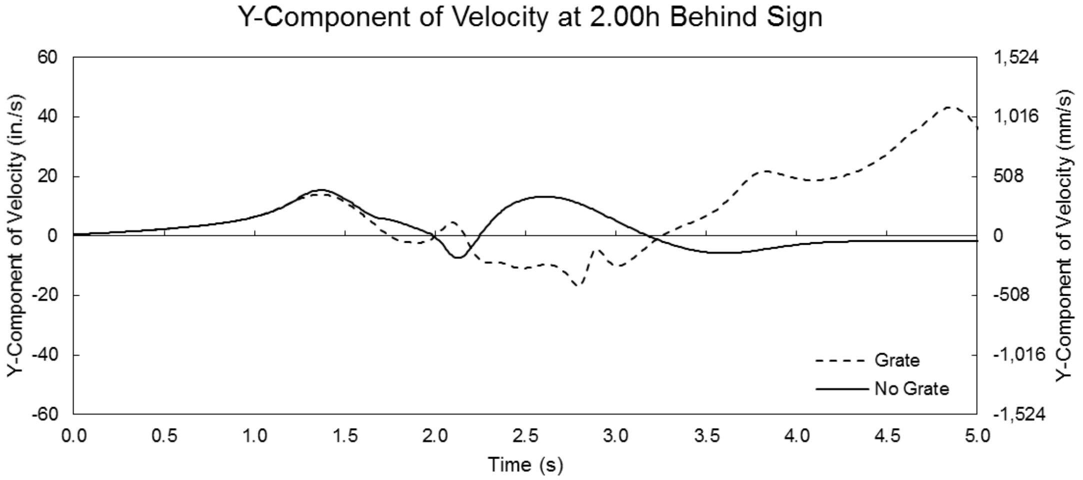

Figure 71 Y-component of velocity for the large sign at V=30 mph (13.4 m/s) at a distance = 2.0h behind the sign

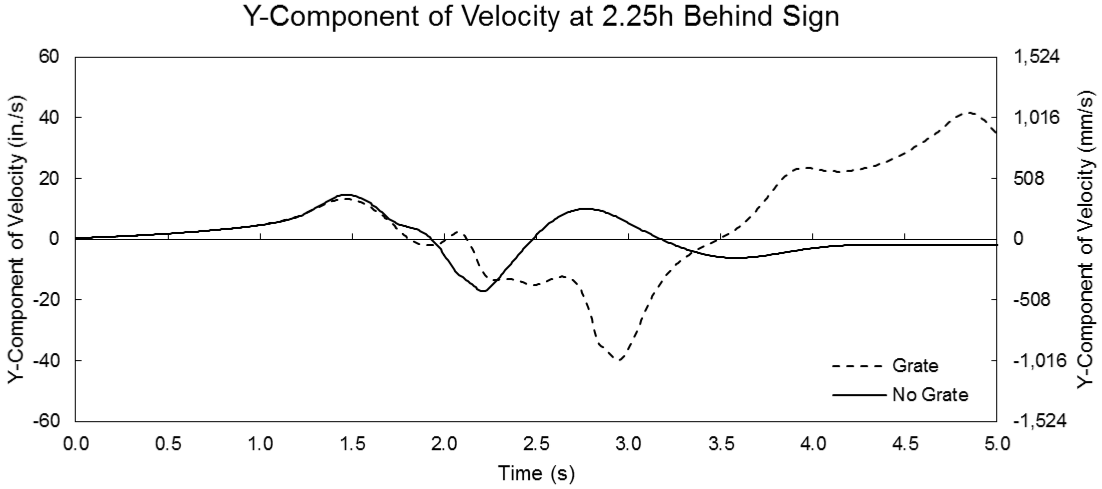

Figure 72 Y-component of velocity for the large sign at V=30 mph (13.4 m/s) at a distance = 2.25h behind the sign

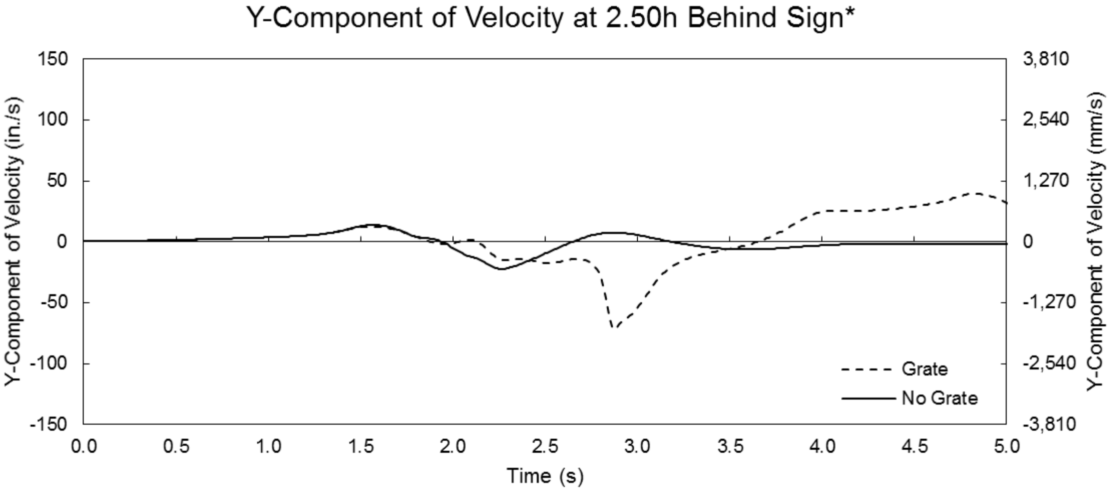

Figure 73 Y-component of velocity for the large sign at V=30 mph (13.4 m/s) at a distance = 2.5h behind the sign

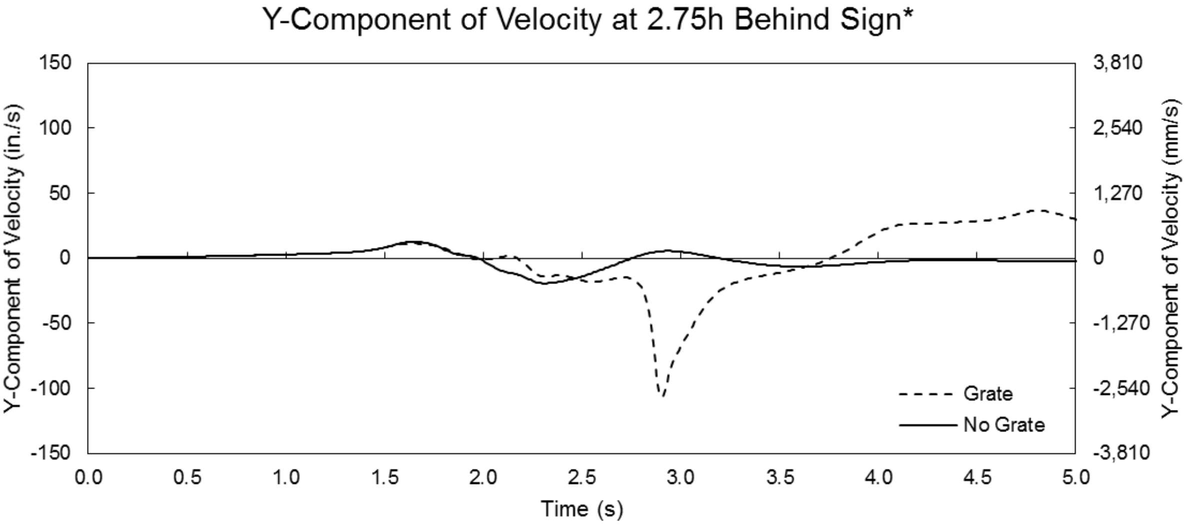

Figure 74 Y-component of velocity for the large sign at V=30 mph (13.4 m/s) at a distance = 2.75h behind the sign

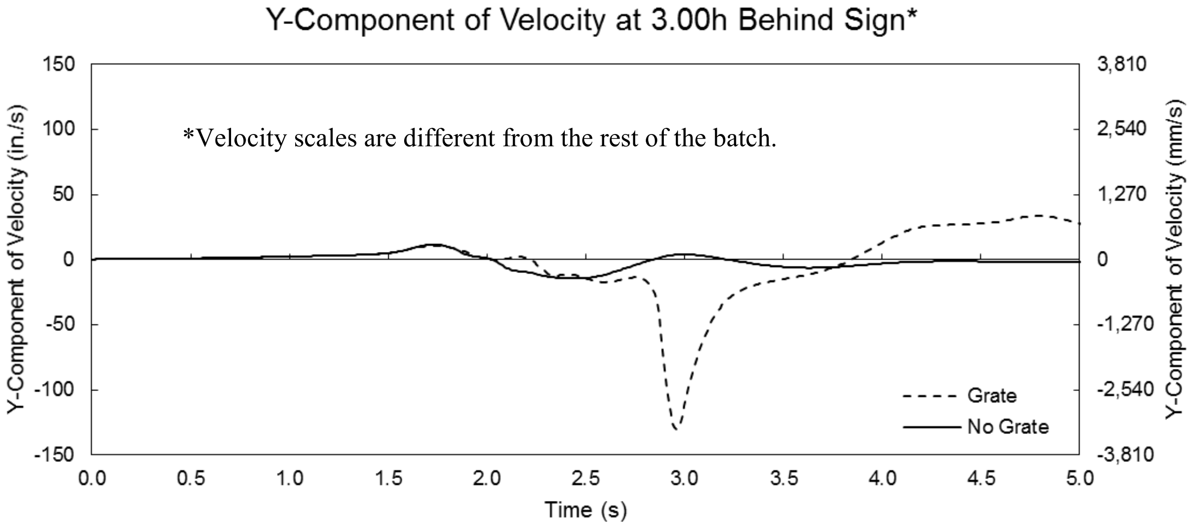

Figure 75 Y-component of velocity for the large sign at V=30 mph (13.4 m/s) at a distance = 3.0h behind the sign

A1.2 – Y-Component of Velocity Behind Large Sign at V=61.2 mph (27.4 m/s)

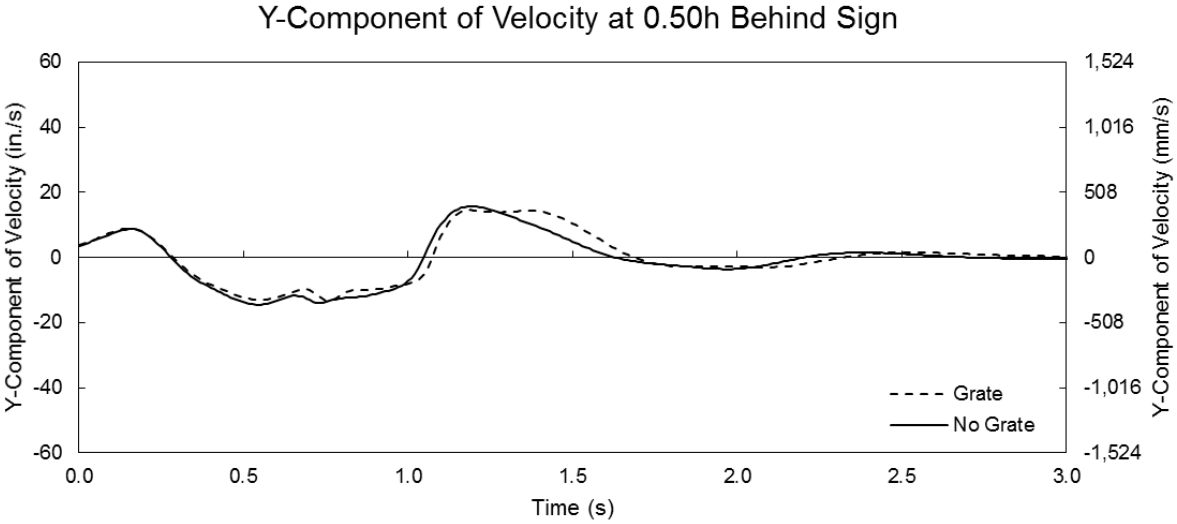

Figure 76 Y-component of velocity for the large sign at V=61.2 mph (27.4 m/s) at a distance = 0.5h behind the sign

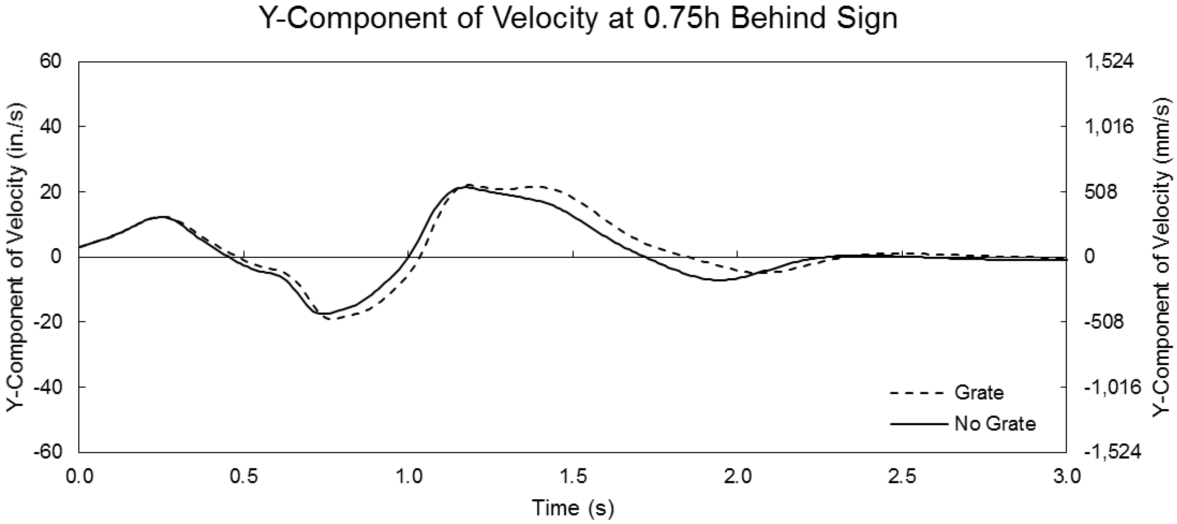

Figure 77 Y-component of velocity for the large sign at V=61.2 mph (27.4 m/s) at a distance = 0.75h behind the sign

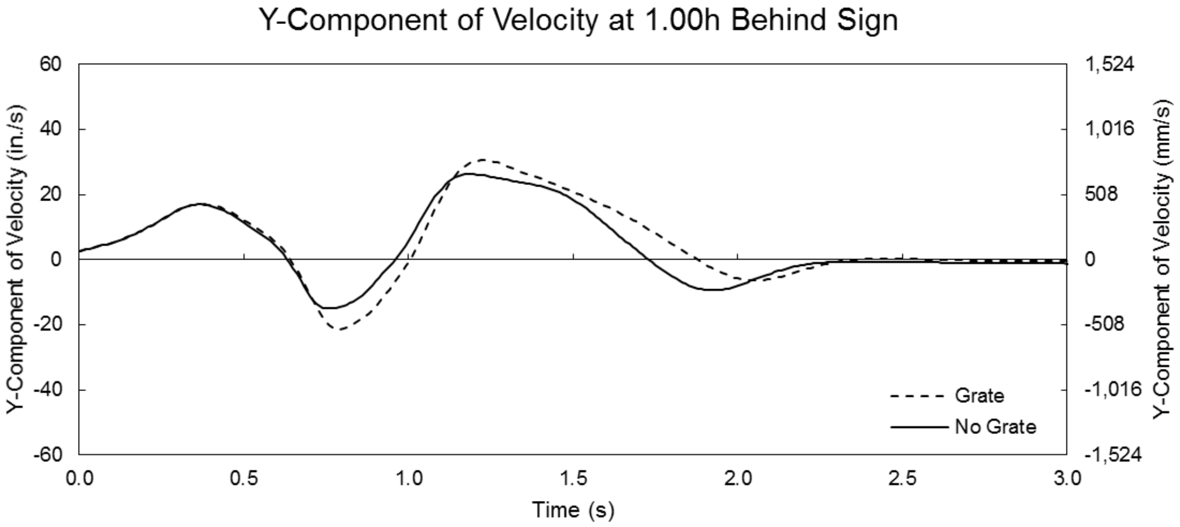

Figure 78 Y-component of velocity for the large sign at V=61.2 mph (27.4 m/s) at a distance = 1.0h behind the sign

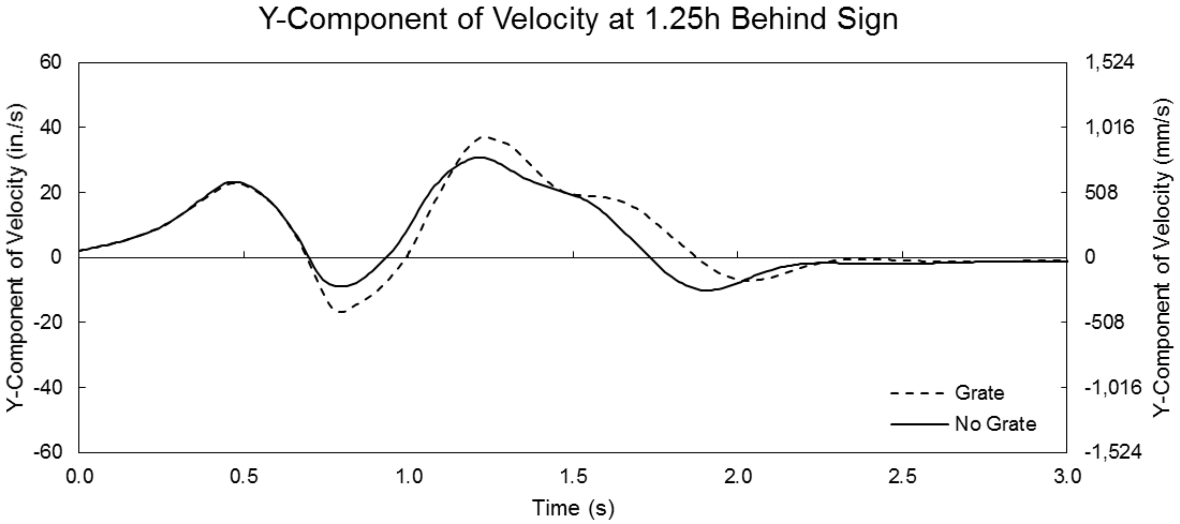

Figure 79 Y-component of velocity for the large sign at V=61.2 mph (27.4 m/s) at a distance = 1.25h behind the sign

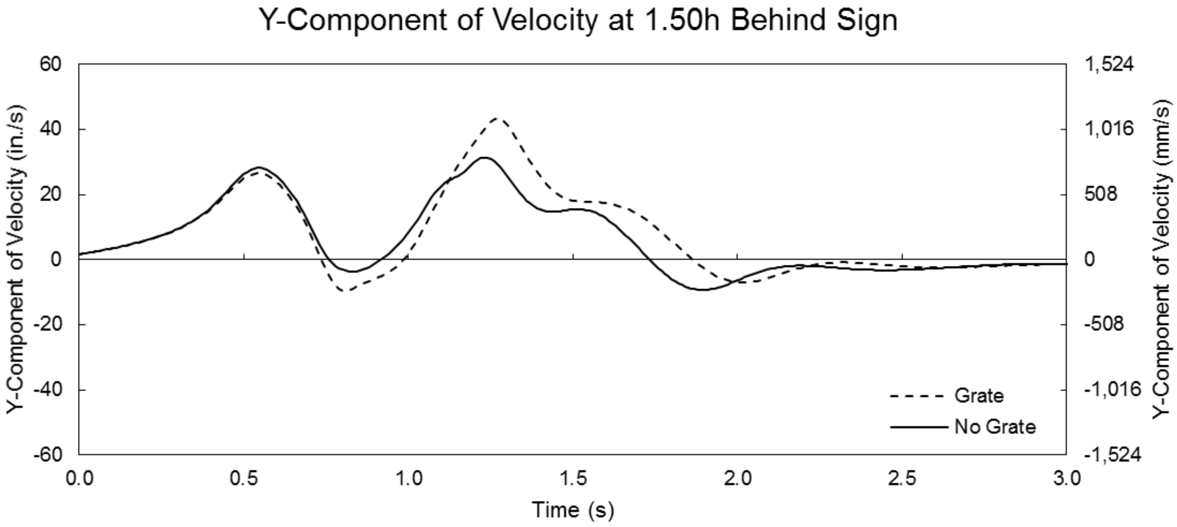

Figure 80 Y-component of velocity for the large sign at V=61.2 mph (27.4 m/s) at a distance = 1.5h behind the sign

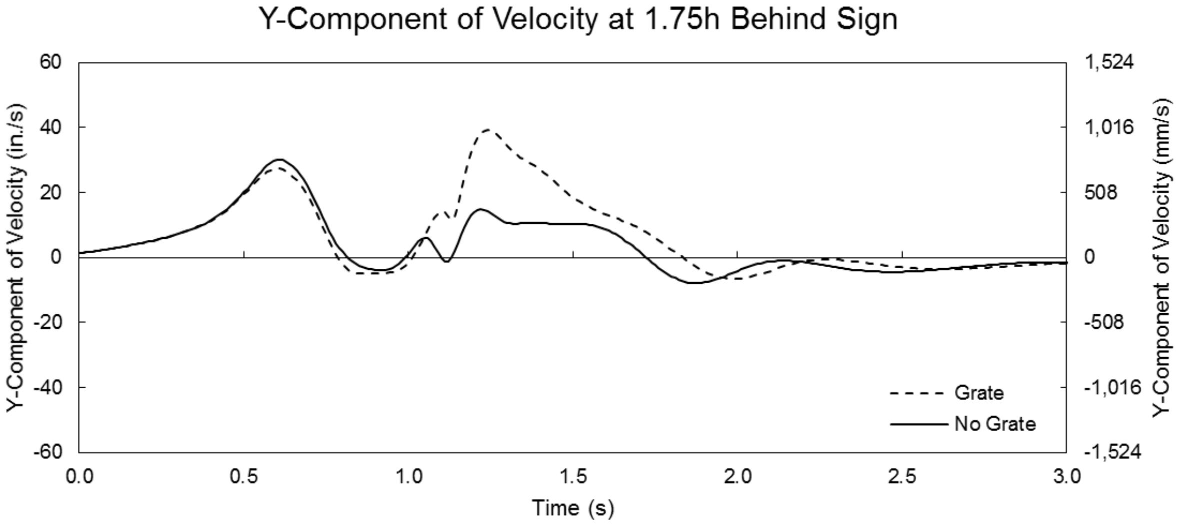

Figure 81 Y-component of velocity for the large sign at V=61.2 mph (27.4 m/s) at a distance = 1.75h behind the sign

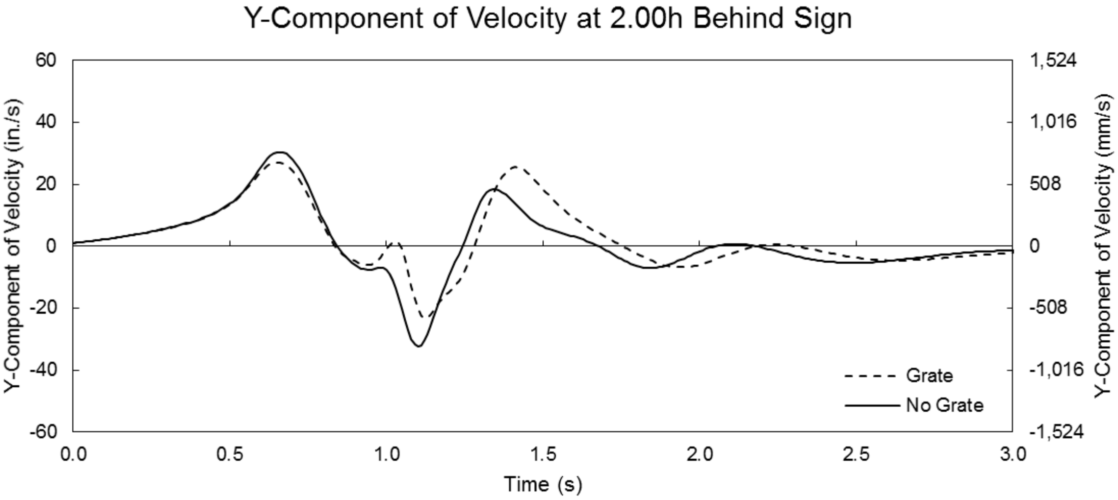

Figure 82 Y-component of velocity for the large sign at V=61.2 mph (27.4 m/s) at a distance = 2.0h behind the sign

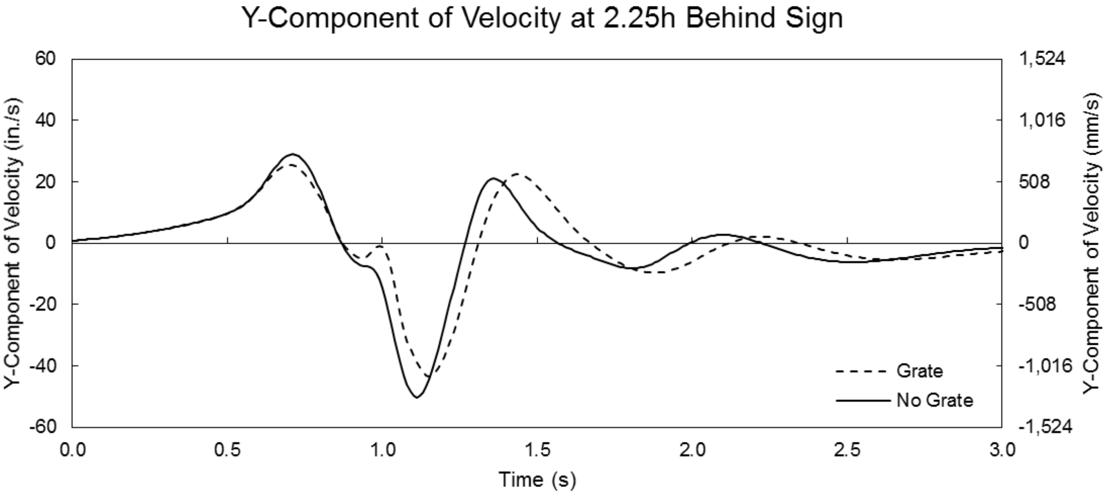

Figure 83 Y-component of velocity for the large sign at V=61.2 mph (27.4 m/s) at a distance = 2.25h behind the sign

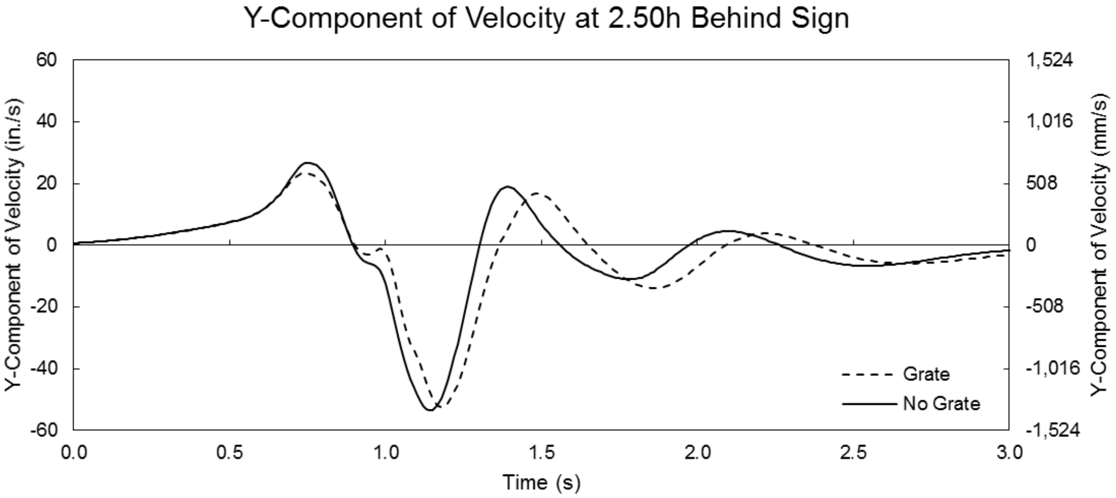

Figure 84 Y-component of velocity for the large sign at V=61.2 mph (27.4 m/s) at a distance = 2.5h behind the sign

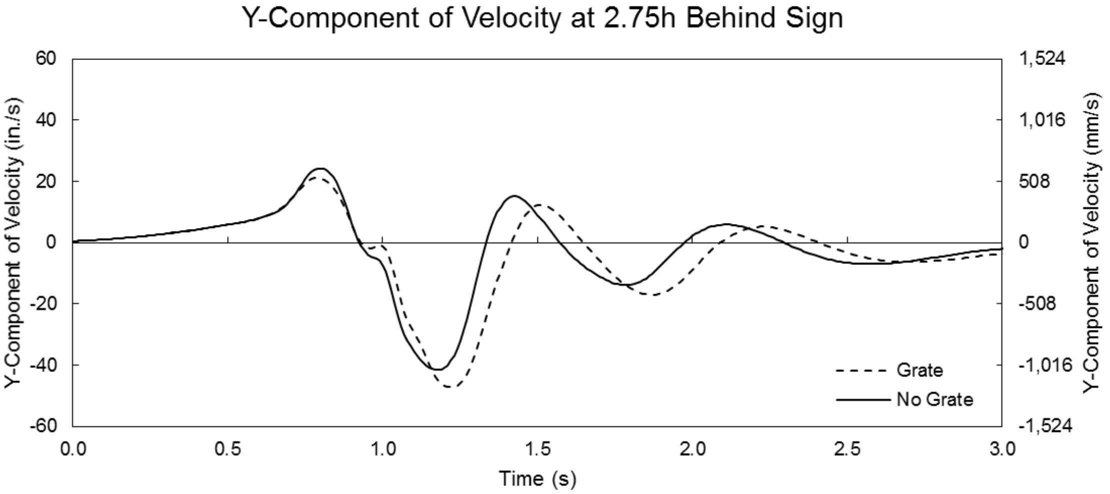

Figure 85 Y-component of velocity for the large sign at V=61.2 mph (27.4 m/s) at a distance = 2.75h behind the sign

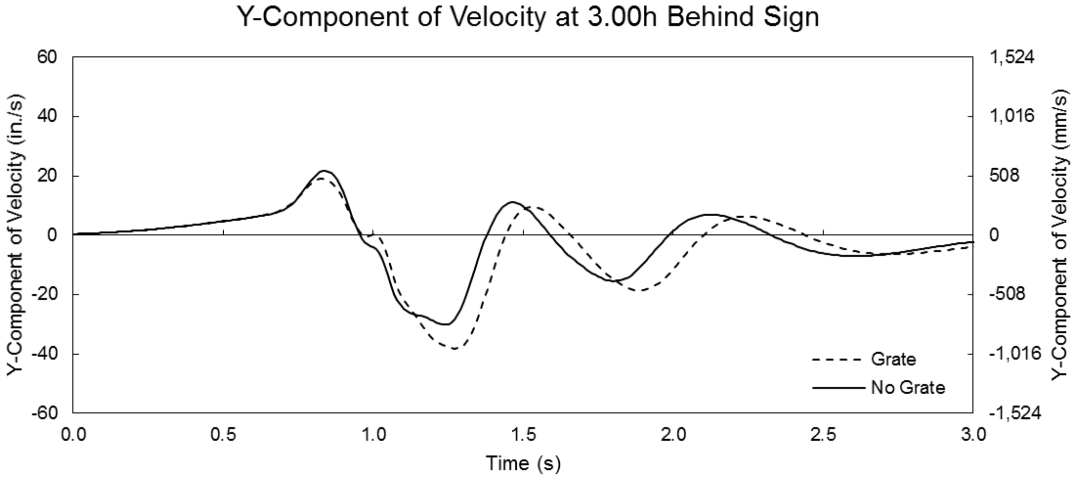

Figure 86 Y-component of velocity for the large sign at V=61.2 mph (27.4 m/s) at a distance = 3.0h behind the sign

A1.3 – Y-Component of Velocity Behind Large Sign at V=105mph (46.9 m/s)

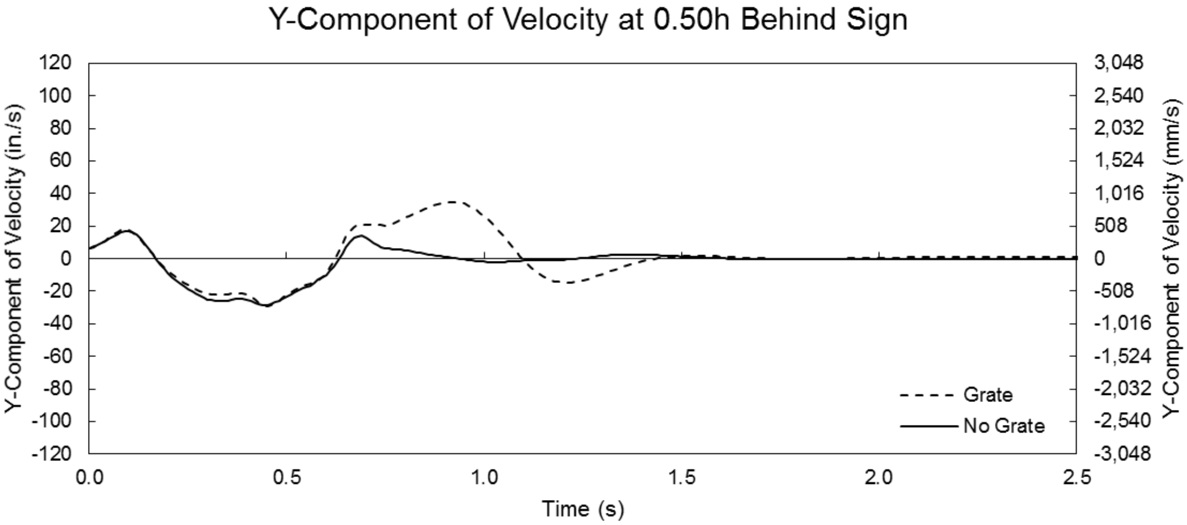

Figure 87 Y-component of velocity for the large sign at V=105 mph (46.9 m/s) at a distance = 0.5h behind the sign

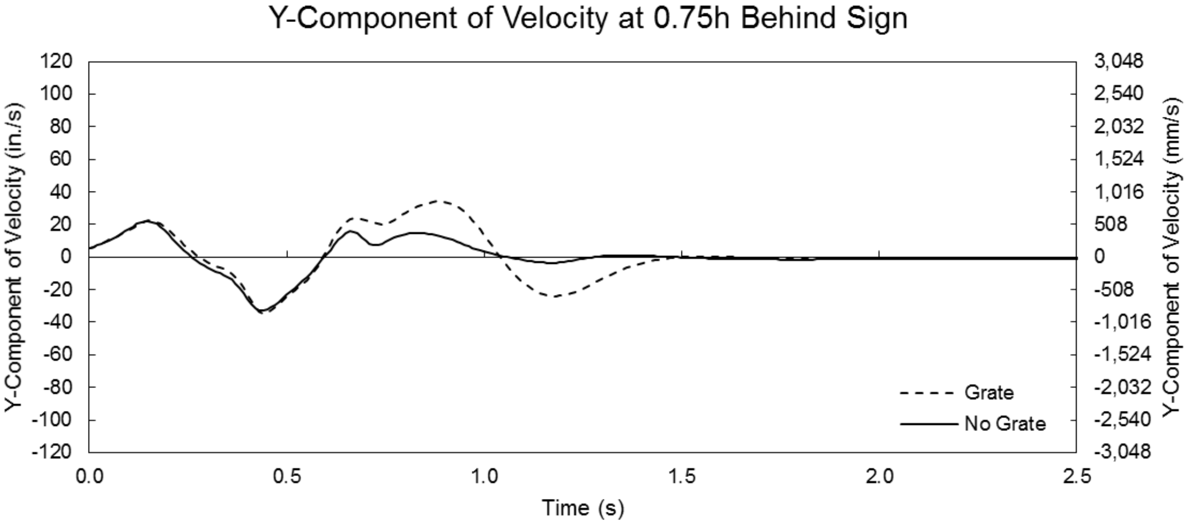

Figure 88   Y-component of velocity for the large sign at V=105 mph (46.9 m/s) at a distance = 0.75h behind the sign

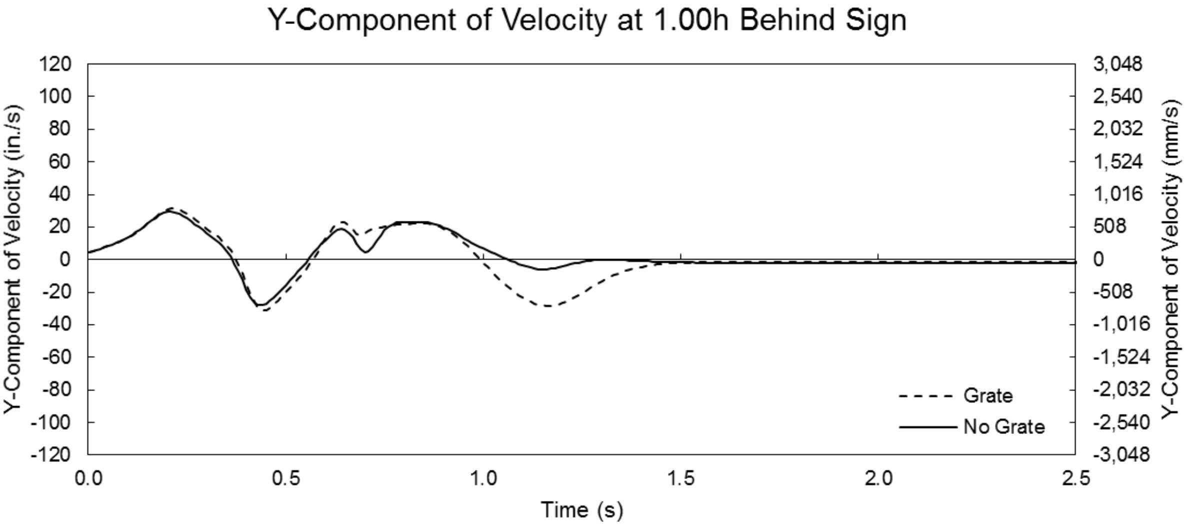

Figure 89 Y-component of velocity for the large sign at V=105 mph (46.9 m/s) at a distance = 1.0h behind the sign

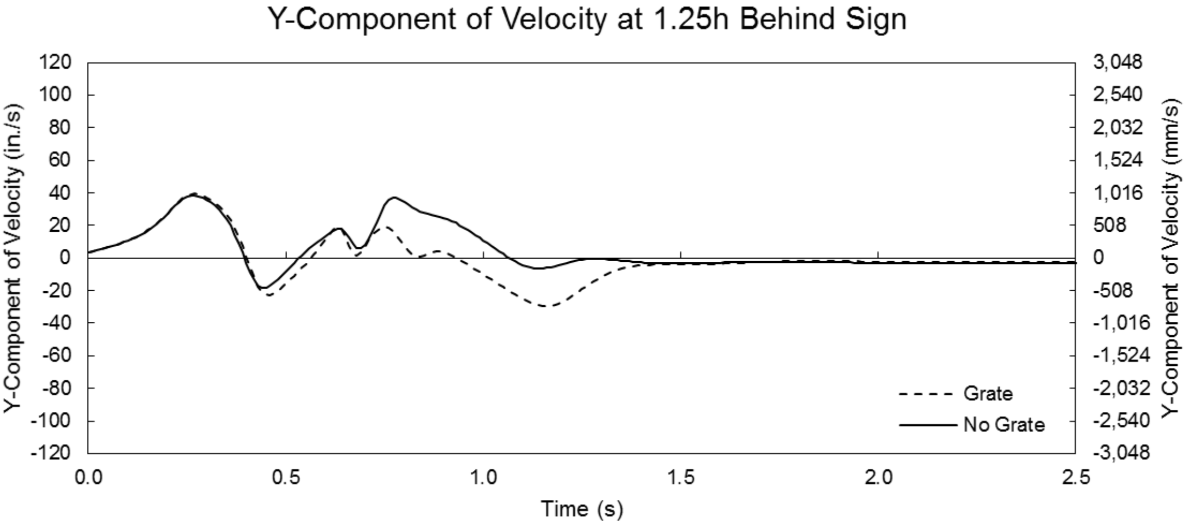

Figure 90 Y-component of velocity for the large sign at V=105 mph (46.9 m/s) at a distance = 1.25h behind the sign

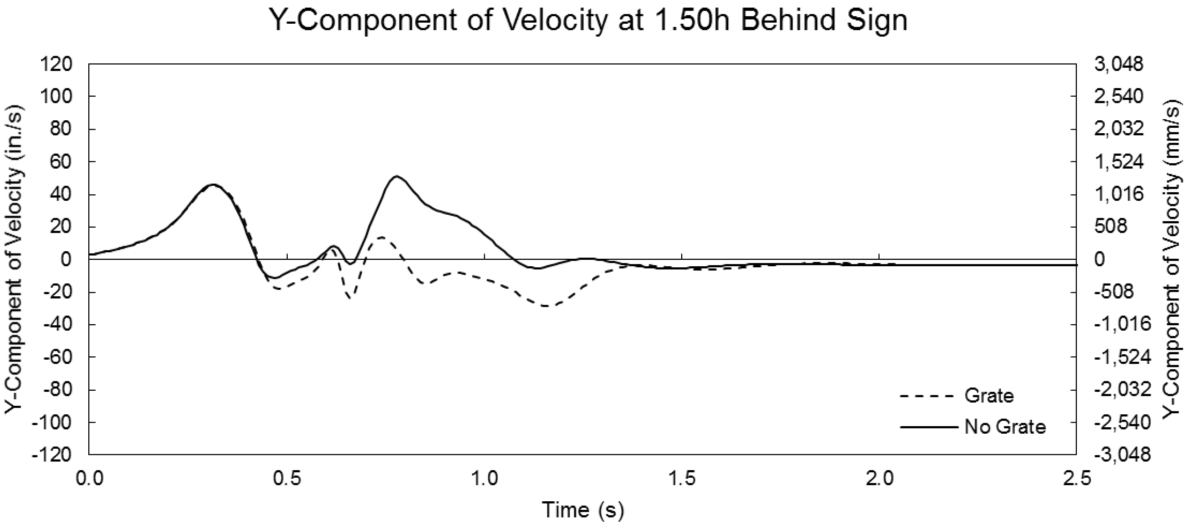

Figure 91 Y-component of velocity for the large sign at V=105 mph (46.9 m/s) at a distance = 1.5h behind the sign

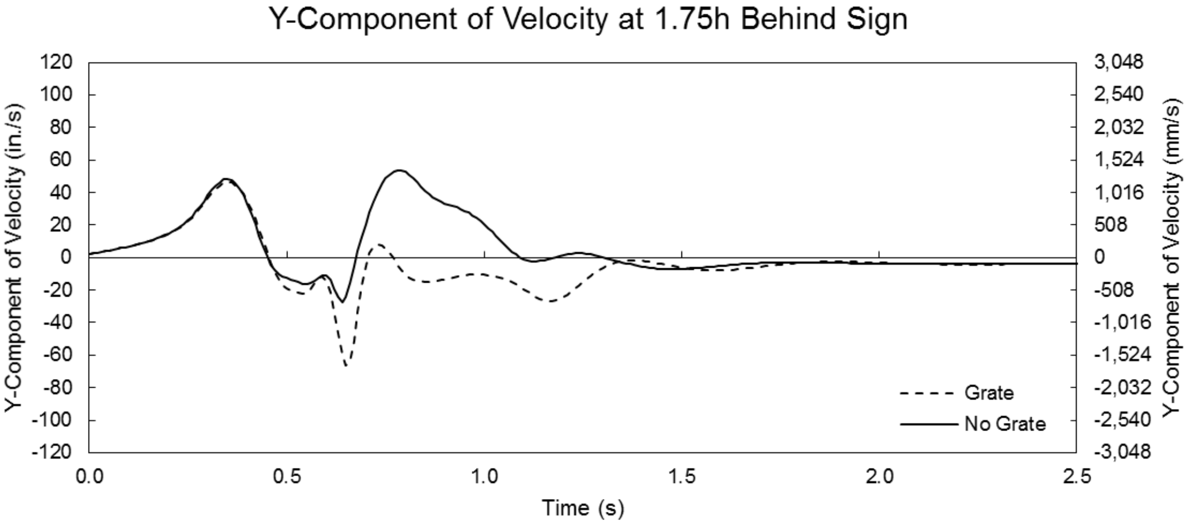

Figure 92 Y-component of velocity for the large sign at V=105 mph (46.9 m/s) at a distance = 1.75h behind the sign

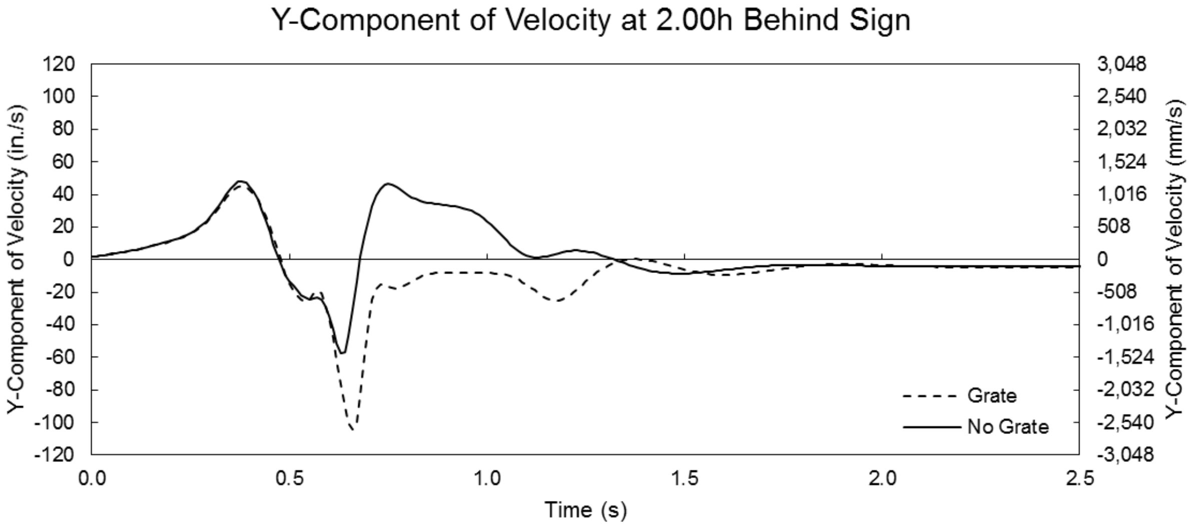

Figure 93 Y-component of velocity for the large sign at V=105 mph (46.9 m/s) at a distance = 2.0h behind the sign

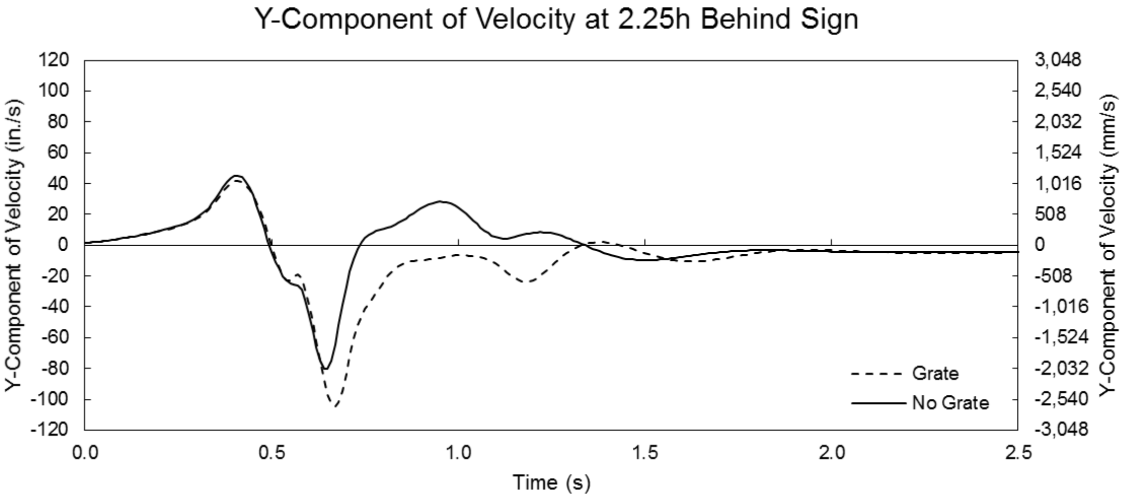

Figure 94 Y-component of velocity for the large sign at V=105 mph (46.9 m/s) at a distance = 2.25h behind the sign

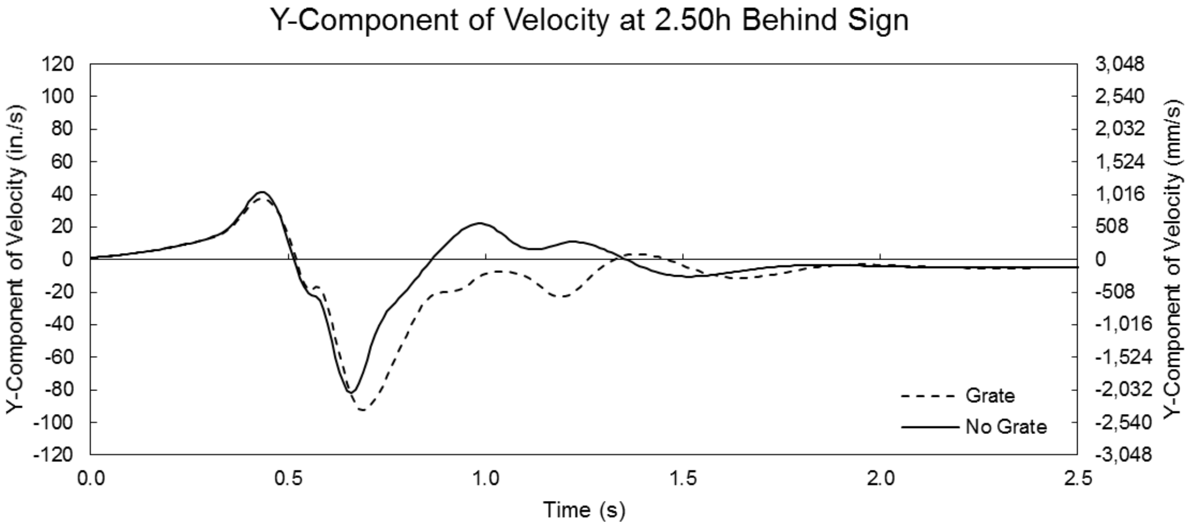

Figure 95 Y-component of velocity for the large sign at V=105 mph (46.9 m/s) at a distance = 2.5h behind the sign

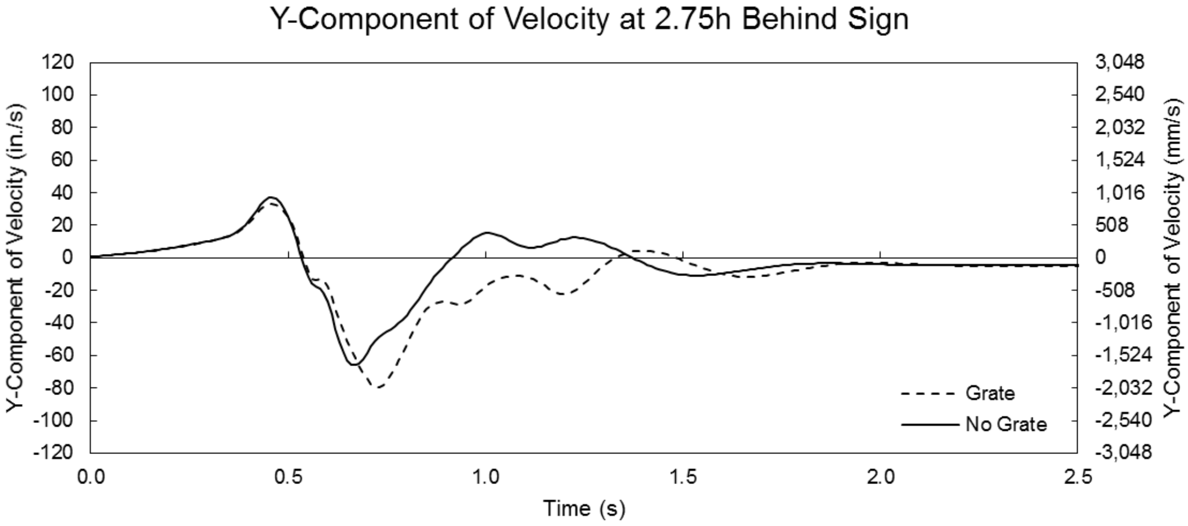

Figure 96 Y-component of velocity for the large sign at V=105 mph (46.9 m/s) at a distance = 2.75h behind the sign

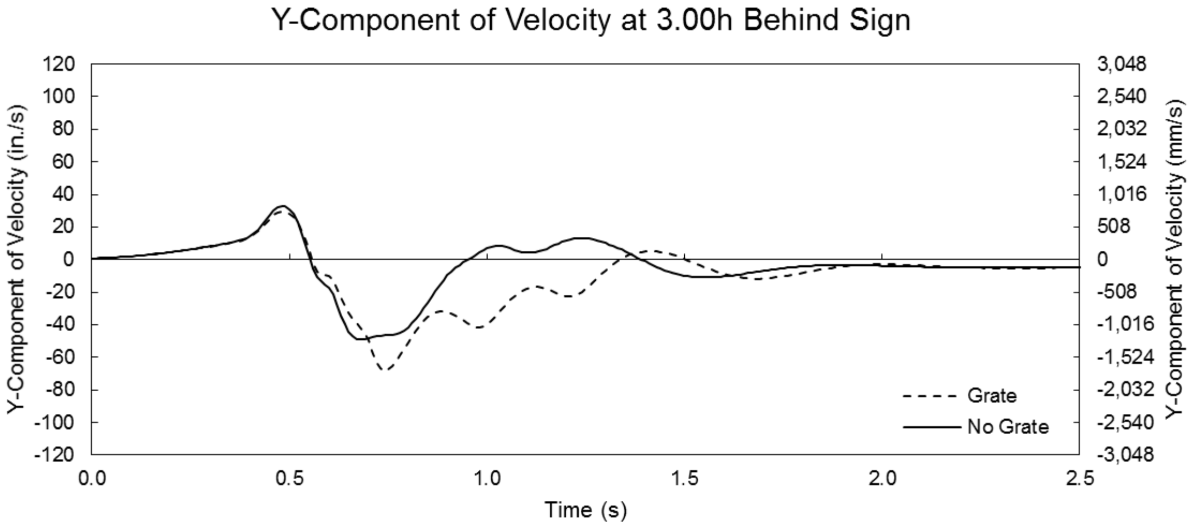

Figure 97 Y-component of velocity for the large sign at V=105 mph (46.9 m/s) at a distance = 3.0h behind the sign

A1.4 – Y-Component of Velocity Behind Medium Sign at V=30 mph (13.4 m/s)

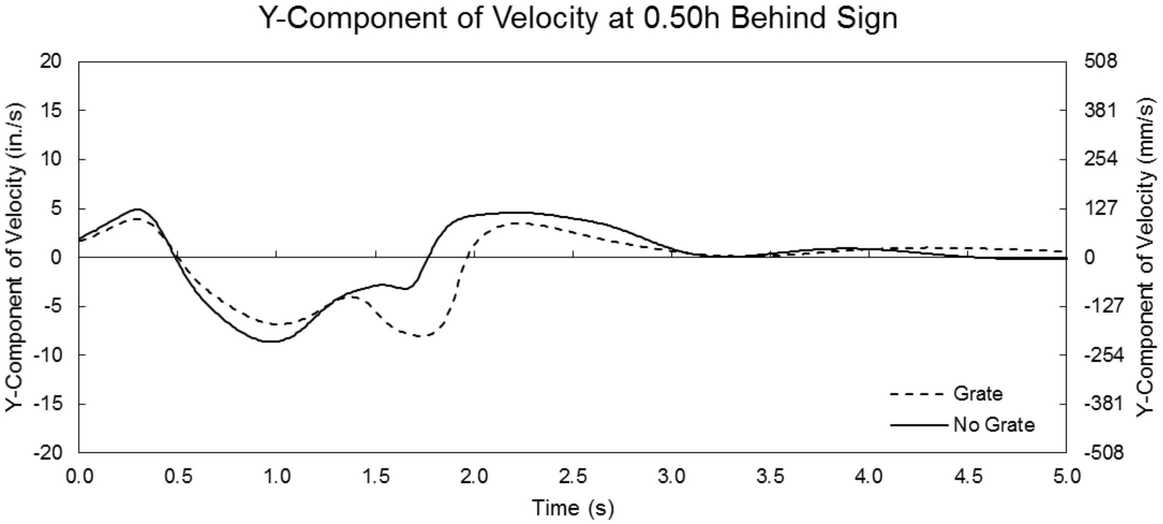

Figure 98 Y-component of velocity for the medium sign at V=30 mph (13.4 m/s) at a distance = 0.5h behind the sign

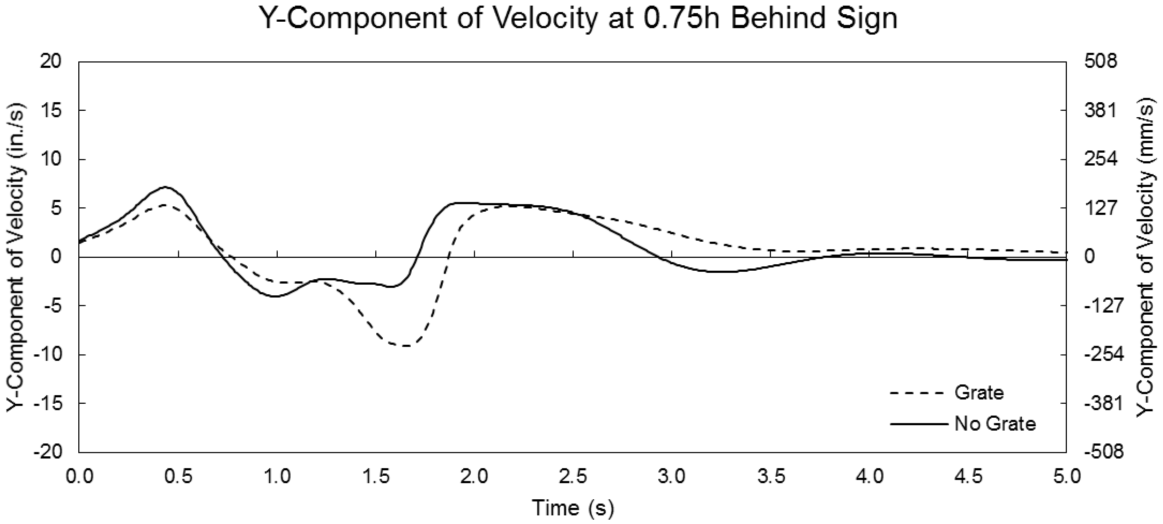

Figure 99 Y-component of velocity for the medium sign at V=30 mph (13.4 m/s) at a distance = 0.75h behind the sign

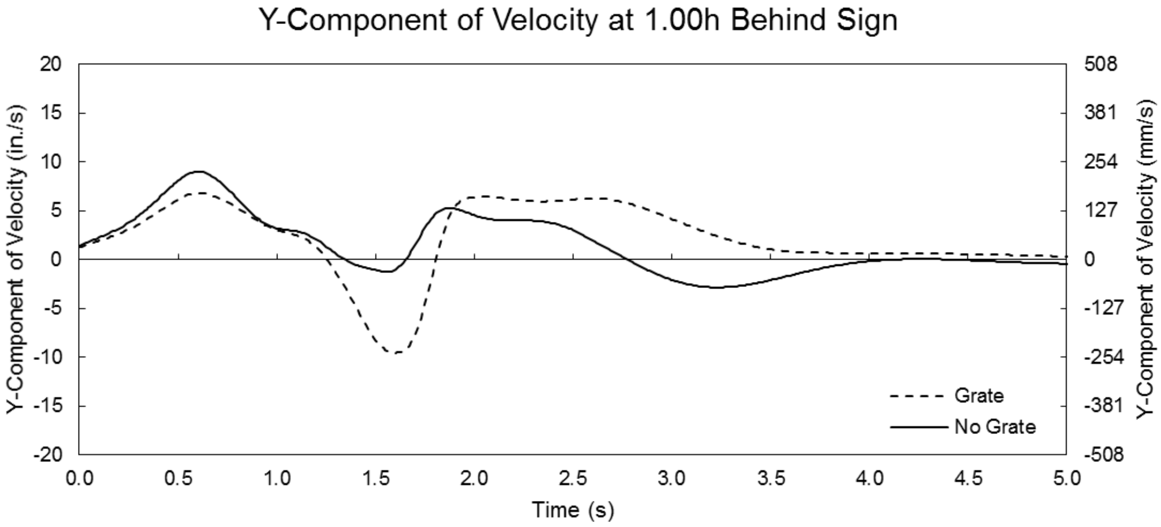

Figure 100 Y-component of velocity for the medium sign at V=30 mph (13.4 m/s) at a distance = 1.0h behind the sign

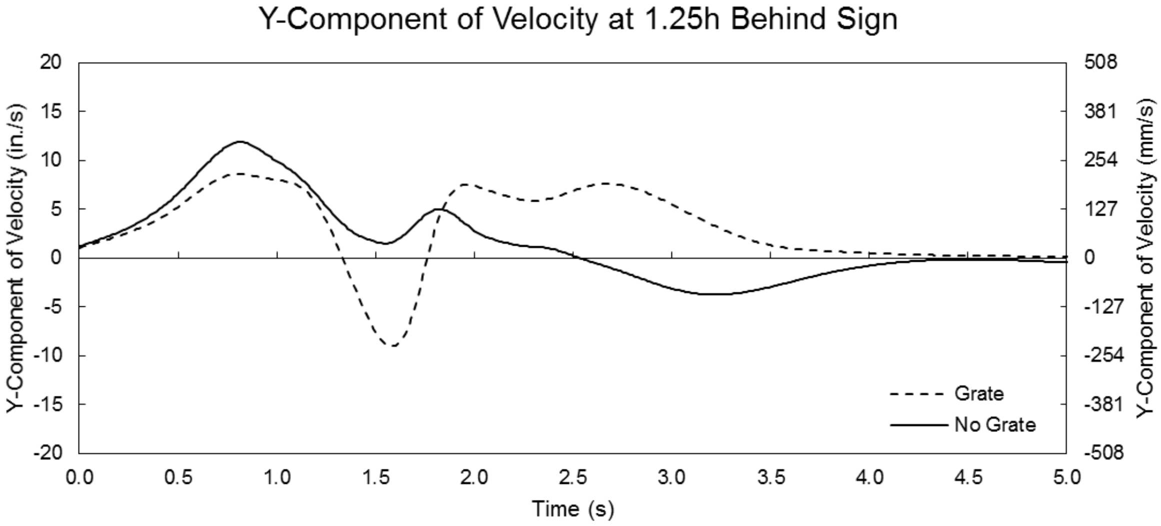

Figure 101 Y-component of velocity for the medium sign at V=30 mph (13.4 m/s) at a distance = 1.25h behind the sign

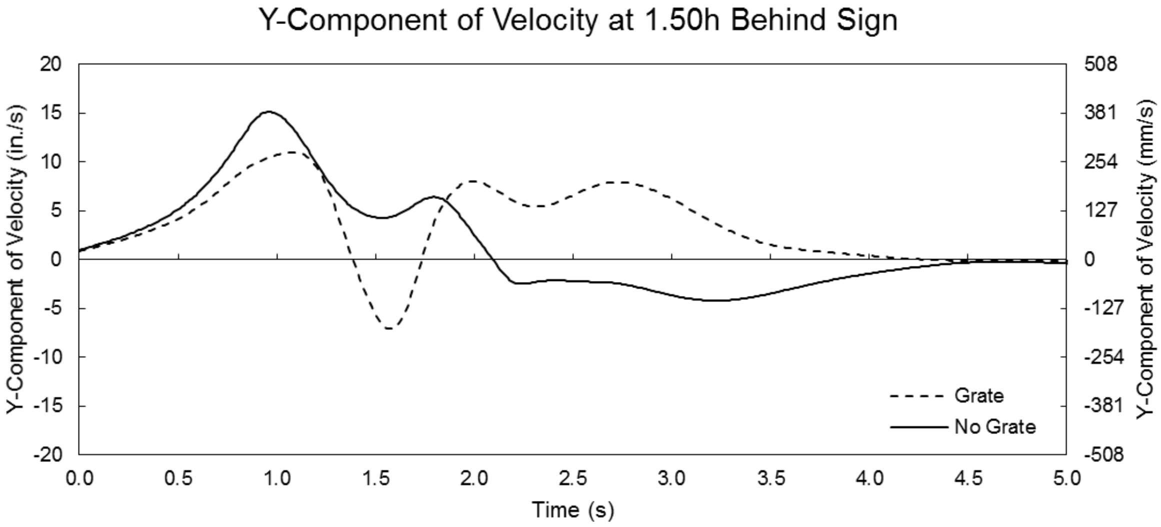

Figure 102 Y-component of velocity for the medium sign at V=30 mph (13.4 m/s) at a distance = 1.5h behind the sign

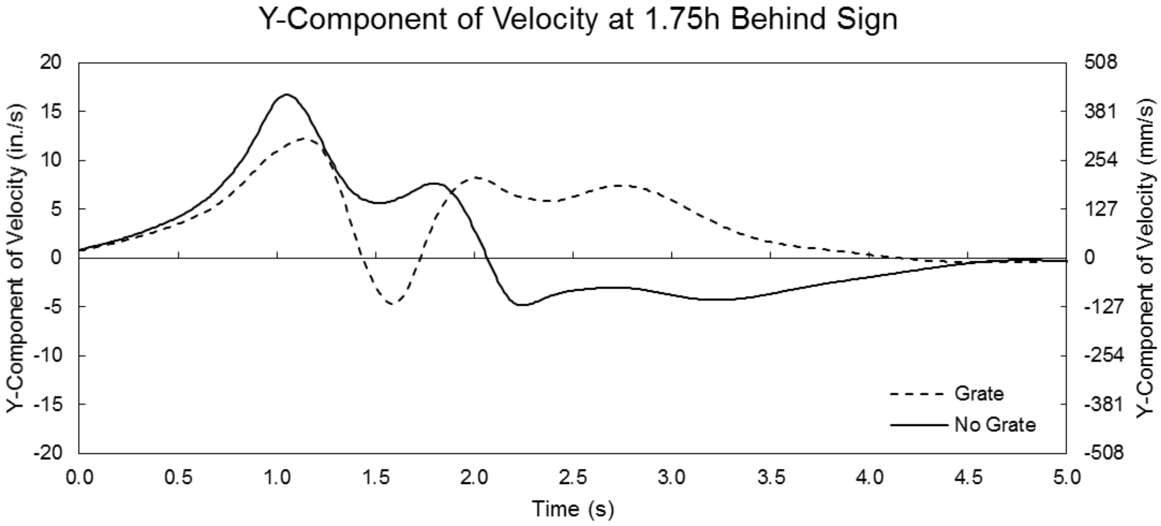

Figure 103 Y-component of velocity for the medium sign at V=30 mph (13.4 m/s) at a distance = 1.75h behind the sign

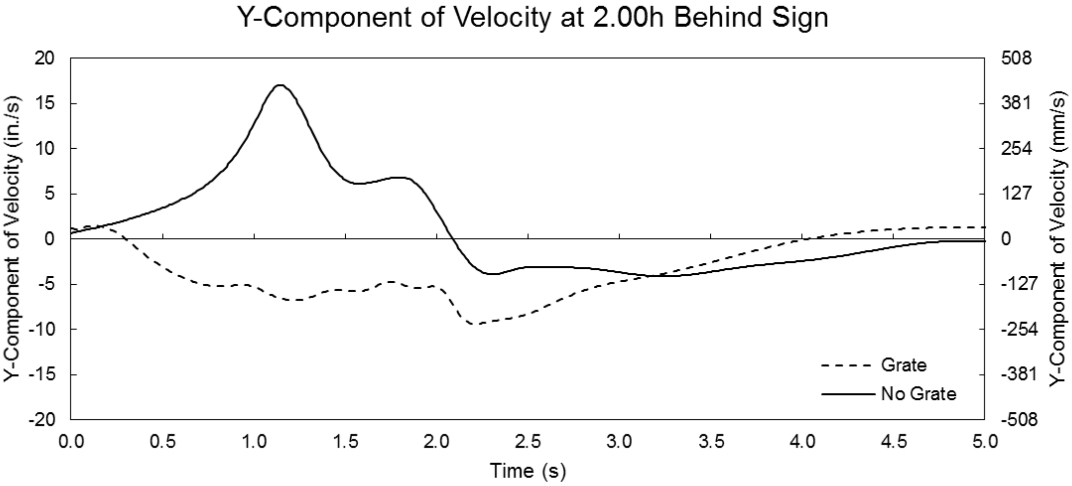

Figure 104 Y-component of velocity for the medium sign at V=30 mph (13.4 m/s) at a distance = 2.0h behind the sign

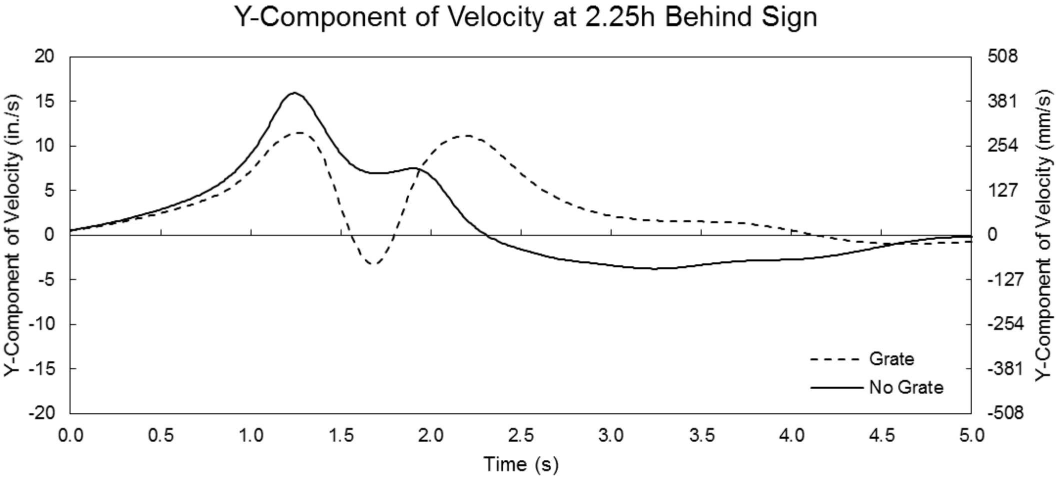

Figure 105 Y-component of velocity for the medium sign at V=30 mph (13.4 m/s) at a distance = 2.25h behind the sign

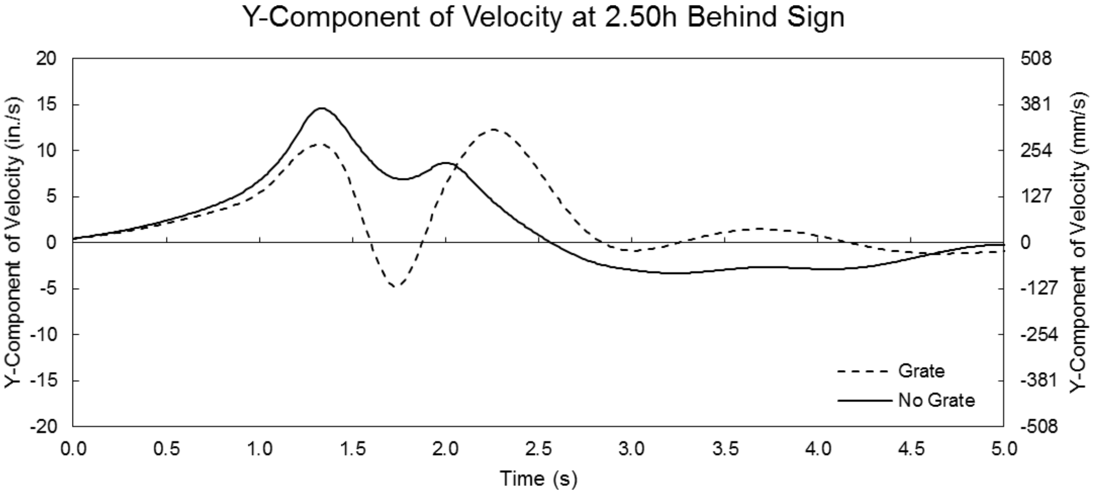

Figure 106 Y-component of velocity for the medium sign at V=30 mph (13.4 m/s) at a distance = 2.5h behind the sign

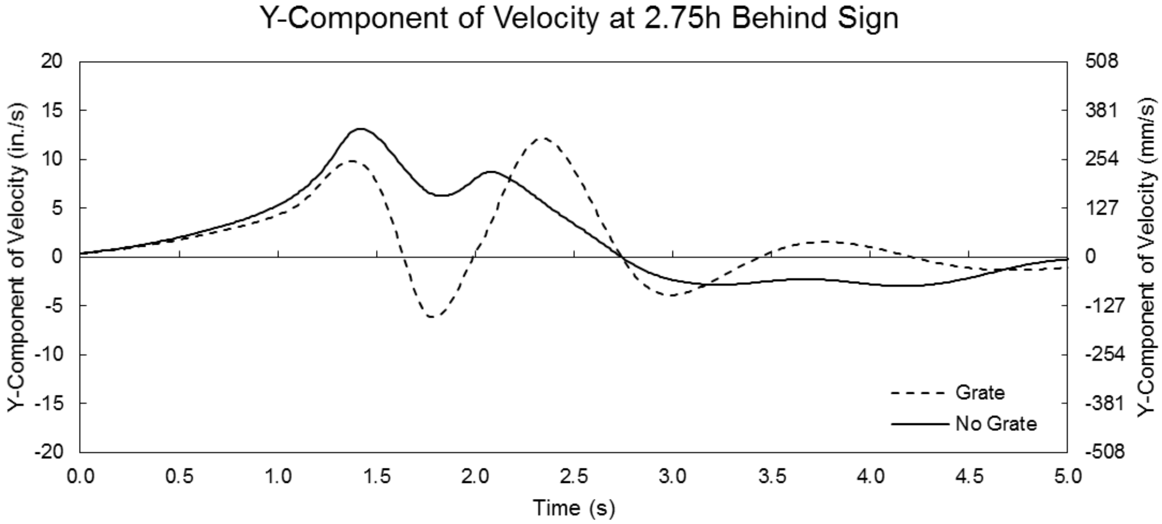

Figure 107 Y-component of velocity for the medium sign at V=30 mph (13.4 m/s) at a distance = 2.75h behind the sign

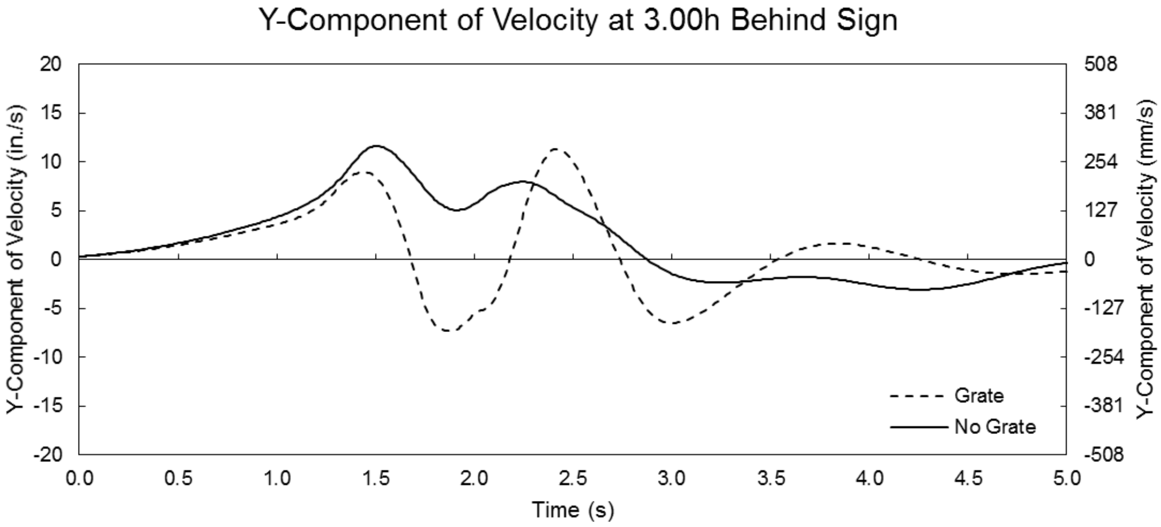

Figure 108 Y-component of velocity for the medium sign at V=30 mph (13.4 m/s) at a distance = 3.0h behind the sign

A1.5 – Y-Component of Velocity Behind Medium Sign at V=61.2 mph (27.4 m/s)

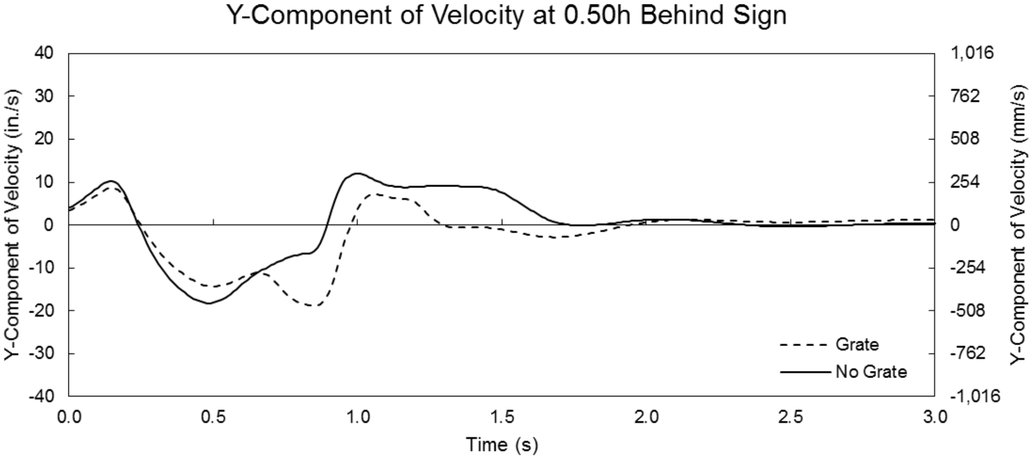

Figure 109 Y-component of velocity for the medium sign at V=61.2 mph (27.4 m/s) at a distance = 0.5h behind the sign

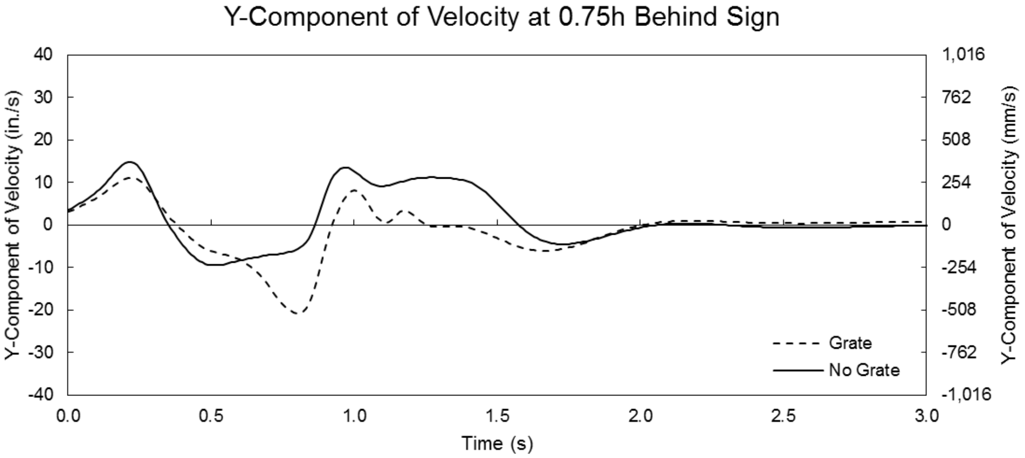

Figure 110 Y-component of velocity for the medium sign at V=61.2 mph (27.4 m/s) at a distance = 0.75h behind the sign

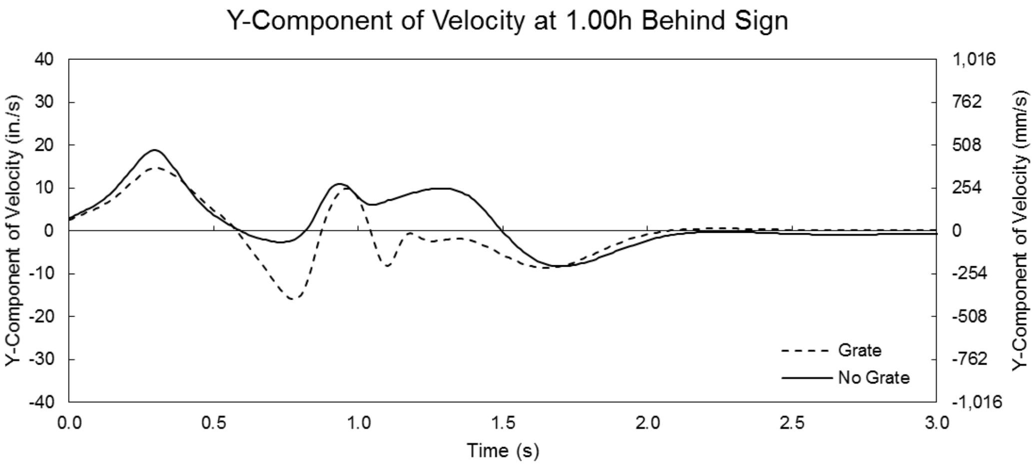

Figure 111 Y-component of velocity for the medium sign at V=61.2 mph (27.4 m/s) at a distance = 1.0h behind the sign

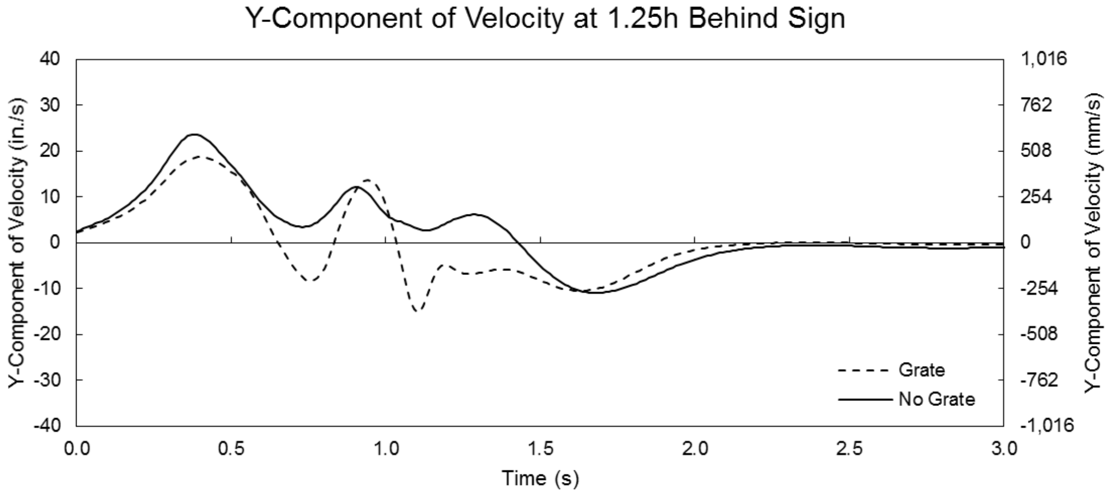

Figure 112 Y-component of velocity for the medium sign at V=61.2 mph (27.4 m/s) at a distance = 1.25h behind the sign

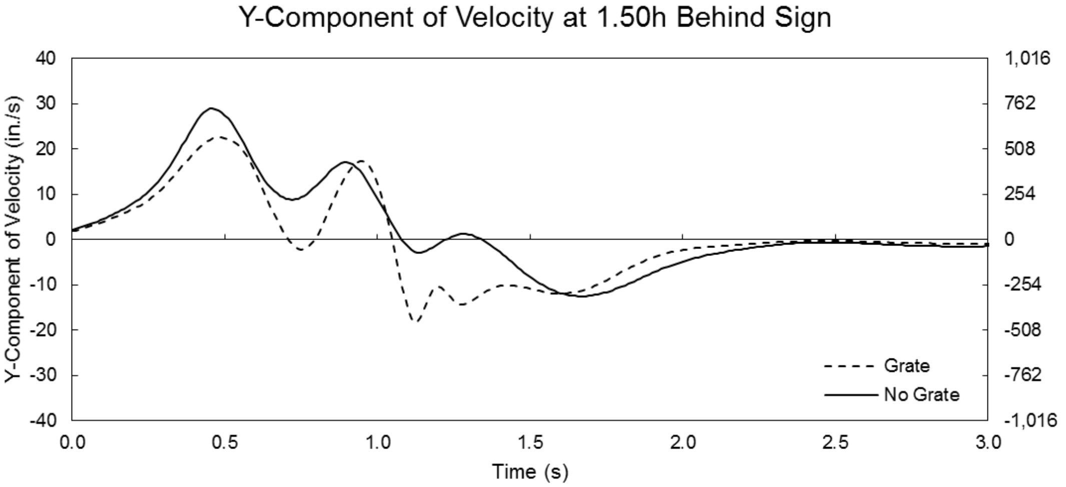

Figure 113 Y-component of velocity for the medium sign at V=61.2 mph (27.4 m/s) at a distance = 1.5h behind the sign

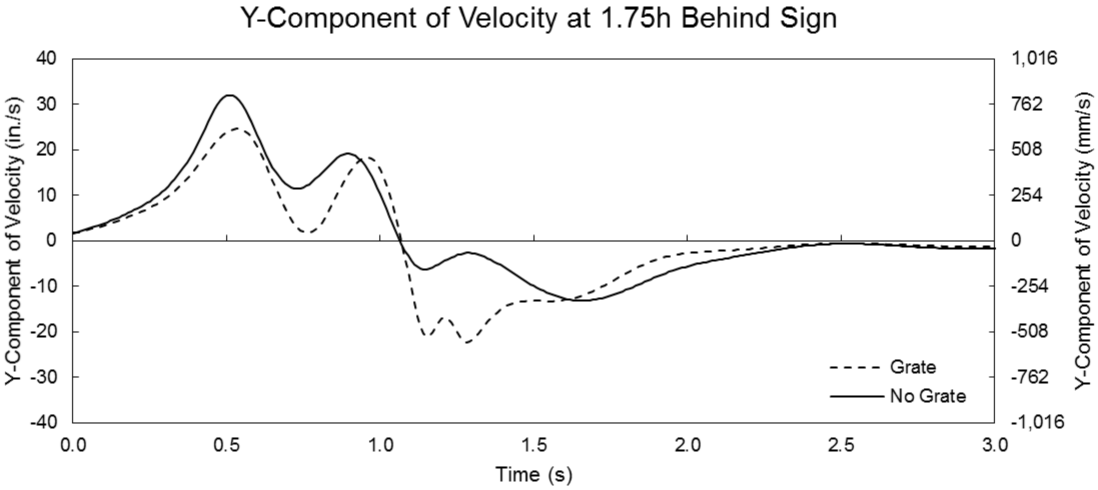

Figure 114 Y-component of velocity for the medium sign at V=61.2 mph (27.4 m/s) at a distance = 1.75h behind the sign

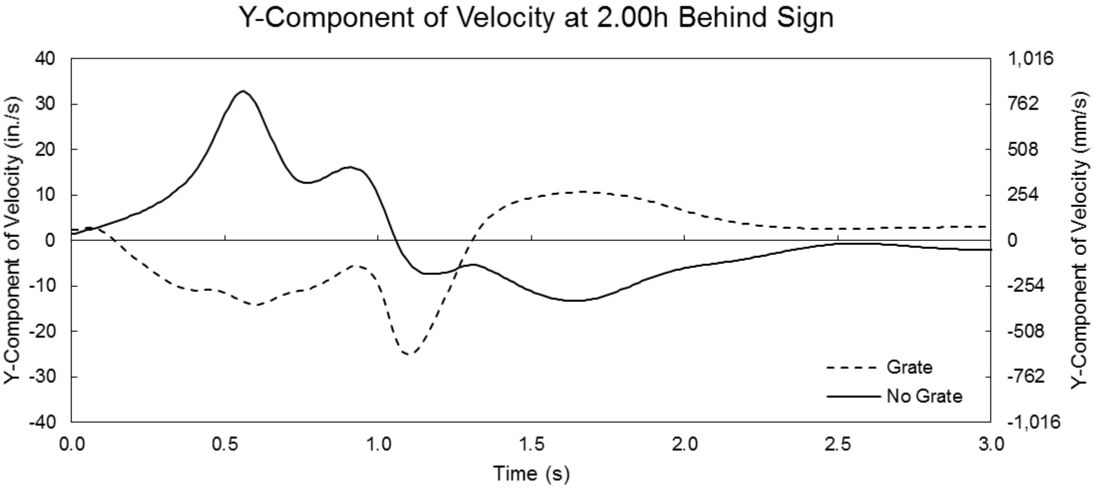

Figure 115 Y-component of velocity for the medium sign at V=61.2 mph (27.4 m/s) at a distance = 2.0h behind the sign

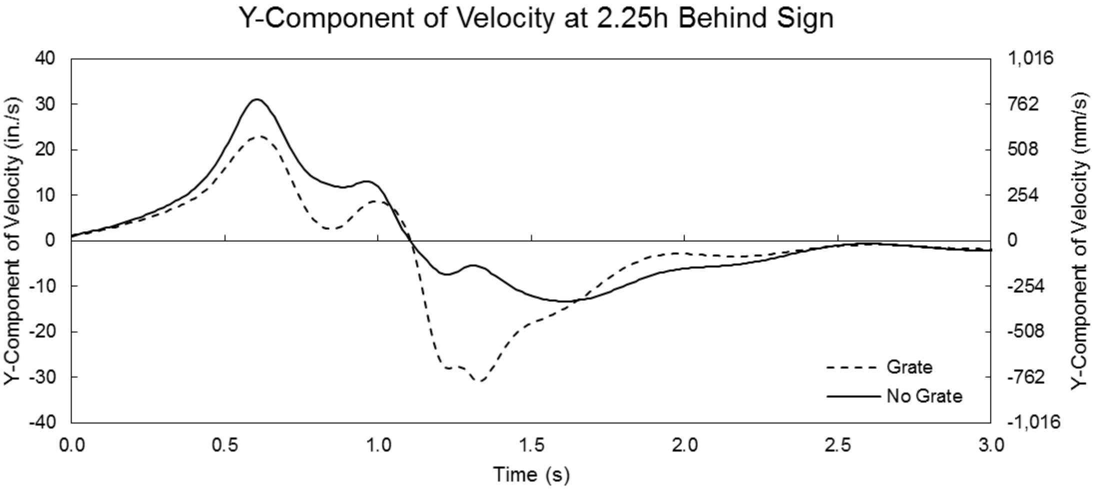

Figure 116 Y-component of velocity for the medium sign at V=61.2 mph (27.4 m/s) at a distance = 2.25h behind the sign

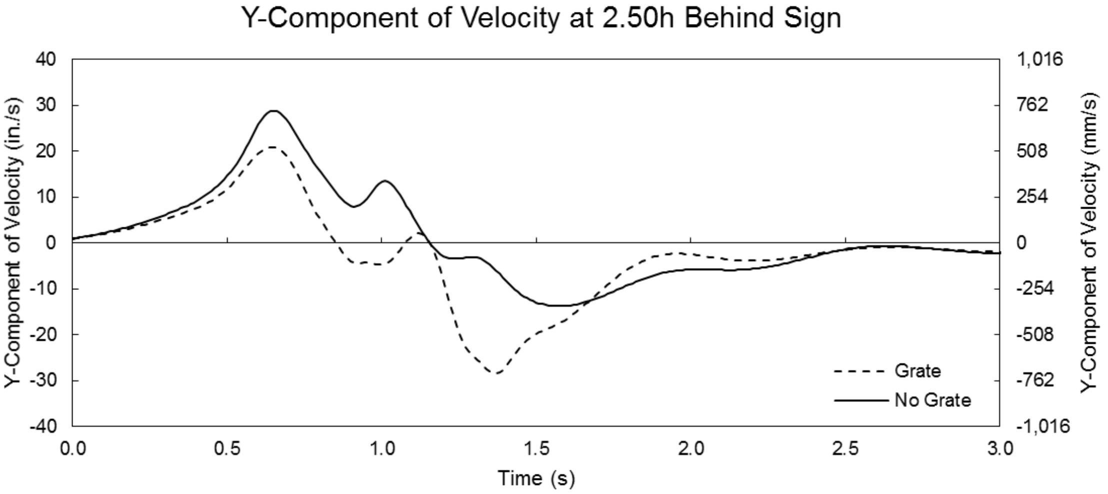

Figure 117 Y-component of velocity for the medium sign at V=61.2 mph (27.4 m/s) at a distance = 2.5h behind the sign

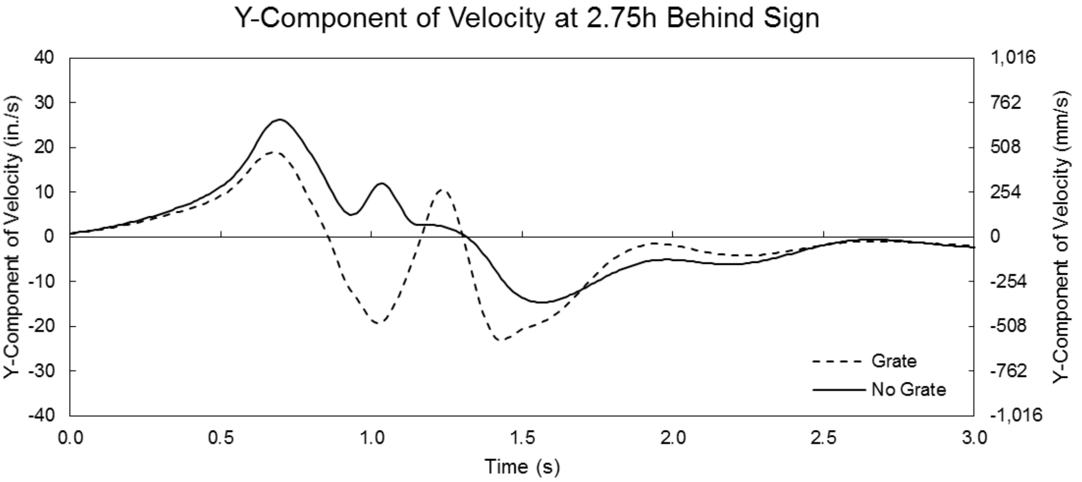

Figure 118 Y-component of velocity for the medium sign at V=61.2 mph (27.4 m/s) at a distance = 2.75h behind the sign

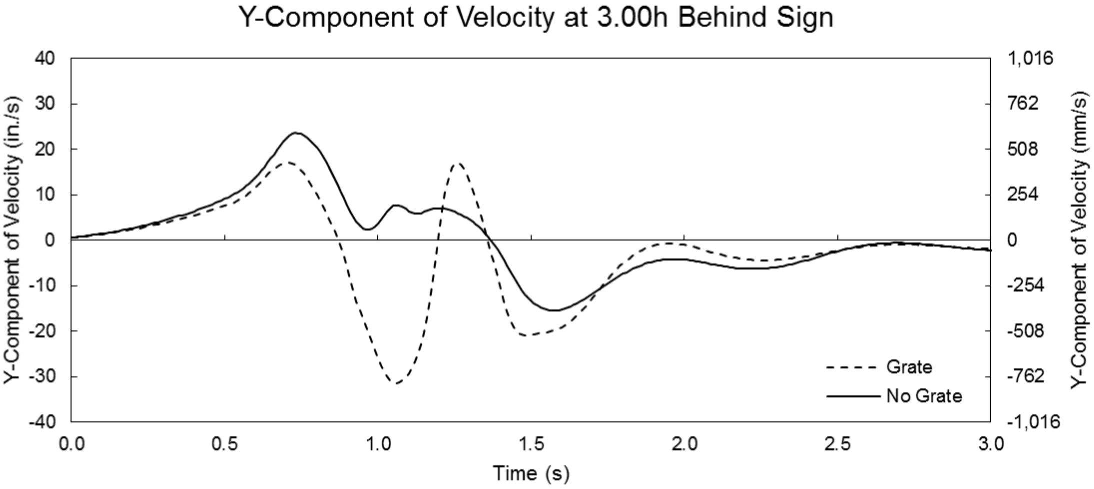

Figure 119 Y-component of velocity for the medium sign at V=61.2 mph (27.4 m/s) at a distance = 3.0h behind the sign

A1.6 – Y-Component of Velocity Behind Medium Sign at V=105mph (46.9 m/s)

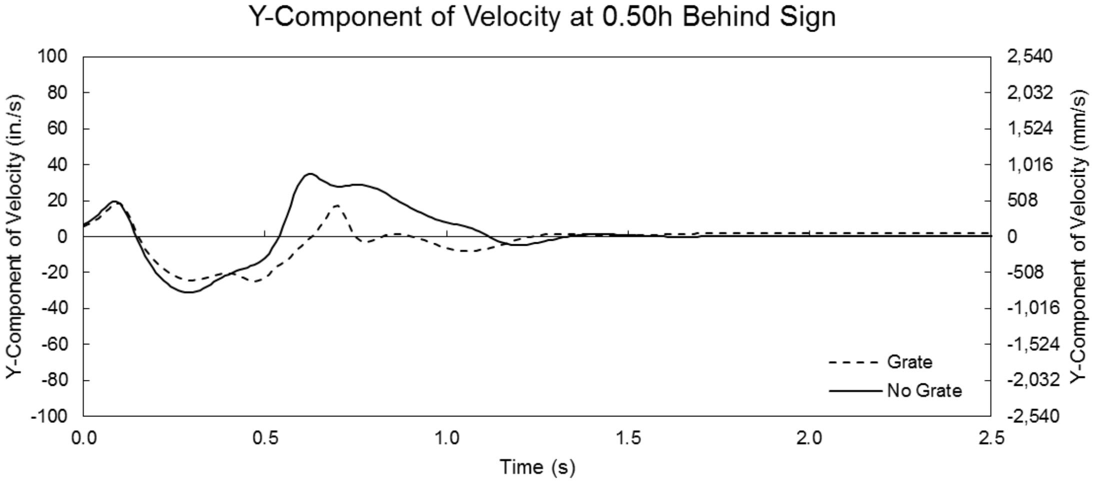

Figure 120 Y-component of velocity for the medium sign at V=105 mph (46.9 m/s) at a distance = 0.5h behind the sign

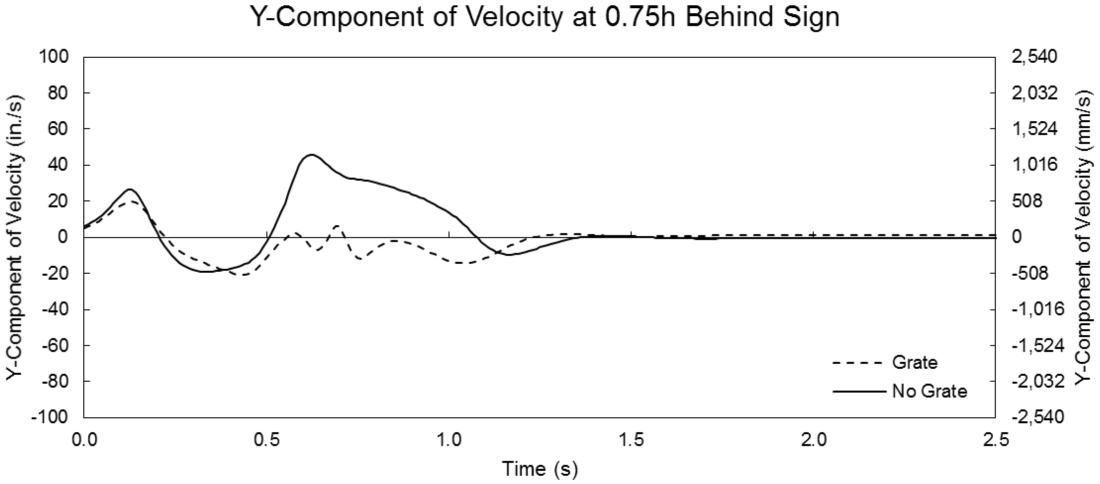

Figure 121 Y-component of velocity for the medium sign at V=105 mph (46.9 m/s) at a distance = 0.75h behind the sign

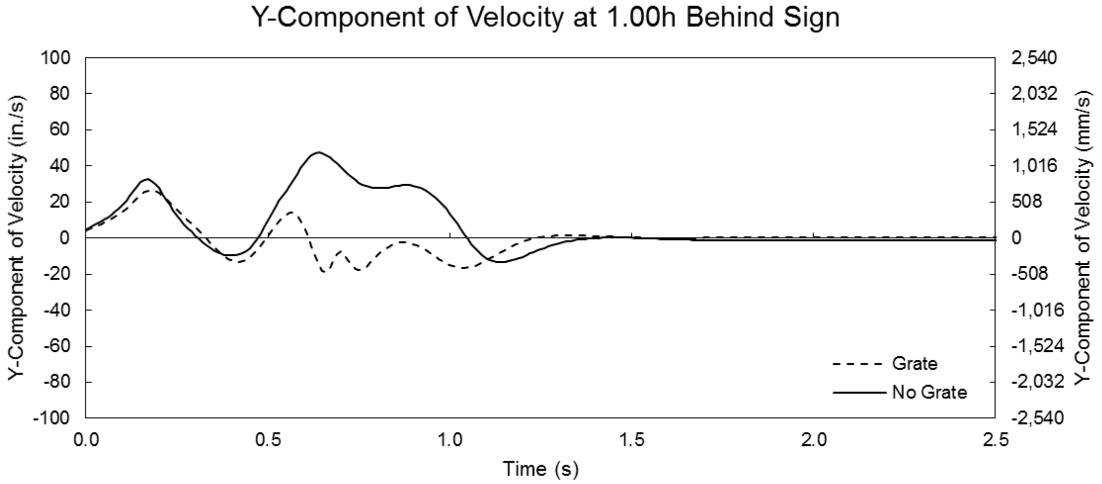

Figure 122 Y-component of velocity for the medium sign at V=105 mph (46.9 m/s) at a distance = 1.0h behind the sign

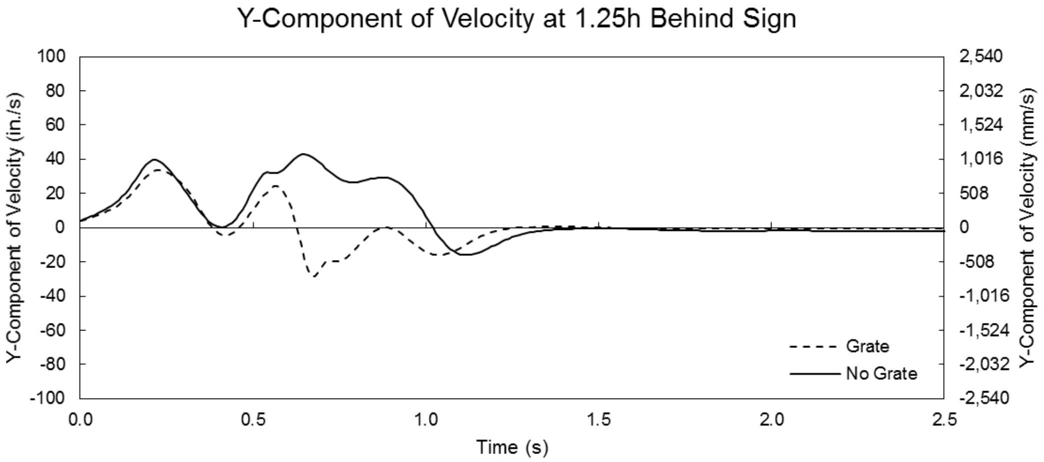

Figure 123 Y-component of velocity for the medium sign at V=105 mph (46.9 m/s) at a distance = 1.25h behind the sign

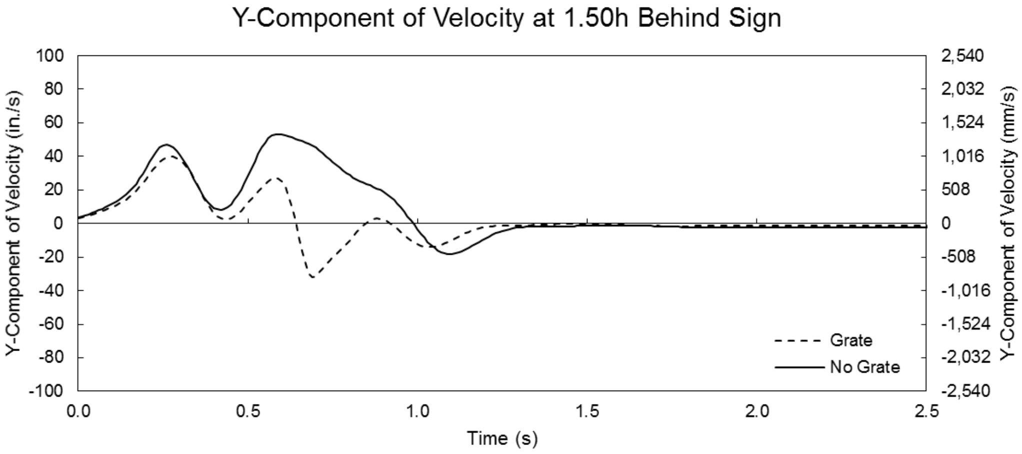

Figure 124 Y-component of velocity for the medium sign at V=105 mph (46.9 m/s) at a distance = 1.5h behind the sign

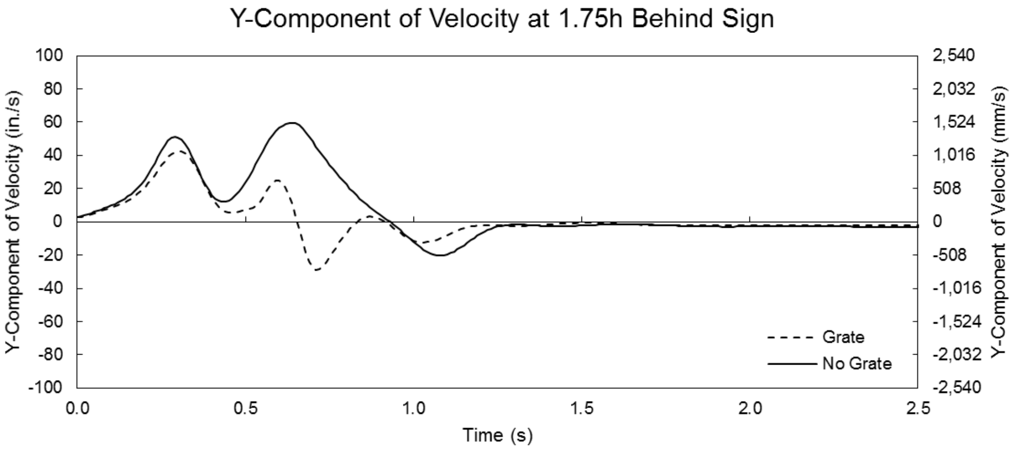

Figure 125 Y-component of velocity for the medium sign at V=105 mph (46.9 m/s) at a distance = 1.75h behind the sign

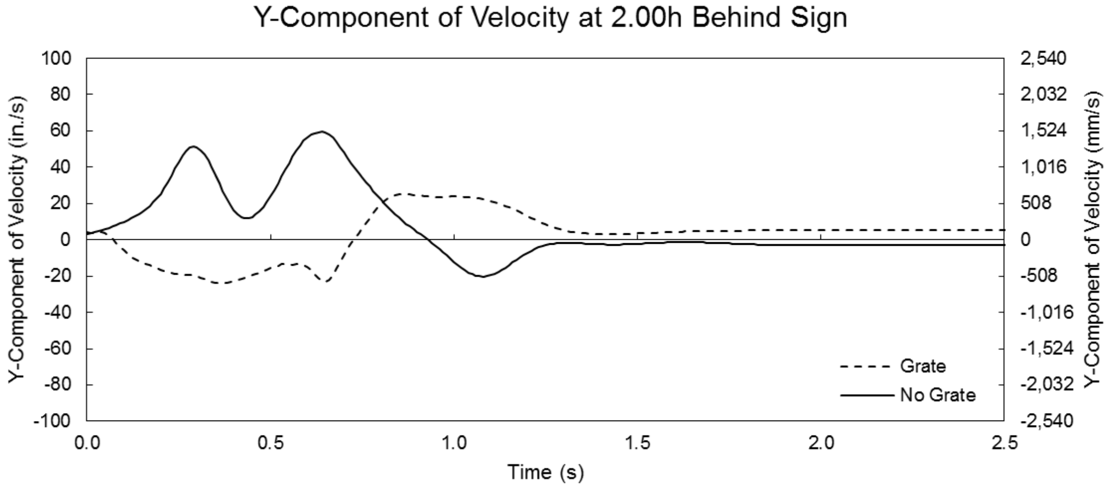

Figure 126 Y-component of velocity for the medium sign at V=105 mph (46.9 m/s) at a distance = 2.0h behind the sign

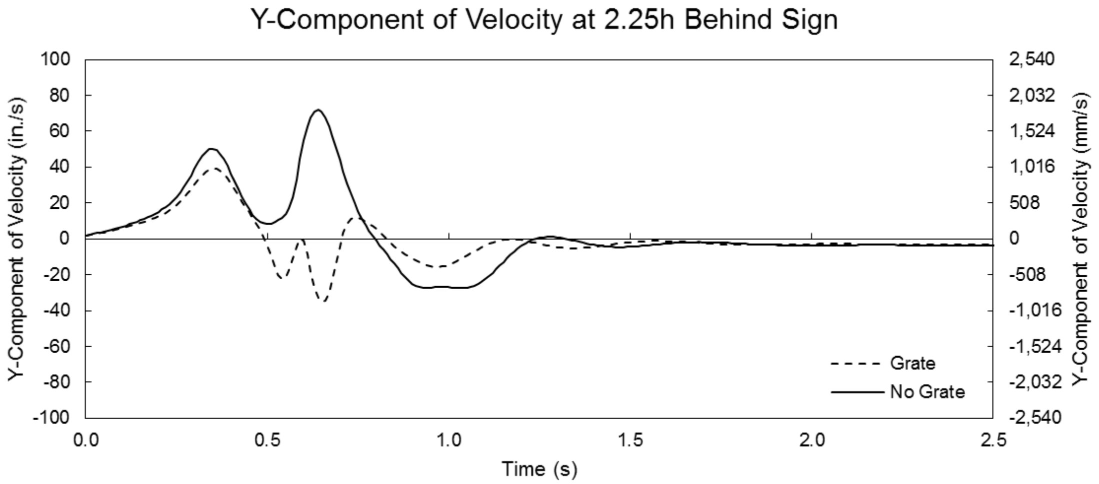

Figure 127 Y-component of velocity for the medium sign at V=105 mph (46.9 m/s) at a distance = 2.25h behind the sign

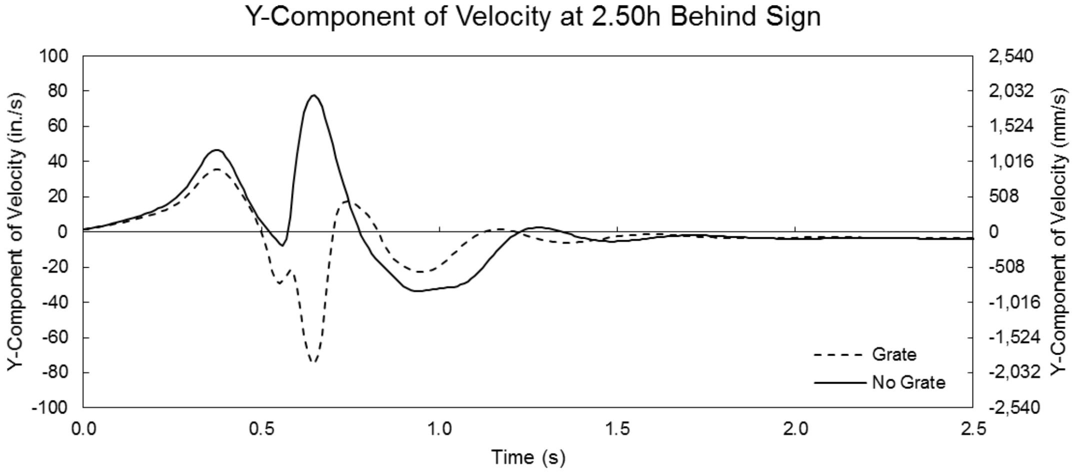

Figure 128 Y-component of velocity for the medium sign at V=105 mph (46.9 m/s) at a distance = 2.5h behind the sign

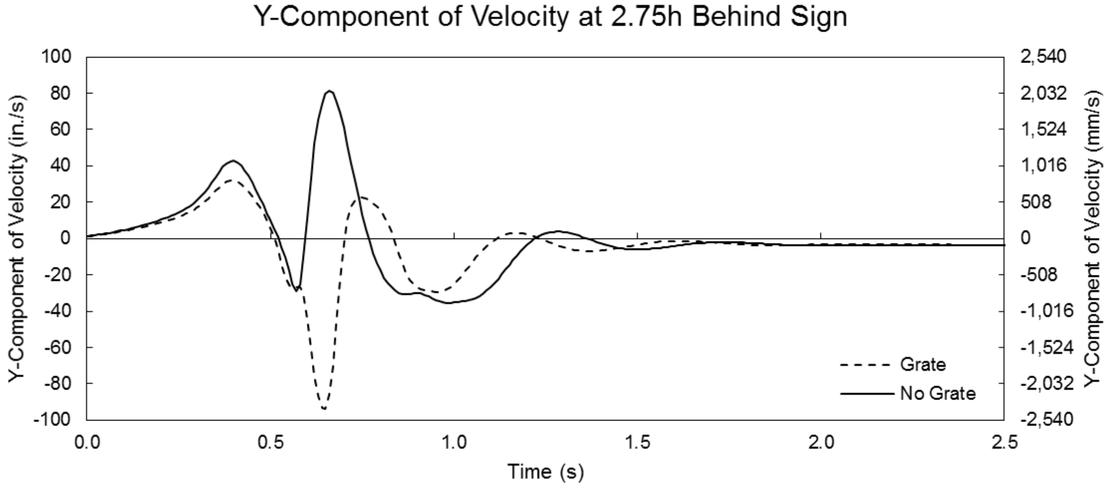

Figure 129 Y-component of velocity for the medium sign at V=105 mph (46.9 m/s) at a distance = 2.75h behind the sign

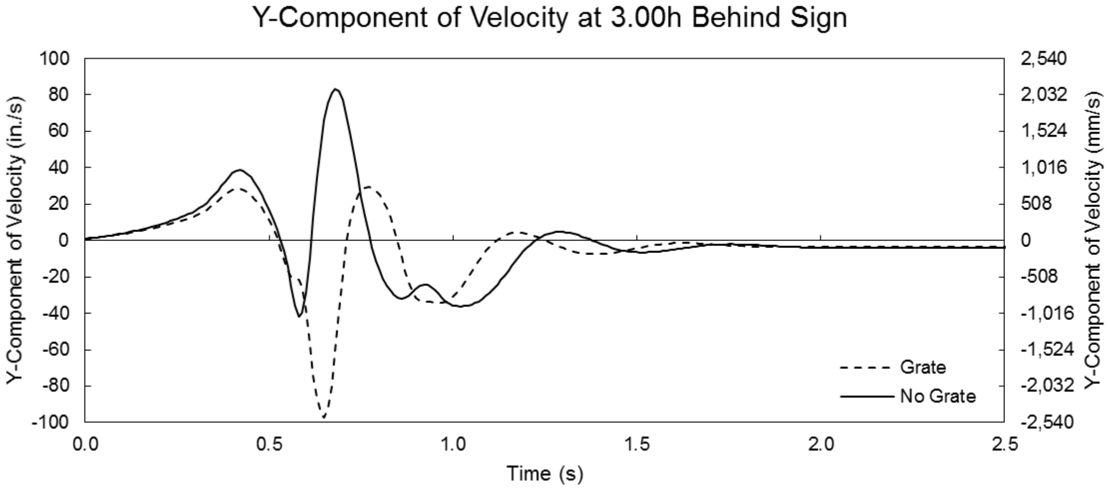

Figure 130 Y-component of velocity for the medium sign at V=105 mph (46.9 m/s) at a distance = 3.0h behind the sign

A1.7 – Y-Component of Velocity Behind Small Sign at V=30 mph (13.4 m/s)

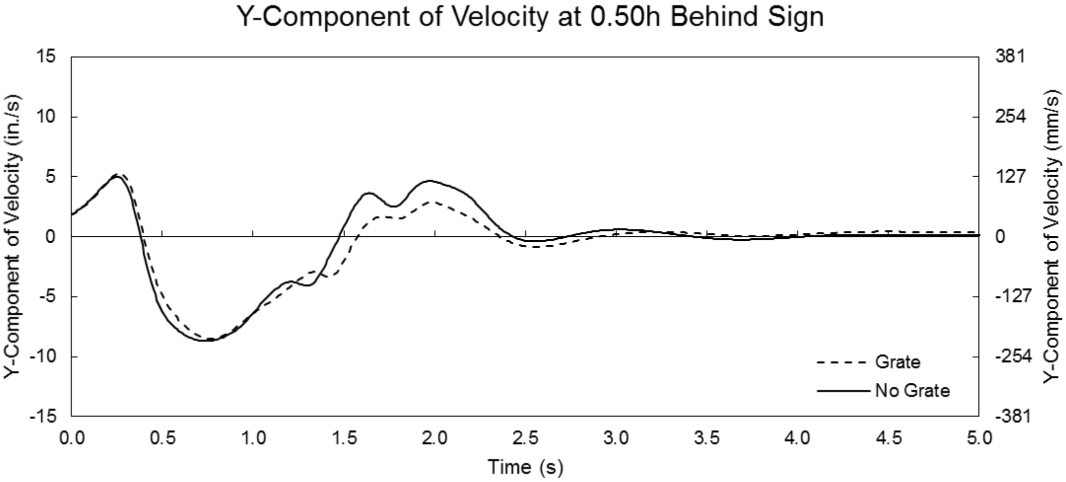

Figure 131 Y-component of velocity for the small sign at V=30 mph (13.4 m/s) at a distance = 0.5h behind the sign

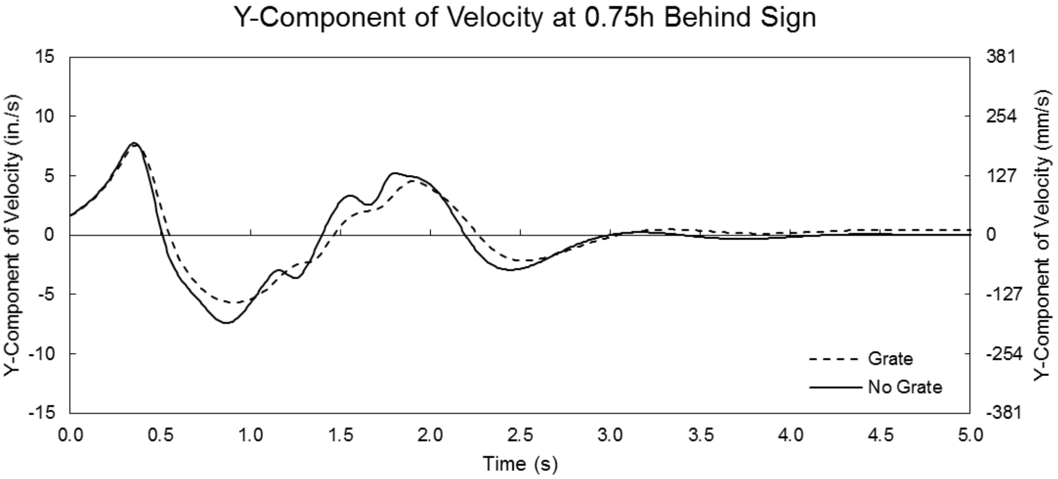

Figure 132 Y-component of velocity for the small sign at V=30 mph (13.4 m/s) at a distance = 0.75h behind the sign

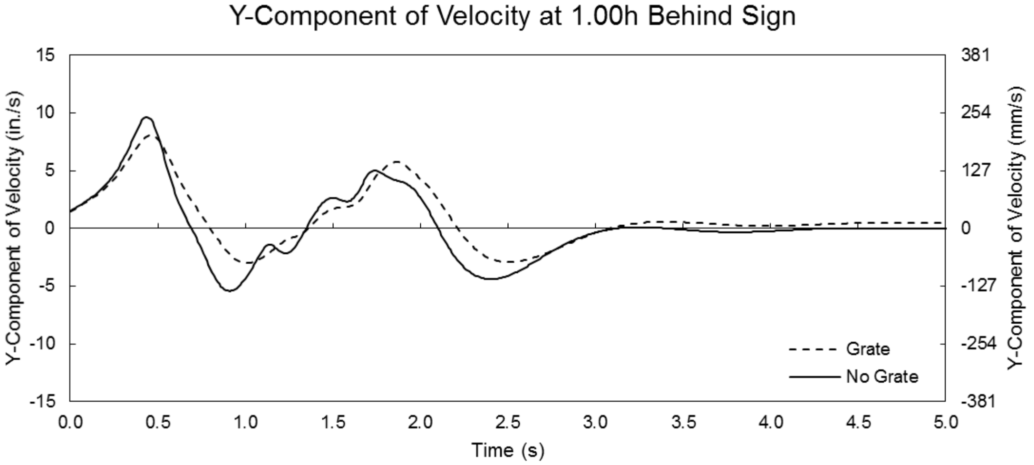

Figure 133 Y-component of velocity for the small sign at V=30 mph (13.4 m/s) at a distance = 1.0h behind the sign

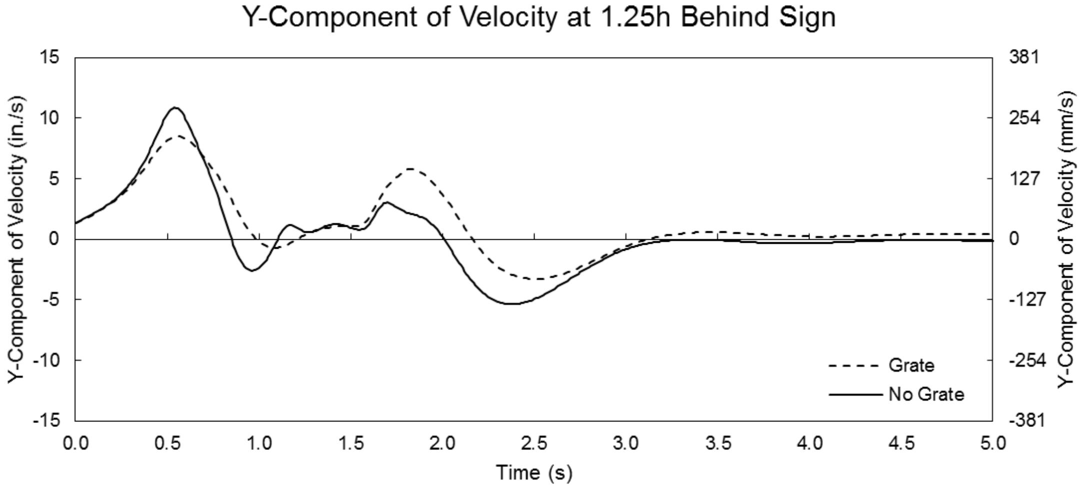

Figure 134 Y-component of velocity for the small sign at V=30 mph (13.4 m/s) at a distance = 1.25h behind the sign

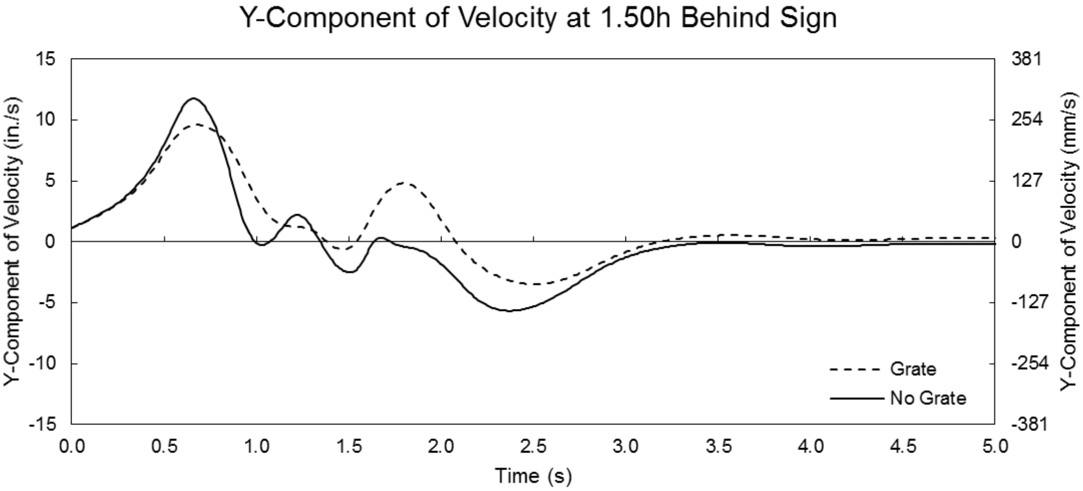

Figure 135 Y-component of velocity for the small sign at V=30 mph (13.4 m/s) at a distance = 1.5h behind the sign

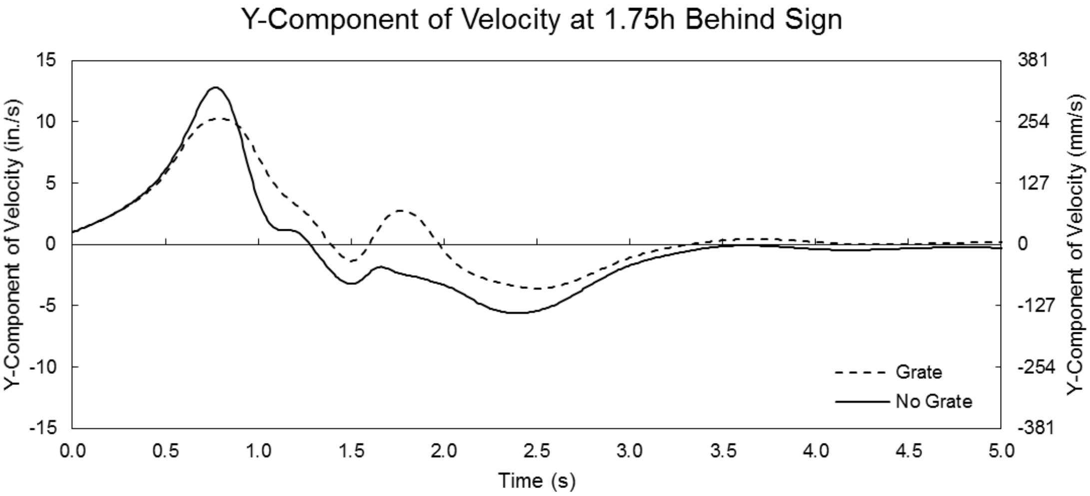

Figure 136 Y-component of velocity for the small sign at V=30 mph (13.4 m/s) at a distance = 1.75h behind the sign

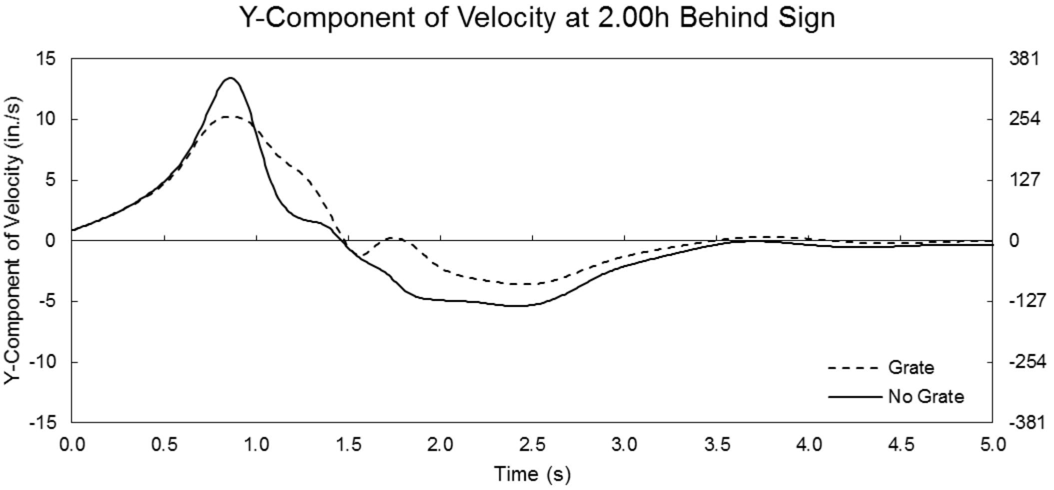

Figure 137 Y-component of velocity for the small sign at V=30 mph (13.4 m/s) at a distance = 2.0h behind the sign

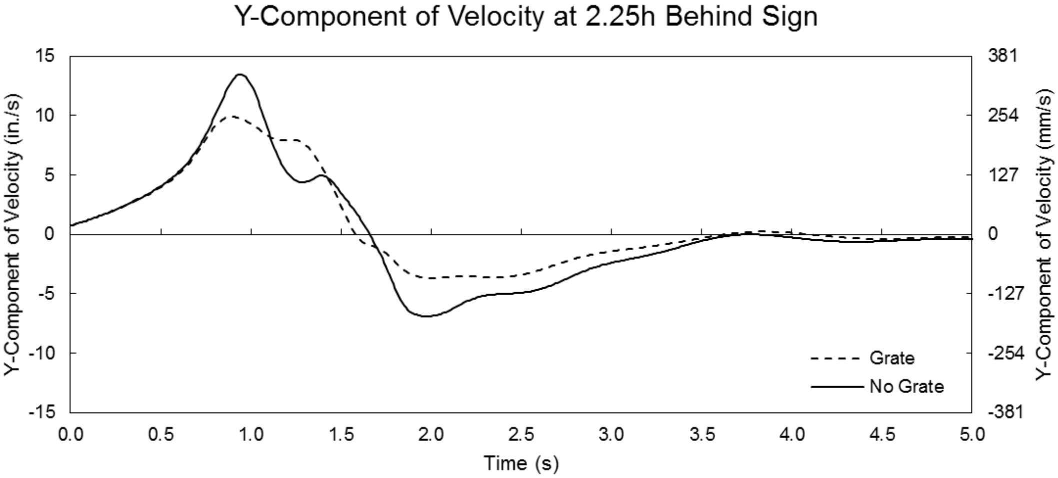

Figure 138 Y-component of velocity for the small sign at V=30 mph (13.4 m/s) at a distance = 2.25h behind the sign

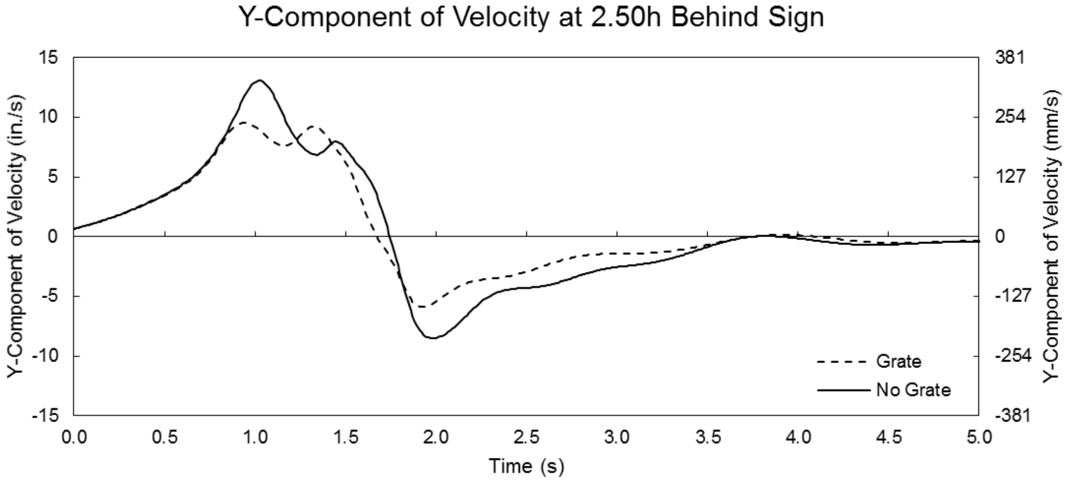

Figure 139 Y-component of velocity for the small sign at V=30 mph (13.4 m/s) at a distance = 2.5h behind the sign

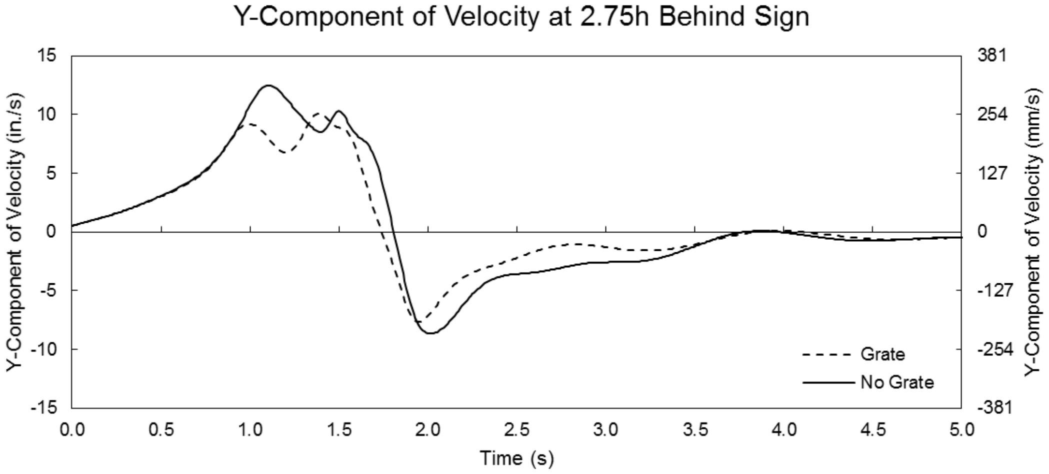

Figure 140 Y-component of velocity for the small sign at V=30 mph (13.4 m/s) at a distance = 2.75h behind the sign

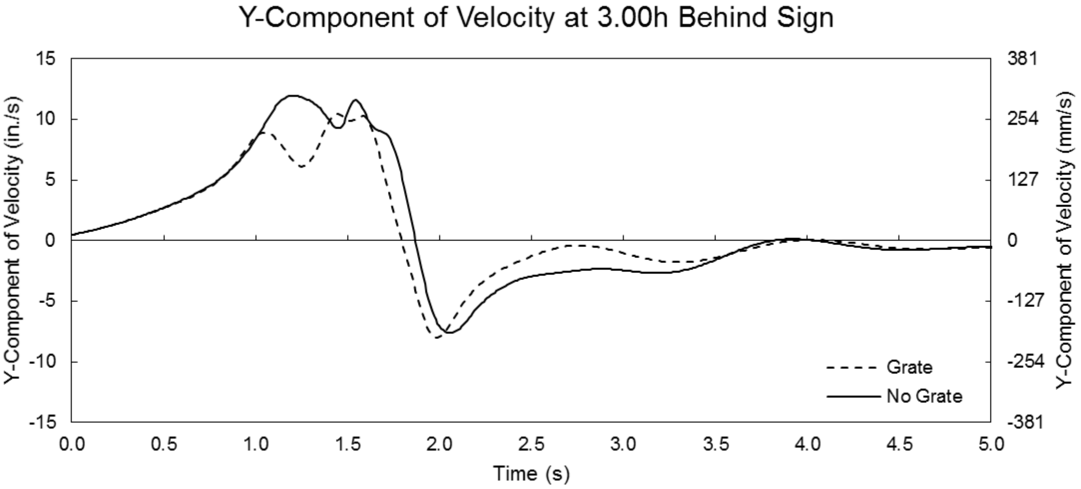

Figure 141 Y-component of velocity for the small sign at V=30 mph (13.4 m/s) at a distance = 3.0h behind the sign

A1.8 – Y-Component of Velocity Behind Small Sign at V=61.2 mph (27.4 m/s)

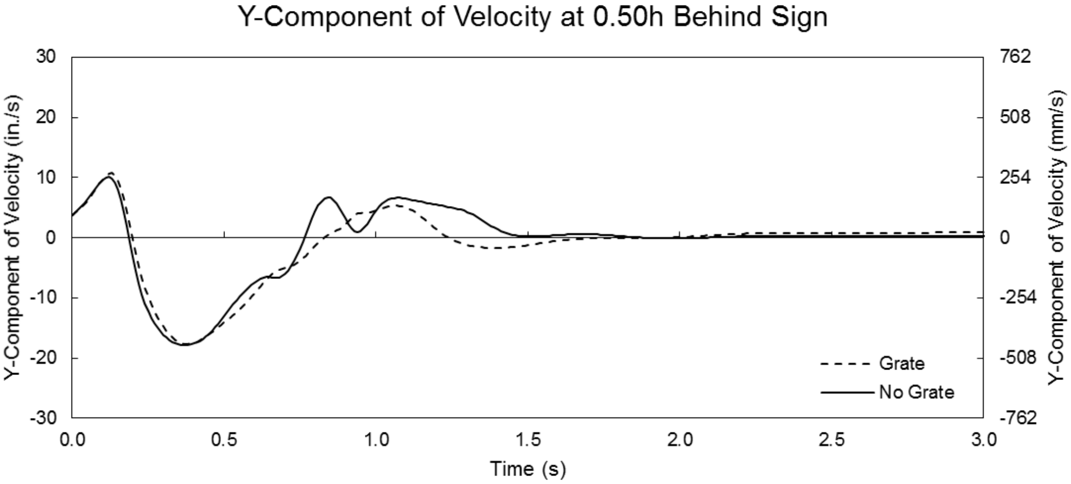

Figure 142 Y-component of velocity for the small sign at V=61.2 mph (27.4 m/s) at a distance = 0.5h behind the sign

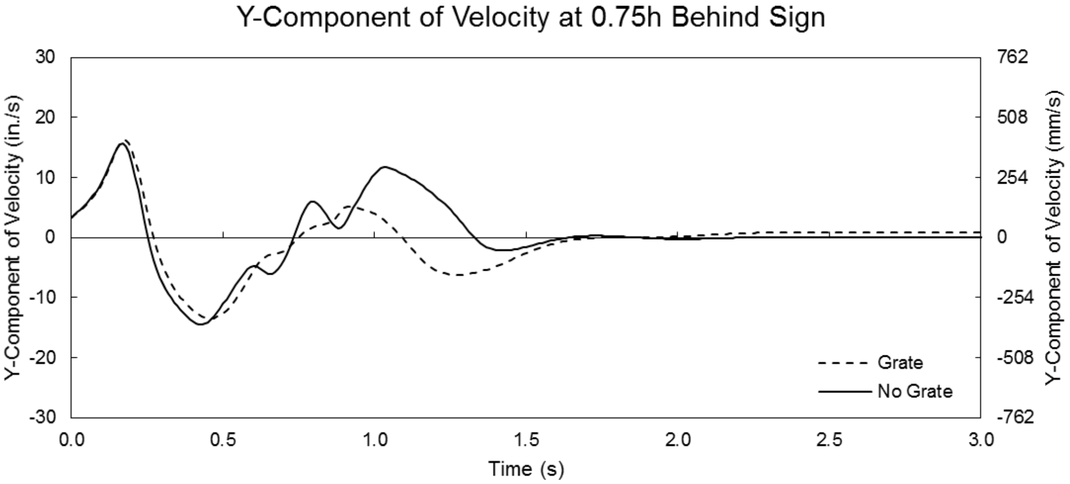

Figure 143 Y-component of velocity for the small sign at V=61.2 mph (27.4 m/s) at a distance = 0.75h behind the sign

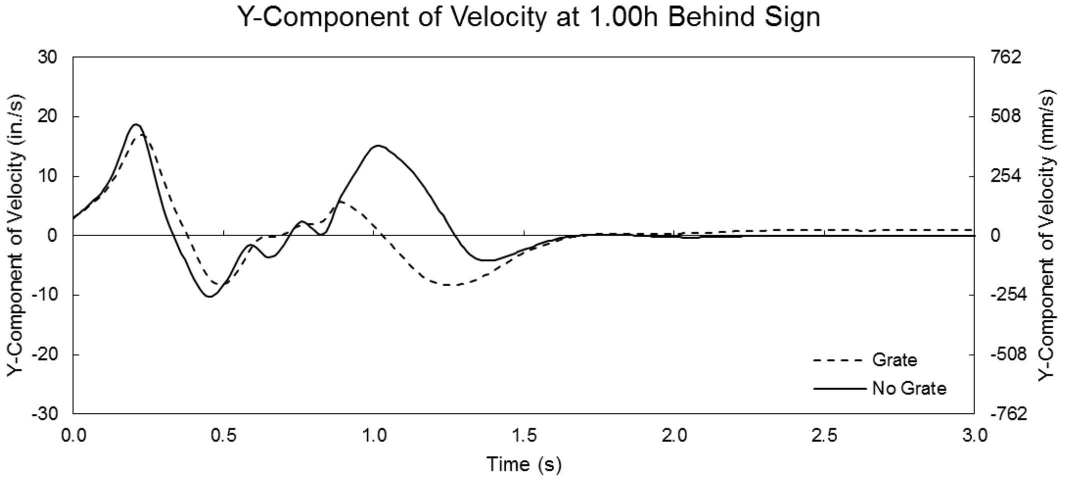

Figure 144 Y-component of velocity for the small sign at V=61.2 mph (27.4 m/s) at a distance = 1.0h behind the sign

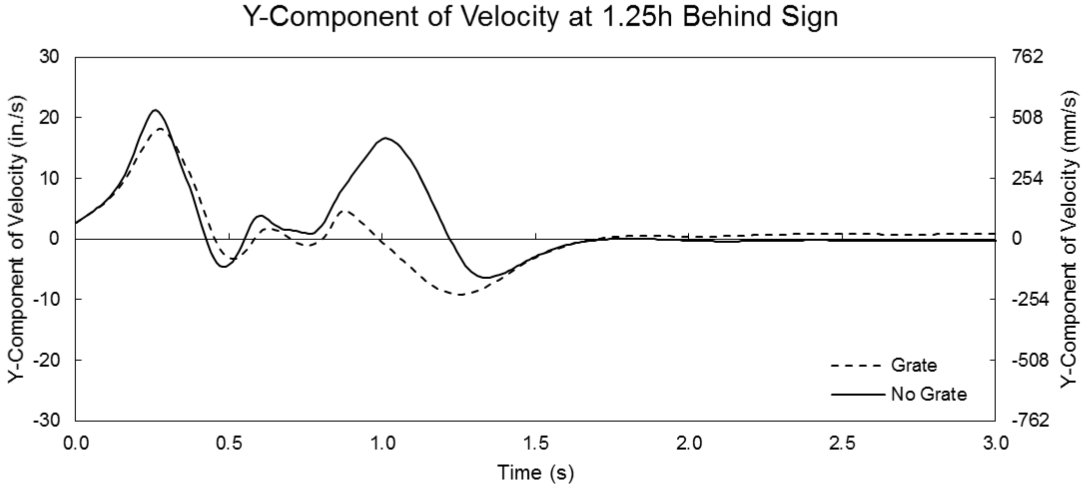

Figure 145 Y-component of velocity for the small sign at V=61.2 mph (27.4 m/s) at a distance = 1.25h behind the sign

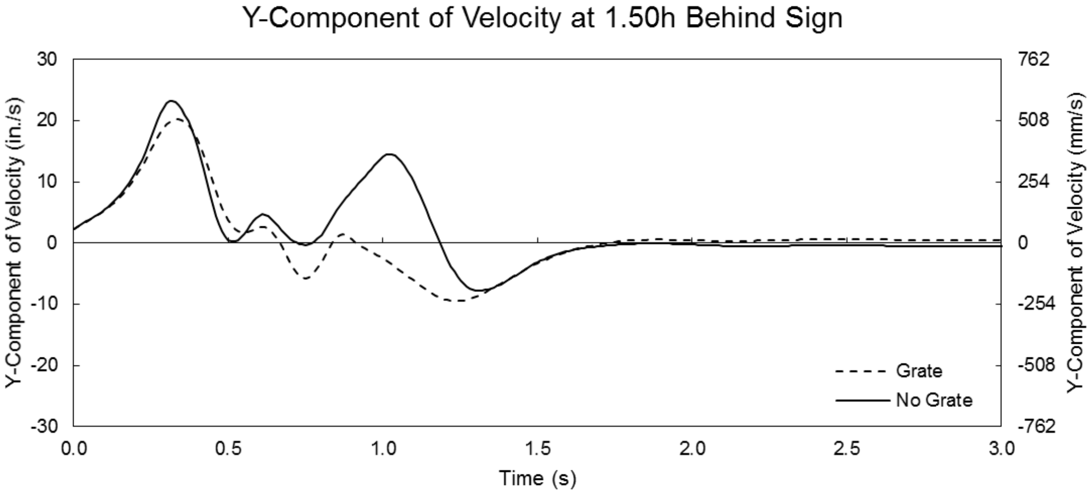

Figure 146 Y-component of velocity for the small sign at V=61.2 mph (27.4 m/s) at a distance = 1.5h behind the sign

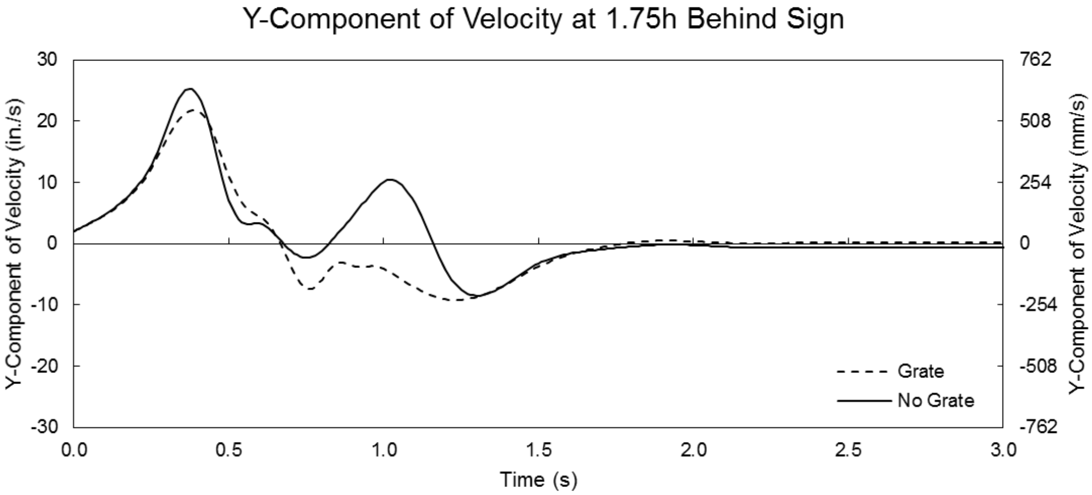

Figure 147 Y-component of velocity for the small sign at V=61.2 mph (27.4 m/s) at a distance = 1.75h behind the sign

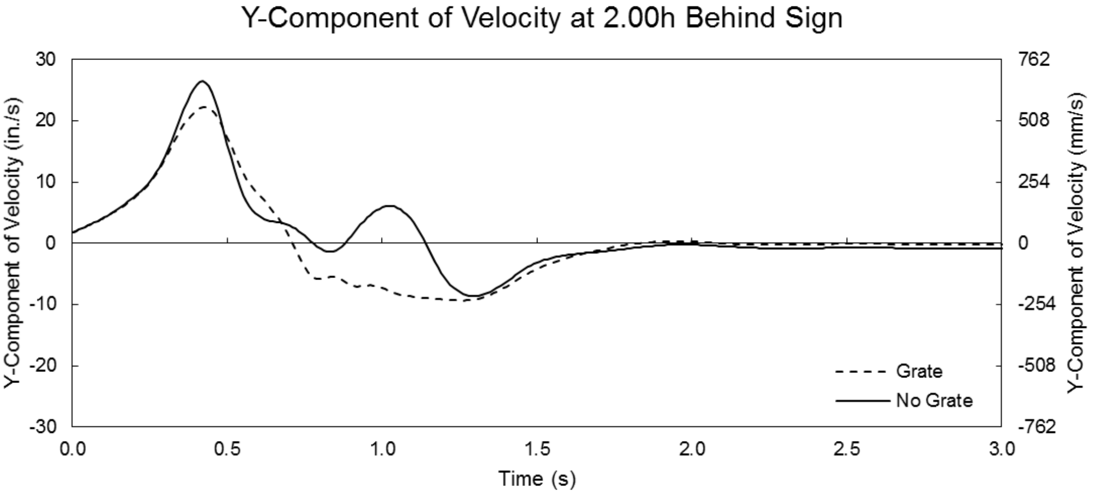

Figure 148 Y-component of velocity for the small sign at V=61.2 mph (27.4 m/s) at a distance = 2.0h behind the sign

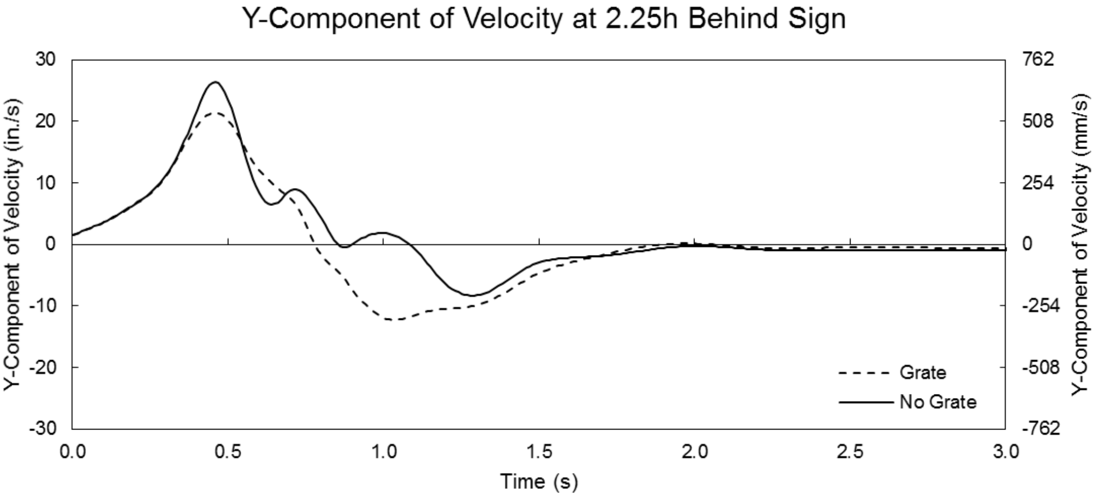

Figure 149 Y-component of velocity for the small sign at V=61.2 mph (27.4 m/s) at a distance = 2.25h behind the sign

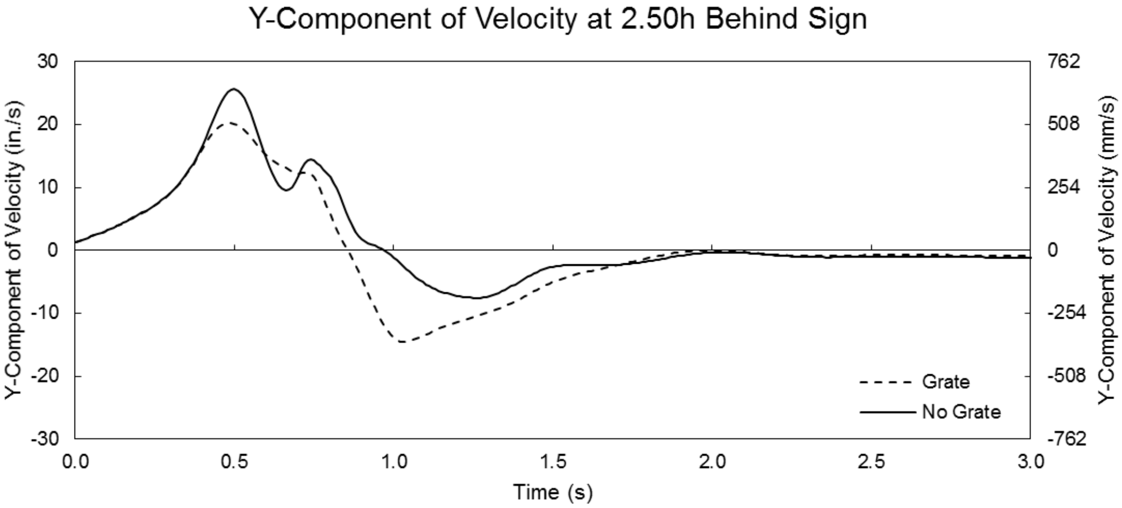

Figure 150 Y-component of velocity for the small sign at V=61.2 mph (27.4 m/s) at a distance = 2.5h behind the sign

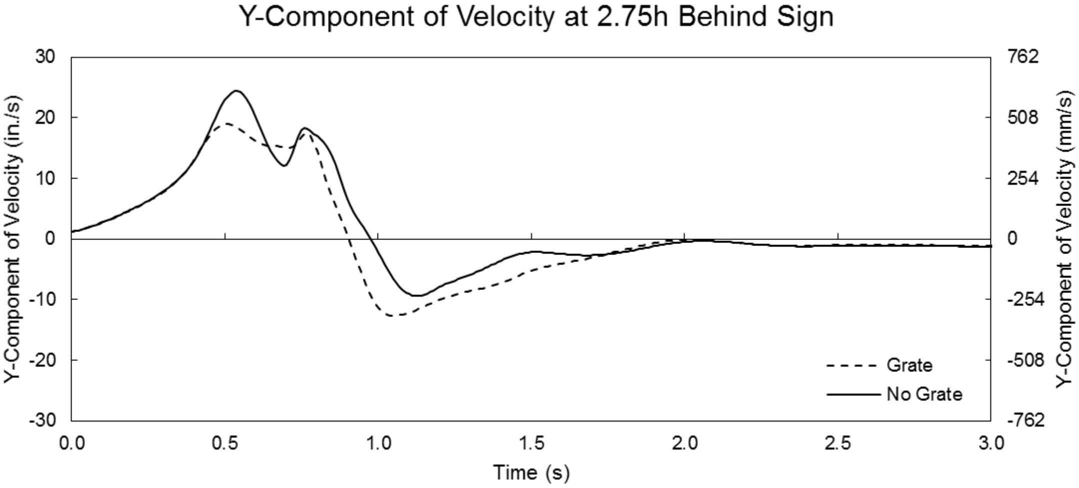

Figure 151 Y-component of velocity for the small sign at V=61.2 mph (27.4 m/s) at a distance = 2.75h behind the sign

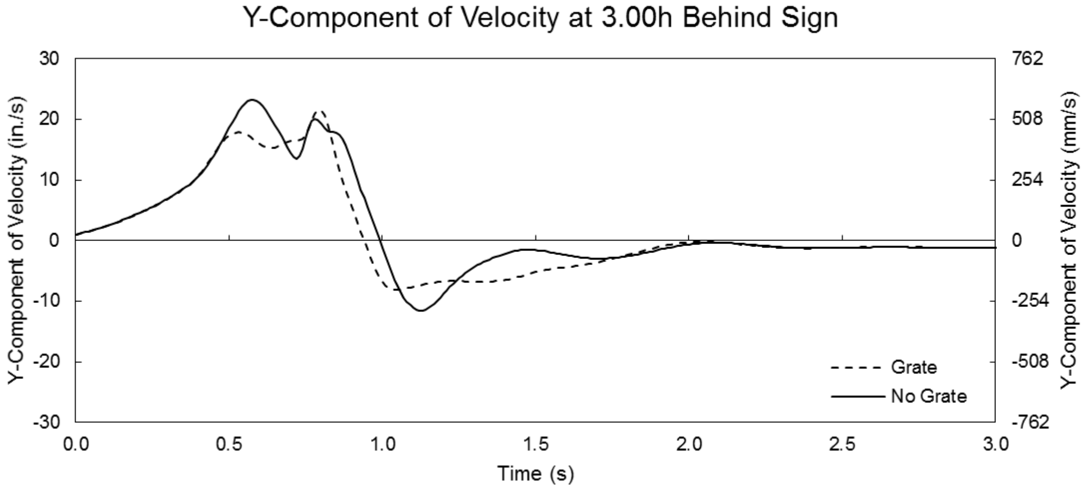

Figure 152 Y-component of velocity for the small sign at V=61.2 mph (27.4 m/s) at a distance = 3.0h behind the sign

A1.9 – Y-Component of Velocity Behind Small Sign at V=105mph (46.9 m/s)

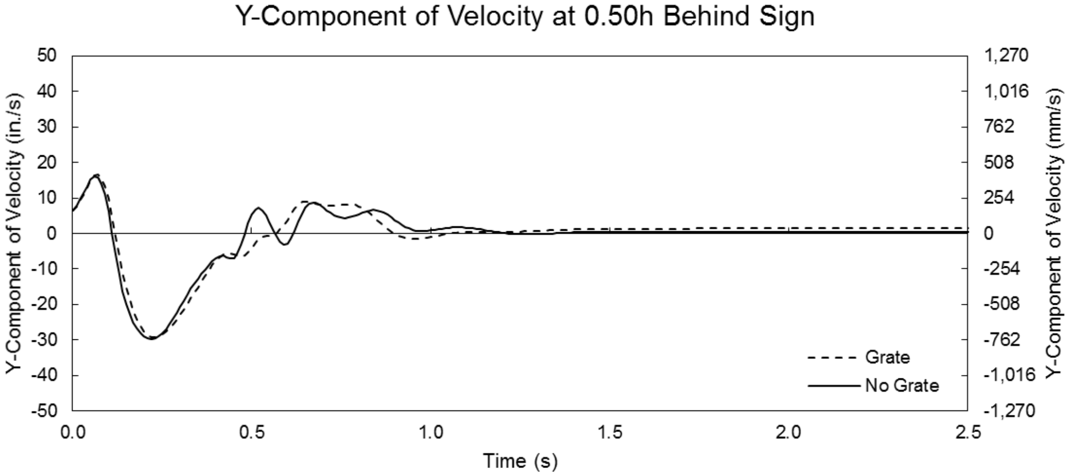

Figure 153 Y-component of velocity for the small sign at V=105 mph (46.9 m/s) at a distance = 0.5h behind the sign

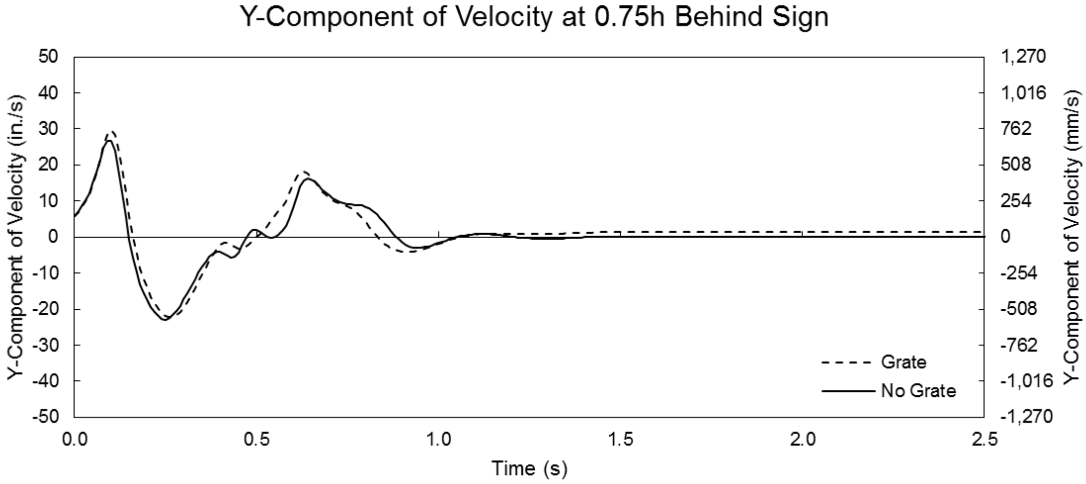

Figure 154 Y-component of velocity for the small sign at V=105 mph (46.9 m/s) at a distance = 0.75h behind the sign

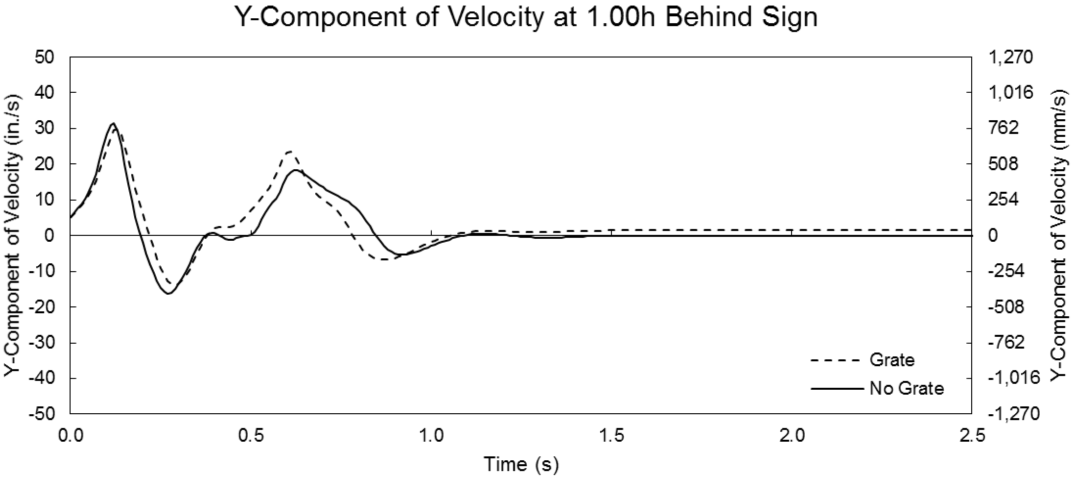

Figure 155 Y-component of velocity for the small sign at V=105 mph (46.9 m/s) at a distance = 1.0h behind the sign

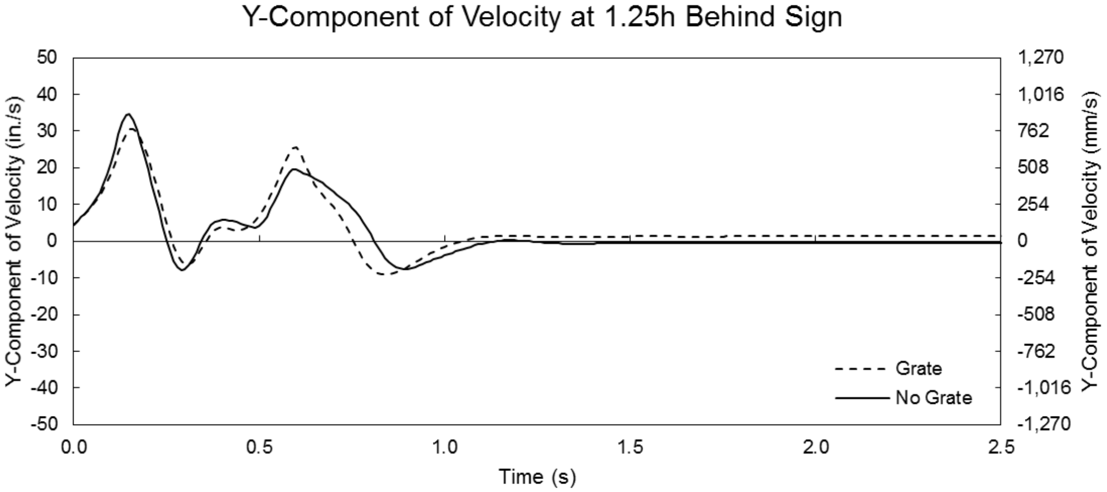

Figure 156 Y-component of velocity for the small sign at V=105 mph (46.9 m/s) at a distance = 1.25h behind the sign

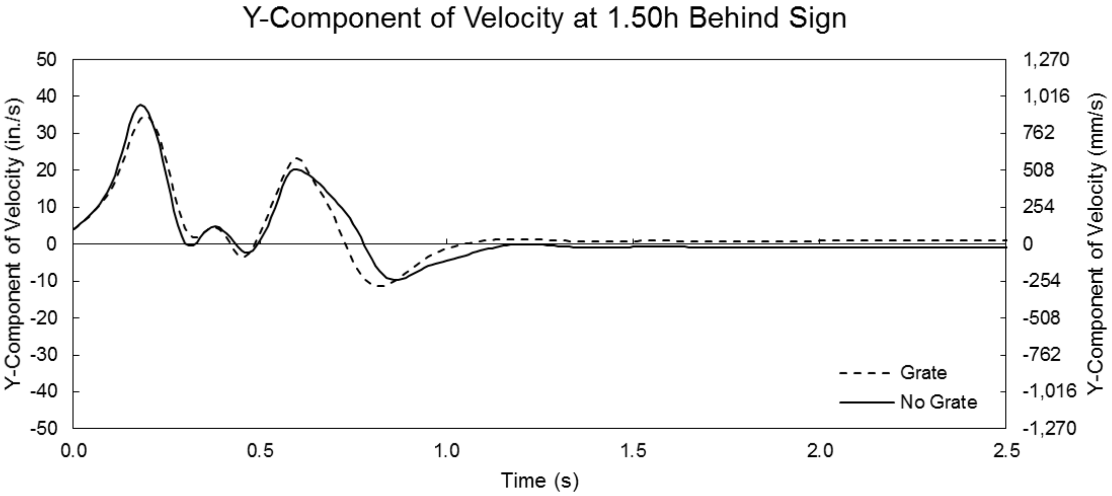

Figure 157 Y-component of velocity for the small sign at V=105 mph (46.9 m/s) at a distance = 1.5h behind the sign

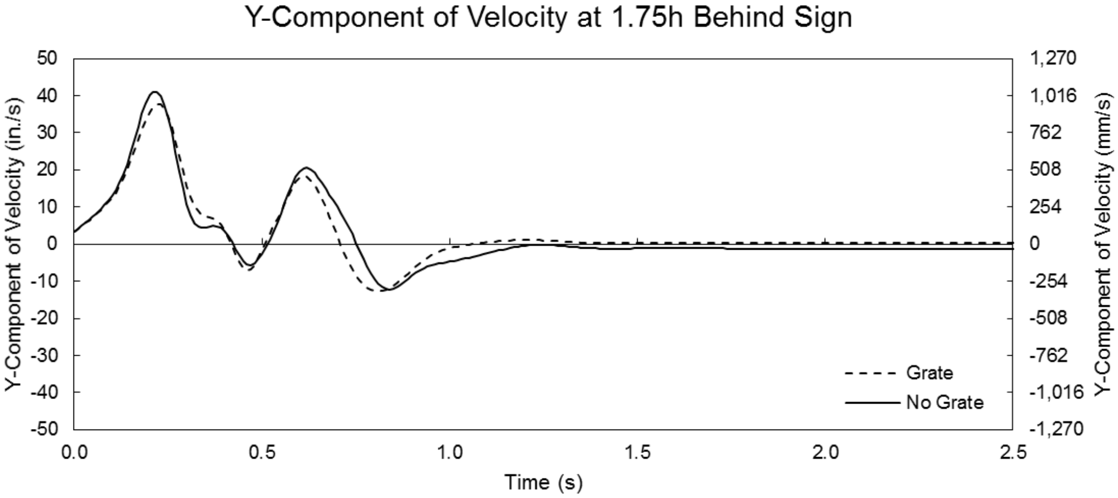

Figure 158 Y-component of velocity for the small sign at V=105 mph (46.9 m/s) at a distance = 1.75h behind the sign

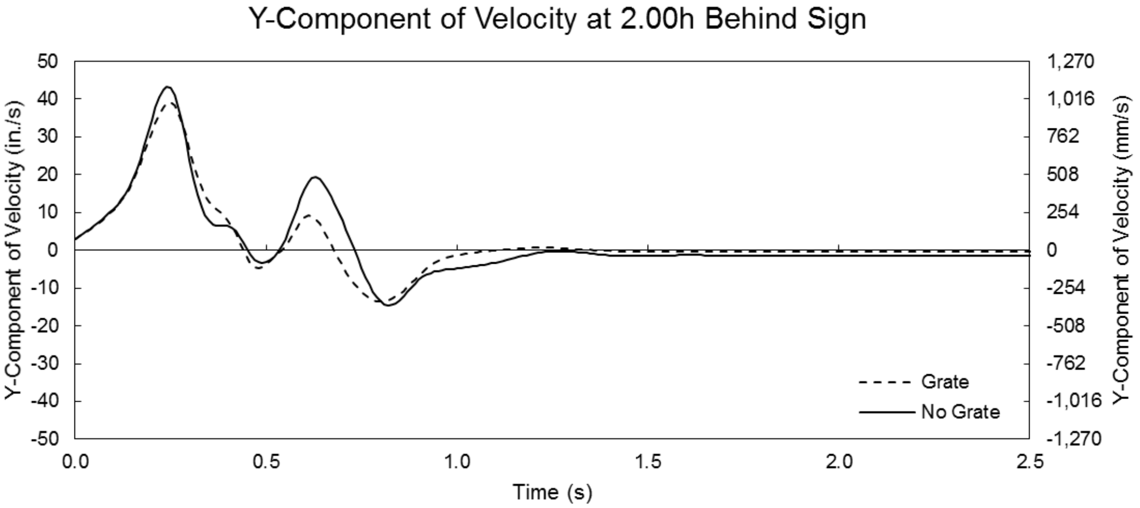

Figure 159 Y-component of velocity for the small sign at V=105 mph (46.9 m/s) at a distance = 2.0h behind the sign

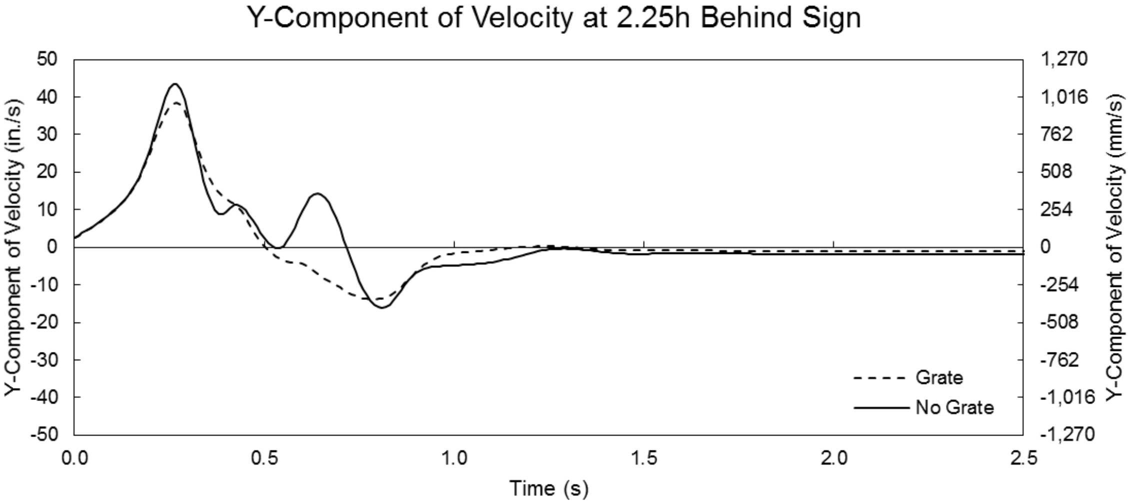

Figure 160 Y-component of velocity for the small sign at V=105 mph (46.9 m/s) at a distance = 2.25h behind the sign

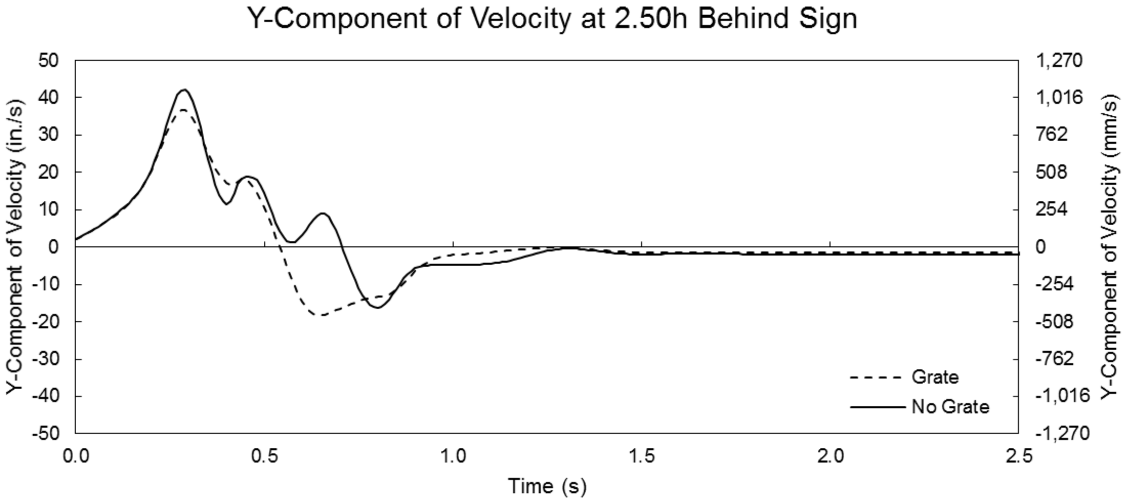

Figure 161 Y-component of velocity for the small sign at V=105 mph (46.9 m/s) at a distance = 2.5h behind the sign

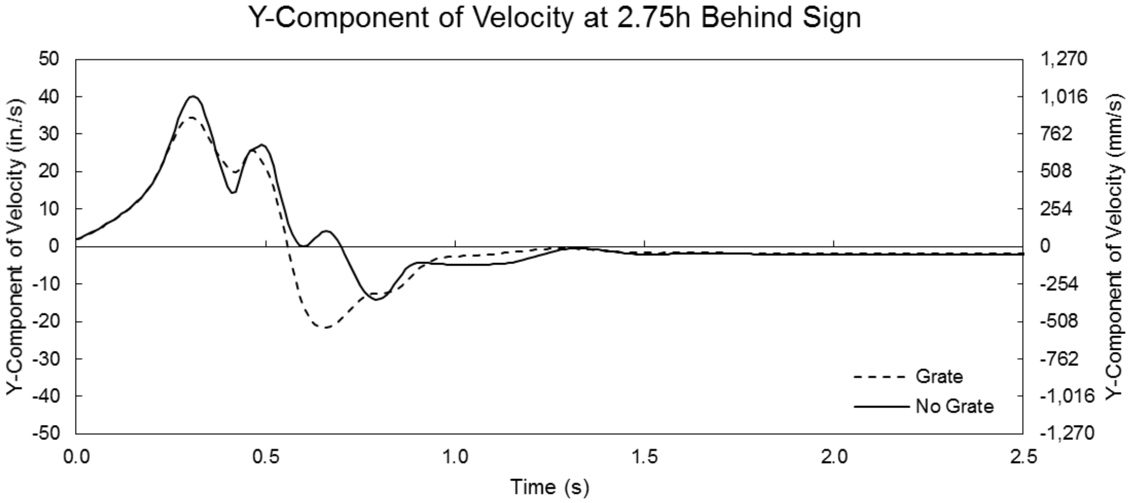

Figure 162 Y-component of velocity for the small sign at V=105 mph (46.9 m/s) at a distance = 2.75h behind the sign

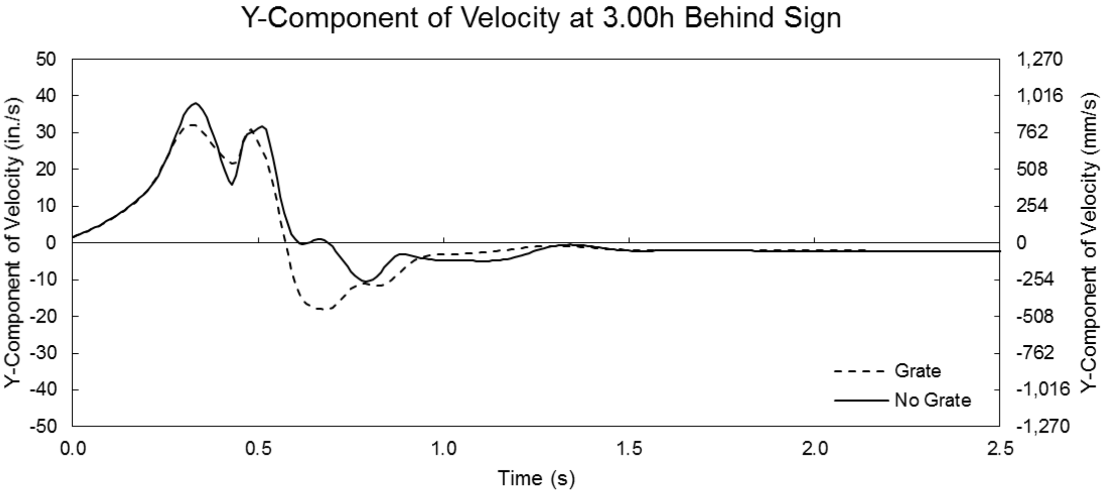

Figure 163 Y-component of velocity for the small sign at V=105 mph (46.9 m/s) at a distance = 3.0h behind the sign

APPENDIX A2

A2.1 – Large Sign Velocity Profile at V=30 mph (13.4 m/s)

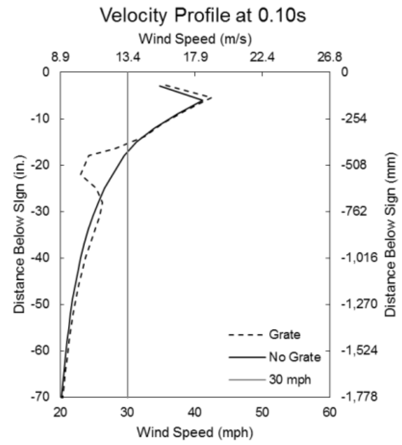

(a)

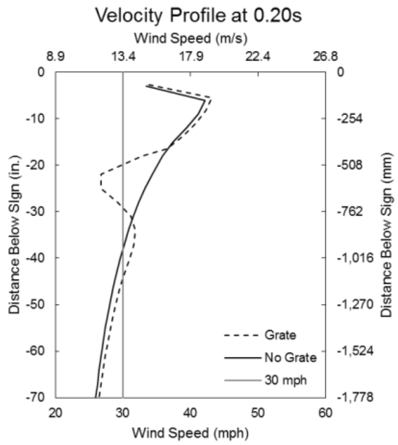

(b)

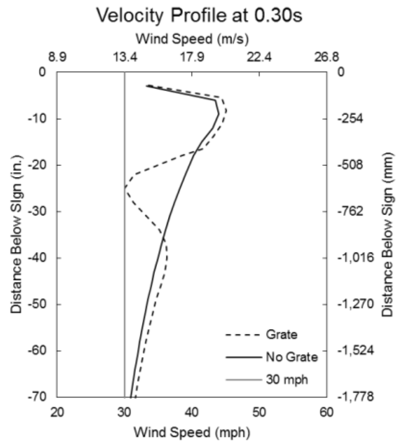

(c)

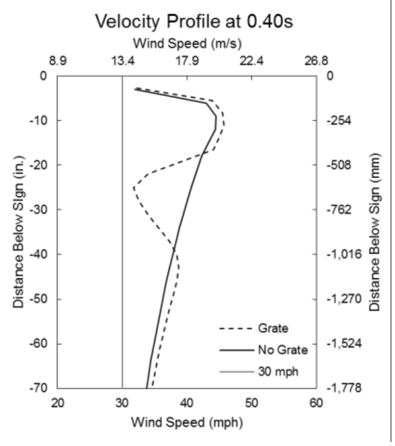

(d)

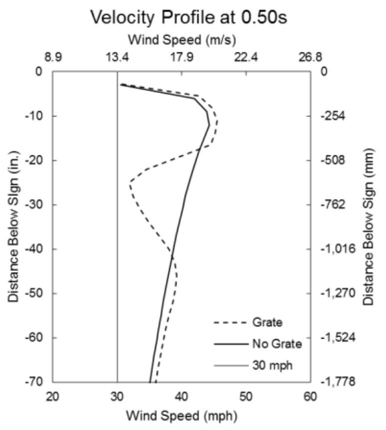

(e)

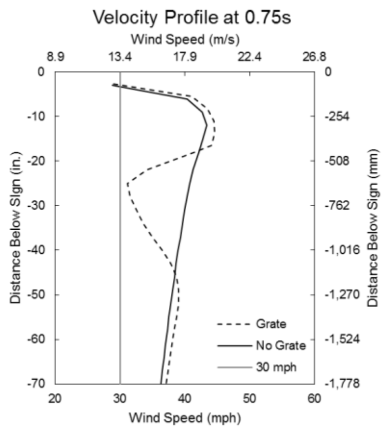

(f)

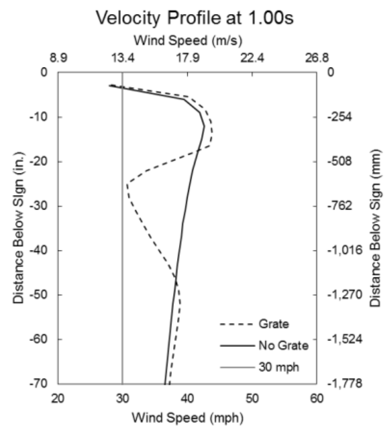

(g)

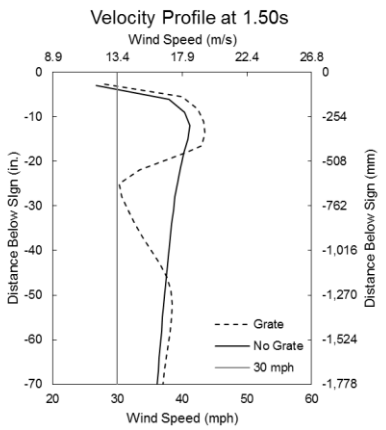

(h)

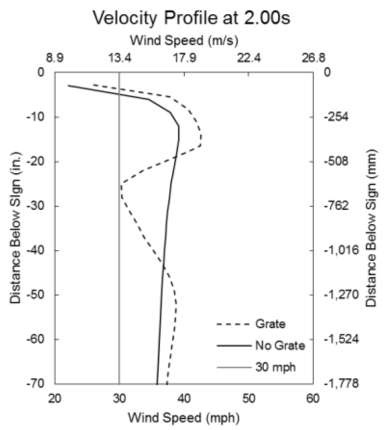

(i)

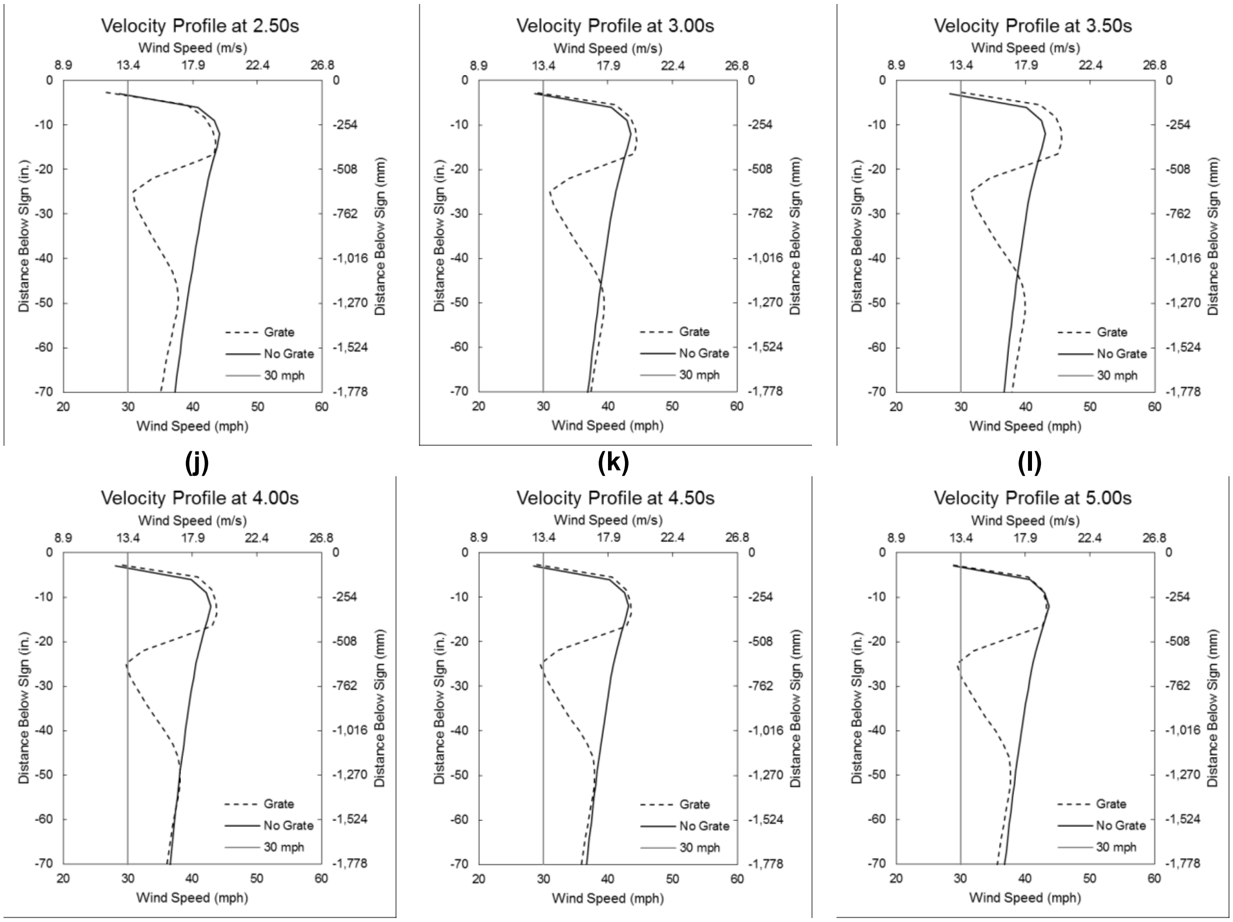

Velocity Profile at 2.50s

Velocity Profile at 3.00s

Velocity Profile at 3.50s

Velocity Profile at 4.00s

Velocity Profile at 4.50s

Velocity Profile at 5.00s

(j) (k) (l)

(m) (n) (o)

Figure 164 Velocity profile below the sign, for the large sign and a wind speed of V=30 mph (13.4 m/s)

A2.2 – Large Sign Velocity Profile at V=61.2 mph (27.4 m/s)

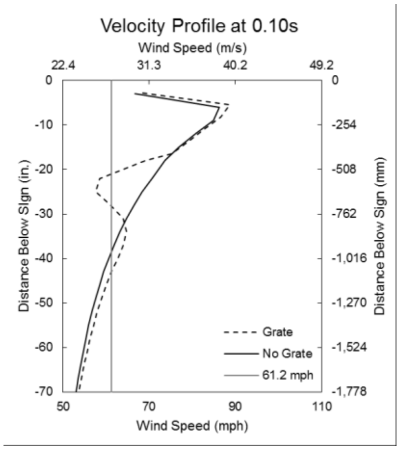

(a)

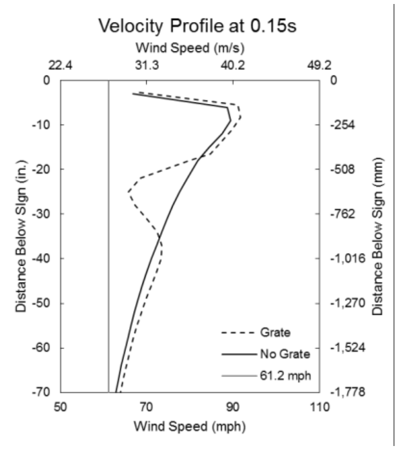

(b)

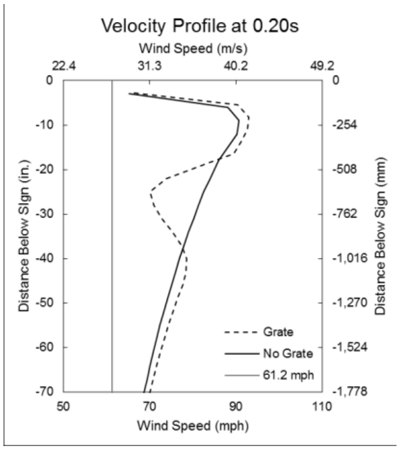

(c)

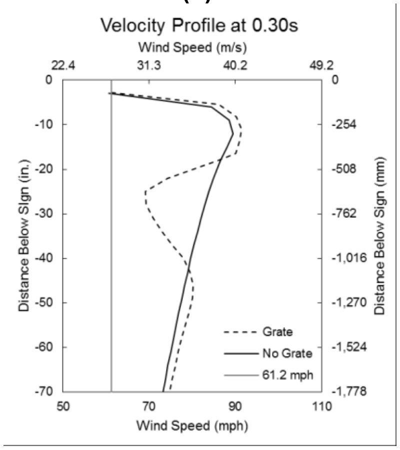

(d)

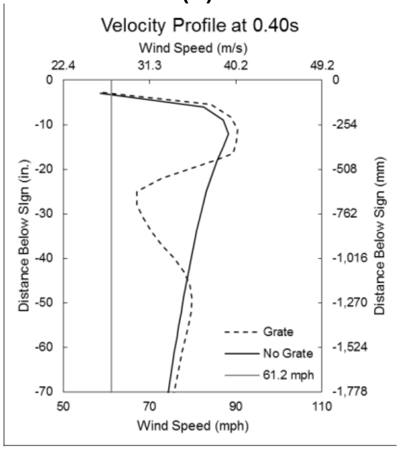

(e)

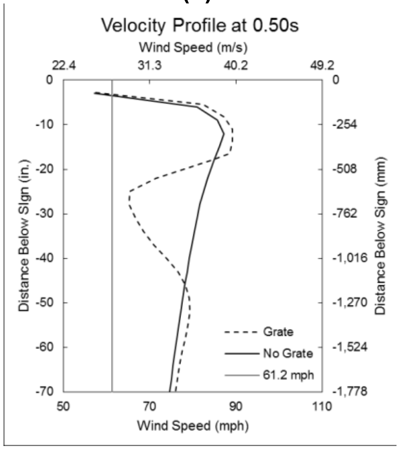

(f)

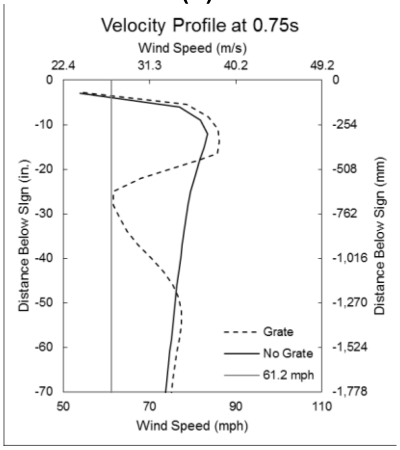

(g)

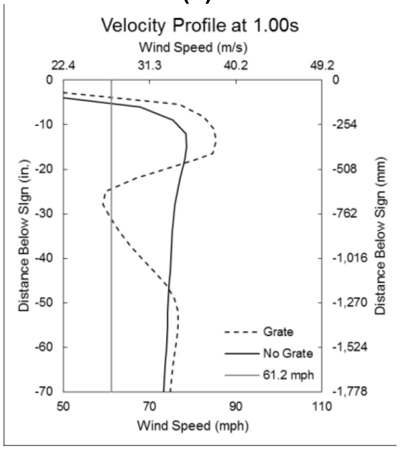

(h)

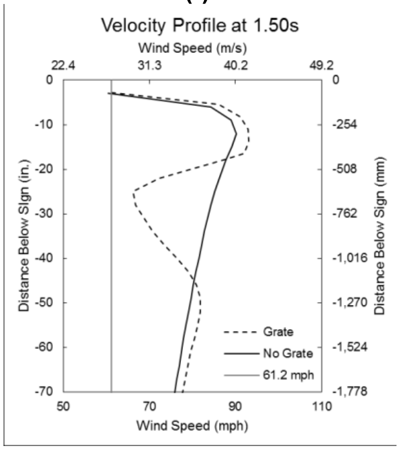

(i)

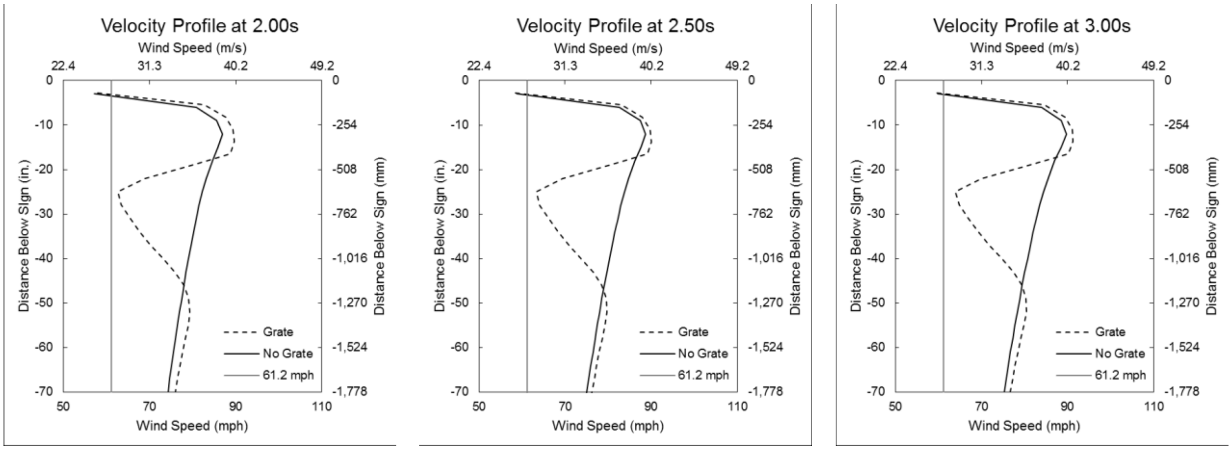

(j) (k) (l)

Figure 165 Velocity profile below the sign, for the large sign and a wind speed of V=61.2 mph (27.4 m/s)

A2.3 – Large Sign Velocity Profile at V=105mph (46.9 m/s)

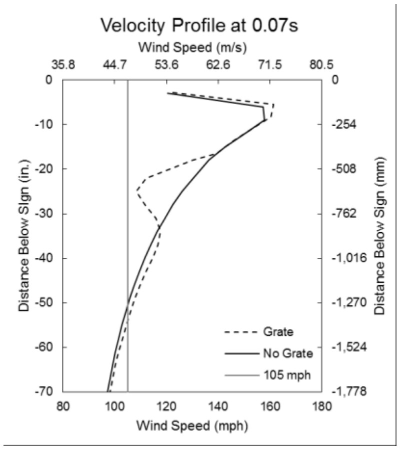

(a)

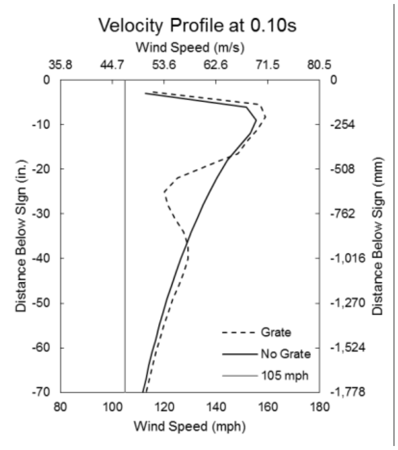

(b)

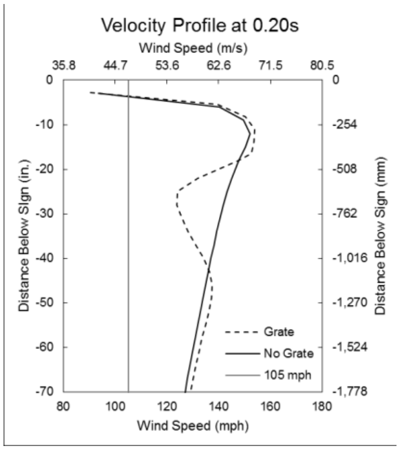

(c)

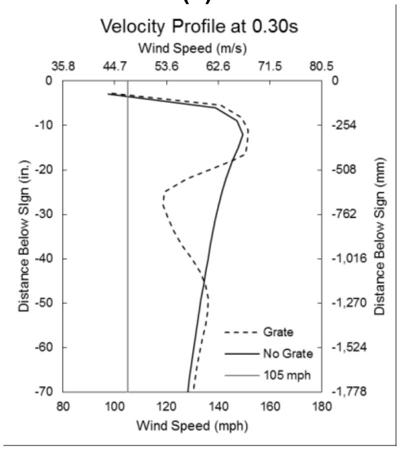

(d)

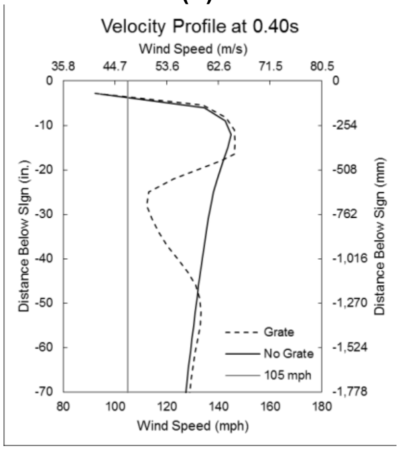

(e)

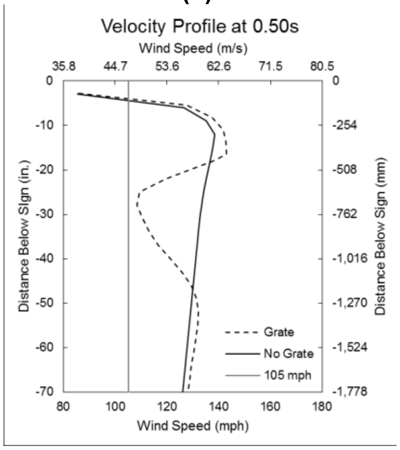

(f)

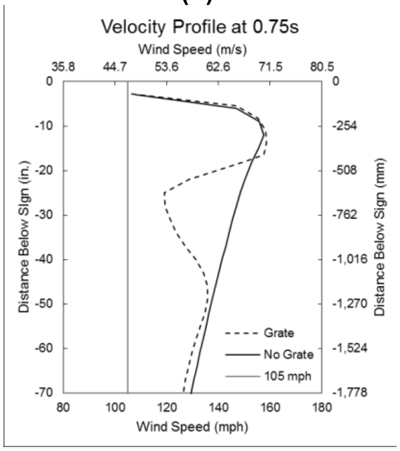

(g)

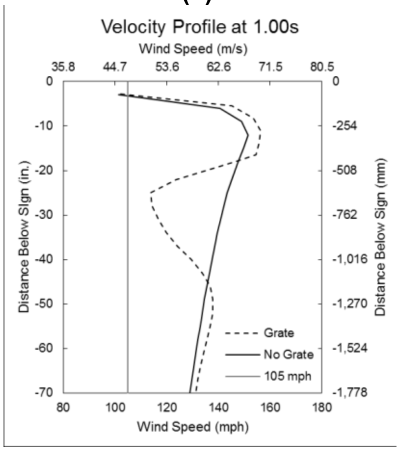

(h)

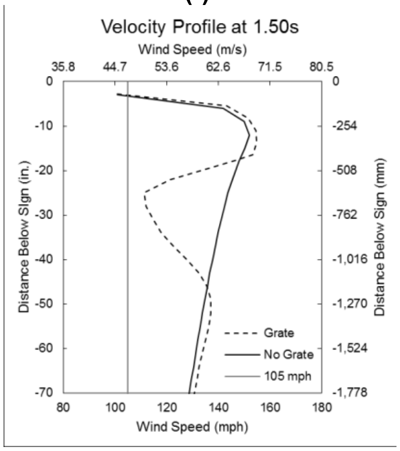

(i)

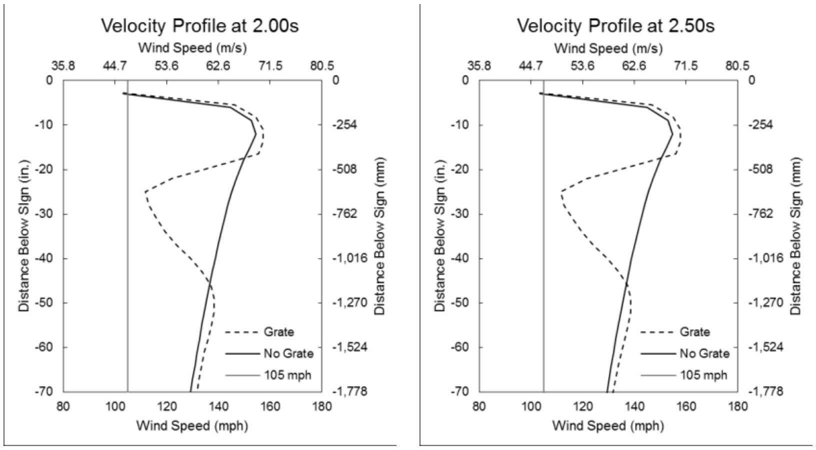

(j) **(k)** **(l)**

Figure 166 Velocity profile below the sign, for the large sign and a wind speed of V=105 mph (46.9 m/s)

A2.4 – Medium Sign Velocity Profile at V=30 mph (13.4 m/s)

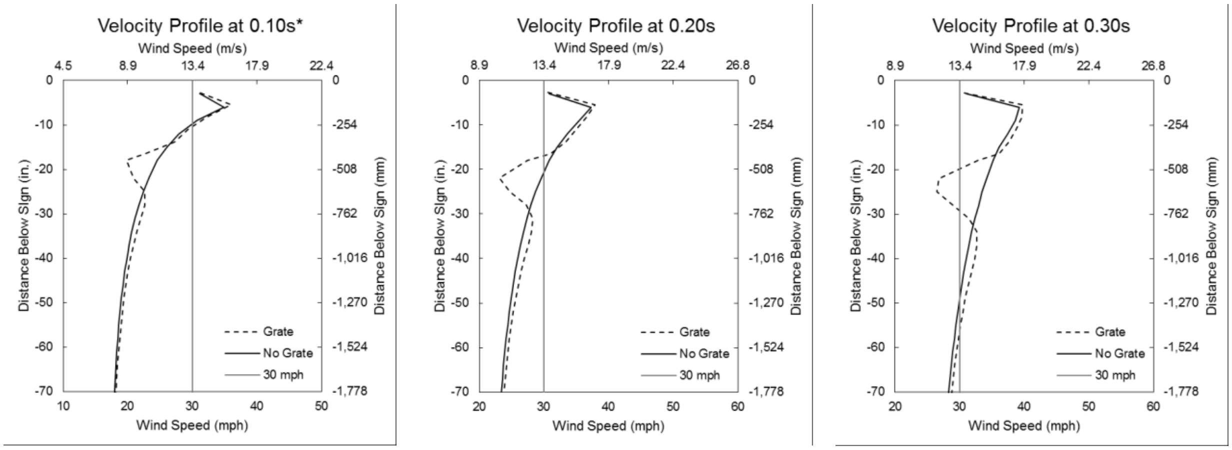

*Wind speed scales are different from the rest of the batch.

(a) **(b)** **(c)**

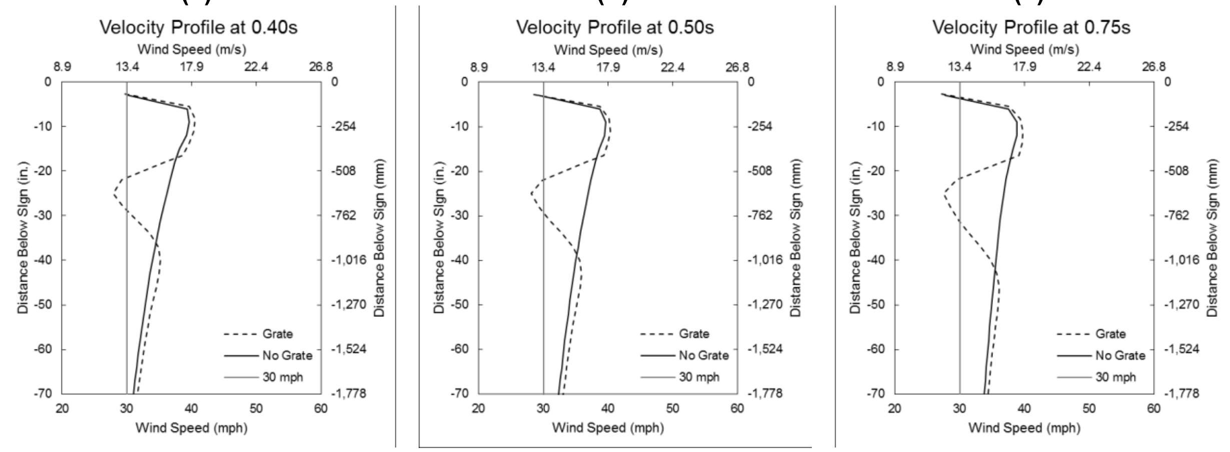

(d) **(e)** **(f)**

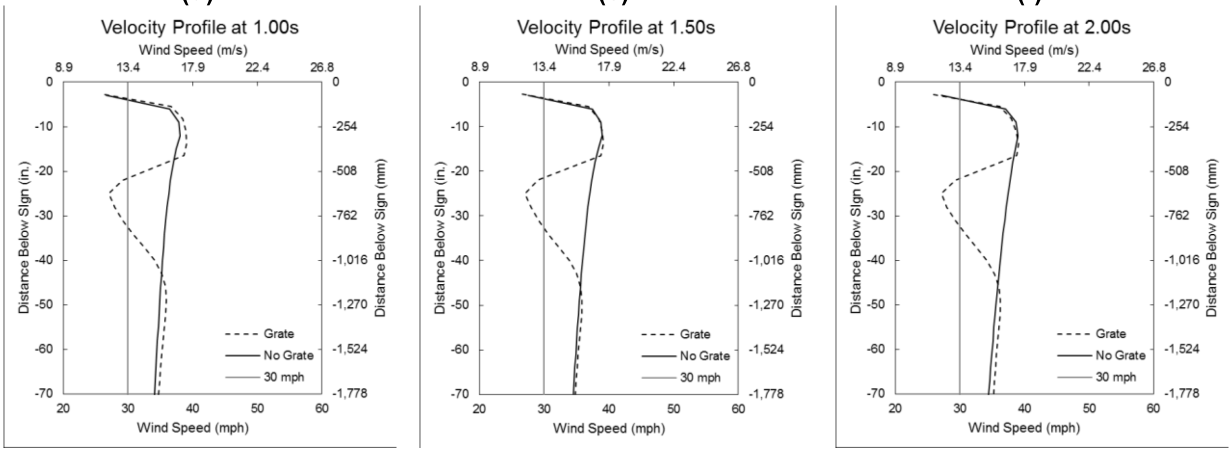

(g) **(h)** **(i)**

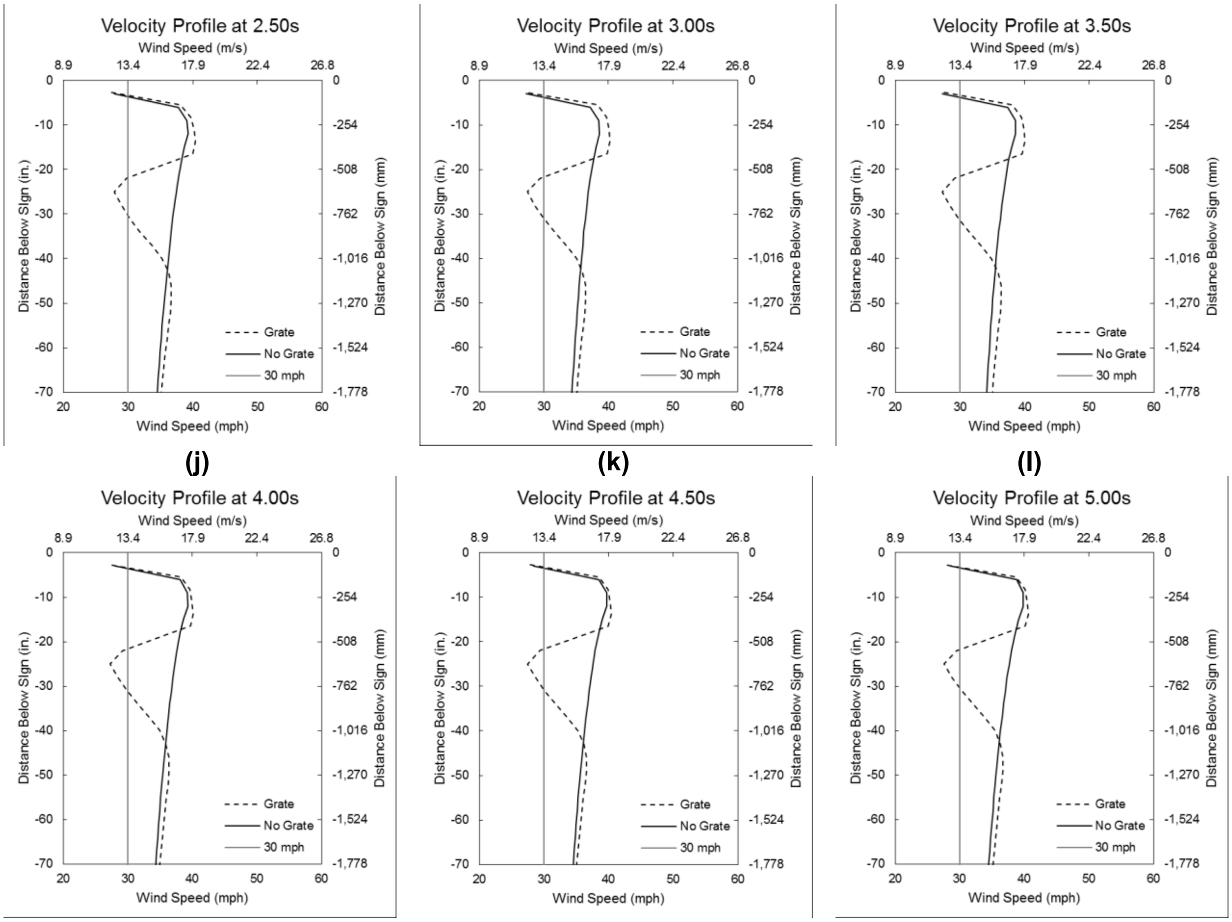

Velocity Profile at 2.50s

Velocity Profile at 3.00s

Velocity Profile at 3.50s

Velocity Profile at 4.00s

Velocity Profile at 4.50s

Velocity Profile at 5.00s

(j) (k) (l)

(m) (n) (o)

Figure 167 Velocity profile below the sign, for the medium sign and a wind speed of V=30 mph (13.4 m/s)

A2.5 – Medium Sign Velocity Profile at V=61.2 mph (27.4 m/s)

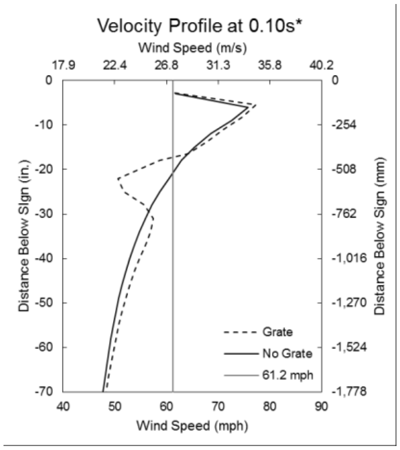

(a)

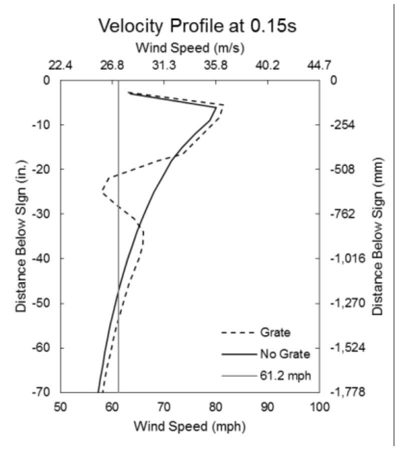

(b)

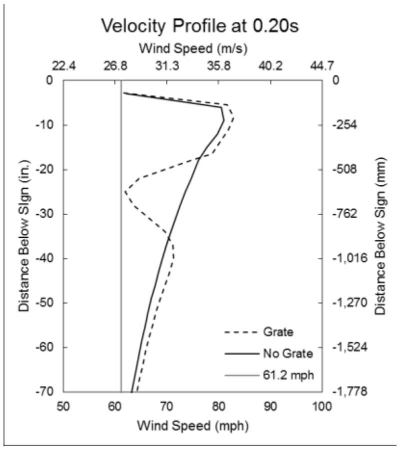

(c)

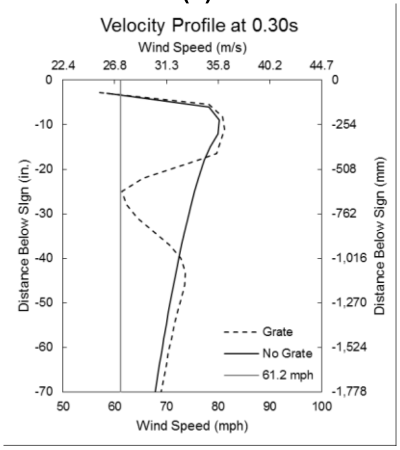

(d)

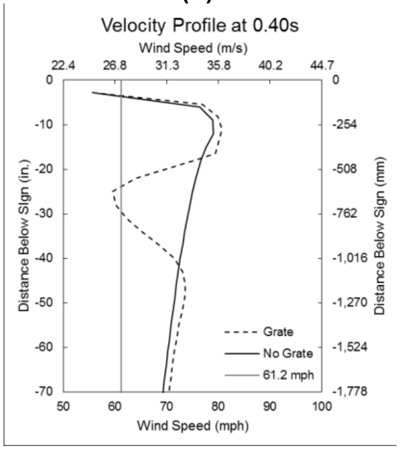

(e)

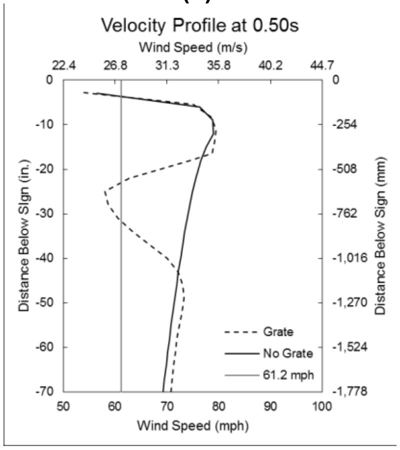

(f)

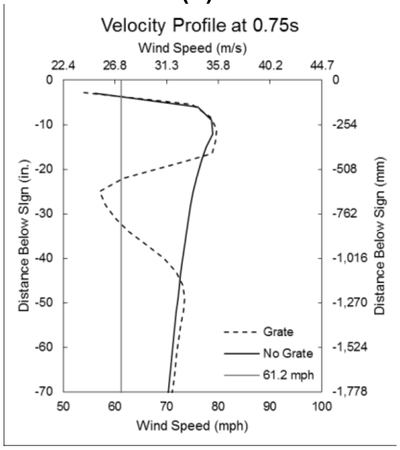

(g)

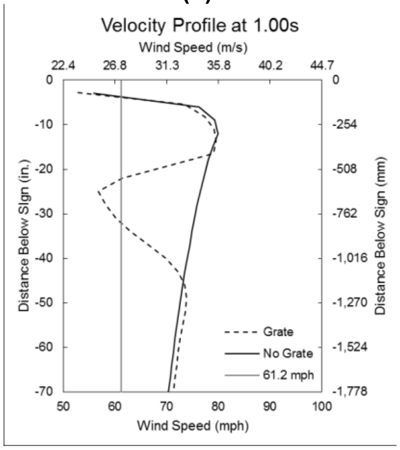

(h)

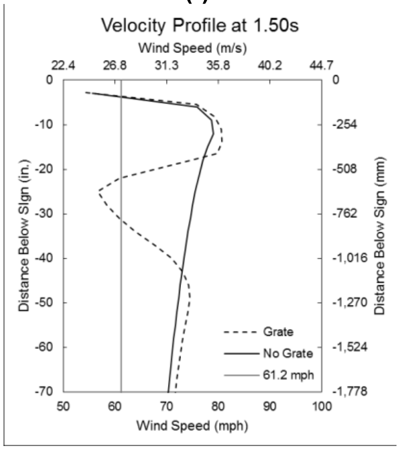

(i)

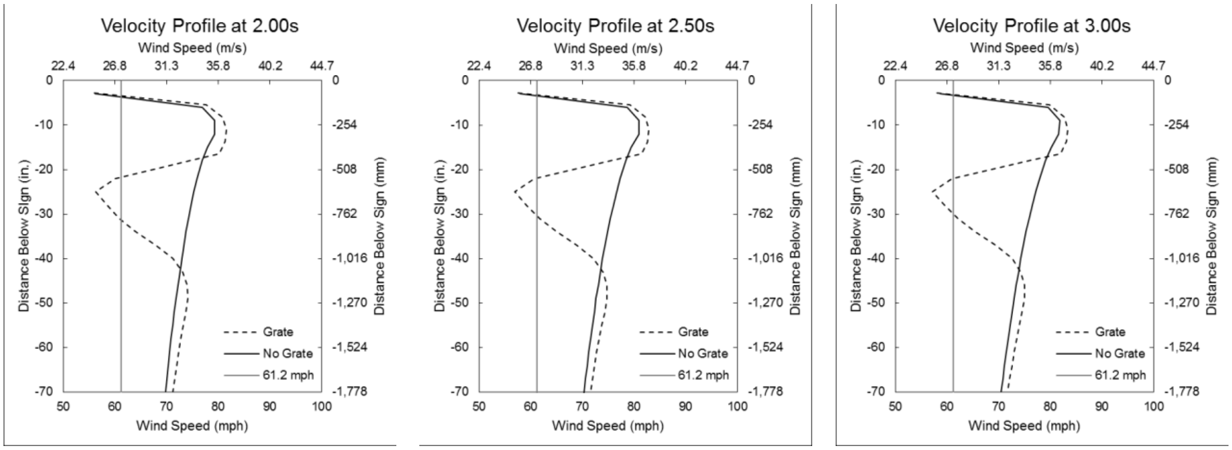

(j) (k) (l)

Figure 168 Velocity profile below the sign, for the medium sign and a wind speed of V=61.2 mph (27.4 m/s)

A2.6 – Medium Sign Velocity Profile at V=105mph (46.9 m/s)

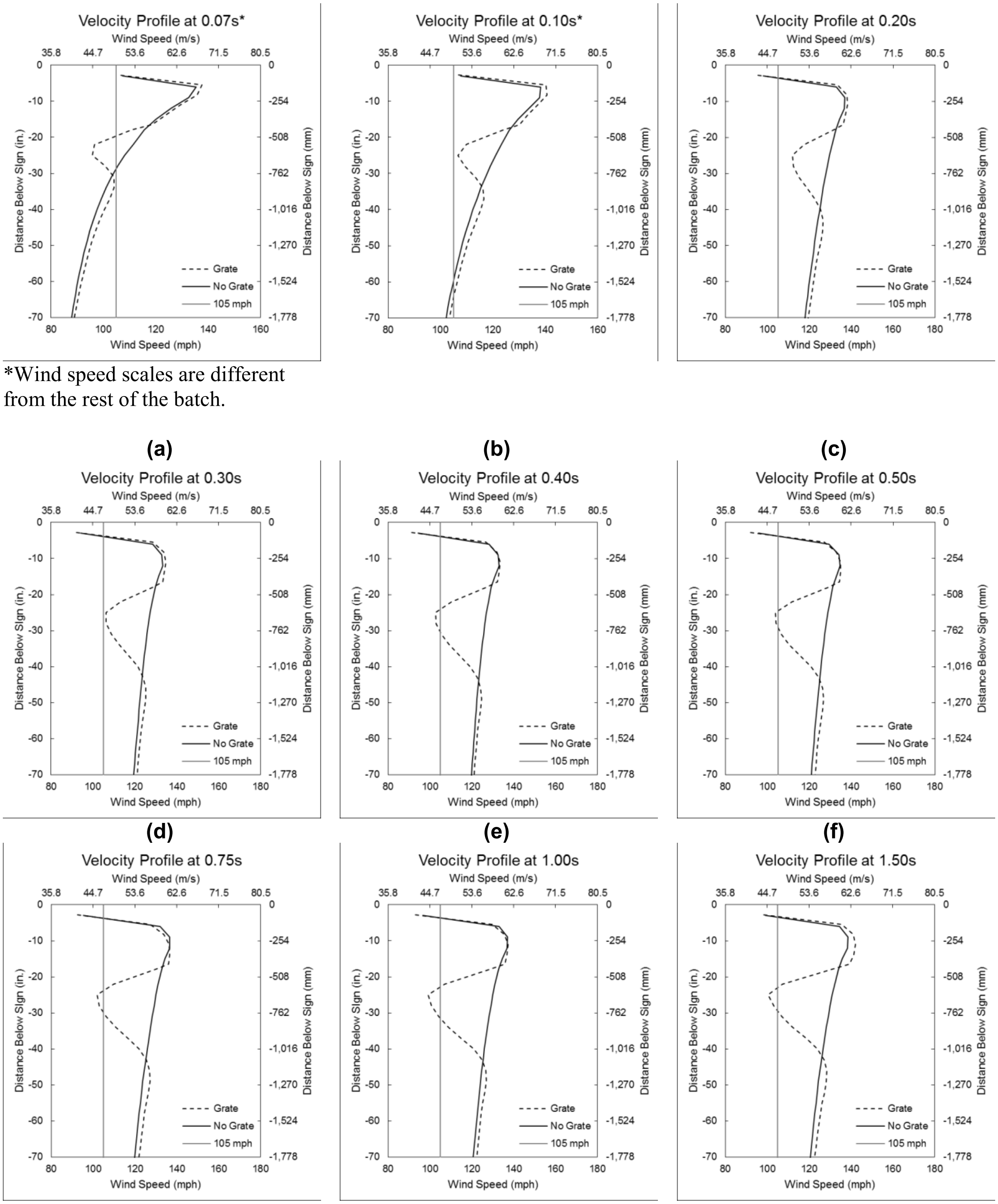

*Wind speed scales are different from the rest of the batch.

(a) (b) (c)

(d) (e) (f)

(g) (h) (i)

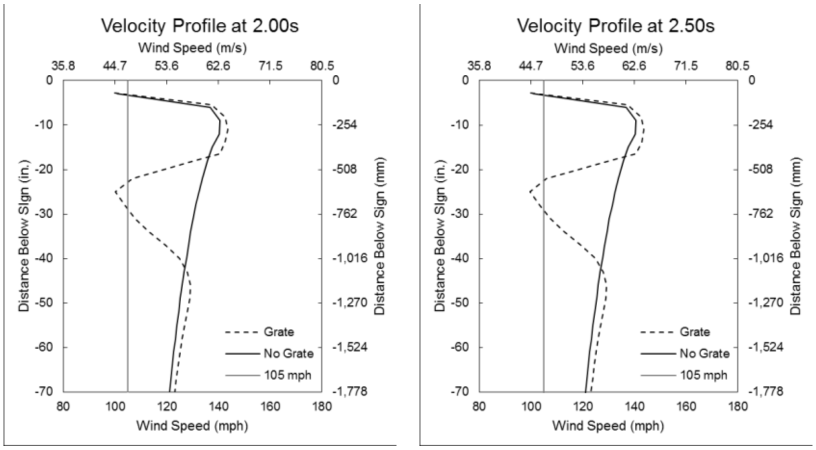

(j) **(k)**

Figure 169 Velocity profile below the sign, for the medium sign and a wind speed of V=105mph (46.9 m/s)

A2.7 – Small Sign Velocity Profile at V=30 mph (13.4 m/s)

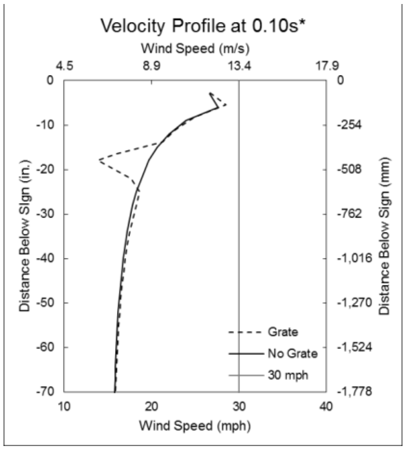

*Wind speed scales are different from the rest of the batch.

(a)

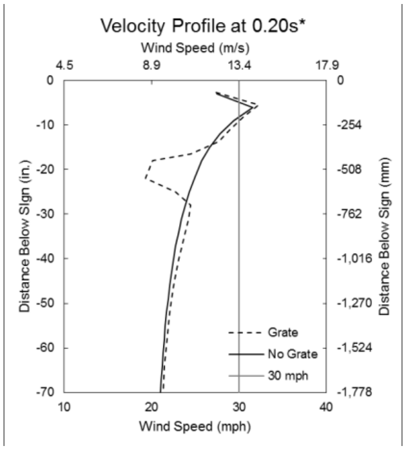

(b)

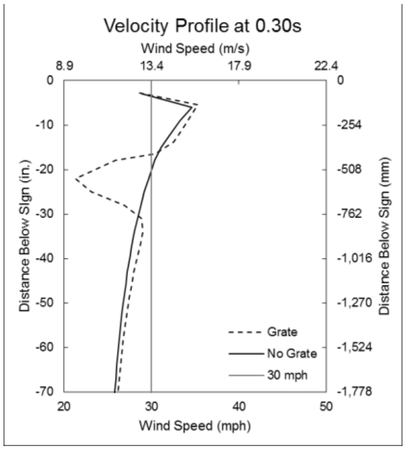

(c)

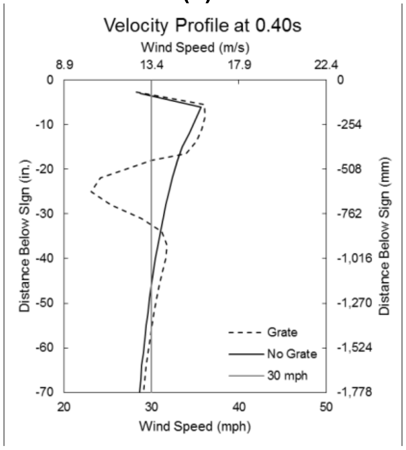

(d)

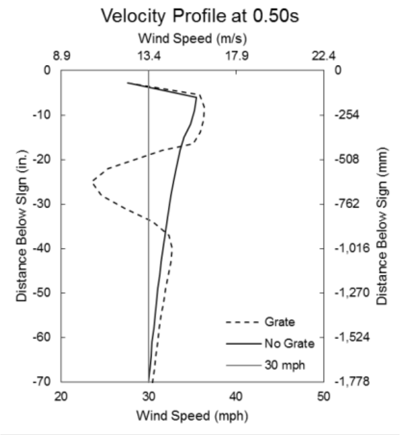

(e)

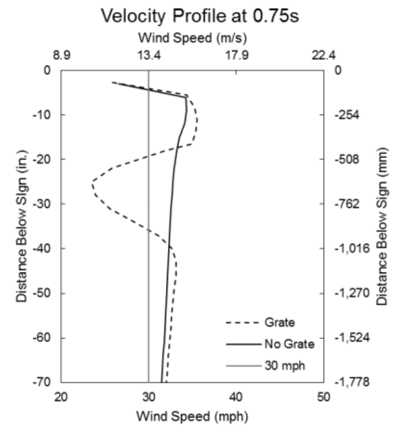

(f)

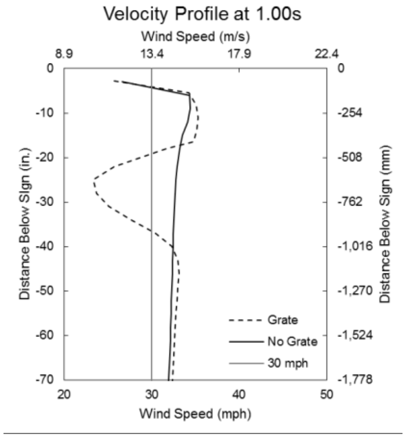

(g)

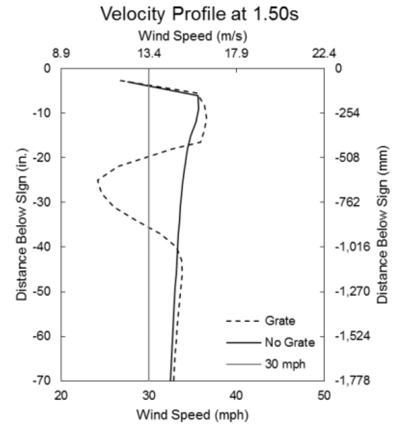

(h)

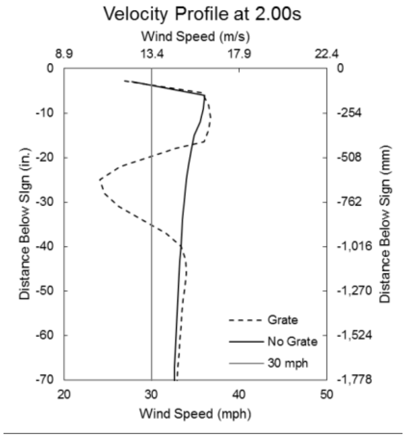

(i)

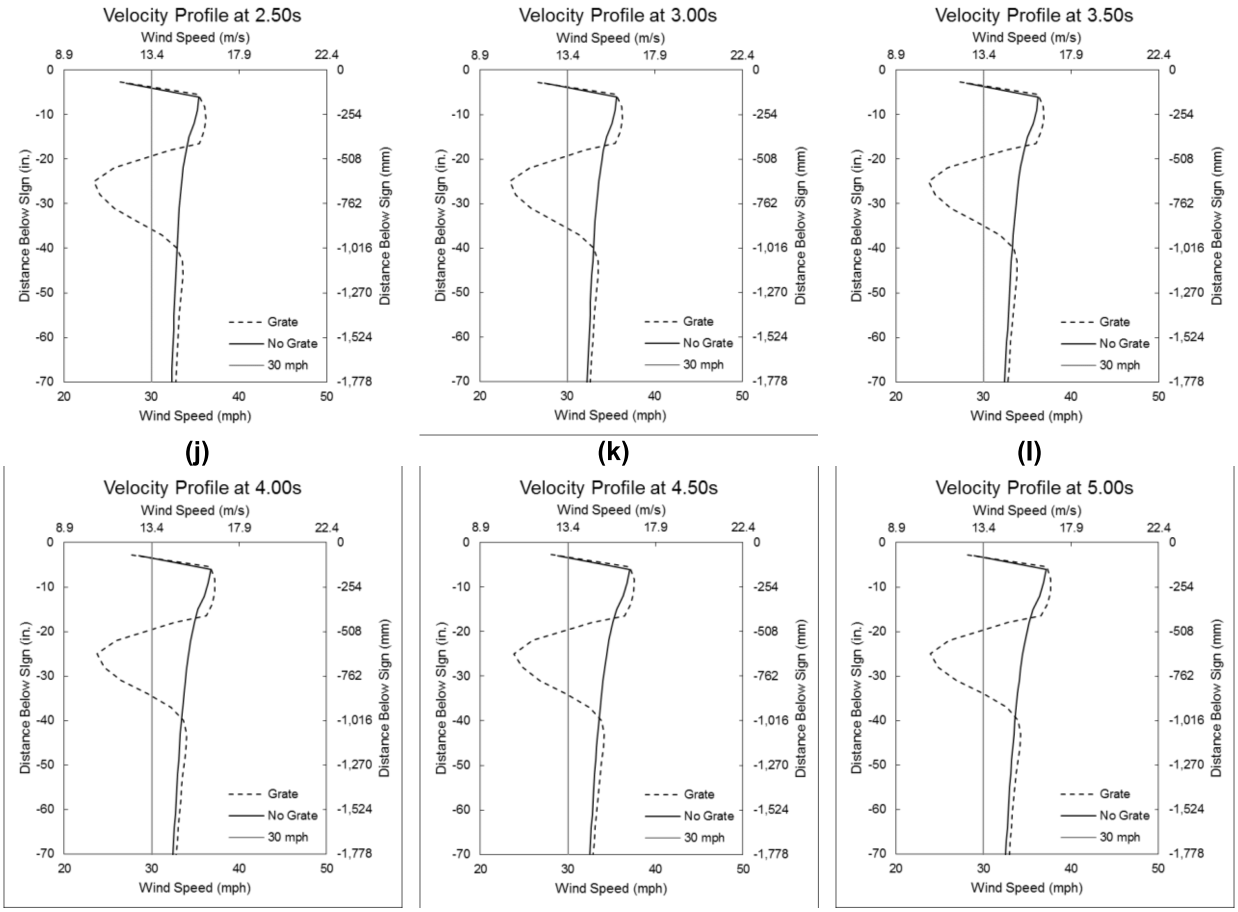
Velocity Profile at 2.50s

Velocity Profile at 3.00s

Velocity Profile at 3.50s

Velocity Profile at 4.00s

Velocity Profile at 4.50s

Velocity Profile at 5.00s

(j) (k) (l)

(m) (n) (o)

Figure 170 Velocity profile below the sign, for the small sign and a wind speed of 30 mph (13.4 m/s)

A2.8 – Small Sign Velocity Profile at V=61.2 mph (27.4 m/s)

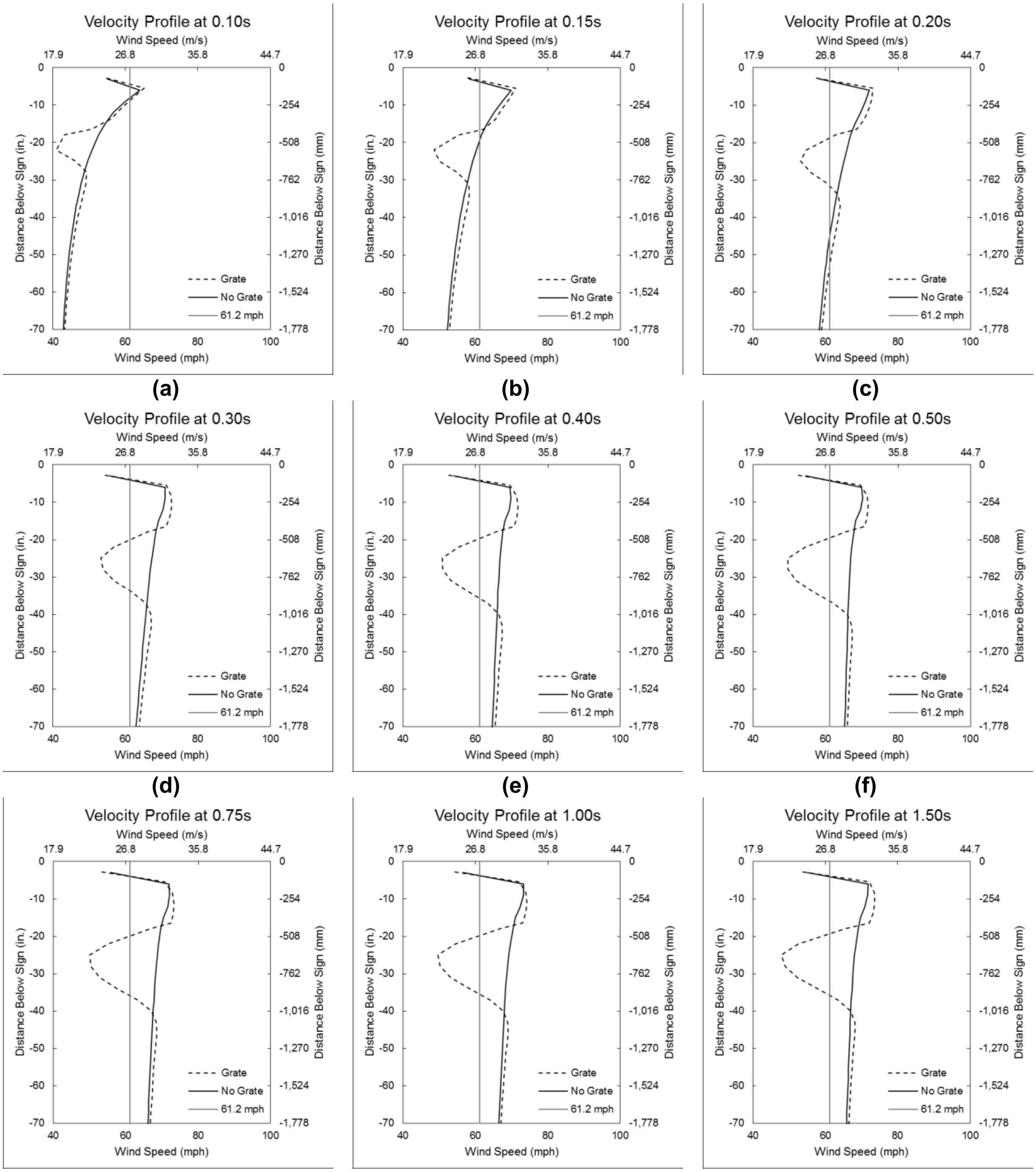

(a) (b) (c)

(d) (e) (f)

(g) (h) (i)

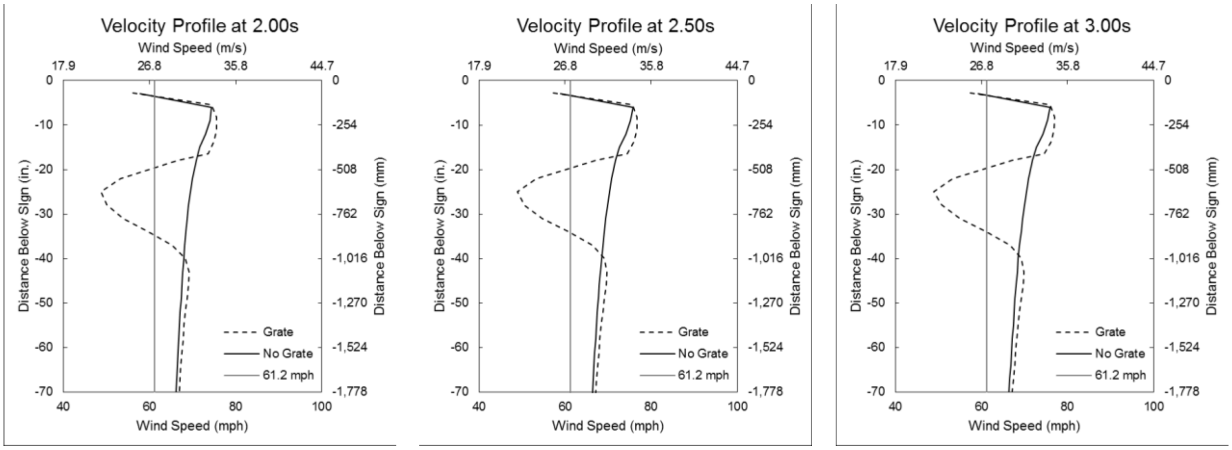

(j) (k) (l)

Figure 171 Velocity profile below the sign, for the small sign and a wind speed of 61.2 mph (27.4 m/s)

A2.9 – Small Sign Velocity Profile at V=105mph (46.9 m/s)

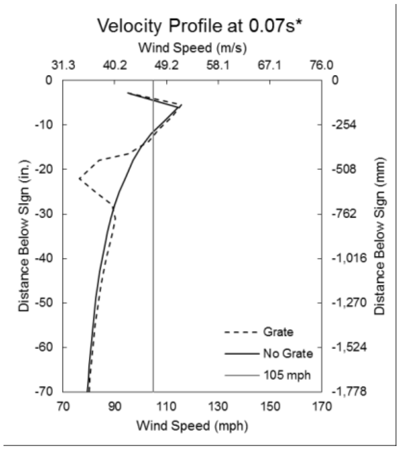

*Wind speed scales are different from the rest of the batch.

(a)

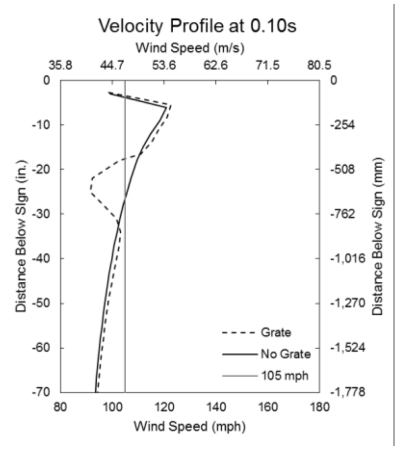

(b)

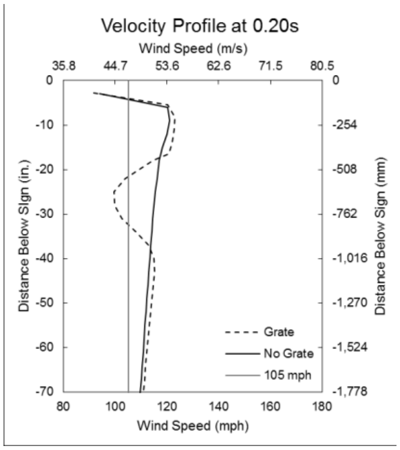

(c)

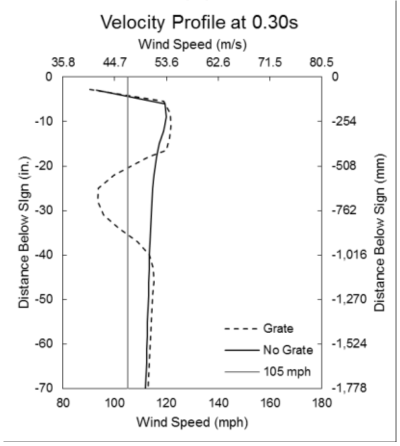

(d)

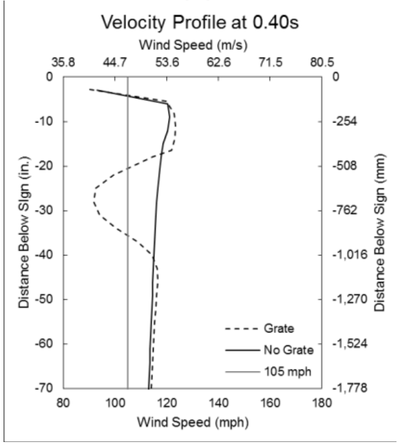

(e)

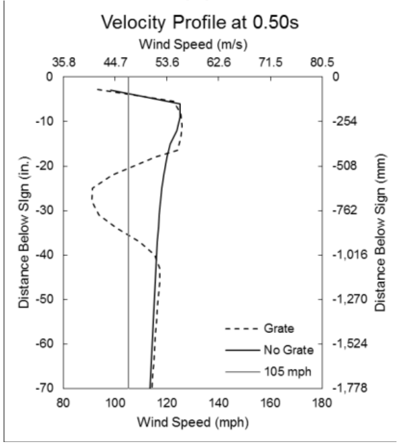

(f)

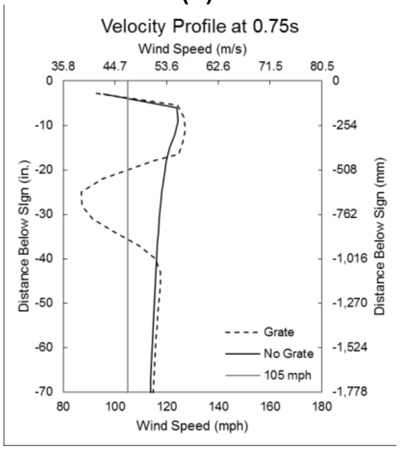

(g)

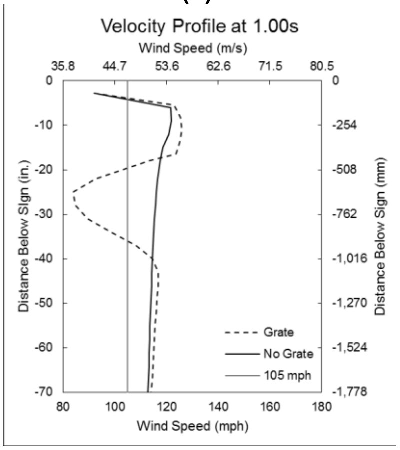

(h)

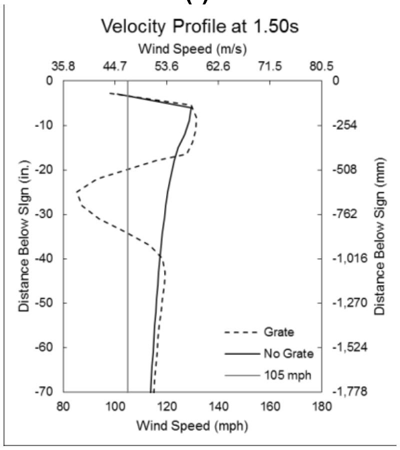

(i)

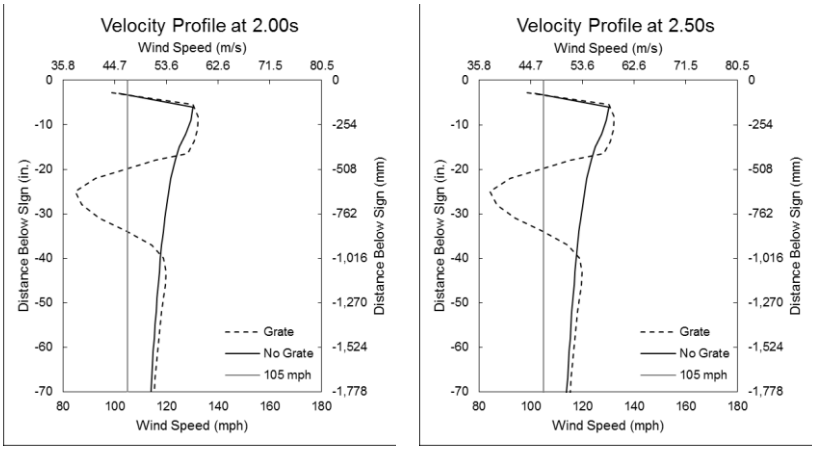

(j) **(k)** **(l)**

Figure 172 Velocity profile below the sign, for the small sign and a wind speed of V=105mph (46.9 m/s)

APPENDIX A3

Table 19 Displacements at V=30 mph (13.4 m/s)

Model	ΔUZ				ΔUY			
	w/ Walkway		w/o Walkway		w/ Walkway		w/o Walkway	
	in.	mm	in.	mm	in.	mm	in.	mm
S20x12-L20-P25	5.13	130.38	4.96	125.91	0.13	3.26	0.04	0.90
S20x12-L20-P27	5.47	139.06	5.29	134.33	0.14	3.44	0.04	0.91
S20x12-L20-P29	5.88	149.40	5.64	143.31	0.14	3.65	0.04	1.04
S20x12-L16-P25	3.88	98.67	3.76	95.43	0.10	2.64	0.03	0.82
S20x12-L16-P27	4.15	105.51	4.05	102.90	0.11	2.81	0.03	0.84
S20x12-L16-P29	4.46	113.24	4.31	109.51	0.11	2.91	0.03	0.86
S20x12-L12-P25	2.88	73.23	2.72	69.18	0.07	1.77	0.02	0.52
S20x12-L12-P27	3.12	79.37	2.99	75.96	0.08	2.03	0.03	0.69
S20x12-L12-P29	3.40	86.24	3.23	82.09	0.09	2.41	0.03	0.83
S16x9-L20-P25	3.44	87.29	3.54	89.81	0.05	1.36	0.05	1.21
S16x9-L20-P27	3.65	92.68	3.72	94.52	0.05	1.39	0.05	1.20
S16x9-L20-P29	3.90	98.98	3.95	100.39	0.06	1.46	0.05	1.37
S16x9-L16-P25	2.52	63.95	2.53	64.37	0.04	1.08	0.03	0.83
S16x9-L16-P27	2.70	68.52	2.73	69.23	0.05	1.24	0.04	1.06
S16x9-L16-P29	2.89	73.48	2.91	73.96	0.05	1.38	0.05	1.24
S16x9-L12-P25	1.71	43.31	1.71	43.36	0.03	0.69	0.02	0.54
S16x9-L12-P27	1.87	47.39	1.87	47.57	0.03	0.89	0.03	0.72
S16x9-L12-P29	2.03	51.51	2.04	51.83	0.05	1.17	0.03	0.82
S12x6-L20-P25	2.08	52.88	2.13	54.22	0.04	0.92	0.03	0.67
S12x6-L20-P27	2.23	56.53	2.27	57.60	0.04	1.09	0.03	0.84
S12x6-L20-P29	2.38	60.35	2.42	61.42	0.05	1.24	0.04	0.91
S12x6-L16-P25	1.46	36.97	1.47	37.35	0.03	0.68	0.02	0.56
S12x6-L16-P27	1.58	40.22	1.60	40.75	0.03	0.79	0.02	0.61
S12x6-L16-P29	1.74	44.13	1.75	44.36	0.04	0.91	0.03	0.65
S12x6-L12-P25	0.97	24.54	0.97	24.74	0.02	0.58	0.02	0.42
S12x6-L12-P27	1.07	27.23	1.09	27.68	0.02	0.60	0.02	0.48
S12x6-L12-P29	1.20	30.41	1.19	30.33	0.03	0.66	0.02	0.52

Table 20 Top Box-Connection Stresses at V=30 mph (13.4 m/s)

Model	S33				S11			
	w/ Walkway		w/o Walkway		w/ Walkway		w/o Walkway	
	ksi	MPa	ksi	MPa	ksi	MPa	ksi	MPa
S20x12-L20-P25	3.91	26.98	3.89	26.82	0.09	0.65	0.03	0.23
S20x12-L20-P27	3.92	27.04	3.91	26.96	0.07	0.50	0.02	0.17
S20x12-L20-P29	3.91	26.95	3.93	27.11	0.06	0.43	0.02	0.14
S20x12-L16-P25	3.41	23.54	3.34	23.03	0.06	0.43	0.02	0.14
S20x12-L16-P27	3.41	23.53	3.37	23.23	0.05	0.35	0.02	0.11
S20x12-L16-P29	3.40	23.46	3.39	23.38	0.05	0.31	0.01	0.10
S20x12-L12-P25	2.89	19.93	2.83	19.54	0.04	0.26	0.01	0.10
S20x12-L12-P27	2.88	19.82	2.81	19.39	0.04	0.26	0.02	0.11
S20x12-L12-P29	2.88	19.88	2.85	19.64	0.04	0.25	0.01	0.10
S16x9-L20-P25	4.17	28.78	4.19	28.91	0.05	0.37	0.03	0.23
S16x9-L20-P27	4.19	28.87	4.18	28.84	0.04	0.25	0.02	0.16
S16x9-L20-P29	4.17	28.72	4.21	29.05	0.03	0.21	0.02	0.16
S16x9-L16-P25	3.58	24.71	3.60	24.81	0.03	0.23	0.02	0.14
S16x9-L16-P27	3.59	24.74	3.58	24.66	0.03	0.18	0.02	0.12
S16x9-L16-P29	3.57	24.65	3.55	24.48	0.03	0.18	0.02	0.14
S16x9-L12-P25	2.96	20.38	2.96	20.40	0.02	0.15	0.01	0.10
S16x9-L12-P27	2.96	20.42	2.95	20.35	0.02	0.15	0.02	0.11
S16x9-L12-P29	2.96	20.40	2.93	20.21	0.02	0.14	0.02	0.11
S12x6-L20-P25	2.02	13.93	2.02	13.95	0.01	0.08	0.01	0.06
S12x6-L20-P27	2.01	13.86	2.01	13.85	0.01	0.08	0.01	0.06
S12x6-L20-P29	2.00	13.80	1.99	13.73	0.01	0.07	0.01	0.06
S12x6-L16-P25	1.68	11.60	1.71	11.76	0.01	0.06	0.01	0.05
S12x6-L16-P27	1.69	11.67	1.72	11.83	0.01	0.06	0.01	0.05
S12x6-L16-P29	1.70	11.71	1.72	11.84	0.01	0.06	0.01	0.05
S12x6-L12-P25	1.34	9.25	1.37	9.45	0.01	0.05	0.01	0.04
S12x6-L12-P27	1.37	9.42	1.39	9.58	0.01	0.05	0.01	0.04
S12x6-L12-P29	1.38	9.53	1.39	9.60	0.01	0.04	0.01	0.04

Table 21 Bottom Box-Connection Stresses at V=30 mph (13.4 m/s)

Model	S33				S11			
	w/ Walkway		w/o Walkway		w/ Walkway		w/o Walkway	
	ksi	MPa	ksi	MPa	ksi	MPa	ksi	MPa
S20x12-L20-P25	5.67	39.11	5.56	38.37	0.16	1.10	0.06	0.40
S20x12-L20-P27	5.70	39.28	5.55	38.26	0.12	0.84	0.04	0.28
S20x12-L20-P29	5.70	39.31	5.52	38.05	0.10	0.71	0.04	0.24
S20x12-L16-P25	4.98	34.37	4.84	33.38	0.11	0.77	0.04	0.25
S20x12-L16-P27	5.02	34.61	4.83	33.33	0.09	0.62	0.03	0.21
S20x12-L16-P29	5.02	34.63	4.81	33.17	0.08	0.55	0.03	0.19
S20x12-L12-P25	4.29	29.60	4.11	28.32	0.07	0.50	0.03	0.17
S20x12-L12-P27	4.30	29.67	4.15	28.63	0.07	0.48	0.03	0.19
S20x12-L12-P29	4.28	29.51	4.10	28.24	0.07	0.49	0.03	0.18
S16x9-L20-P25	5.23	36.04	5.22	35.96	0.09	0.63	0.06	0.40
S16x9-L20-P27	5.24	36.13	5.20	35.87	0.06	0.43	0.04	0.28
S16x9-L20-P29	5.23	36.07	5.18	35.69	0.05	0.36	0.04	0.27
S16x9-L16-P25	4.47	30.79	4.43	30.52	0.06	0.44	0.04	0.27
S16x9-L16-P27	4.48	30.91	4.44	30.61	0.07	0.50	0.05	0.34
S16x9-L16-P29	4.49	30.98	4.45	30.71	0.05	0.34	0.04	0.26
S16x9-L12-P25	3.65	25.17	3.62	24.93	0.04	0.30	0.03	0.20
S16x9-L12-P27	3.68	25.38	3.67	25.29	0.06	0.42	0.04	0.31
S16x9-L12-P29	3.72	25.68	3.71	25.60	0.04	0.29	0.03	0.20
S12x6-L20-P25	2.40	16.58	2.43	16.77	0.02	0.14	0.01	0.10
S12x6-L20-P27	2.41	16.60	2.44	16.81	0.02	0.15	0.02	0.11
S12x6-L20-P29	2.41	16.62	2.45	16.86	0.02	0.14	0.01	0.10
S12x6-L16-P25	2.06	14.18	2.04	14.06	0.02	0.13	0.01	0.10
S12x6-L16-P27	2.05	14.13	2.02	13.93	0.02	0.14	0.02	0.11
S12x6-L16-P29	2.03	13.99	2.05	14.15	0.02	0.12	0.01	0.09
S12x6-L12-P25	1.68	11.60	1.67	11.50	0.02	0.12	0.01	0.09
S12x6-L12-P27	1.68	11.60	1.66	11.41	0.02	0.11	0.01	0.08
S12x6-L12-P29	1.67	11.49	1.68	11.57	0.01	0.09	0.01	0.08

Table 22 Pole Stresses at V=30 mph (13.4 m/s)

Model	S21			
	w/ Walkway		w/o Walkway	
	ksi	MPa	ksi	MPa
S20x12-L20-P25	3.42	23.56	3.23	22.27
S20x12-L20-P27	3.71	25.58	3.54	24.41
S20x12-L20-P29	3.96	27.31	3.91	26.94
S20x12-L16-P25	3.34	23.00	3.20	22.08
S20x12-L16-P27	3.46	23.87	3.44	23.73
S20x12-L16-P29	3.85	26.54	3.81	26.30
S20x12-L12-P25	3.35	23.07	3.12	21.52
S20x12-L12-P27	3.62	24.98	3.48	24.02
S20x12-L12-P29	4.04	27.83	3.81	26.26
S16x9-L20-P25	1.96	13.54	2.00	13.78
S16x9-L20-P27	2.15	14.86	2.25	15.49
S16x9-L20-P29	2.39	16.45	2.47	17.05
S16x9-L16-P25	1.93	13.32	1.98	13.64
S16x9-L16-P27	2.16	14.89	2.22	15.33
S16x9-L16-P29	2.36	16.28	2.42	16.65
S16x9-L12-P25	1.89	13.04	1.91	13.17
S16x9-L12-P27	2.08	14.36	2.12	14.60
S16x9-L12-P29	2.32	16.02	2.31	15.91
S12x6-L20-P25	1.38	9.52	1.46	10.04
S12x6-L20-P27	1.56	10.77	1.62	11.17
S12x6-L20-P29	1.71	11.76	1.73	11.92
S12x6-L16-P25	1.35	9.32	1.41	9.70
S12x6-L16-P27	1.52	10.48	1.54	10.65
S12x6-L16-P29	1.67	11.54	1.69	11.66
S12x6-L12-P25	1.30	8.95	1.30	8.95
S12x6-L12-P27	1.41	9.73	1.44	9.90
S12x6-L12-P29	1.55	10.66	1.57	10.84

Table 23 Displacements at V=61.2 mph (27.4 m/s)

Model	ΔUZ				ΔUY			
	w/ Walkway		w/o Walkway		w/ Walkway		w/o Walkway	
	in.	mm	in.	mm	in.	mm	in.	mm
S20x12-L20-P25	20.94	531.86	21.00	533.39	0.38	9.64	0.30	7.63
S20x12-L20-P27	22.36	567.91	22.39	568.58	0.42	10.66	0.34	8.72
S20x12-L20-P29	23.91	607.39	23.95	608.23	0.55	13.84	0.44	11.22
S20x12-L16-P25	16.34	414.98	16.44	417.60	0.30	7.70	0.24	6.08
S20x12-L16-P27	17.11	434.49	17.59	446.66	0.33	8.45	0.25	6.47
S20x12-L16-P29	18.26	463.84	18.29	464.63	0.35	8.77	0.27	6.85
S20x12-L12-P25	12.07	306.46	11.99	304.56	0.28	6.99	0.20	5.12
S20x12-L12-P27	13.18	334.75	13.13	333.49	0.26	6.59	0.20	5.09
S20x12-L12-P29	14.33	364.01	14.23	361.33	0.27	6.80	0.22	5.54
S16x9-L20-P25	14.10	358.10	14.39	365.49	0.30	7.58	0.21	5.46
S16x9-L20-P27	14.90	378.52	14.97	380.13	0.31	7.94	0.22	5.48
S16x9-L20-P29	15.77	400.64	15.85	402.50	0.33	8.48	0.22	5.49
S16x9-L16-P25	10.64	270.21	10.66	270.65	0.25	6.23	0.16	4.00
S16x9-L16-P27	11.35	288.17	11.33	287.78	0.25	6.25	0.18	4.63
S16x9-L16-P29	12.06	306.34	12.13	307.99	0.27	6.84	0.19	4.92
S16x9-L12-P25	7.55	191.86	7.46	189.55	0.18	4.67	0.11	2.90
S16x9-L12-P27	8.25	209.52	8.11	205.87	0.20	5.16	0.12	3.00
S16x9-L12-P29	8.91	226.39	8.80	223.51	0.21	5.22	0.13	3.21
S12x6-L20-P25	8.31	211.04	8.49	215.54	0.11	2.72	0.10	2.46
S12x6-L20-P27	8.89	225.90	9.08	230.57	0.10	2.58	0.09	2.37
S12x6-L20-P29	9.54	242.20	9.70	246.36	0.10	2.66	0.09	2.28
S12x6-L16-P25	5.92	150.47	6.06	153.98	0.09	2.40	0.08	1.95
S12x6-L16-P27	6.43	163.37	6.54	166.20	0.10	2.42	0.07	1.88
S12x6-L16-P29	6.93	176.08	7.07	179.54	0.09	2.23	0.08	1.96
S12x6-L12-P25	4.16	105.77	4.30	109.15	0.08	1.99	0.06	1.65
S12x6-L12-P27	4.56	115.80	4.70	119.30	0.08	2.06	0.06	1.61
S12x6-L12-P29	4.98	126.38	5.07	128.68	0.08	2.08	0.07	1.67

Table 24 Top Box-Connection Stresses at V=61.2 mph (27.4 m/s)

Model	S33				S11			
	w/ Walkway		w/o Walkway		w/ Walkway		w/o Walkway	
	ksi	MPa	ksi	MPa	ksi	MPa	ksi	MPa
S20x12-L20-P25	16.40	113.05	16.65	114.80	0.29	2.01	0.21	1.46
S20x12-L20-P27	16.39	113.01	16.73	115.33	0.26	1.77	0.19	1.31
S20x12-L20-P29	16.41	113.14	16.81	115.94	0.25	1.70	0.21	1.44
S20x12-L16-P25	14.25	98.24	14.30	98.61	0.21	1.42	0.15	1.06
S20x12-L16-P27	14.22	98.05	14.41	99.39	0.17	1.19	0.15	1.04
S20x12-L16-P29	14.15	97.57	14.52	100.11	0.16	1.10	0.15	1.01
S20x12-L12-P25	12.19	84.05	12.25	84.46	0.15	1.07	0.13	0.88
S20x12-L12-P27	12.13	83.62	12.18	83.96	0.13	0.87	0.12	0.84
S20x12-L12-P29	12.16	83.84	12.18	83.98	0.12	0.81	0.11	0.76
S16x9-L20-P25	17.30	119.31	17.23	118.83	0.25	1.74	0.12	0.81
S16x9-L20-P27	17.29	119.21	17.09	117.87	0.21	1.45	0.09	0.65
S16x9-L20-P29	17.19	118.53	17.09	117.83	0.18	1.23	0.09	0.59
S16x9-L16-P25	15.00	103.45	14.97	103.24	0.18	1.26	0.08	0.57
S16x9-L16-P27	15.00	103.39	14.86	102.46	0.15	1.05	0.07	0.49
S16x9-L16-P29	14.93	102.93	14.73	101.57	0.13	0.91	0.06	0.42
S16x9-L12-P25	12.54	86.48	12.52	86.34	0.13	0.91	0.06	0.40
S16x9-L12-P27	12.53	86.43	12.44	85.80	0.11	0.74	0.05	0.35
S16x9-L12-P29	12.49	86.14	12.31	84.90	0.10	0.70	0.05	0.35
S12x6-L20-P25	8.16	56.23	8.23	56.72	0.04	0.24	0.03	0.18
S12x6-L20-P27	8.13	56.03	8.17	56.34	0.03	0.21	0.02	0.17
S12x6-L20-P29	8.10	55.88	8.11	55.93	0.03	0.17	0.02	0.15
S12x6-L16-P25	6.84	47.16	7.01	48.36	0.03	0.20	0.02	0.16
S12x6-L16-P27	6.88	47.46	7.05	48.58	0.03	0.17	0.02	0.14
S12x6-L16-P29	6.92	47.71	7.04	48.52	0.02	0.16	0.02	0.13
S12x6-L12-P25	5.59	38.55	5.74	39.54	0.02	0.14	0.02	0.11
S12x6-L12-P27	5.64	38.87	5.78	39.88	0.02	0.13	0.01	0.10
S12x6-L12-P29	5.69	39.23	5.77	39.77	0.02	0.12	0.01	0.09

Table 25 Bottom Box-Connection Stresses at V=61.2 mph (27.4 m/s)

Model	S33				S11			
	w/ Walkway		w/o Walkway		w/ Walkway		w/o Walkway	
	ksi	MPa	ksi	MPa	ksi	MPa	ksi	MPa
S20x12-L20-P25	23.84	164.35	23.88	164.62	0.48	3.31	0.36	2.45
S20x12-L20-P27	23.92	164.93	23.80	164.13	0.43	2.94	0.32	2.19
S20x12-L20-P29	23.93	164.99	23.67	163.18	0.41	2.86	0.35	2.41
S20x12-L16-P25	20.94	144.35	20.85	143.78	0.36	2.48	0.28	1.92
S20x12-L16-P27	21.05	145.12	20.80	143.44	0.31	2.13	0.27	1.85
S20x12-L16-P29	21.04	145.07	20.69	142.63	0.28	1.91	0.26	1.78
S20x12-L12-P25	18.03	124.30	17.84	123.02	0.28	1.96	0.22	1.52
S20x12-L12-P27	18.13	125.03	17.83	122.97	0.25	1.73	0.21	1.43
S20x12-L12-P29	17.96	123.87	17.75	122.36	0.22	1.55	0.19	1.33
S16x9-L20-P25	21.54	148.52	21.32	147.00	0.42	2.87	0.20	1.39
S16x9-L20-P27	21.56	148.68	21.27	146.63	0.36	2.47	0.16	1.11
S16x9-L20-P29	21.51	148.34	21.17	145.96	0.30	2.05	0.14	1.00
S16x9-L16-P25	18.49	127.50	18.26	125.88	0.34	2.34	0.16	1.11
S16x9-L16-P27	18.54	127.86	18.30	126.20	0.28	1.92	0.13	0.92
S16x9-L16-P29	18.57	128.07	18.37	126.63	0.24	1.64	0.11	0.77
S16x9-L12-P25	15.63	107.74	15.23	105.02	0.25	1.72	0.11	0.79
S16x9-L12-P27	15.48	106.74	15.39	106.08	0.21	1.44	0.10	0.66
S16x9-L12-P29	15.61	107.62	15.51	106.93	0.20	1.38	0.10	0.68
S12x6-L20-P25	9.77	67.34	9.79	67.53	0.07	0.47	0.05	0.37
S12x6-L20-P27	9.73	67.06	9.86	68.01	0.07	0.46	0.05	0.33
S12x6-L20-P29	9.72	67.03	9.89	68.19	0.05	0.36	0.04	0.30
S12x6-L16-P25	8.51	58.71	8.51	58.69	0.06	0.42	0.05	0.32
S12x6-L16-P27	8.47	58.38	8.41	57.97	0.05	0.37	0.04	0.27
S12x6-L16-P29	8.37	57.70	8.36	57.63	0.05	0.33	0.04	0.25
S12x6-L12-P25	7.09	48.88	7.09	48.90	0.05	0.31	0.04	0.26
S12x6-L12-P27	7.05	48.64	7.00	48.24	0.04	0.29	0.03	0.23
S12x6-L12-P29	6.95	47.94	6.91	47.61	0.04	0.24	0.03	0.20

Table 26 Pole Stresses at V=61.2 mph (27.4 m/s)

Model	S21			
	w/ Walkway		w/o Walkway	
	ksi	MPa	ksi	MPa
S20x12-L20-P25	14.13	97.43	13.79	95.11
S20x12-L20-P27	15.22	104.91	15.17	104.59
S20x12-L20-P29	16.41	113.14	16.75	115.48
S20x12-L16-P25	13.96	96.26	13.50	93.06
S20x12-L16-P27	14.43	99.46	14.84	102.31
S20x12-L16-P29	16.16	111.42	16.43	113.32
S20x12-L12-P25	14.08	97.08	13.55	93.40
S20x12-L12-P27	14.96	103.13	15.06	103.81
S20x12-L12-P29	16.93	116.72	16.52	113.87
S16x9-L20-P25	8.04	55.41	8.17	56.35
S16x9-L20-P27	8.85	61.04	9.16	63.15
S16x9-L20-P29	9.81	67.62	10.03	69.16
S16x9-L16-P25	7.90	54.49	8.16	56.25
S16x9-L16-P27	8.76	60.40	9.10	62.78
S16x9-L16-P29	9.75	67.24	9.88	68.15
S16x9-L12-P25	8.01	55.25	8.04	55.47
S16x9-L12-P27	8.76	60.39	8.90	61.36
S16x9-L12-P29	9.70	66.90	9.71	66.93
S12x6-L20-P25	5.55	38.27	5.84	40.24
S12x6-L20-P27	6.24	43.00	6.42	44.29
S12x6-L20-P29	6.76	46.61	7.09	48.90
S12x6-L16-P25	5.54	38.22	5.65	38.96
S12x6-L16-P27	6.18	42.58	6.25	43.11
S12x6-L16-P29	6.69	46.12	6.59	45.41
S12x6-L12-P25	5.49	37.83	5.52	38.03
S12x6-L12-P27	5.97	41.15	6.01	41.46
S12x6-L12-P29	6.46	44.52	6.59	45.45

Table 27 Displacements at V=105mph (46.9 m/s)

Model	ΔUZ				ΔUY			
	w/ Walkway		w/o Walkway		w/ Walkway		w/o Walkway	
	in.	mm	in.	mm	in.	mm	in.	mm
S20x12-L20-P25	66.38	1686.08	64.51	1638.60	0.92	23.24	1.24	31.51
S20x12-L20-P27	70.87	1800.10	68.72	1745.60	0.94	23.82	1.14	29.08
S20x12-L20-P29	75.66	1921.82	73.27	1861.07	0.90	22.83	1.03	26.27
S20x12-L16-P25	49.78	1264.44	48.31	1227.16	0.82	20.79	1.12	28.47
S20x12-L16-P27	53.62	1362.03	52.04	1321.78	0.78	19.75	1.09	27.57
S20x12-L16-P29	57.76	1467.14	55.95	1421.13	0.79	20.04	1.00	25.46
S20x12-L12-P25	35.01	889.21	34.58	878.43	0.60	15.21	0.80	20.32
S20x12-L12-P27	38.28	972.20	37.76	959.16	0.60	15.29	0.85	21.67
S20x12-L12-P29	41.85	1062.90	40.92	1039.27	0.61	15.37	0.87	22.20
S16x9-L20-P25	42.93	1090.54	42.46	1078.49	0.47	11.83	0.42	10.56
S16x9-L20-P27	45.56	1157.32	45.12	1146.16	0.48	12.23	0.45	11.40
S16x9-L20-P29	47.75	1212.79	47.70	1211.65	0.52	13.17	0.48	12.14
S16x9-L16-P25	31.09	789.59	30.70	779.73	0.44	11.10	0.31	7.75
S16x9-L16-P27	33.31	846.15	32.86	834.56	0.39	9.96	0.27	6.89
S16x9-L16-P29	35.85	910.71	35.13	892.27	0.38	9.70	0.30	7.74
S16x9-L12-P25	21.26	539.89	21.18	537.89	0.31	7.76	0.36	9.11
S16x9-L12-P27	23.29	591.44	22.93	582.43	0.32	8.18	0.31	7.91
S16x9-L12-P29	25.25	641.31	24.85	631.13	0.34	8.62	0.27	6.97
S12x6-L20-P25	23.36	593.40	23.93	607.89	0.21	5.42	0.21	5.35
S12x6-L20-P27	24.87	631.64	25.39	645.02	0.24	6.22	0.22	5.66
S12x6-L20-P29	26.40	670.62	26.75	679.52	0.26	6.69	0.24	5.98
S12x6-L16-P25	17.36	441.01	17.96	456.22	0.19	4.80	0.20	5.16
S12x6-L16-P27	18.68	474.35	19.15	486.38	0.20	5.02	0.18	4.64
S12x6-L16-P29	19.96	506.86	20.67	524.97	0.22	5.51	0.20	4.97
S12x6-L12-P25	12.18	309.27	12.61	320.30	0.15	3.74	0.13	3.33
S12x6-L12-P27	13.37	339.55	13.91	353.20	0.15	3.88	0.14	3.52
S12x6-L12-P29	14.67	372.57	15.07	382.66	0.18	4.49	0.15	3.69

Table 28 Top Box-Connection Stresses at V=105mph (46.9 m/s)

Model	S33				S11			
	w/ Walkway		w/o Walkway		w/ Walkway		w/o Walkway	
	ksi	MPa	ksi	MPa	ksi	MPa	ksi	MPa
S20x12-L20-P25	48.76	336.22	48.78	336.35	0.73	5.03	0.57	3.95
S20x12-L20-P27	48.77	336.30	48.93	337.40	0.60	4.16	0.51	3.51
S20x12-L20-P29	48.66	335.53	49.18	339.12	0.51	3.51	0.44	3.06
S20x12-L16-P25	42.33	291.85	42.03	289.80	0.52	3.56	0.53	3.63
S20x12-L16-P27	42.32	291.78	42.15	290.62	0.43	2.95	0.47	3.23
S20x12-L16-P29	42.15	290.60	42.17	290.75	0.39	2.68	0.42	2.87
S20x12-L12-P25	35.59	245.36	35.49	244.71	0.36	2.47	0.42	2.86
S20x12-L12-P27	35.61	245.51	35.26	243.10	0.36	2.48	0.45	3.09
S20x12-L12-P29	35.40	244.10	35.48	244.60	0.32	2.20	0.41	2.84
S16x9-L20-P25	50.20	346.14	50.09	345.36	0.48	3.30	0.35	2.38
S16x9-L20-P27	50.05	345.13	49.73	342.89	0.35	2.39	0.26	1.77
S16x9-L20-P29	49.99	344.70	49.58	341.88	0.30	2.05	0.22	1.48
S16x9-L16-P25	43.44	299.53	43.40	299.24	0.34	2.33	0.22	1.55
S16x9-L16-P27	36.00	248.22	36.00	248.22	0.30	2.10	0.20	1.37
S16x9-L16-P29	43.25	298.23	42.77	294.88	0.23	1.61	0.16	1.09
S16x9-L12-P25	36.29	250.25	36.35	250.67	0.20	1.39	0.16	1.10
S16x9-L12-P27	36.27	250.08	36.13	249.13	0.18	1.22	0.14	0.93
S16x9-L12-P29	36.17	249.36	35.80	246.84	0.16	1.13	0.12	0.81
S12x6-L20-P25	23.36	161.09	23.56	162.46	0.11	0.72	0.08	0.52
S12x6-L20-P27	23.28	160.54	23.43	161.54	0.10	0.66	0.07	0.50
S12x6-L20-P29	23.24	160.24	23.30	160.63	0.09	0.60	0.07	0.52
S12x6-L16-P25	19.57	134.96	20.07	138.35	0.09	0.64	0.07	0.48
S12x6-L16-P27	19.72	135.95	20.20	139.29	0.08	0.58	0.06	0.43
S12x6-L16-P29	19.85	136.89	20.22	139.43	0.08	0.53	0.06	0.39
S12x6-L12-P25	16.20	111.71	16.62	114.63	0.07	0.47	0.04	0.26
S12x6-L12-P27	16.26	112.08	16.60	114.46	0.07	0.45	0.04	0.26
S12x6-L12-P29	16.34	112.65	16.60	114.43	0.06	0.44	0.04	0.27

Table 29 Bottom Box-Connection Stresses at V=105mph (46.9 m/s)

Model	S33				S11			
	w/ Walkway		w/o Walkway		w/ Walkway		w/o Walkway	
	ksi	MPa	ksi	MPa	ksi	MPa	ksi	MPa
S20x12-L20-P25	70.61	486.85	69.99	482.56	1.21	8.32	0.99	6.84
S20x12-L20-P27	70.92	488.96	69.81	481.37	1.03	7.13	0.86	5.96
S20x12-L20-P29	71.03	489.76	69.48	479.05	0.84	5.81	0.73	5.06
S20x12-L16-P25	62.08	428.03	61.22	422.12	0.91	6.26	0.90	6.18
S20x12-L16-P27	62.39	430.17	61.05	420.91	0.77	5.32	0.81	5.59
S20x12-L16-P29	62.38	430.12	61.08	421.13	0.71	4.90	0.71	4.91
S20x12-L12-P25	53.61	369.62	52.48	361.82	0.68	4.67	0.79	5.47
S20x12-L12-P27	53.40	368.19	52.29	360.55	0.66	4.53	0.82	5.64
S20x12-L12-P29	53.20	366.81	52.16	359.63	0.58	3.99	0.76	5.27
S16x9-L20-P25	62.43	430.46	61.73	425.64	0.80	5.50	0.60	4.12
S16x9-L20-P27	62.03	427.73	61.60	424.72	0.64	4.42	0.44	3.02
S16x9-L20-P29	62.45	430.57	61.36	423.11	0.51	3.49	0.38	2.59
S16x9-L16-P25	53.54	369.18	52.84	364.31	0.64	4.44	0.44	3.02
S16x9-L16-P27	36.00	248.23	36.00	248.22	0.79	5.43	0.51	3.53
S16x9-L16-P29	53.78	370.82	53.19	366.74	0.39	2.67	0.29	2.02
S16x9-L12-P25	44.71	308.30	44.11	304.15	0.42	2.87	0.32	2.18
S16x9-L12-P27	44.84	309.14	44.59	307.46	0.35	2.40	0.25	1.76
S16x9-L12-P29	45.23	311.89	44.99	310.21	0.33	2.25	0.22	1.52
S12x6-L20-P25	28.09	193.71	28.03	193.27	0.19	1.29	0.15	1.00
S12x6-L20-P27	27.81	191.75	28.09	193.71	0.19	1.30	0.15	1.02
S12x6-L20-P29	27.74	191.28	28.34	195.43	0.17	1.16	0.14	0.94
S12x6-L16-P25	24.43	168.47	24.49	168.88	0.19	1.28	0.13	0.93
S12x6-L16-P27	24.35	167.87	24.24	167.13	0.17	1.15	0.12	0.82
S12x6-L16-P29	24.12	166.29	23.99	165.44	0.16	1.11	0.12	0.80
S12x6-L12-P25	20.34	140.27	20.44	140.95	0.13	0.87	0.09	0.64
S12x6-L12-P27	20.29	139.88	20.47	141.16	0.11	0.78	0.09	0.60
S12x6-L12-P29	20.06	138.30	19.82	136.64	0.12	0.81	0.09	0.61

Table 30 Pole Stresses at V=105mph (46.9 m/s)

Model	S21			
	w/ Walkway		w/o Walkway	
	ksi	MPa	ksi	MPa
S20x12-L20-P25	42.24	291.24	40.47	279.05
S20x12-L20-P27	45.85	316.17	44.47	306.64
S20x12-L20-P29	48.74	336.03	49.12	338.65
S20x12-L16-P25	40.50	279.28	39.14	269.87
S20x12-L16-P27	42.52	293.19	43.40	299.25
S20x12-L16-P29	47.99	330.92	48.18	332.22
S20x12-L12-P25	40.46	278.97	39.20	270.27
S20x12-L12-P27	43.49	299.84	44.32	305.56
S20x12-L12-P29	49.10	338.51	48.56	334.84
S16x9-L20-P25	23.29	160.58	23.68	163.24
S16x9-L20-P27	26.77	184.60	26.60	183.38
S16x9-L20-P29	28.46	196.25	29.18	201.20
S16x9-L16-P25	22.94	158.18	23.63	162.90
S16x9-L16-P27	25.83	178.08	26.35	181.71
S16x9-L16-P29	28.26	194.84	28.93	199.46
S16x9-L12-P25	23.24	160.22	23.27	160.46
S16x9-L12-P27	25.42	175.26	25.69	177.11
S16x9-L12-P29	28.13	193.94	27.98	192.93
S12x6-L20-P25	16.03	110.51	16.91	116.56
S12x6-L20-P27	18.01	124.16	18.59	128.18
S12x6-L20-P29	19.52	134.62	19.85	136.89
S12x6-L16-P25	16.11	111.04	16.94	116.79
S12x6-L16-P27	17.89	123.36	18.96	130.74
S12x6-L16-P29	19.67	135.60	19.35	133.43
S12x6-L12-P25	16.00	110.30	16.43	113.26
S12x6-L12-P27	17.05	117.57	17.29	119.24
S12x6-L12-P29	18.51	127.65	19.96	137.60

Appendix B

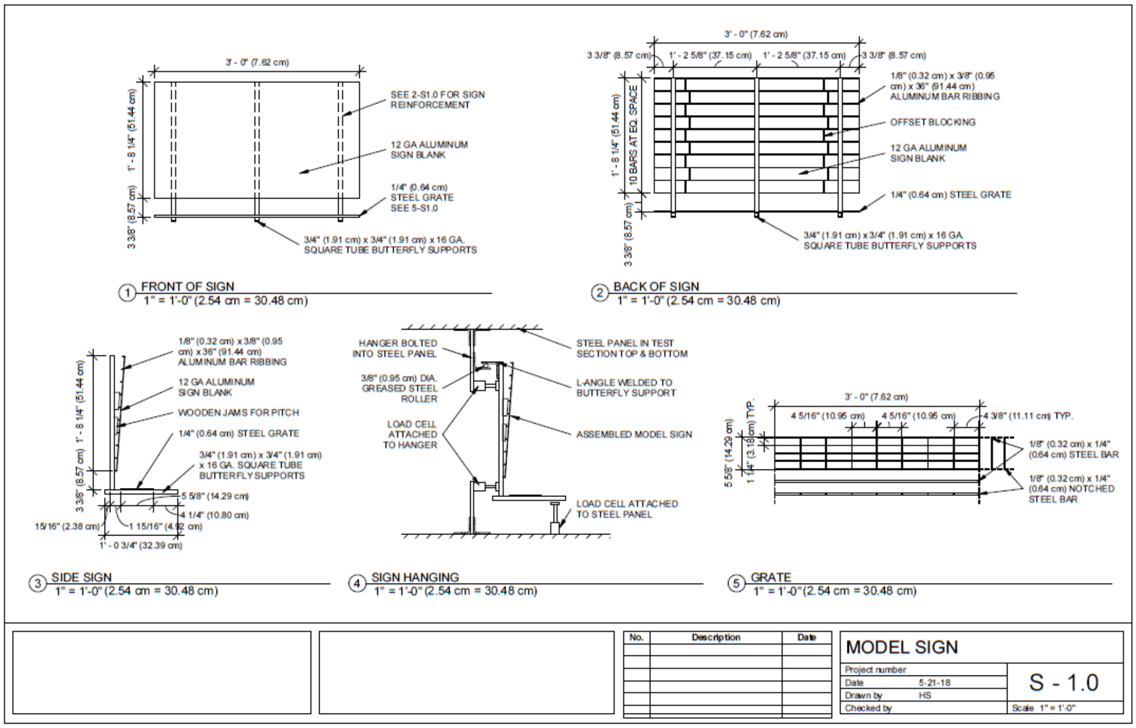

Figure 173 Schematic of model sign used in wind tunnel testing at the University of Kansas

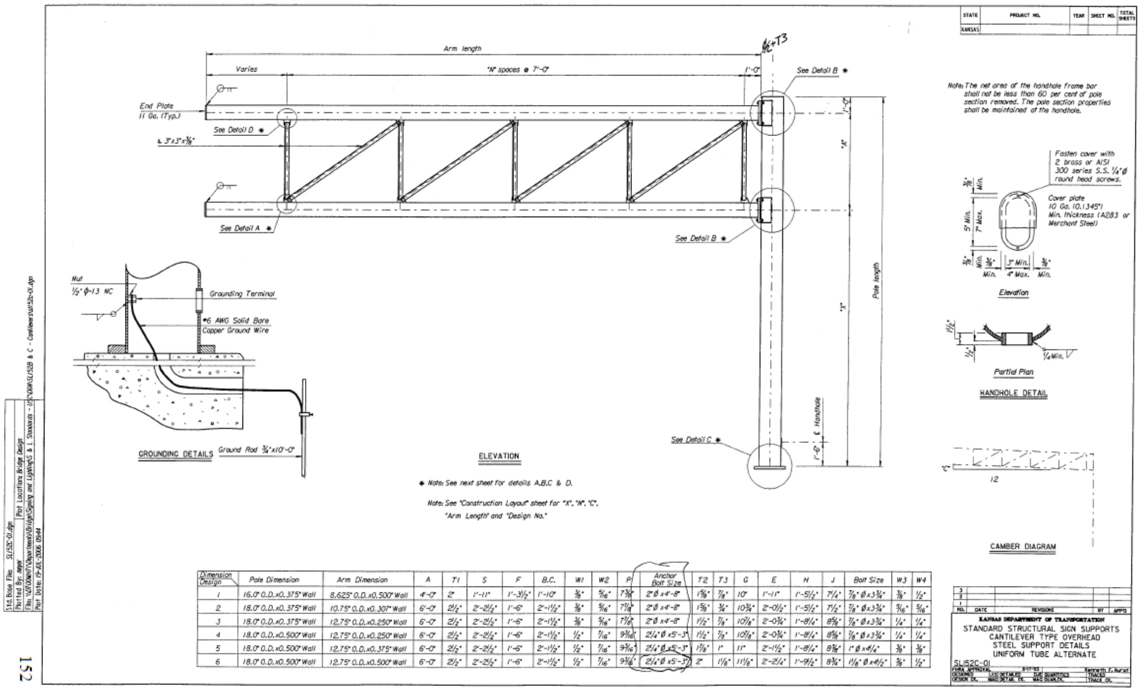

✱ Note: See next sheet for details A,B,C & D.

Note: See "Construction Layout" sheet for "X", "N", "C", "Arm Length" and "Design No."

Dimension / Design	Pole Dimension	Arm Dimension	A	T1	S	F	B.C.	W1	W2	P	Anchor Bolt Size	T2	T3	G	E	H	J	Bolt Size	W3	W4
1	16.0" O.D.x0.375" Wall	8.625" O.D.x0.500" Wall	4'-0"	2"	1'-11"	1'-3½"	1'-10"	⅜"	5/16"	7⅜"	2"Ø x4'-8"	1⅝"	⅞"	10"	1'-11"	1'-5½"	7¼"	⅞" Ø x3¾"	⅜"	½"
2	18.0" O.D.x0.375" Wall	10.75" O.D.x0.307" Wall	6'-0"	2½"	2'-2½"	1'-6"	2'-1½"	⅜"	5/16"	7⅞"	2"Ø x4'-8"	1⅝"	¾"	10¾"	2'-0½"	1'-5½"	7½"	⅞" Ø x3¾"	5/16"	5/16"
3	18.0" O.D.x0.375" Wall	12.75" O.D.x0.250" Wall	6'-0"	2½"	2'-2½"	1'-6"	2'-1½"	⅜"	5/16"	7⅞"	2"Ø x4'-8"	1½"	⅞"	10⅞"	2'-0¾"	1'-8¼"	8⅝"	⅞" Ø x3¾"	¼"	¼"
4	18.0" O.D.x0.500" Wall	12.75" O.D.x0.250" Wall	6'-0"	2½"	2'-2½"	1'-6"	2'-1½"	½"	7/16"	9 3/16"	2¼"Ø x5'-3"	1½"	⅞"	10⅞"	2'-0¾"	1'-8¼"	8⅝"	⅞" Ø x3¾"	¼"	¼"
5	18.0" O.D.x0.500" Wall	12.75" O.D.x0.375" Wall	6'-0"	2½"	2'-2½"	1'-6"	2'-1½"	½"	7/16"	9 3/16"	2¼"Ø x5'-3"	1⅞"	1"	11"	2'-1½"	1'-8¼"	8¾"	1" Ø x4¼"	⅜"	⅜"
6	18.0" O.D.x0.500" Wall	12.75" O.D.x0.500" Wall	6'-0"	2½"	2'-2½"	1'-6"	2'-1½"	½"	7/16"	9 3/16"	2¼"Ø x5'-3"	2"	1⅛"	11⅛"	2'-2¼"	1'-9½"	8¾"	1⅛" Ø x4½"	⅜"	½"

Figure 174 KDOT standard detail for cantilevered structural sign supports

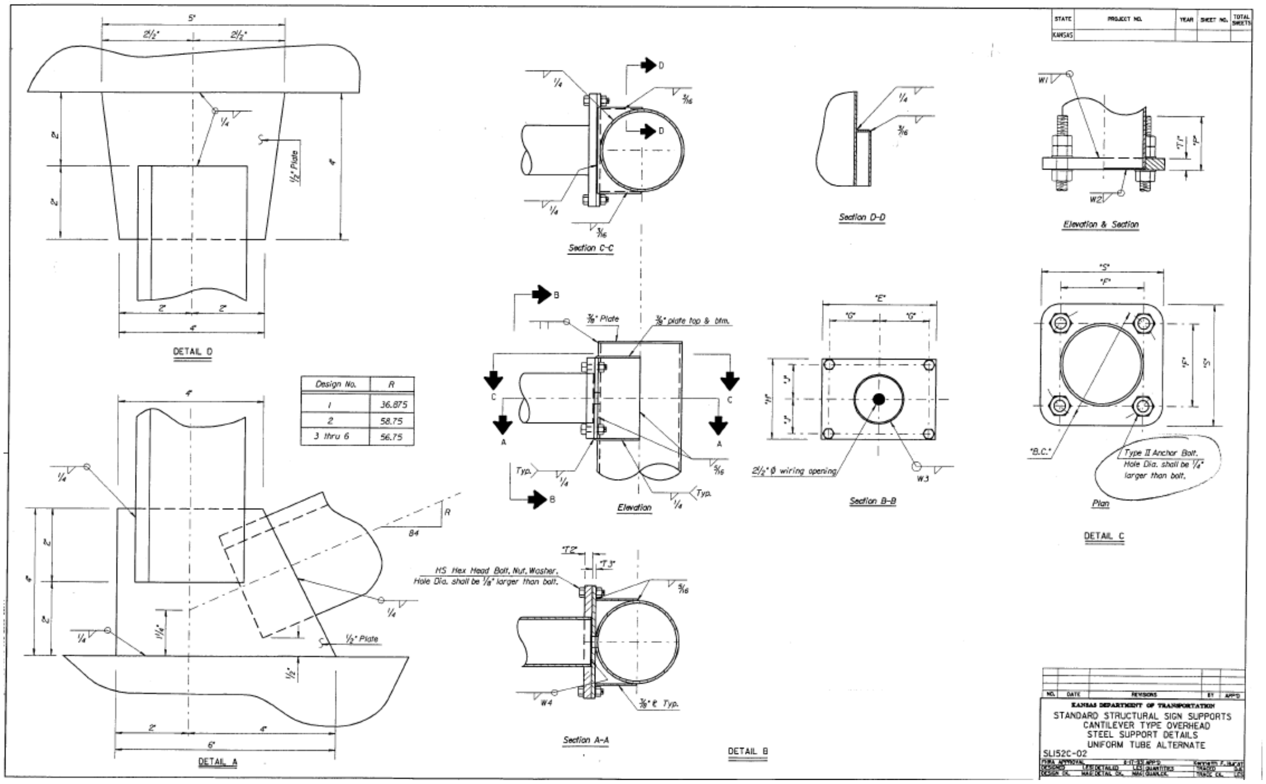

Figure 175 KDOT standard detail for cantilevered structural sign supports

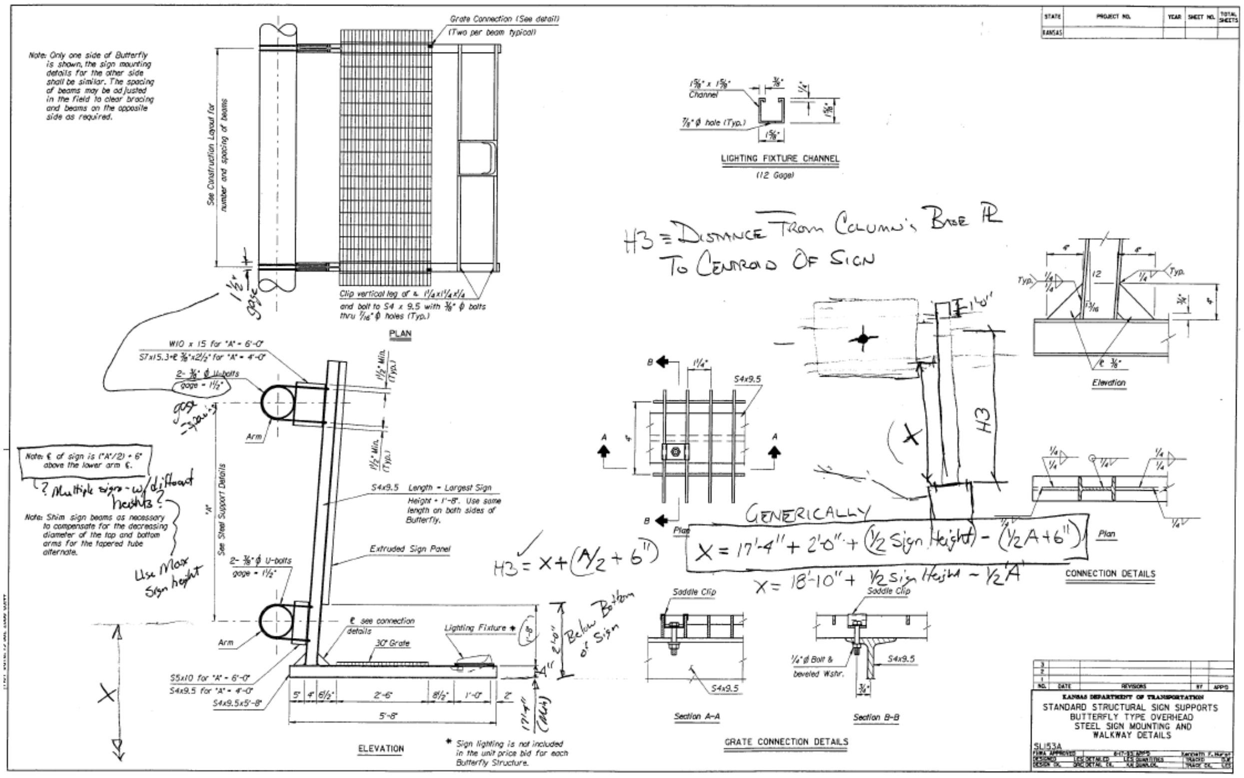

Figure 176 KDOT standard detail for cantilevered structural sign supports